universität wien

DISSERTATION

Titel der Dissertation

„The Catalytic Properties of Chabazite -

A Computational Study“

Verfasser

Mag. Florian Göltl

angestrebter akademischer Grad

Doktor der Naturwissenschaften (Dr. rer. nat.)

Wien, 2011

Studienkennzahl lt. Studienblatt:	A 411
Dissertationsgebiet lt. Studienblatt:	Physik
Betreuerin / Betreuer:	o. Univ.-Prof. i. R. Dr. Dipl.-Ing. Jürgen Hafner

Acknowledgements

I want to thank my supervisor Jürgen Hafner for giving me the chance to write a thesis in a highly interesting field. His support, advice and guidance made this thesis possible. Throughout all those years he has been the perfect role model as far as his passion for science is concerned.

I also want to thank Doris Vogtenhuber, Tomas Bučko and Michael Pöltl for kindly and patiently helping me with every problem I had concerning chemistry, zeolites or any battles I had to fight using computers or VASP over the last four years.

Special thanks go to Andreas Grüneis and Andris Gulans who did not only help me to arrive at a deeper understanding of the theoretical foundations but also made it possible for me to apply new methods implemented by them in VASP.

I also want to thank my colleagues Laurids Schimka, Thomas Franz, Lubomir Benco, Nikola Seriani, Joachim Paier, Judith Harl, Kerstin Hummer, Leif Eric Hintzsche, Martijn Marsman and Georg Kresse for discussion and advice.

Special thanks go to Sowmya Sathyanarayana Murthy for proof-reading this thesis which helped me to smoothen my sometimes edgy phrasing.

Last but not least I want to thank my parents for their generous support throughout my entire education.

Abstract

Zeolites are the most widely used catalysts in industry. Their special structure makes them model-systems for catalysis in confinement. The reactions themselves take place inside the material and can not be observed directly by experimental methods. To arrive at a fundamental understanding of the underlying processes the use of theoretical methods is required. Recent advances in methodology and increase in computational resources allow the use of high level methods for entire zeolite systems. In this thesis the impact of high level methods on the description of chabazite, the zeolite with the smallest unit cell, is investigated.

In the beginning we give a short overview of the applications of zeolites in general and a short review of two important catalytical processes, namely the adsorption and conversion of hydrocarbons in zeolites and NO removal from exhaust gases using zeolite catalysts.

It is followed by two chapters explaining the the theoretical foundations of this work. In these chapters a short review of the fundamentals of electronic structure calculations, their computational implementation and Jacob's Ladder of Density Functional Theory is given.

In the second part Cu- and Co-exchanged chabazite is investigated. For this system the description of d-states poses major difficulties for standard Generalized Gradient Approximations in the Density Functional Theory framework. In these chapters we critically review the impact of the addition of exact exchange in PBE0 and HSE hybrid functionals and compare their performance to PW91 and PBE density functionals. We test their performance in three areas, namely (i) structural properties, (ii) the description of optical properties and the DOS and (iii) adsorption of CO and NO.

The third part deals with adsorption of methane, ethane and propane in Na- and protonated chabazite. The main problem for electronic structure calculations in these systems is the inclusion of van der Waals interactions. The (semi-)local approximations of DFT are not able to capture these interactions correctly, but several approaches to solve this problem have been proposed. The addition of an empirical force field to standard DFT functionals (PBE-d), the truly nonlocal vdW-DF, the Adiabatic-Connection Fluctuation Dissipation Theorem in its Random Phase Approximation (RPA, RPA-HF) and second order Møller-Plesset perturbation theory (MP2). Results from these methods are compared with experiment and an extrapolation mechanism to account for finite temperature effects is proposed. We also justify this approach by comparing to MD-simulations using PBE-d.

Zusammenfassung

In industriellen katalytischen Prozessen sind Zeolithe heute die meistverwendeten Katalysatoren. Ihre spezielle poröse Struktur verleiht ihnen sehr spezielle Eigenschaften wie eine hohe Stabilität und hohe Selektivität. Katalytischen Prozesse in diesen Materialen finden typischerweise im inneren des Minerals statt was vor allem für das grundlegenden Verständnis eben dieser Prozesse theoretische Modellierung erforderlich macht. Die Verbesserung der Algorithmen und der Anstieg der Rechenleistung in den letzten Jahren ermöglicht nun den Einsatz sehr kostspieliger Methoden unter der Benützung von periodischen Randbedingungen. In dieser Arbeit wird der Einfluss dieser "high-level" Methoden auf die Beschreibung von Chabazit, dem Zeolith mit der kleinsten Einheitszelle, untersucht.

Die Arbeit beginnt mit einer kurzen Einführung über Anwendungen von Zeoliten im Allgemeinen und zu zwei katalytischen Anwendungen im speziellen, nämlich der Adsorption und Konversion von Alkanen in Zeoliten und der Entfernung von NO aus Abgasen mittels Zeolit-Katalysatoren.

Der folgende Teil behandelt die theoretischen Grundlagen. In kurzen Worten wird das grundlegende, elektronische Vielteilchenproblem sowie die Grundlagen der Dichtefunktionaltheorie sowie die aktuelle Implementierung dieser Methoden in Computerprogrammen dargelegt. Auch die Methoden unterschiedlicher Komplexität, die in der so genannten "Jacob's Ladder" der Dichtefunktionalthorie zusammengefasst sind, werden erklärt.

Im zweiten Teil wird Cu- und Co- ausgetauscher Chabazite untersucht. Für die Standardmethoden in der Dichtefunktionaltheorie, die sogennante Generalized Gradient Approximation, stellt die korrekte Beschreibung der d-Zustände von Übergangsmetallen große Probleme dar. Zur Lösung dieses Problems wird in so genannten Hybrid-Funktionalen Hartree-Fock Austausch mit Standard-Dichtefunktionalen gemischt. In diesem Teil wird die Effektivität dieses Ansatzes für die Hybrid Funktionale PBE0 und HSE untersucht. Resultate für Strukturen, elektronische Struktur und die Adsorption von CO und NO werden sowohl mit experimentellen Daten als auch mit den Standard-Dichtefunktionalen PBE und PW91 verglichen.

Der dritte Teil behandelt die Adsorption von Methan, Ethan und Propan in Na- und protoniertem Chabazit. Das Hauptproblem in diesen Systemen ist die Beschreibung der nicht-lokalen van der Waals Wechselwirkungen. Die (semi-)lokalen Näherungen der Dichtefunktionaltheorie können solche Wechselwirkungen prinzipiell nicht beschreiben. Um diese Problem zu lösen gibt es mehrere Ansätze: Die Addition eines empirischen Kraftfeldes (PBE-d), ein Dichtefunktional mit einem nicht-lokalen Korrelationsanteil (vdW-DF), das so genannte Adiabatic-Connection Fluctuation Dissipation Theorem in seiner Random-Phase Näherung sowie Møller-Plesset Störungstheorie zweiter Ordnung

(MP2). In diesem Teil der Arbeit wird die Effektivität dieser Methoden genau untersucht und mit dem Experiment verglichen. Um diesen Vergleich zu ermöglichen wird ein Extrapolationsmechanismus vorgeschlagen und mit Molekulardynamik-Rechnungen auf PBE-d Niveau verglichen.

Contents

1 Introduction

One of the most powerful tools in theoretical physics is the educated guess. We owe great achievements like the law of gravity, the quantization of radiation or the exact form of the impulse operator in quantum mechanics to the intuition of some of the unquestionably most brilliant minds in the world of physics. These achievements originated in a sleight of mind and could only be justified retrospectively.

This approach is of major importance when facing the solution of the many body problem in quantum mechanics. I first encountered it when I was still an undergraduate student in a lecture on quantum mechanics of large systems. We had spent months to prove the stability of matter when we arrived at density functional theory. The professor finished the proofs of the Hohenberg-Kohn theorems with the words "And these two theorems give you the permission to guess." At that time I did not entirely understand what that meant but I was fascinated.

Over the past two decades density functional theory has proven to be the most successful approach in electronic structure calculations. It simplifies the unsolvable quantum mechanical many body problem. Already in classical mechanics the $\frac{1}{|\mathbf{r}-\mathbf{r}'|}$ term in the energy expression leads to non-analytically solvable problems. This translates into quantum mechanics, where also the iterative solution of the problem for systems of chemical interest is impossible due to enormous computational cost.

The Hohenberg-Kohn theorems allow the substitution of the $\frac{1}{|\mathbf{r}-\mathbf{r}'|}$ operator by a so called exchange-correlation expression. If the exact form of this functional were known, it would lead to exact results, but up until now it has not been found. Therefore it has to be approximated. Many theoretical restrictions exist, but in the end the choice of the correct functional form comes down to intuition. Despite its obvious flaws and lack of theoretical foundation in a mathematical sense, in 1998 Walter Kohn received the Nobel Prize in chemistry for developing density functional theory. Today many different density functionals exist and they are summarized and classified in a framework nicknamed Jacob's Ladder. The theoretical background, some general comments on the computational implementation and the differences between different density functionals and post density functional methods will be discussed in chapters 3 and 4 of part I.

This work deals with the catalytic properties of zeolites. Zeolites are very important industrial catalysts. They are a group of micro- and mesoporous materials mainly consisting of Si and O. They are unique in the sense that chemical reactions take place inside the material and the confinement inside the porous structure leads to a very high selectivity towards the desired end-products. A more detailed discussion of zeolites and its applications in chemistry will follow in the next chapter.

Historically seen zeolites are a topic mainly investigated at an experimental level.

The processes themselves take place inside the material, which poses significant difficulties to imaging techniques. Therefore a more detailed understanding using theoretical methods is highly desirable. Together with my supervisor Jürgen Hafner I investigated the properties of catalytically active TM-sites in chabazite. Experimentally seen there are three ways of probing the properties of these active sites. X-ray diffraction can give you a rough guideline of the structures encountered in these systems. But adsorption sites are not distributed regularly in the structure. This clearly biases the results. A second experimental technique is the use of emission and adsorption spectroscopy. Every TM-site gives a very unique spectrum, which again can be used to draw conclusion about the chemical environment of the site. The third method is the measurement of IR wavenumbers of tracer molecules. These IR frequencies change with the bonding environment of the molecule.

In chapter 4 we describe the structural properties of Cu and Co extra framework sites in different spin states, in chapter 5 we investigate the densities of states, the impact of the spin state and based on Koopman's theorem the possible first excited states. In chapter 6 we take a small detour to investigate the chemical bonding in gas phase carbonyls and nitrosyls and study the adsorption of CO and NO in TM-exchanged chabazite. The main focus of these chapters is to investigate the impact of the use of hybrid functionals compared to standard density functionals. Chapters 4, 5 and 6, which form part II are planned to be published as a series of papers as soon as writing of this thesis is finished.

Most catalytic processes in zeolites involve hydrocarbons. They are highly polarizable and a large amount of attractive forces between the alkane and the zeolite can be attributed to van der Waals interactions. These interactions are not included in standard semi-local density functional theory. In chapters 7 and 8 of part III we investigate the adsorption of methane, ethane and propane in Na- and protonated chabazite. We use state of the art DFT and post-DFT methods, which are designed to describe van der Waals interactions accurately. In chapter 9 we compare the performance of 0K energy minimization to finite temperature molecular dynamics simulations. Furthermore we investigate the possibility of reducing computational cost by applying an embedding approach. Chapter 7 was already published in the Journal of Chemical Physics (JCP 134, 064102), the data contained in chapter 8 will be published after writing of this thesis is finished.

2 Zeolites

Summary

In this chapter we give a short introduction to zeolites. We start out by discussing the basic chemical composition and discuss some of the most common structures. It is followed by a discussion of basic applications. In the end we give a short review of the use of zeolites in two major catalytical processes, namely the adsorption and conversion of alkanes in zeolites and the de NO_x reaction.

2.1 Chemical Composition and Structures

The term zeolites stands for a class of materials, which are chemically composed by Si and O with the chemical structure SiO_2. Contrary to quartz, which has the same chemical composition, in zeolites SiO_4-tetrahedrons (T-sites) are linked via the O atoms and form a micro- or mesoporous structure.

These structures are mainly determined by the ring-structures formed. If the framework is dominated by 4-O, 6-O, 8-O, 10-O and 12-O rings, large cavities are formed. The basic building block in these structures is very often a double 6-O ring (D6R) structure and these structures only vary in the way these building blocks are linked. Very prominent examples for these structures are the Chabazite structure ((a) in Fig. 2.1), where the D6Rs are linked directly, and the faujasite structure ((b) in Fig. 2.1, where the different D6R-structures are linked by 6-O rings. Another very prominent example of zeolites containing large cavities is the Linde Type A structure ((c) in Fig. 2.1), where the sodalite cages are not linked via a D6R structure but a double 4-O ring structure. While these structures themselves form a smaller sodalite cage with a diameter of about 11Å, in Faujasite and Linde Type A these structures form an even larger supercage.

If there are also 5-O membered rings are included in the structure, a network of channels can be built. For these zeolites, mordenite ((d) in Fig. 2.1 and the MFI-structure ((e) in Fig. 2.1) are perfect examples. In ferrierite ((f) in Fig. 2.1) the channel structure is linked by cavities, which leads to very special properties.

These zeolite frameworks can be activated by substituting one of the Si atoms by Al. The lower number of valence electrons can not saturate the four bonds to the surrounding O atoms, leading (similar to a doped semi-conductor) to a local charge deficit. These activated O atoms show a very high reactivity and active sites can be (and usually are) created. The zeolite structures can be protonated, where a hydrogen

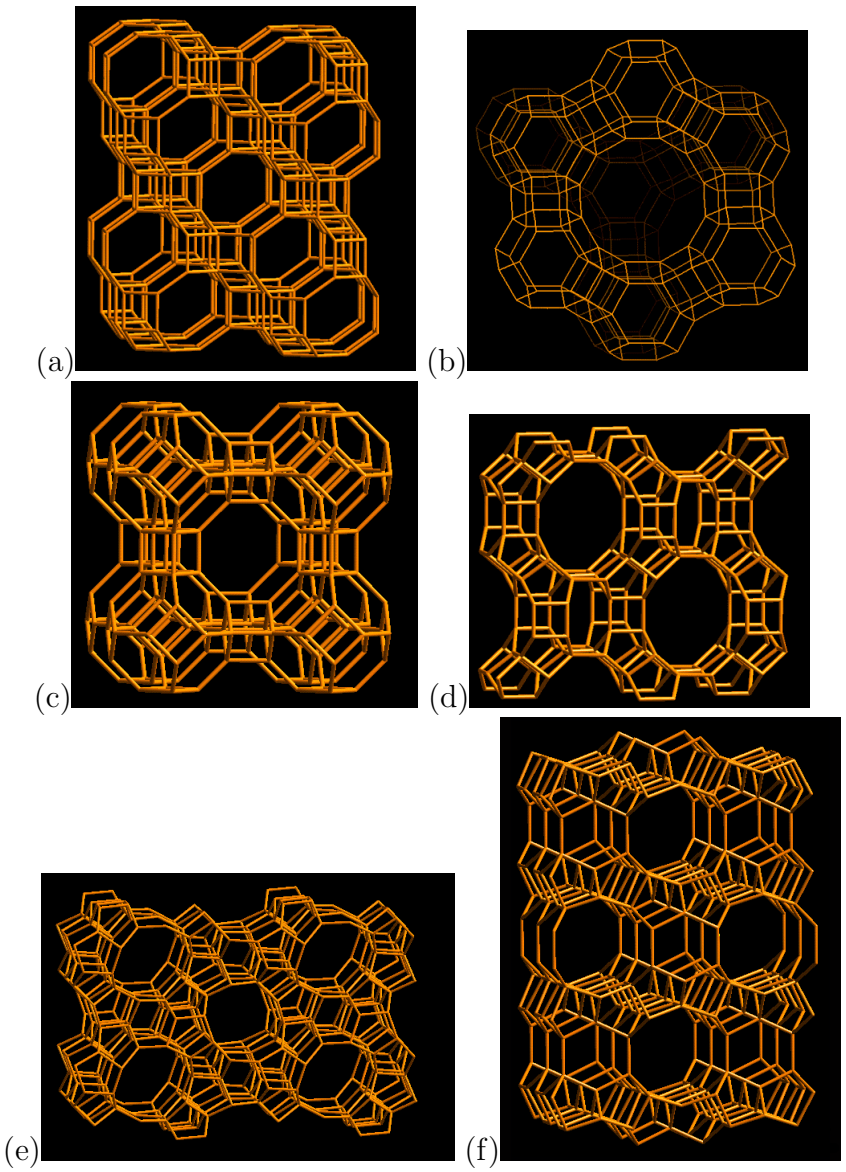

Figure 2.1: Many different types of zeolite structures exist. Sometimes they form a structure of cavities like in (a) chabazite, (b)faujasite or (c) Linde type A, sometimes they form a channel structure like in (d) mordenite or (e) MFI and also combinations like in ferrierite. Yellow lines mark Si-O-Si bonds with Si atoms sitting at the cutting points of the lines. The pictures were taken from the Atlas of zeolite structures [1]

atom is adsorbed to the activated O atoms, or ion exchanged [1], with the desired atom type forming the active site.

2.2 Applications

The chemical composition, special structural properties and stability lead to a wide array of applications for zeolites. In their natural appearance the cavities of the zeolites are usually filled with water. After heating them the water is removed making the remaining zeolites highly hydrophilic. This property is the reason why zeolites are used in cat litter as well as in the cooling system of beer barrels, where water is partially adsorbed by the zeolites leading to a lower temperature in the remaining liquid.

In nature very often Na-exchanged zeolites are encountered. The Na atom only binds very weakly to the framework and can easily be replaced by other atoms. This makes zeolites great ion-exchangers. They are used in detergents [2] as well as filtering media in fishtanks or even in cleaning polluted soils [2]. In the nuclear accidents in Three-Mile Island and Fukushima the property for ion-exchange was used to bind the large radioactive atoms.

Their ability to adsorb molecules makes zeolites great storage media for gases [3]. Also in agriculture zeolites are used as storage media for fertilizers, donating the fertilizer to the soil over an extended period of time. Zeolites have also been discussed as carrier media for medication in pharmaceutical industry[4, 5].

Their regular micro- or mesoporous structure is of the size of many molecules of chemical interest. Therefore zeolites can either be used as molecular sieves [6] or also as host for ordering nano-structures[7]. When active sites are present, zeolites can also be used as catalysts. Their high stability and their regular shaped cavities even make zeolites model systems for catalysis in confinement. When zeolites were introduced as catalysts in crude oil refinement, the yield of the process was increased by as much as 10%. Ion exchanged zeolites is also a prime material for removing NO from exhaust gases [8, 9].

2.3 Understanding processes within zeolites

In zeolites all chemical processes happen within the material, which poses a certain problem for experimental techniques. While the structural properties of the zeolite framework can be determined by x-ray scattering techniques, problems start to arise describing the chemically active sites. On surfaces advances in STM imaging enabled experimentalists to visualize the chemical active sites, a method not available for zeolites since the surface, as already mentioned, lies within the material. The irregular

[1] This term actually originates from the creation of these catalytically sites. Natural Zeolites contain (depending on the place of formation) Na or Ca atoms, which are then exchanged while creating the desired active site in the zeolite structure

[2] which is actually their main commercial use

distribution of Al sites within the zeolitic structures also poses problems for x-ray diffraction techniques, which are in principle not able to describe the exact chemical environment of the adsorption sites.

This only leaves indirect methods to describe adsorption sites. The most common method is to measure IR frequencies, which allow conclusions regarding chemical bonding. These can be either the oscillation frequencies of the adsorption sites (e.g. in protonated zeolites) or the IR frequencies of tracer molecules like CO adsorbed to said active sites. Another method is to investigate the excitation and emission spectrum of the adsorption sites, which is especially effective for transition metal atoms.

Another important aspect is describing the diffusion, adsorption and conversion of hydrocarbons in zeolites. Of course adsorption isotherms (from which Henry's constant can be derived) and enthalpies as well as diffusion constants can be measured. Also the product distribution of cracking and isomerization processes can easily be determined. But the exact underlying remains unclear.

While experimental techniques are certainly successful it is necessary to use theoretical methods to arrive at a deeper level of understanding of the processes inside the zeolite structure. The theoretical methods can be roughly separated into three categories.

In the first category methods using empirically fitted interaction potentials in molecular simulations are found. Using these methods rather large parts of the zeolitic structure can be sampled at high computational efficiency. Since empirical potentials are used it is impossible to describe problems including covalent bonding such as conversion reactions or the characterization of adsorption sites.

For these problems it is best to use electronic structure methods such as density functional theory. Here the many-particle electronic Schrödinger equation is solved in an approximation, which can be used to obtain very accurate[3] predictions concerning bonds formation and breaking at a reasonable cost. In these calculations the charge-density is calculated which leads to forces. They can be used for structural relaxation to arrive at ground-state geometries and energies.

While these ground state properties can be obtained at very reasonable cost today many adsorption properties especially for hydrocarbons at finite temperature mainly depend upon thermodynamic properties. Clearly a 0K energy minimization does not contain this kind of information[4]. To describe chemical reactions accurately, the forces obtained by electronic structure calculations can be used to perform molecular dynamics or rare events simulations such as transition path sampling. Only the increase in computational efficiency in recent years has made these very expensive methods accessible.

In the following we will discuss two processes of major industrial importance, which are the main framework for the studies in parts II and III. In the following we will give a short discussion of the adsorption and catalytic conversion of hydrocarbons in

[3]The accuracy of electronic structure calculations obviously depends on the quality of the approximation used.

[4]Even though it can be attempted using transition state theory, where errors are often huge

zeolites and the role of zeolites in NO-exhaust gas removal.

Alkane adsorption and conversion in zeolites

The adsorption and catalytic conversion of hydrocarbons using zeolites is of major industrial importance. While the adsorption processes allow a separation of a mixture of different hydrocarbons, the cracking or isomerization of hydrocarbons leads for instance to a higher yield in oil refinement. For these processes the exact microscopic structure of the zeolite determines the end-products.

The adsorption and conversion of alkanes in zeolites is a five step process. In a first step the alkane enters the zeolitic structure. in a second step the alkane diffuses to the active sites, afterwards it is adsorbed, converted (either cracked or isomerized) and in a last step the end products exit the zeolite. All those processes are visualized in Fig. 2.2. Even though these five steps are part of one process the understanding of every single one of them requires different techniques, which can again be used to make suggestions for improvement.

The process of entering a zeolite pore for a molecule in the gas phase is by now means trivial. Theoretical studies by Skoulidas and Scholl [11] and Ford and Glandt [12] showed, that direct entering of the pores for with a kinetic diameter which is comparable to the size of the molecules is practically excluded. This also implies, that a different mechanism has to be found to describe the entering of alkane molecules into the zeolite.

Such a process (the transport and sorption properties of aromatic molecules in ZSM-5) has been studied extensively by Reitmeier and coworkers [13, 14, 15] using fast time-resolved infrared spectroscopy. They linked different experimental and theoretical studies to arrive at the following picture Fig. 2.3 . In the first step the gas phase molecule is physisorbed weakly to the outer zeolite surface. The acceptance of the adsorption when a collision between a molecule and the outer zeolite surface is not only determined by the adsorption energy gained but also to a large amount by the entropy lost in this process, since the degrees of freedom are severely restricted when the molecule is bound to a two dimensional surface. Once the molecule is in this surface state it can freely move on this surface. It can now diffuse to active sites and can enter the inside of the zeolite structure.

Reitmeier and coworkers realized that the most important step in this processes is the formation of the surface state. Using the knowledge about the loss of entropy on a surface state they modified the outer surface of the zeolite using a silica coating which in turn leads to a larger outer pore structure which acts like a funnel and increases the adsorption rate of said molecules[5].

After the molecule has entered the pores it has to diffuse to the active sites. This process takes place at the inside of the zeolite. Only diffusion coefficients can be

[5] At this point it is important to stress that it is impossible for a molecule to enter the pores, if it is too large to fit in. This is actually the reason why zeolites are also used to sieve mixtures of molecules.

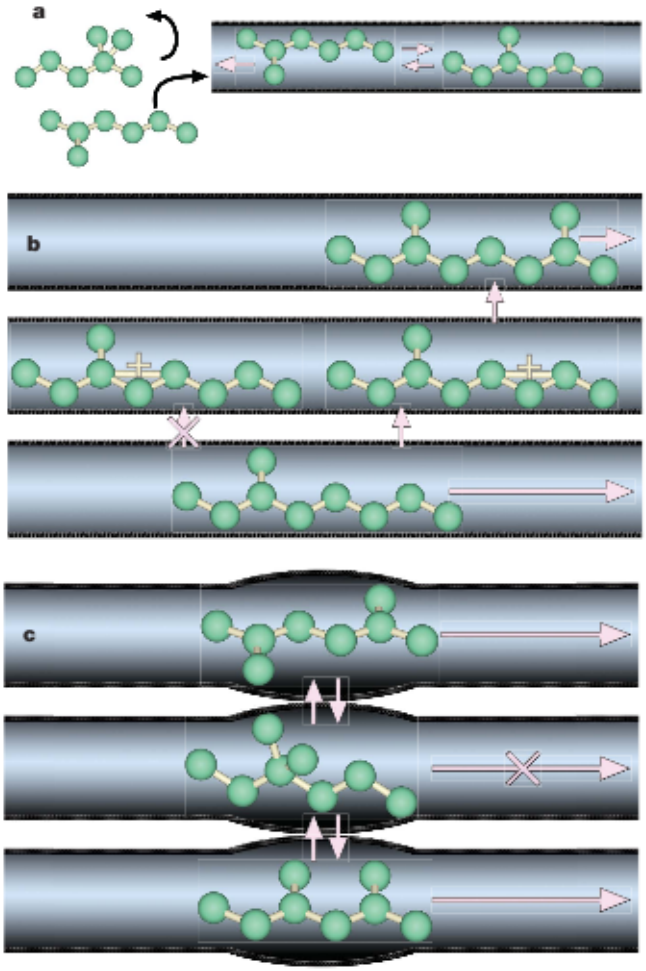

Figure 2.2: This figure schematically shows the steps in the conversion of alkanes in acidic zeolites. (a) In a first step the alkane has to enter the zeolite structure. (b) Afterwards the alkane diffuses to the active site where the proton is donated to the alkane forming an carbenium ion. (c) Now this carbenium ion either isomerizes or is cracked. The final product is determined by the shape of the cavity and the ability of the end-product to diffuse out of the zeolite. This figure was originally published in [10]

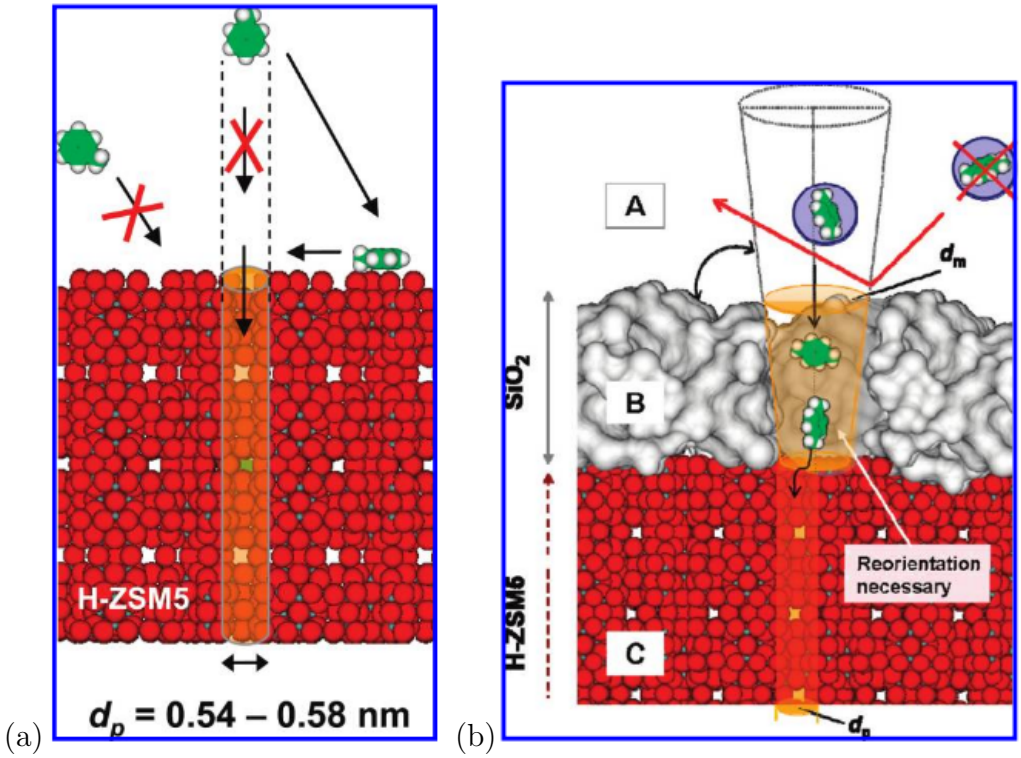

Figure 2.3: This figure displays toluene molecules entering the pore of H-ZSM-5. (a) In the unmodified material the toluene molecules can not enter the pores directly, but must enter a surface state before diffusing into the pores. (b) A silicon coating modifies the surface in a way that the molecules can, similar to a funnel, enter the pores directly. These pictures were initially published in [15].

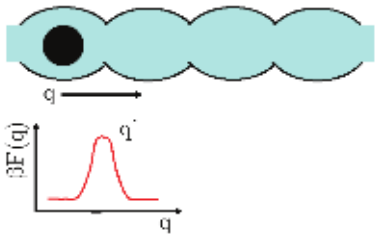

Figure 2.4: When a molecule moves between different zeolite cavities q and q' it has to pass a potential energy barrier which blocks diffusion. This is the most simple approach to simulate diffusion inside zeolite structures. This picture was initially published in [16].

measured in experiment but may vary by as much as an order of magnitude for different experimental techniques. Clearly a deeper theoretical understanding of these problems is necessary to be able to understand these problems at a microscopic level. Several theoretical methods have been developed to deal with these problems which have been described in [16].

Clearly the rate of diffusion depends on the shape of the zeolite framework as well as on the size and shape of the molecule investigated. When a molecule moves between two cavities it can not move freely. It will encounter a barrier when passing the window connecting those two pores(for a schematic display see Fig. 2.4). The motion between cavities can be linked to the diffusion properties of the material. The energy barrier for passage can be calculated and transition-state theory can be used to make an estimate for the diffusion-speed. The problems with the use of transition-state theory are manyfold in this context. It is not easy to find the actual minimum-energy transition between two cavities and even if it was known, how often will the transition be attempted?

Far more efficient are MD-algorithms, which allow the simulation of the motion of a particle in a periodic zeolite cell. These calculations are usually performed using classical forcefields and due to higher computational efficiency the framework atoms are often kept fixed. With such calculations the experimentally measured quantities can be predicted at a very high level of accuracy.

Also the adsorption properties can be obtained in a similar way. The actual bond between molecules and active sites is very weak and hardly affect the interactions between molecules and the cavity walls. This together with the comparably low cost compared to electronic structure methods allows the treatment of extended systems at different pressures.

The treatment of adsorption using electronic structure calculation is very difficult. This is caused by the nature of interactions between hydrocarbons and zeolites. The bonding between the molecule and the zeolite can be split up in two contributions. The molecule forms a weak chemical bond with the adsorption site but is also bonded to the cavity wall by van der Waals interactions. These interactions are truly non-local

and are not described by the standard methods of density functional theory. It also not clear how the thermal motion of the molecule affects adsorption energies. We will deal with these problems in Part III, where we model the adsorption of short alkanes in chabazite at different levels of theory.

The most important reaction for zeolite catalysts is the cracking and isomerization of hydrocarbons. When the molecule is adsorbed to a Brønstedt acid site within the zeolite the proton can be transferred to the molecule creating a carbenium ion. In such reactions the actual chemical structure of the molecule and the zeolite structure changes. To account for that electronic structure theory is needed. But especially for these reactions entropic effects are of major importance. To properly describe these reactions Bučko et al. performed transition-path sampling studies to simulate the proton transfer [17] and and the actual cracking of propane in protonated chabazite [18]. They could properly identify reaction mechanisms and were able to explain the product distribution.

For industry the reaction itself is only of minor importance. The point of interest is the selectivity of the catalyst. Clearly this selectivity depends on the size and shape of the cavity. A product can only be formed and released from the zeolite if it fits into the cavities of the zeolite and can diffuse out. Smit and Maesen used configurational-bias Monte Carlo to scan a large number of zeolite structures [10]. Furthermore they are trying to create a database which will allow them to predict the shape-selectivity of reactions using zeolite catalysts.

NO removal from exhaust gases using zeolite catalysts

NO is an exhaust gas from burning fossil fuels. It is, however, a gas causing environmental problems. In high concentrations it can cause acid rain and is also involved in the ozone layer depletion. Today a large part of our energy production depends on the burning of fossil fuels and for environmental reasons it is highly desireable to remove NO from exhaust gases.

NO itself is thermodynamically unstable but the breaking of the bond has a very high activation energy of about 364 kJ/mol. Therefore a catalyst is needed to arrive at reasonable reaction rates. In vehicles mainly metal surfaces and TM oxide surface are used as catalysts. They have a very high hydrothermal stability, which is of great advantage when used in connection with gasoline engines. Cu-exchanged zeolites show a very high catalytic activity for this process but there low hydrothermal stability only allows applications in stationary power plants where reaction conditions are more favorable.

The reaction of NO decomposition itself is rather simple. The basic process is described by the formula

$$NO \rightarrow 1/2N_2 + 1/2O_2. \tag{2.1}$$

While the main reaction is very basic the mechanism of NO decomposition in Cu-exchanged zeolites is not entirely clear. This process has been first described by Iwamoto et al. [19, 20, 21, 22]. The only experimental evidence is the measurement of

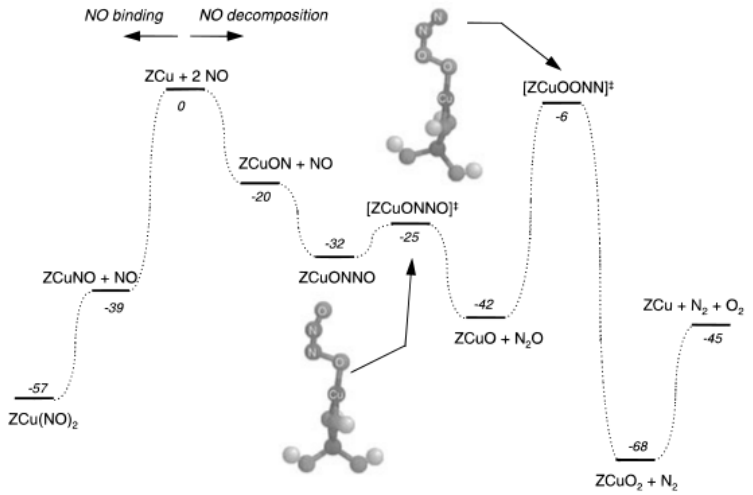

Figure 2.5: This figure schematically shows the reaction path for the NO decomposition. Initially a Cu-ONNO complex is formed. From this complex N_2O is desorbed and readsorbed to form a CuOONN complex, which is then decomposed into O_2 and N_2. This figure was originally published in [24].

IR-wavenumbers of adsorbed NO molecules in Cu-zeolites [23]. Those measurements indicate the existence of NO^-, NO^+ and N_2O^- species in the zeolite material, which are adsorbed to the Cu active site and can form CuNO and $Cu(NO)_2$ species.

Investigating the further catalytic conversion is more complicated and different reaction paths have been suggested using electronic structure calculations. The differences in those reaction-paths is the formation of the N-N bond. Schneider et al. proposed in [24] the formation of Cu-ON-NO adsorption complex. From this complex N_2O desorbs leaving a single O atom adsorbed at the Cu active site. In a second step the N_2O molecule adsorbs with the oxygen end of the molecule to the single O atom leading to Cu-OONN, from which N_2 and O_2 are formed. The entire pathway is illustrated in Fig. 2.5. The downside to this explanation is the initial formation of the Cu-ON-NO adsorption complex. It is assumed that in a first step a NO molecule adsorbs to Cu to form Cu-ON. In the second step a gas phase NO molecule adsorbs to the N atom. But from electronic structure calculations we know that NO preferentially adsorbs in a Cu-NO geometry to the active site.

An alternative approach was suggested by Spoto et al [25]. In the first step $Cu(NO)_2$ is formed. From this species N_2O is desorbed and by adsorption of two NO molecules a $Cu(N_2O_3)$ complex is formed. This then desorbs as N_2, O_2 and N_2O.

Up until today the true mechanism is unknown. The main problem is the inaccuracy of the methods used. Especially the interactions between the TM d-states and the molecule pose a problem for the usually applied general gradient approximation. This leads to a far too high adsorption energy for NO molecules allowing adsorption complexes like $Cu(NO)_3$ or $Cu(NO)_4$ [26]. Clearly the performance of higher level

methods has to be tested. We will perform these test in part II of this thesis.

Part I

Theoretical Background and Methods

3 Theoretical Background

Summary

In this chapter the theoretical background for this work is introduced. Starting from the many-body Hamiltonian for electronic and nuclear motion the so called Born-Oppenheimer approximation is applied, which decouples the electronic and nuclear motion. For the solution of the electronic problem, the expressions of exchange and correlation and their meanings are introduced, followed by a discussion of the Hohenberg-Kohn theorems and Kohn-Sham Density Functional Theory. In the final part of the chapter, a way towards computational treatment of the variational equations of Kohn-Sham DFT is discussed. Most of the time only a basic overview of the ideas is given, since an exact treatment would go far beyond the scope of this text. For a more detailed discussion the interested reader is referred to the books and articles cited in this text.

3.1 The Problem

When considering the many body problem in quantum mechanics, it is necessary to solve the Schrödinger equation for the following Hamiltonian

$$H = \sum_{i=1}^{n} \left[\frac{\mathbf{p_i}^2}{2m} - \sum_{k=1}^{K} \frac{Z_k e^2}{|\mathbf{r_i} - \mathbf{R_k}|} + \sum_{i<j} \frac{e^2}{\mathbf{r_i} - \mathbf{r}_j} \right] + \sum_{k=1}^{K} \left[\frac{\mathbf{P_k}^2}{2M_k} + \sum_{k<l} \frac{e^2 Z_k Z_l}{|\mathbf{R_k} - \mathbf{R_l}|} \right], \quad (3.1)$$

where n is the number of electrons, $\mathbf{r_i}, \mathbf{p_i}, m$ are electron coordinates, momenta and mass and K is the number of nuclei, $\mathbf{R_k}, \mathbf{P_k}, M_k$ are nuclear coordinates, momenta and masses. To solve the Schrödinger equation a wave-function is needed.

$$\tilde{\Psi}(\mathbf{r_1}, s_1, \mathbf{r_2}, s_2, \ldots, \mathbf{r_n}, s_n, \mathbf{R_1}, i_1, \ldots, \mathbf{X_K}, i_K) \quad (3.2)$$

This wave-function $\tilde{\Psi}$ naturally depends on all electron and nuclear coordinates $(\mathbf{r_i}, \mathbf{R_k})$ and spins (s_i, i_k). To solve the Schrödinger equation

$$H\tilde{\Psi} = E\tilde{\Psi} \quad (3.3)$$

is by no means trivial. Therefore simplifications are necessary. Comparing the masses of electrons and nucleons (neutrons, protons) and considering that nuclei typically consist of several nucleons shows that nuclear masses M_k are several orders of magnitude larger than the electron mass m leads to the so called Born-Oppenheimer or adiabatic

approximation [27]. Here the nuclear masses in equ. 3.1 are set to infinity leading to the Hamiltonian

$$H = \sum_{i=1}^{N} \left(\frac{\mathbf{p_i}^2}{2m} - \sum_{k=1}^{K} \frac{Z_k e^2}{|\mathbf{r_i} - \mathbf{R_k}|} + \sum_{j<i} \frac{e^2}{|\mathbf{r_i} - \mathbf{r_j}|} + \sum_{k<l} \frac{e^2 Z_k Z_l}{|\mathbf{R_k} - \mathbf{R_l}|} \right). \tag{3.4}$$

This Hamiltonian is now free of nuclear momenta. Evaluating the energy equation equ. 3.3 and using a product ansatz for the wave-function

$$\begin{aligned} \tilde{\Psi}(\mathbf{r_1}, s_1, \mathbf{r_2}, s_2, \ldots, \mathbf{r_n}, s_n, \mathbf{R_1}, i_1, \ldots, \mathbf{R_K}, i_K) = \\ \Psi(\mathbf{r_1}, s_1, \mathbf{r_2}, s_2, \ldots, \mathbf{r_n}, s_n)\Phi(\mathbf{R_1}, i_1, \mathbf{R_2}, i_2, \ldots, \mathbf{R_K}, i_K) \end{aligned} \tag{3.5}$$

leads to an equation, where the nuclear degrees of freedom (after multiplying with Φ^* from the left) can be integrated out, leading to an equation for the electronic degrees of freedom only, with an added constant term for coulombic core interaction (originating from the last term of equ. 3.4). Ignoring this last term (since it is only a constant with respect to the electronic coordinates) leads to an equation for the electronic problem.

At this point the alert reader might ask questions about the meaning of this approximation and the solution of the equation with respect to nuclear coordinates. Physically seen, this approximation assumes that due to the higher mass of the nuclei and their higher inertia the electronic movement is very fast compared to the nuclear movement. Therefore the electronic structure can always be seen as equilibrated with respect to the comparably slow motion of the nuclei (this is why this approximation is called the adiabatic approximation). The nuclear problem is then afterwards solved as a (far more simple) classical equation with coulombic forces obtained from the equilibrated electron densities and the other nuclear coordinates.

3.2 On the Electronic Problem, Exchange and Correlation

Hartree Theory and the Electrostatic Interaction

The most simple way to solve the electronic problem is the so called Hartree method [28]. Here one has to solve the energy functional

$$\begin{aligned} E = \min_{\{\phi_1,\ldots,\phi_n\}} E^H[\phi_1, \ldots, \phi_n] = \\ = \min_{\{\phi_1,\ldots,\phi_n\}} \int d^3\mathbf{r} \left(\sum_{i=1}^{n} \phi_i^*(\mathbf{r})(\nabla^2 + V(\mathbf{r}))\phi_i(\mathbf{r}) + \frac{1}{2} \sum_{i,j} \int d^3\mathbf{r}' \frac{|\phi_i(\mathbf{r}|)^2 |\phi_j(\mathbf{r}')|^2}{|\mathbf{r} - \mathbf{r}'|} \right). \end{aligned} \tag{3.6}$$

In this equation (and for the remainder of this text) the electronic charge e, the mass m and $\frac{1}{4\pi\epsilon_0}$ are set to 1 and atomic units are used. Also for simplicity of notation the

spins as variables have been dropped. But a generalization of the following formulas containing the spin as variable explicitly can be made without problems.

The ground state energy is obtained by a minimization of the energy equation E^H with respect to a set of one electron wave-functions ϕ_i. The solution of this minimization problem will be discussed at a later point in this text, since it is similar in many theories treating the solution of bosonic or fermionic ground state problem. At this point it is important to note, that the only interactions between the one electron wave-functions are of electrostatic nature and are summarized in the last term of equ. 3.6. The electronic density is obtained by

$$n(\mathbf{r}) = \sum_i |\phi_i(\mathbf{r})|^2, \tag{3.7}$$

where every electronic orbital is occupied by a maximum of 2 electrons. This is actually the only place, where the Pauli exclusion principle is included in Hartree theory. This (besides its performance in comparison to experiment) was actually one of the major drawbacks of this theory and it was clear, that this problem had to be addressed.

Hartree-Fock Theory and the Electronic Exchange Energy

Usually the ground state energy in quantum mechanics is obtained by minimization of the functional

$$E = \min_{\Psi} \frac{\langle \Psi | H | \Psi \rangle}{\langle \Psi | \Psi \rangle}. \tag{3.8}$$

Therefore choosing a proper form of Ψ together with a suitable form of Hamiltonian H should lead to a functional $E[\{\phi_i\}]$ (ideally depending on a set of one electron orbitals ϕ_i only) to solve for the ground state energy of the electronic problem. While the choice of the Hamiltonian is straightforward

$$H = \sum_i \nabla_i + V(\mathbf{r_i}) + \sum_{i<j} \frac{1}{|\mathbf{r_i} - \mathbf{r_j}|}, \tag{3.9}$$

the choice of wave-function Ψ is more tricky. For reasons of simplicity of mathematical treatment it should be possible to represent Ψ in terms of single electron wave-functions ϕ_i and for physical reasons it should be antisymmetric $\Psi(\dots, \mathbf{r_i}, \dots, \mathbf{r_j}, \dots) = -\Psi(\dots, \mathbf{r_j}, \dots, \mathbf{r_i}, \dots)$. It was John C. Slater who proposed to use the determinant of a matrix of single electron states (the so called Slater-determinant [29]) as a wave-function for the many body problem.

$$\Psi(\mathbf{r_1}, \mathbf{r_2}, \dots, \mathbf{r_n}) = \frac{1}{\sqrt{N!}} \begin{vmatrix} \phi_1(\mathbf{r_1}) & \phi_2(\mathbf{r_1}) & \dots & \phi_n(\mathbf{r_1}) \\ \phi_1(\mathbf{r_2}) & \phi_2(\mathbf{r_2}) & \dots & \phi_n(\mathbf{r_2}) \\ \vdots & \vdots & & \vdots \\ \phi_1(\mathbf{r_n}) & \phi_2(\mathbf{r_n}) & \dots & \phi_n(\mathbf{r_n}) \end{vmatrix} \tag{3.10}$$

Now inserting equs. 3.10 and 3.9 into equ.3.8 leads to the so called Hartree-Fock [30] energy functional

$$E^{HF}[\phi_1,,\phi_n] = \int d^3\mathbf{r} \left(\sum_{i=1}^{n} \phi_i(\mathbf{r})^*(\nabla^2 + V(\mathbf{r}))\phi_i(\mathbf{r}) + \right.$$
$$\left. + \frac{1}{2}\sum_{i,j} \int d^3\mathbf{r}' \frac{|\phi_i(\mathbf{r})|^2|\phi_j(\mathbf{r}')|^2}{|\mathbf{r}-\mathbf{r}'|} - \frac{1}{2}\sum_{i,j} \int d^3\mathbf{r}' \frac{\phi_i^*(\mathbf{r})\phi_j^*(\mathbf{r}')\phi_i(\mathbf{r}')\phi_j(\mathbf{r})}{|\mathbf{r}-\mathbf{r}'|} \right). \quad (3.11)$$

Comparing this result with the Hartree energy equation 3.6 shows that taking the antisymmetry of Ψ into account explicitly in the construction of the wave-function leads to an additional term in equ. 3.11, the so called exchange term.

Variational Calculus and Hartree-Fock Equations

In Hartree-Fock theory (as well as in Hartree theory) the energy minimum of the Hartree Fock functional given in equ. 3.11 is defined as the ground state energy. All minima are usually obtained by finding those functions, for which the variation of the functional with respect to these functions is 0.

$$\frac{\delta E^{HF}}{\delta \phi_i^*} = 0 \quad (3.12)$$

Now applying this logic for all ϕ_i under the normalization condition $|\phi_i|^2 = 1$ leads to a set of n coupled integro-differential equations of the form

$$\left\{ \nabla^2 + V(\mathbf{r}) + \frac{1}{2}\sum_j \left(\frac{|\phi_j(\mathbf{r}')|^2\phi_i^*(\mathbf{r})}{|\mathbf{r}-\mathbf{r}'|} - \frac{1}{2}\frac{\phi_j^*(\mathbf{r}')\phi_j(\mathbf{r})\phi_i^*(\mathbf{r}')}{|\mathbf{r}-\mathbf{r}'|} \right) \right\} \phi_i(\mathbf{r}) = \epsilon_i\phi_i(\mathbf{r}). \quad (3.13)$$

Here ϵ_i is a Lagrange multiplier originating from the normalization condition, which can be interpreted as a one particle energy within Hartree-Fock theory. A similar approach can be applied to all variational methods minimizing the energy functional with respect to wave-functions like Hartree or Density Functional Theory or Multi-Reference Self Consistent Field approaches. Solving these equations is by no means trivial and will be addressed later in the text.

Configuration Interaction and Correlation

A very prominent gedanken-experiment in theoretical solid state physics is to insert a charged particle in a uniform electron gas. After the insertion, the electrons will due to the perturbation start to occupy excited states to shield the long ranged coulomb interaction of the inserted particle and again other electrons will start to shield the effect of the excitation of the electrons which are not in their ground states and so forth. Taking this into account it is smart to change the form of the wave-function given in equ. 3.10. The Hartree-Fock approach only describes the n lowest eigenstates

of the problem, but if the obtained charge-density is used also all unoccupied states can be calculated. Following the logic of the previously mentioned gedanken-experiment, the wave-function in equ. 3.10 could be changed into

$$\Psi(\mathbf{r_1},\ldots,\mathbf{r_n}) = c_0\Phi_0 + \sum_{i=1}^{n}\sum_{k=n+1}^{\infty} c_1(i,k)\Phi_1(i,k) + \\ + \sum_{1\le i<j}^{n}\sum_{n+1\le k<l}^{\infty} c_2(i,j,k,l)\Phi_2(i,j,k,l) + \ldots \tag{3.14}$$

where Φ_a is a Slater determinant containing a excited states and the arguments specify the substituted states. The c_as are prefactors, obeying the normalization condition

$$\sum c_i(\ldots)^2 = 1, \tag{3.15}$$

where summation runs over all prefactors. Inserting the wave-function given in equ. 3.14 instead of equ. 3.10 into the variational equation 3.8, leads to a very complicated equation of single electron orbitals, which will be discussed only qualitatively in this spot. Again the standard Hartree-term (the electrostatic interaction between the charge densities) and the Fock-term (describing the exchange interaction) are obtained, but additionally interaction terms between excited states are added. These interactions have the form of

$$\frac{\phi_i^*(\mathbf{r})\phi_j^*(\mathbf{r'})\phi_k(\mathbf{r})\phi_l(\mathbf{r'})}{|\mathbf{r}-\mathbf{r'}|} \tag{3.16}$$

where the indices i,j,k,l can take any number from 1 to ∞ (excluding those combinations already accounted for in the Hartree and Fock terms). The summation over all these terms and the summation over the exchange contribution from the excited Slater determinants is the so called correlation interaction.

An important point to notice is, that while in the previous problem the energy was minimized with respect to the one particle wave-functions, in this so called Configuration Interaction (CI) approach [31, 32] the energy is minimized with respect to the prefactors c_i of the Slater-determinants. Since the summation in equ. 3.14 goes to ∞ this problem is not exactly soluble. Therefore the series has to be truncated at a certain point. But even a truncation at very low cut-off levels is already extraordinarily costly and still leads to very bad scaling with system size. Even Coupled Cluster Singles Doubles (CCSD)[33, 34], where various simplification are made to the series in equ. 3.14 scales with $O(N^7)$. Therefore another method is needed to allow the efficient treatment of larger systems.

3.3 Density Functional Theory

While quantum-chemical methods like CI and CCSD or also Multi Configuration Self-Consistent Field Methods (MC-SCF) [35] provide highly accurate results, their main drawback is the high computational cost needed to solve these equations for larger

system sizes. This is actually the reason why different approaches are used as the system size increases. Probably the most popular approach also applied in this work is Kohn-Sham Density-Functional Theory (DFT). It actually has big similarities with Hartree Theory, but now an additional term depending on $v^{xc}(n(\mathbf{r}))$ is added. This exchange-correlation potential is introduced to mimic the effects of the very complicated exchange and correlation expressions in HF Theory and CI. Even though there exist very simple expressions for v^{xc}, such as the Local Density Approximation (LDA), especially in the last years more sophisticated (and also computationally more expensive) approximations have been introduced. In this section, the basic ideas in form of the Hohenberg-Kohn Theorems and the Kohn-Sham ansatz will be discussed.In the next section we will closely the argumentation in Chapter 6 of [36].

The Hohenberg-Kohn Theorems

The Hohenberg-Kohn Theorems [37] are the basis for all density functional calculations. They are quite general and are not only applied in electronic structure calculations but also in systems like neutron stars or bosonic problems. The proofs of these theorems are very basic and will therefore be included in this text.

Theorem I: For any system of interacting particles in an external potential $V_{ext}(\mathbf{r})$, the potential $V_{ext}(\mathbf{r})$ is determined uniquely, except for a constant, by the ground state particle density $n_0(\mathbf{r})$.
Corollary I: Since the Hamiltonian is thus fully determined, except for a constant shift of the energy, it follows, that the many-body wave-functions for all states (ground and excited) are determined. Therefore all properties of the system are fully determined given only the ground state density $n_0(\mathbf{r})$.
Theorem II: A universal functional for the energy $E[n]$ in terms of the density $n(\mathbf{r})$ can be defined, valid for for any external potential $V_{ext}(\mathbf{r})$. For any particular $V_{ext}(\mathbf{r})$, the exact ground state energy of this system is the global minimum of this functional, and the density that minimizes this functional is the exact ground state density $n_0(\mathbf{r})$.
Corollary II: The functional $E[n]$ alone is sufficient to determine the exact ground state energy and density. In general, excited states of electrons must be determined by other means.

The Proof of Theorem I

Consider two different external potentials $V_{ext}^{(1)}(\mathbf{r})$ and $V_{ext}^{(2)}$. There also exists a Hamiltonian associated with each of these two potentials $H^{(1)}$ and $H^{(2)}$ and corresponding minimizing wave-functions $\Psi^{(1)}$ and $\Psi^{(2)}$. They obey following conditions

$$\langle\Psi^{(1)}|H^{(1)}|\Psi^{(1)}\rangle = E^{(1)}\langle\Psi^{(2)}|H^{(2)}|\Psi^{(2)}\rangle = E^{(2)} \tag{3.17}$$

with $E^{(1)}$ and $E^{(2)}$ being the ground state energies of the aforementioned Hamiltonians.

$\Psi^{(1)}$ and $\Psi^{(2)}$ are assumed to have the same ground state density $n_0(\mathbf{r})$. Since $\Psi^{(2)}$

is not the ground state of $H^{(1)}$,

$$E^{(1)} = \langle \Psi^{(1)} | H^{(1)} | \Psi^{(1)} \rangle < \langle \Psi^{(2)} | H^{(1)} | \Psi^{(2)} \rangle \tag{3.18}$$

and

$$\begin{aligned} \langle \Psi^{(1)} | H^{(1)} | \Psi^{(1)} \rangle &= \langle \Psi^{(1)} | H^{(2)} | \Psi^{(1)} \rangle + \langle \Psi^{(1)} | H^{(1)} - H^{(2)} | \Psi^{(1)} \rangle = \\ &= E^{(2)} + \int d^3\mathbf{r} \left[V_{ext}^{(1)}(\mathbf{r}) - V_{ext}^{(2)}(\mathbf{r}) \right] n_0(\mathbf{r}) \end{aligned} \tag{3.19}$$

which gives

$$E^{(1)} < E^{(2)} + \int d^3\mathbf{r} \left[V_{ext}^{(1)}(\mathbf{r}) - V_{ext}^{(2)}(\mathbf{r}) \right] n_0(\mathbf{r}). \tag{3.20}$$

Similar considerations for $E^{(2)}$ lead to

$$E^{(2)} < E^{(1)} + \int d^3\mathbf{r} \left[V_{ext}^{(2)}(\mathbf{r}) - V_{ext}^{(1)}(\mathbf{r}) \right] n_0(\mathbf{r}). \tag{3.21}$$

Adding the last two equations leads to

$$E^{(1)} + E^{(2)} < E^{(1)} + E^{(2)}, \tag{3.22}$$

which is a contradiction, proofing the first Hohenberg-Kohn Theorem that potentials leading to the same unique ground state density must not differ by more than a constant. Since the Hamiltonian is now uniquely determined by the ground state density, also the wave-function of any state and therefore also all properties of the systems are in principle determined. The ground state density can now be obtained by the wave-function with the lowest energy. Which again implies Corollary I.

The Proof of Theorem II

The first part in the proof of Theorem II is to define carefully what exactly a functional of the density is and over which densities the functional should be minimized. Since we are interested in ground state densities of a Hamiltonian with an external potential, it is necessary to restrict the space of densities to so called "V-representable" densities, which are ground state densities of the electronic Hamiltonian with some external potential V_{ext}. On this space of densities it is now possible to construct a functional of these densities. It should contain the kinetic energy as well as the internal energy and the energy of the electronic interaction with the potential.

$$\begin{aligned} E^{HK}[n] &= T[n] + E_{int} + \int d^3\mathbf{r} V_{ext}(\mathbf{r}) n(\mathbf{r}) \\ &\equiv F^{HK}[n] + \int d^3\mathbf{r} V_{ext}(\mathbf{r}) n(\mathbf{r}) \end{aligned} \tag{3.23}$$

where $T[n]$ is the kinetic and $E_{int}[n]$ the internal energy functionals, summarized as the so called Hohenberg-Kohn energy functional $F^{HK}[n]$, which must be universal since both are only functionals of the density.

Following Theorem I, the ground state density $n^{(1)}(\mathbf{r})$ is directly related to the external potential $V_{ext}^{(1)}$. The Hohenberg-Kohn energy now corresponds (following the logic applied above) to the ground state energy of the Hamiltonian $H^{(1)}$, which again has a ground state wave-function $\Psi^{(1)}$,

$$E^{(1)} = E^{HK}[n^{(1)}] = \angle\Psi^{(1)}|H^{(1)}|\Psi^{(1)}\rangle \tag{3.24}$$

Since any other density $n^{(2)}$ will lead to a higher energy, this proves Theorem II. If F^{HK} was known exactly the minimization of the energy expression 3.23 with respect to the density would then lead to the exact ground state theory and energy, proving Corollary II. But it is important to note, that this functional only determines only the ground state properties and no further conclusions concerning excited states can be drawn.

The Ideas of Kohn and Sham - The Way Towards Density Functional Theory

Even though the Hohenberg-Kohn Theorems show that the system can be described by the ground state density, which can be obtained by solving the Hohenberg-Kohn functional, they are of no use in actually solving the problem. The main problem is, that the exact functional is not given and especially the internal energy E_{int} describing the interactions of the electrons with each other (already discussed earlier) causes major problems. Additionally it is not clear over which densities one should minimize. At this point Kohn-Sham Density Functional Theory [38] comes into play.

The main idea of Kohn and Sham was, to introduce the Kohn-Sham energy functional

$$E^{KS}[n] = T^{KS}[n] + E_{Hartree}[n] + E_{xc}[n] + \int d^3\mathbf{r} V_{ext}(\mathbf{r}) n(\mathbf{r}) \tag{3.25}$$

where $T^{KS}[n]$ is the kinetic energy contribution of the Kohn-Sham system, $E_{Hartree}$ is the already introduced Hartree energy (the last term in equ. 3.6) and E_{xc} describes all remaining interactions. Comparing E^{KS} with E^{HK} (see equ. 3.23) leads to

$$E_{xc}[n] = T[n] - T^{KS}[n] + E_{int}[n] - E_{Hartree}[n]. \tag{3.26}$$

Since all terms on the right hand side of the last equation are functionals of the density, E_{xc} must also be a functional of the density. It describes all interactions previously called exchange and correlation plus the errors made in the kinetic energy due to the simplified ansatz for the density.

As already discussed in the section about CI, the true ansatz for the wave-function (and therefore also the true ansatz for the density) will be rather complicated and will

lead to exorbitant computational costs. Therefore Kohn and Sham chose an ansatz similar to Hartree theory. Here the $\psi_i(\mathbf{r})$s independent particle solutions, with

$$n(\mathbf{r}) = \sum_{i=0}^{n} |\psi_i(\mathbf{r})|^2, \tag{3.27}$$

which leads to a functional solved more easily.

Variational Calculus and the Kohn-Sham Equations

Since the Kohn-Sham energy is a functional which leads to the ground state energy when minimized with respect to the density, one can now apply variational calculus to find

$$E_0^{KS} = \min_{n(\mathbf{r})} E^{KS}[n] \tag{3.28}$$

If one now assumes, $n_0(\mathbf{r})$ is the minimizing density with corresponding ψ_is, then

$$\frac{\delta E^{KS}[n_0]}{\delta \psi_i^*} = 0. \tag{3.29}$$

leading to

$$\begin{aligned} \frac{\delta E^{KS}[n_0]}{\delta \psi_i^*} = \frac{\delta T^{KS}}{\delta \psi_i^*} + \left(\frac{\delta E_{Hartree}[n]}{\delta n} + \frac{\delta E_{xc}[n]}{\delta n} + \right. \\ \left. + \frac{\delta \int d^3\mathbf{r} V_{ext}(\mathbf{r}) n(\mathbf{r})}{\delta n} \right) \frac{\delta n}{\delta \psi_i^*} - \epsilon_i \left(\int d^3\mathbf{r} \frac{\delta n(\mathbf{r})}{\delta \Psi_i^*} - N \right) = 0, \end{aligned} \tag{3.30}$$

where the last term represents the normalization condition $\int d^3\mathbf{r} n(\mathbf{r}) = N$ multiplied by Lagrange multiplier ϵ_i. Now inserting

$$T^{KS} = \int d^3\mathbf{r} \sum_{i=1}^{n} \psi_i(\mathbf{r})^* \nabla^2 \psi_i(\mathbf{r}) \tag{3.31}$$

$$E_{Hartree} = \int d^3\mathbf{r} d^3\mathbf{r}' \frac{n(\mathbf{r}) n(\mathbf{r}')}{|\mathbf{r} - \mathbf{r}')} \tag{3.32}$$

$$E_{xc} = \int d^3\mathbf{r} V_{xc} n(\mathbf{r}) \tag{3.33}$$

into equ. 3.30 with V_{xc} being the exchange-correlation potential leads to

$$\int d^3\mathbf{r} \left(\nabla^2 + \left(\int d^3\mathbf{r}' \frac{n(\mathbf{r}')}{|\mathbf{r} - \mathbf{r}'|} + V_{xc} + V_{ext}(\mathbf{r}) \right) - \epsilon_i \right) \psi_i = 0. \tag{3.34}$$

Since this equation describes non-zero wave-functions ψ_i, it can only hold, if the expression in brackets is zero. Applying this procedure for all ψ_is leads to n coupled integro-differential equations, the so called Kohn-Sham equations.

$$\left(\nabla^2 + \left(\int d^3\mathbf{r}' \frac{n(\mathbf{r}')}{|\mathbf{r} - \mathbf{r}'|} + V_{xc} + V^{ext}(\mathbf{r})\right)\right)\psi_i = \epsilon_i \psi_i \tag{3.35}$$

The dependencies of V_{xc} were left out consciously and it is defined as he variational quantity

$$V_{xc} = \frac{\delta E_{xc}}{\delta n}. \tag{3.36}$$

The argumentation until now was very general and the exact E_{xc} is not known. In all calculations it is approximated and depending on the level of approximation, it will depend on different variables. A more detailed discussion of these approximations will be given in the next chapter on the Jacob's Ladder of Density Functional Theory.

The same variational calculus can be applied to the Hartree- or Hartree-Fock energy expressions, leading to the Hartree and Hartree-Fock equations respectively.

The Problems with Kohn-Sham Density Functional Theory

Kohn-Sham Density Functional Theory is very successful in describing a wide variety of systems and has become the method of choice in wide areas of theoretical chemistry and theoretical solid state physics. Nevertheless there are still some fundamental problems not solved up until now.

The first question to ask is, whether any density of interacting electrons can be represented by a density of non interacting electrons. Even though it is obviously true for idealized systems of the homogeneous electron gas and can be proven for simple one or two electron problems (see exercise 7.2 and 7.13 in [36]) or for small deviations from the homogeneous electron gas [38], it has never been generally proven. It is still the Kohn-Sham ansatz, which is only justified by its success in describing many properties of the system appropriately.

Another serious drawback comes from the construction of the theory. Only one eigenvalue of the single electron wave-functions has a real physical meaning. This is the eigenvalue of the highest occupied state. It corresponds to the ionization energy of the system. All other eigenvalues are artificial quantities, only needed to construct the proper density leading to the correct ground state theory. Even if one assumes that ground state energy and density are exact, no further conclusions can be drawn about excited states. This holds true despite Corollary I of Hohenberg and Kohn and even more so for the excited state properties within Kohn-Sham DFT. For these purposes excited state theories like GW [39] have to be applied.

3.4 Solving the Kohn-Sham Equations

When computationally solving the Kohn-Sham (or Hartree-Fock) equations, several steps have to be taken. The first step is the Self-Consistent Field (SCF) approach, which describes a scheme to iteratively solve coupled integro-differential equations. The second step is to represent the wave-functions in terms of a basis set like plane waves or

localized orbitals. To make calculations faster, pseudopotentials are introduced, which are based on the assumption, that electrons occupying low lying energy levels do not contribute to bonding and influence the other states only by the influence of their electronic charge, which is summarized in said pseudopotential. Having now obtained the charge density, the forces on the ions can be calculated and can be used to obtain a new geometry.

The Self Consistent Field Cycle

The Kohn-Sham equations in 3.35 are a set of coupled integro-differential equations. It is impossible to solve them analytically. Therefore an iterative scheme has to be applied, the so called SCF method. Before starting the calculations, an initial guess $n_0(\mathbf{r})$ for the charge density is made. This guess is then used as input density $n_{in}(\mathbf{r})$ to create the effective potential V_{eff} in the Kohn-Sham equations. V_{eff} is the sum of all potential energy terms acting on the electrons,

$$V_{eff}(\mathbf{r}, \mathbf{r}', n(\mathbf{r}), n(\mathbf{r}')) = V_{ext}(\mathbf{r}) + V_{Hartree}(\mathbf{r}, \mathbf{r}', n(\mathbf{r}')) + V_{xc}. \tag{3.37}$$

Again the dependencies of V_{xc} are consciously left out, since the exact dependencies depend on the level of approximation used. But V_{xc} usually depends on the charge density $n(\mathbf{r})$ or variables associated with it (like the gradient of $n(\mathbf{r})$ or ψ_is used to construct $n(\mathbf{r})$, therefore the arguments of V_{eff} do not have to be adapted. This newly obtained $V_{eff}(\mathbf{r}, \mathbf{r}', n_0(\mathbf{r}), n_0(\mathbf{r}'))$ is then kept fixed and used to solve the Kohn-Sham equations. The Kohn-Sham eigenfunctions are then used to calculate the new charge density $n_{out}(\mathbf{r})$.

This new charge density $n_{out}(\mathbf{r})$ usually varies from the original charge density $n_{in}(\mathbf{r})$. At the end of the cycle, the system is tested for so called self-consistency. Self-consistency means, that a certain criterion is applied to assess the difference between $n_{in}(\mathbf{r})$ and $n_{out}(\mathbf{r})$. If this criterion is fulfilled, the cycle is stopped and the result is seen as the converged result. If it is not fulfilled, the cycle is started again with a new charge-density $n_{in}^{new}(\mathbf{r})$, generally based upon a mixture of $n_{in}(\mathbf{r})$ and $n_{out}(\mathbf{r})$. $n_{in}^{new}(\mathbf{r})$ is then used to create a new effective potential V_{eff}^{new}, which is then again used to solve the Kohn-Sham equation. This is clearly an iterative scheme, since

$$V_i \rightarrow n_i \rightarrow V_{i+1} \rightarrow n_{i+1} \rightarrow \ldots, \tag{3.38}$$

where i denotes the step in the iteration. This cycle is repeated until self consistency is reached. For a graphical representation see Fig. 3.1.

Similar procedures can also be used to solve the Hartree and Hartree-Fock equations, with the density replaced by a set of wave-functions $\{\psi_i\}$.

The Basis Set Issue

In mathematics, every function can be described by a set of basis-functions. Usually there are multiple ways to choose a basis-set. To simplify the mathematical treatment,

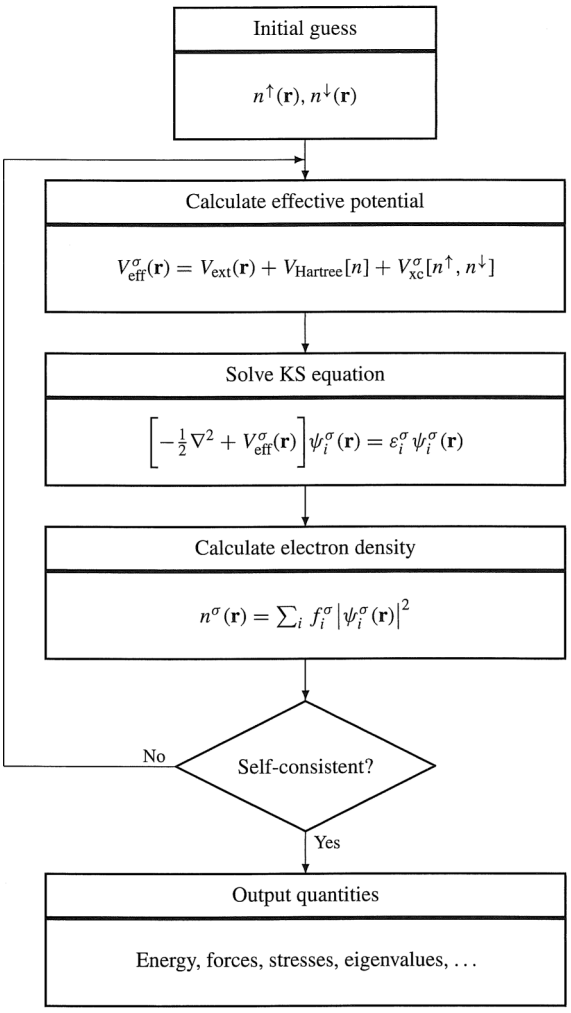

Figure 3.1: This picture originally published in chapter 7 of [36] shows the SCF-cycle. At the beginning an initial guess of the charge density is created. This guess is then used to create an effective potential V_{eff}, which is again used to solve the Kohn-Sham equations. From the solution of those equations a new density is created and is tested for self-consistency. If it fails, a new charge density is created and the loop starts again, if it passes, the new result is seen as the converged density.

usually a set of functions ϕ_i is chosen, which obey the orthonormality conditions

$$\langle \phi_i | \phi_j \rangle = \delta_{ij} \tag{3.39}$$

where $\langle | \rangle$ is short for a predefined multiplication and

$$\delta_{ij} = \begin{array}{c} 1 \text{ for } i = j \\ 0 \; else \end{array} \tag{3.40}$$

is the Kronecker δ. Any function Ψ can then be displayed as

$$\Psi = \sum_i c_i \phi_i \tag{3.41}$$

where the c_is can be calculated by

$$c_i = \langle \Psi | \phi_i \rangle. \tag{3.42}$$

The choice of basis-functions does in principle not matter, as long as the chosen set is complete (as many wave-functions as the dimensionality of the space) and the orthonormality conditions are satisfied. Computational treatment is easier (and results are more insightful), when a basis-set adapted to the symmetry of the problem is chosen.

Returning to our given problem, there are generally two different classes of materials one wants to describe. In quantum chemistry molecules are of great interest and in theoretical solid state physics solids and therefore extended periodic systems are investigated. These two system classes require very different approaches. On the one hand, the wave-functions are usually seen to be localized at the atomic centers of molecules, which are best described by localized orbitals like Slater (STO) [40] or Gaussian Type Orbitals (GTO)[41]. On the other hand the periodic boundary conditions of solids as described by the Bloch Theorem [42] are best described by plane waves.

On the one hand, it is easy to develop the obtained wave-function in terms of atomic orbitals when using localized orbitals, which greatly simplifies the understanding of chemical bonding in the specific systems. Also cells with large amounts of vacuum can easily be described, since basis-functions only sample the area, which is of physical interest (namely the area in the vicinity of atoms). Very often it is also possible to tailor your basis-set to the required needs. A special basis-set can be selected for every single atom and the number of basis-functions is generally proportional to the number of atoms in the system. Careful selection of these basis-functions can lead to a very efficient treatment of the problem only requiring very few basis-functions (especially when treating cells containing large amounts of vacuum or molecules). On the other hand, problems start to arise with the treatment of metals, where wave-functions typically have a long range tail expanding over many atoms. A localized basis-set is also overcomplete, which means, that the integral over different site basis-functions $\int \phi_i(\mathbf{r} - \mathbf{R_k}) \phi_j(\mathbf{r} - \mathbf{R_l}) \neq 0$, which leads to the so called basis-set superposition error (BSSE).

Plane-waves are ideally suited to describe problems with periodic boundary conditions such as metals. Here there is no problem with the description of the non-localized wave-functions. The set of plane waves is complete and therefore the accuracy of the description of the system can be influenced by only one parameter, the energy cut-off. When additionally introducing pseudopotentials (see next section), calculations of the valence band in metals only require a rather low energy cut-off which greatly increases computational efficiency. In problems where the wave-function varies quickly and large gradients of the density can be expected (like in molecules, on surfaces or valence-bands without pseudopotentials), the kinetic energy is generally large, therefore a large energy cut off is needed. Also the number of plane waves is determined by the cell-size, which is of large advantage when calculating dense materials, but becomes a disadvantage when treating systems containing large amounts of vacuum. Another point of criticism is also the incompleteness of the plane-wave basis-set. Since the series has to be truncated at a certain point (at the energy cut-off), a certain inaccuracy has to be expected, but in contrast to the BSSE for localized orbitals these errors are rather transparent, since they only depend on the energy cut-off parameter, while the BSSE depends on the choice of every single atomic basis-set.

Even though the computational treatment of the electronic problem focuses heavily on localized and plane-wave basis-sets it is important to note, that these are not the natural basis-functions of the problem. The natural basis functions of the problem are functions having the same symmetry as the Hamiltonian and are therefore the eigenfunctions of the operator, each corresponding to an eigenvalue, which again can be associated with an energy. Or expressed more clearly: Finding solutions to a Hamiltonian means to search for the natural basis-set obeying the same symmetry constraints as the Hamiltonian, which again is the ideal basis-set for the given problem. Auxiliary basis-sets are only needed to allow for an iterative, computational treatment.

Pseudopotentials and the Projector Augmented Wave Method

As already mentioned, in plane wave calculations a very high energy cut off is needed when calculating the all electron problem. This originates from the orthogonality conditions. Since the core levels of any atom typically have very few nodes, orthonormality requires valence electrons to have many nodes. This fact inspired Fermi and coworkers [43, 44] in the middle of the 1930s to speculate about a simplification of the problem.

The reasoning behind all pseudopotential methods is to assume, that low lying atomic energy levels do not contribute actively in bonding. Only valence electrons do. Therefore an effective potential acting on valence electrons is introduced. This potential contains the charge resulting from the ionic potential and the nucleus. When applied correctly, this approximation allows to obtain a "soft" pseudo-wave-function in the core region and a wave-function corresponding to the true wave-function in the interstitial area, where bonding phenomena usually take place (see Fig. 3.2).

There is no unique set of pseudopotentials, but each different potential will lead to a different pseudo-wave-function in the core area. There are, however some desirable properties the pseudopotetials should obey.

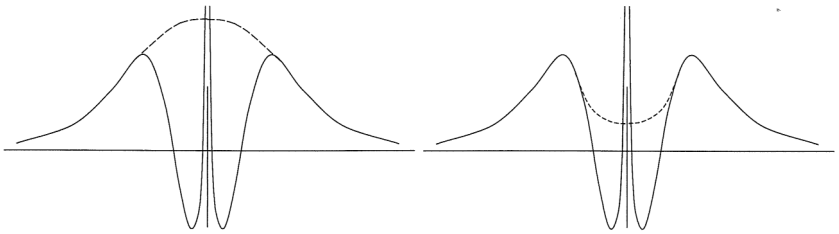

Figure 3.2: Due to orthogonality condition valence wave-functions very often have many nodes demanding a high accuracy in the basis-set to allow a proper sampling. To circumvent this problem pseudopotentials are used, which allow pseudo wave-functions. In this graph the original 3s wavefunction (solid line) and two possibilities for the pseudo wave-function (dashed lines) are displayed. The picture is taken from [36].

- The core region of the potential should not be too large, to allow a proper description of bonding
- The potential should lead to a very "soft" pseudo-wave-function. This allows for a treatment using a low energy cut-off.
- Ideally the norm of the wave-function and therefore the charge should be conserved

A method which has proven to be very efficient is the so called Projector Augmented Wave (PAW) Method by Blöchl [45, 46]. Here space is divided into spherical areas around the nuclei (like a muffin tin, see Fig. 3.3) and an interstitial region. Around the nuclei, the wave-function is projected onto a pseudo-wave-function orthogonal to the core states, which are evaluated on a radial grid around the core. Together with the frozen core approximation (the core-states are kept fixed) this allows for a very efficient treatment of even large systems.

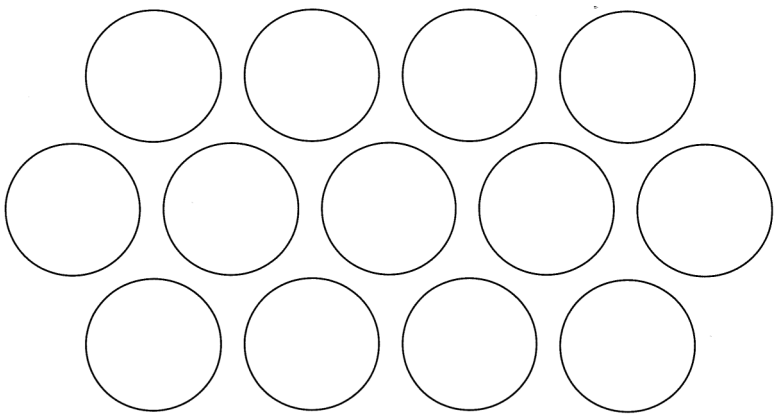

Figure 3.3: When using the PAW method an additional pseudo-potential acts in the regions around the nuclei on the electronic wave-function. In the two dimensional projection displayed here this looks like a muffin-tin. A proper sampling of the wave-functions is achieved by choosing suitable boundary conditions. This picture is taken from [36]

4 Jacob's Ladder of Density Functional Theory

Summary

The equations of Kohn-Sham Density Functional Theory (DFT) were in principle exact, if the exact E_{xc} was known. Finding this exact expression for E_{xc} is however an extraordinarily challenging task and it has not been achieved up until now. When performing DFT calculations, an approximation for E_{xc} is used. These approximations vary in computational demands and accuracy and are usually summarized in the so called "Jacob's Ladder of Density Functional Theory". This ladder has five rungs, and with each rung the quality of the approximation increases.

- On the first rung functionals depend on the local density $n(\mathbf{r})$ (Local Density Approximation (LDA))
- On the second rung functionals depend on the local density $n(\mathbf{r})$ and its gradient $\nabla n(\mathbf{r})$ (Generalized Gradient Approximation (GGA))
- On the third rung functionals depend on the local density $n(\mathbf{r})$, its gradient $\nabla n(\mathbf{r})$ and the kinetic energy density $\tau(\mathbf{r})$(meta-GGA)
- On the fourth rung functionals depend non-locally on the density $n(\mathbf{r}), n(\mathbf{r}')$ or the occupied orbitals $\phi^o(\mathbf{r}), \phi^o(\mathbf{r}')$.
- On the fifth rung functionals depend non-locally on the occupied or unoccupied orbitals $\phi^o(\mathbf{r}), \phi^o(\mathbf{r}'), \phi^u(\mathbf{r}), \phi^u(\mathbf{r}')$.

In this chapter we give a discussion of the various approximations focusing of the methods used in this work.

4.1 Jacob's Ladder

In DFT the quality of calculations is always determined by the quality of the approximation of E_{xc}. Numerous approximations exist and they are categorized in the Jacob's Ladder of DFT, introduced by John Perdew [47]. The idea is based upon the biblical picture of Jacob dreaming of a ladder connecting heaven and earth [48]. Similar to this picture, each rung of the ladder leads the aspiring physicist closer to density functional heaven, a functional describing the physical problems with errors smaller

than 1 kJ/mol. As one steps up the ladder the approximations become more and more accurate but at the same time more expensive.

How to Construct a Density Functional

Before turning to the different rungs of the ladder and the functionals associated with them we will first take a small detour and ask the question how functionals are generally designed. Especially the functionals on the first three rungs of the ladder are rather crude approximations to the true E_{xc}. A non-local quantity is approximated by a local or semi-local functional, which clearly is a steep task to achieve. In these approximations a functional form is chosen which depends on a set of parameters. At this point two different schools of thought come into play.

In the first a functional depending on an arbitrary number of parameters is chosen. The functional is optimized to give best agreement with standardized set of materials or molecules. These sets contain a certain number of materials each posing a specific theoretical difficulty. Very often functionals are found, which give very good agreement for one dataset but work badly for anotherone. Equipped with this knowledge the alert user has to decide, what difficulties are encountered in the problems he wants to treat and can choose the suitable functional. This approach is very popular in the chemistry community.

Another approach is to first investigate the problem more closely. A proper exchange-correlation functional must obey a certain set of restrictions (see e.g. [49]), which are derived theoretically. Some of them are more obvious, e.g. that the induced exchange hole density must be negative ($n_x(\mathbf{r}, \mathbf{r}') \leq 0$) and must present an electron deficit of exactly one electron ($\int d^3\mathbf{r} d^3\mathbf{r}' n_x(\mathbf{r}, \mathbf{r}') = -1$), some of them need a more sophisticated theoretical analysis like satisfying the Lieb-Oxford bound [50]. These constraints rarely lead to exact parameterization, but give an upper and lower bound for the parameters in the chosen ansatz. Within these bounds parameters are then again fitted to minimize errors with respect to experimental test datasets. This approach is very popular among theoretical physicists, since it is claimed to be fully "ab-initio", while the previous method is seen as highly empirical.

While the first approach might lead to very accurate results for system within the benchmark-dataset it is very often not transferable to a more general set of systems often neglecting basic physical intuition. This leads to such absurd effects, that semi-local meta-GGAs can predict van der Waals interactions, a phenomenon that clearly depends on the dynamic polarizability of density in a finite distance. Only obeying the already mentioned restrictions ensures a correct behavior for a wide range of systems.

The ideal Functional?

Even though no expression for the ideal density functional has not been found, it is still worthwhile to discuss the properties it should have and compare them to the approximations described later in this chapter. Most of these methods make simplifications like the local or semi-local description of the exchange and correlation energies, others

(especially the fifth rung methods) use a rather inefficient approach in calculating the correlation energy.

The ideal functional should be able to describe all systems at chemical accuracy. This condition implies, that it must be correct in the free electron gas limit as well as the hydrogen atom limit. Furthermore it must be able to also describe the subtle effects of dispersion interactions which are of major importance for many systems. Only a non-local functional in the exchange as well as in the correlation energy expression can achieve that.

To also guarantee the computational efficiency[1] the inclusion non-occupied orbitals should be omitted. A point of discussion is, wether such a functional can capture all correlation effects caused by the formation of quasiparticles described by excited slater determinants in quantum chemistry. This can be illustrated when keeping V_{ext} in the proofs of the Hohenberg-Kohn theorems constant. Following a similar logic as in the original proofs the density alone defines all ground state properties and therefore implicitly also all unoccupied orbitals of the given problem. Therefore the correlation energy must only depend on $n(\mathbf{r})$ and $n(\mathbf{r}')$.

While the correlation energy is not known exactly and poses large difficulties, an exact expression for the exchange energy is known. Since the Kohn-Sham ansatz of n noninteracting electrons occupying only the lowest n KS-orbitals is used, the exchange interaction is by definition exactly described by the Fock term in the Hartree-Fock energy expression already discussed in previous chapters. All other effects are then summarized in the correlation contribution.

4.2 The First Three Rungs - Local and Semi-Local Approximations

The functionals of the first three rungs are all local or semi-local functionals. Their high efficiency and accuracy makes them the most often used functionals in DFT.

The First Rung - the Local Density Approximation

Already in their original work [38] Kohn and Sham believed, that an approximation for E_{xc} depending only on the local density $n(\mathbf{r})$ should be sufficient to describe the exchange and correlation interaction in metals sufficiently well. The energy expression for the so called Local Density Approximation (LDA) then takes the following simple form

$$E_{xc}^{LDA} = \int d^3\mathbf{r} n(\mathbf{r}) \epsilon_{xc}^{hom}(n(\mathbf{r})) =$$
$$= \int d^3\mathbf{r} n(\mathbf{r}) (\epsilon_x^{hom}(n(\mathbf{r}) + \epsilon_c^{hom}(n(\mathbf{r})). \tag{4.1}$$

[1] and to avoid convergence problems

ϵ_{xc}^{hom} is the exchange-correlation energy density per electron and ϵ_x^{hom} and ϵ_c^{hom} are the corresponding exchange and correlation energy densities. For a spin-polarized calculation $n(\mathbf{r})$ has to be substituted by $n^{\uparrow}(\mathbf{r}) + n^{\downarrow}(\mathbf{r})$ which leads to the Local Spin Density Approximation (LSDA).

These energy densities depend only on the charge-density $n(\mathbf{r})$. It is therefore a suitable way to investigate exchange and correlation contributions in a standardized test system and transfer them to the actual functional. The most suitable test system for the LDA is the so called homogeneous electron gas. This system is represented by a uniform positive potential, which is compensated by a uniform electron cloud. While the exchange energy for this problem can be calculated analytically, the correlation energy of the homogeneous electron gas is obtained from quantum monte-carlo calculations. These results are then used in the parameterization of ϵ_{xc}^{hom} [51]. The superscript *hom* indicates the parameterization with respect to the homogeneous electron gas.

As simple as this approximation might seem it is still extraordinarily useful. Especially for metallic systems where the charge density is close to the homogeneous electron gas impressive results can be achieved. Nevertheless the LDA is overbinding for most cases and sometimes favors to the wrong magnetic groundstate in some materials like iron [52]. The approximation has its restrictions. For systems with fluctuating charge densities like molecules or covalently bound materials the LDA fails to give reasonable results.

The Second Rung - the Generalized Gradient Approximation

Due to the restrictions of the LDA in treating charge densities with large fluctuations, the next step in improving the LDA is the addition of a term describing these fluctuations. Usually the gradient of the density should give a good indication of these fluctuations, which then naturally leads to the so called Generalized Gradient Approximation (GGA).

In the GGA, the energy expression 4.1 is extended by a gradient dependent term $F_{xc}(n(\mathbf{r}), \nabla n(\mathbf{r}))$.

$$E_{xc}^{GGA} = \int d^3\mathbf{r} n(\mathbf{r}) \epsilon_{xc}(n(\mathbf{r}), \nabla n(\mathbf{r})) =$$
$$\equiv \int d^3\mathbf{r} n(\mathbf{r}) \epsilon_x^{hom}(n(\mathbf{r}) F_{xc}^{hom}(n(\mathbf{r}), \nabla n(\mathbf{r})). \tag{4.2}$$

Spin dependence of F_{xc} can be achieved in a similar way as in the LDA by again substituting $n(\mathbf{r})$ by $n^{\uparrow}(\mathbf{r}) + n^{\downarrow}(\mathbf{r})$ and $\nabla n(\mathbf{r})$ by $\nabla n^{\uparrow}(\mathbf{r}) + \nabla n^{\downarrow}(\mathbf{r})$.

The explicit F_{xc} only depends on the dimensionless quantity

$$s_m = \frac{|\nabla^m n|}{(2k_F)^m n} = \frac{|\nabla^m n|}{2^m (3\pi^2)^{\frac{m}{3}} n^{(1+m/3)}}. \tag{4.3}$$

where k_F is the length of the Fermi wavevector of the homogeneous electron gas

$$k_F = 3\pi^2 n^{\frac{1}{3}}. \tag{4.4}$$

The first natural step for improvement over LDA would be an expansion of E_{xc} in terms of the density and its gradient as originally proposed by Kohn and Sham. The lowest order expansion coefficients can be calculated analytically [53, 49] to give

$$F_x = 1 + \frac{10}{81}s_1^2 + \frac{146}{2025}s_2^2 + \dots \tag{4.5}$$

for the exchange part of F_{xc}. The correlation part is more difficult to treat but is usually an approximation to RPA (see section 4.3) or beyond RPA calculations. The problem with this gradient expansion is, that it is only valid for small gradients (since only then does the series converge) and even worsens the description in materials with large density gradients. Furthermore this expansion does not satisfy some important sum-rules [49].

Numerous changes have been suggested. The most successful of them apply a real space cut-off for the approximated energy cut-off. While these functionals give similar values for the physically relevant region of $s_1 \leq 3$, they explicitly vary in the $s_1 \to \infty$ limit. The most successful of these functionals are the functionals of Perdew and Wang in 1991 (PW91) [54] and Perdew Burke and Ernzerhof (PBE)[55]. On one hand these two functionals satisfy almost all theoretical constraints and can therefore be truly seen as "ab-initio" and on the other hand they lead to excellent results. Even though they lead to very similar results (see Fig. 4.1), it is the method of construction, which favors the PBE functional.

The GGAs correct for the overbinding of the LDA leading to a slight underbinding and lead to improved results in solids as well as in molecules. Within the PBE-form there is however still a certain degree of freedom within parameterization which has lead to numerous variations fitted to optimize the description of solids (PBEsol [56]) or molecules (RPBE [57] or revPBE[58]).

The Third Rung- Meta-GGAs

Functionals on the third rung additionally take the kinetic energy density τ into account. This is still a semi-local approximation so the question to ask is, what physical insight can be gained from additionally adding the kinetic energy density as a variable. At first sight τ only contributes to E_{xc} as a higher order in the expansion 4.5. But looking more closely this approximation has a deeper physical meaning.

τ can be expressed as the second derivative of the charge density and is therefore a measure of the curvature of the density. While the gradient of the density alone can only identify extrema of the charge density, the curvature as an additional parameter can now help to determine whether the given extremum is a maximum or minimum of the charge density. This feature can then also be used to identify bonding and anti-bonding orbitals.

The functional fulfilling the most theoretical constraints is the functional by Tao, Perdew, Staroverov and Scuseria [59]. Using TPSS leads to a slight improvement over PBE as far as lattice constants and surface energies are concerned, but slightly worsens the description of quantities like the bulk modulus [60].

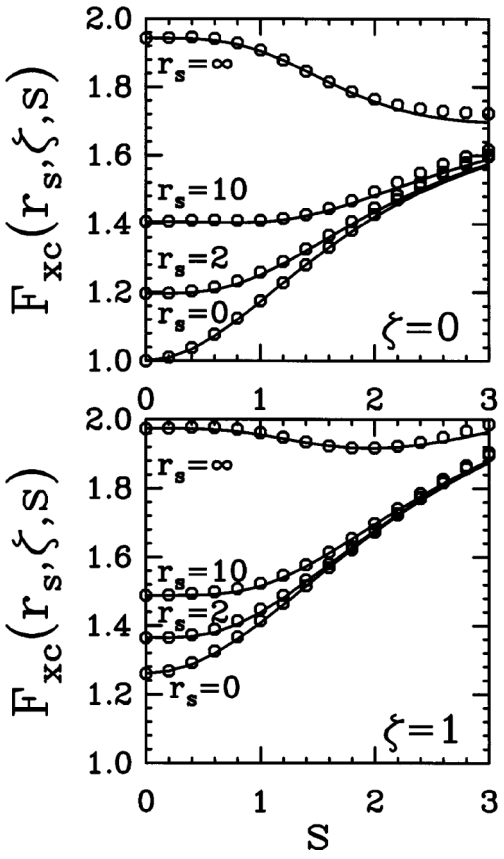

Figure 4.1: In this graph the values of F_{xc} are displayed for PBE (solid lines) and PW91 (circles). For two values of the spin polarization $\zeta = 0$ (upper picture) and $\zeta = 1$ (lower picture). They show very similar results (with slight deviations for larger values of s), indicating a similar performance. This graph was originally published in [55].

As finishing remarks on the local and semi-local functionals it must be mentioned, that even though they are probably the most often used functionals in DFT calculations, there are still some theoretical objections to these functionals. The first point of criticism is that due to construction, the exchange and correlation contribution should not be seen separately. Each on its own is not a good approximation to the true exchange or correlation energies respectively. Only error cancellation in the combination of those two leads to a good description.

Since the exchange-correlation energy only depends on the total density, there is also an unphysical self exchange and self-correlation contribution contained within these functionals. This interaction of electrons with themselves leads to a too large delocalization of the orbitals, an effect which is especially observed for the d- and f-metals and leads to problems in their description.

Another big obstacle is the inclusion of van der Waals (vdW) interactions in these functionals. Due to the (semi-)locality of the functionals no information of distant charge densities can be obtained and therefore no vdW interactions can be described. This effect can only be cured by the inclusion of auxiliary force-fields.

Spin polarized calculations and magnetic moment

Up until now we only discussed DFT using a general charge density $n(\mathbf{r})$ but DFT can easily be generalized to give a proper description of magnetic properties of systems. To achieve that the density has to be split in a spin up and spin down component

$$n(\mathbf{r}) = n^{\uparrow}(\mathbf{r}) + n^{\downarrow}(\mathbf{r}), \tag{4.6}$$

where $n^{\uparrow}$ and $n^{\downarrow}$ denote spin up and spin down density components[2] . To keep the discussion simple the axis of spin polarization will be the same for the entire system. A more general discussion for non-collinear spin densities can be found in [61, 62, 63, 64].

For spin polarized systems the exchange and correlation contribution to the energy functional has to be rewritten to

$$E_{xc}[n^{\uparrow}, n^{\downarrow}] = \int d^3\mathbf{r} n(\mathbf{r}) \epsilon_{xc}(n^{\uparrow}, n^{\downarrow}). \tag{4.7}$$

For the exchange contribution it is straightforward to show that a spin-scaling relation in the form of

$$E_x[n^{\uparrow}, n^{\downarrow}] = \frac{1}{2}(E_x[2n^{\uparrow}] + E_x[2n^{\downarrow}]) \tag{4.8}$$

holds and the correlation contribution depends on the entire charge density $n(\mathbf{r})$ anyway. Therefore the KS equations can be solved leading to a set of spin up and spin down orbitals.

[2]This discussion is also possible by defining the polarizability $\zeta = n^{\uparrow}(\mathbf{r}) - n^{\downarrow}(\mathbf{r})$ and using the density $n(\mathbf{r}$ and ζ as variables. This leads to an equivalent description with a slightly modified functional form.

The occupation number N for spin up and spin down states can then be obtained by

$$N^{\uparrow,\downarrow} = \int_{-\infty}^{E_F} dED^{\uparrow,\downarrow}, \tag{4.9}$$

where E_F is the Fermi energy of the system and D is the desity of states. Clearly the difference between $N^{\uparrow}$ and $N^{\downarrow}$ is the total magnetic moment of the given system.

In an unconstrained calculation the system is allowed to relax freely and the E_F is determined by the electron number in the system. But it might be desireable to fix the magnetic moment to e.g. calculate an excited state of a given molecule[3][65]. The magnetic moment is given by

$$M = N^{\uparrow} - N^{\downarrow} = \int_{-\infty}^{E_F^{\uparrow}} dED^{\uparrow} - \int_{-\infty}^{E_F^{\downarrow}} dED^{\downarrow}. \tag{4.10}$$

For a local energy minimum of M $E_F^{\uparrow} = E_F^{\downarrow}$. This is not the case for an excited state. Here $E_F^{\uparrow}$ and $E_F^{\downarrow}$ are defined by the number of spin up and spin down electrons.

Including van der Waals Interactions - Force-Field Methods

When looking at charge densities, they are usually not static but fluctuate. These fluctuations create dipole moments which again induce dipole moments in other regions. The interaction between these dipole moments is called van der Waals (vdW) interaction. The exact description of these phenomena within a DFT framework is by no means trivial and usually needs an inclusion of unoccupied orbitals or at least a non-local expression for the correlation energy. These features are only found at the higher rungs of the Jacob's ladder. But for the local or semi-local functionals a workaround can be found.

In this workaround (here we are discussing the PBE-d(2) approach by Grimme [66]) a term is added in the total energy equation

$$E_{tot} = E_{DFT} + E_{disp}. \tag{4.11}$$

The additional term E_{disp} corresponds to all dispersion interactions in the system. The dispersion energy

$$E_{disp} = -s_6 \sum_{i=1}^{n-1} \sum_{j=i+1}^{n} \frac{C_6^{ij}}{\mathbf{r}_{ij}^6} f_{dmp}(\mathbf{r}_{ij}) \tag{4.12}$$

primarily depends on a factor $\frac{1}{\mathbf{r}_{ij}^6}$ multiplied by C_6^{ij}. Here $\mathbf{r}_{ij}$ (for a graphical visualization see Fig. 4.2) is the distance between atomic cores i and j and C_6^{ij} is the corresponding C_6 factor depending on the polarizability of the two atoms. In PBE-d(2) it is defined by

$$C_6^{ij} = \sqrt{C_6^i C_6^j}, \tag{4.13}$$

[3]In a system with degenerate energy-levels close to E_F fixing the magnetic moment might lead to faster electronic and ionic convergence.

where C_6^i is a predefined factor for atom i.

The r_{ij}^{-6} behavior shows a really steep increase when atoms are getting to close. Therefore the damping-function

$$f_{dmp}(\mathbf{r}_{ij}) = \frac{1}{1 + e^{-d(\mathbf{r}_{ij}/\mathbf{R}_r - 1)}} \tag{4.14}$$

is introduced, which obviously prevents atoms from interacting when closer than the sum of the atomic radii $\mathbf{R}_r$.

Depending on the choice of functional, the global scaling parameter s_6 in equ. 4.12 can be adjusted to give a reasonable adjustment to the total energy.

The success of such forcefield methods crucially depends on the choice of atomic polarizability parameters C_6^i. These parameters typically vary for different bonding configurations. C_6^i factors for many of these configurations were calculated by Wu and Yang [67], but in the PBE-d(2) only weighted averages are used leading to only one coefficient for every element.

Especially in recent research some improvements were suggested to PBE-d(2). All of them try to find means to identify the bonding environment of the considered atom, either by considering the charge density surrounding the atom [68] or counting the nearest neighbors [69].

From a computational point of view these forcefield methods have the huge advantage of being very efficient even for large systemsizes. This makes this method the method of choice in extremely expensive calculations like molecular dynamics simulations [18, 70] or in simulating large biological systems [71].

4.3 The High Rungs of the Ladder

The higher two rungs of the ladder generally depend on non-local approximations of E_{xc}. This significantly increases computational cost and accuracy. Especially the (extraordinarily costly) inclusion of unoccupied orbitals poses problems for calculations. It is generally seen to be the key ingredient in obtaining a truly ab initio inclusion of vdW interactions in DFT-like calculations.

In this section we will first focus on the inclusion of exact (Hartree-Fock) exchange in functionals leading to the so called hybrid functionals. This will be followed by a discussion of the Adiabatic Connection Fluctuation Theorem in its Random Phase Approximation (RPA), a method from the fifth rung of the ladder. Even though it is not a DFT method a short discussion of Møller-Plesset perturbation theory will be given. After that we will discuss non-local approximations to the correlation functional like the vdW-DF and will show that in principle a non-local description of the correlation energy should suffice.

Hybrid Functionals - Treating Exchange Non-Locally

Already by definition exact exchange is generally obtained by describing exchange by using the Fock term introduced in the previous chapter as exchange operator. But as

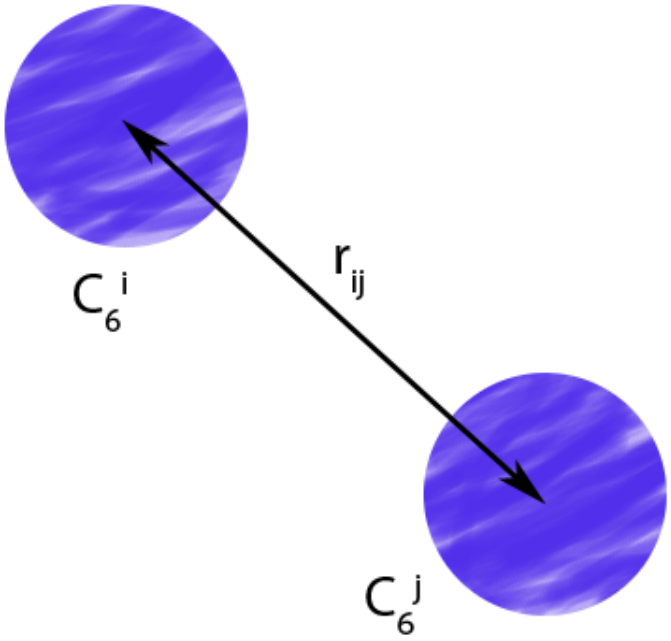

Figure 4.2: When applying a forcefield for vdW interactions between two particles their distance r_{ij} and their respective polarizabilities, which are captured by the so called C_6 parameters are of major importance. The main contribution to vdW-interactions has the form of $f(C_6^i, C_6^j)/r_{ij}^6$ with every forcefield having a special form of $f(C_6^i, C_6^j)$

already discussed, the exact exchange term can not totally replace a semi-local expression since the necessary error cancellation would be lost. Usually a hybrid approach is used, where only a part of the semi-local exchange energy is replaced.

$$E = aE_x^{HF} + (1-a)E_x^{KS-DFT} + E_c^{KS-DFT} \tag{4.15}$$

with $0 \leq a \leq 1$. For $a = 0$ the original functional is obtained and for $a = 1$ full Hartree-Fock exchange is included. There is also a certain freedom in the choice of the used semi-local approximation.

In their very popular hybrid functional Perdew, Burke and Ernzerhof found, based on theoretical considerations, the optimal choice of a to be 0.25 [72]. Together with the PBE functional this forms the PBE0 functional.

$$E^{PBE0} = 0.25E_x^{HF} + 0.75E_x^{PBE} + E_c^{PBE} \tag{4.16}$$

The non-locality of the exchange expression leads to a increased computational cost, especially in solids with their uniform charge distribution. Following the ideas of Heyd, Scuseria and Ernzerhof [73], a significant increase in computational efficiency can be achieved by only including short ranged exchange contributions. This leads to the so called HSE functionals.

$$E^{HSE} = 0.25E_x^{HF,sr,\mu} + 0.75E_x^{PBE,sr,\mu} + E_x^{PBE,lr,\mu} + E_c^{PBE} \tag{4.17}$$

where lr denotes long range and sr short ranged contributions. The range separation is obtained by the error function approach

$$\frac{1}{\mathbf{r}} = S_\mu(\mathbf{r}) + L_\mu(\mathbf{r}) = \frac{erfc(\mu\mathbf{r})}{\mathbf{r}} + \frac{efc(\mu\mathbf{r})}{\mathbf{r}}. \tag{4.18}$$

Here $erfc(\mu\mathbf{r}) = 1 - efc(\mu\mathbf{r})$, with the specific cut-off parameter μ. In their original work Heyd, Scuseria and Ernzerhof suggested to use $\mu = 0.3$ (HSE03, [73]), while they corrected it to $\mu = 0.207$ (HSE06[74]) in later work.

In a series of papers, Paier et al [75, 76, 77, 78] systematically investigated the performance of their implementation of hybrid functionals in a plane-wave basis-set and found a set of interesting properties.

The combination of the underbinding GGAs (PBE: 2-3% too large lattice constants) and the overbinding HF exchange leads to a slight overbinding (PBE0/HSE03: 1% too small lattice constants) using hybrid functionals. Interestingly screening the exact exchange does not change this behavior, even though it alters the energetics of the bonding as we will discuss in later chapters. A similar improvement is found for the bulk modulus.

Compared to PBE atomization energies for non-metallic systems are of a similar accuracy when using hybrid functionals. For metallic systems an even stronger tendency to underestimate the atomization energies is observed. While PBE underestimate heats of formation, hybrid functionals lead to markedly better results.

Also obtained band gaps show a better agreement with experiment. While PBE0 slightly overestimates the band gap for semiconductors, HSE03 shows band gaps in

excellent agreement with experiment for small and medium gap systems. For large gap systems an underestimation is observed (but still better results are obtained than for standard semi-local functionals). For metallic systems the band widths are overestimated.

In 3d metals semi-local density functionals lead to 3d states which are spatially too delocalized. This follows from the self-exchange that is included in these functionals which only depend on the densities. Exact exchange usually leads to too localized states. Mixing these two methods corrects for these two effects and leads to a significant improvement of lattice constants for instance in transition metal oxide materials.

The admixture of exact exchange leads to a too large exchange splitting in 3d transition metals which in turn leads to a preference of higher spin states in these systems, sometimes sometimes resulting in the preference the wrong spin ground state.

The Fifth Rung

Strictly speaking functionals of the fifth rung are not density functionals per se[4]. While the exchange contribution usually is the Hartree Fock equation, the correlation contributions only depend on occupied and unoccupied orbitals. In this section we will discuss two methods, the Adiabatic Connection Fluctuation Dissipation Theorem in its Random Phase Approximation (RPA) and second order Møller Plesset perturbation theory (MP2). While the energy expression in the RPA can still be separated into exchange and correlation contribution and can in principle be solved variationally using an optimized effective potential (OEP) approach, MP2 (even though it depends on Hartree Fock orbitals) is a perturbative approach.

As different as these methods in principle seem, they share one property. Even though they lead to a very high accuracy, the inclusion of unoccupied orbitals leads to extremely high computational demands and furthermore these methods often show bad scaling with systemsize.

The Adiabatic Connection Fluctuation Dissipation Theory in its Random Phase Approximation (RPA)

The problem within DFT is to exchange the actual Coulomb electron-electron interaction operator by the more easily treatable exchange-correlation energy E_{xc}. A way to achieve that is the so called Adiabatic Connection. The Fluctuation Dissipation Theorem then relates this quantity to the response of the electronic problem to an external perturbation. Applying formulas obtained from Time-Dependent DFT and the so called Random Phase Approximation leads to a computationally treatable expression for the correlation energy. In this text the proofs will only be sketched and the most important steps will be given. For a more detailed discussion we want to refer the reader to [79].

The Hohenberg-Kohn Theorems state that it suffices to calculate the density of the system to obtain the remaining quantities associated with it. Within DFT this is

[4]which is the reason why they are sometimes not included in the Jacob's Ladder.

achieved by substituting the fully interacting problem by a problem of non interacting electrons, which is only influenced by an additional potential. The main problem is to find a relation between the energy of the fully interacting problem (and therefore the Coulomb interaction energy also influenced by electronic excitations) and the exchange-correlation energy E_{xc}, which is used in many calculations. A way to achieve that is the so called adiabatic connection.

In the adiabatic connection a new Hamiltonian is introduced

$$H(\lambda) = T + V^{\lambda} + \lambda V_{ee}, \tag{4.19}$$

where T denotes the kinetic energy operator and V_{ee} is the Coulomb operator $\frac{1}{|\mathbf{r}-\mathbf{r}'|}$. The coupling constant λ on the one hand defines, how much of the electronic interactions are turned on. On the other hand it also influences the potential energy acting on a single electron V^{λ} to keep the ground state density constant. λ can vary between 0 and 1 and the two limiting cases represent the fully interacting system ($\lambda = 1$) and the Kohn-Sham system ($\lambda = 0$). It is also interesting to note, that for $\lambda = 1$ V^{λ} corresponds to V_{ext}, the external potential, and for $\lambda = 0$, V^{λ} corresponds to $V_{ext} + V_{xc}$, the sum of the external and the exchange correlation potential.

Expressing the total energy for both limiting cases, and subtracting them and making use of the Hellman Feynman theorem leads to the following expression for the Hartree-exchange-correlation energy E_{xc}^{H}

$$E_{xc}^{H} = \int_0^1 d\lambda \, \langle \Psi(\lambda) | V_{ee} | \Psi(\lambda) \rangle \,, \tag{4.20}$$

where $\Psi(\lambda)$ is the ground state wave-function corresponding to the λ interacting system. This formula is now completely free of kinetic energy contributions which has the advantage, that the explicit construction of the one particle density matrix can be avoided.

In the next step, the so called fluctuation dissipation theorem is applied. This theorem states that any system responds to a spontaneous fluctuation in the same way it responds to an external perturbation. In this case, the effects of spontaneous density fluctuations within the system can be described in the same way as the response of the system to a small time dependent additional potential, which is described by the density-density response function χ. Application of this theorem leads to the exchange-correlation energy

$$E_{xc} = -\frac{1}{2} \int_0^1 d\lambda \int d^3\mathbf{r} d^3\mathbf{r}' \frac{1}{|\mathbf{r}-\mathbf{r}'|} \left\{ n(\mathbf{r}) \delta(\mathbf{r}-\mathbf{r}') + \frac{1}{\pi} \int_0^{\infty} d\omega \chi^{\lambda}(\mathbf{r}, \mathbf{r}', i\omega) \right\}. \tag{4.21}$$

It is important to note, that the Hartree energy contribution has already been separated from E_{xc}^{H} for this equation.

Now using the explicit form of the independent particle response function and applying a little more algebra (for the exact details of the derivation of the previous formula and this step we want to refer the reader to [79]) allows us to separate also the

Hartree-Fock exchange contribution from this expression, leading to a new expression for E_{xc}

$$E_{xc} = E_x[\{\psi^{KS}\}] - \\ - \int_0^1 d\lambda \int d^3\mathbf{r} \int d^3\mathbf{r}' \frac{1}{|\mathbf{r}-\mathbf{r}'|} \int_0^\infty \frac{d\omega}{2\pi} \left\{\chi^\lambda(\mathbf{r},\mathbf{r}',i\omega) - \chi^{KS}(\mathbf{r},\mathbf{r}',i\omega)\right\}. \quad (4.22)$$

In this equation χ^λ is again the response function of the λ interacting system and χ^{KS} is the response function of the Kohn-Sham system. Now the correlation energy (the second part on the right hand side of equ. 4.22) is only one expression. The Hartree-Fock exchange energy is now evaluated for $\left\{\psi^{KS}\right\}$, the wave-functions of the Kohn-Sham system.

Expression 4.22 is in principle exact, but difficulties occur when performing the λ integration, since the exact form of χ^λ is not exactly known. Nevertheless, χ^λ and χ^{KS} are linked via the so called Dyson-equation

$$\chi^\lambda(\mathbf{r},\mathbf{r}',i\omega) = \chi^{KS}(\mathbf{r},\mathbf{r}',i\omega) + \\ + \int d^3\mathbf{r_1} d^3\mathbf{r_2} \chi^{KS}(\mathbf{r},\mathbf{r_1},i\omega) \left(\frac{\lambda}{|\mathbf{r_1}-\mathbf{r_2}|} + f_{xc}^\lambda(\mathbf{r_1},\mathbf{r_2},i\omega)\right) \chi^\lambda(\mathbf{r_2},\mathbf{r}',i\omega). \quad (4.23)$$

While the exchange correlation kernel f_{xc} is a well defined quantity, problems start to arise from the λ dependence.

To circumvent problems, in the so called Random Phase Approximation (RPA) [80, 81, 82] this f_{xc}^λ is set to 0. After using a little bit of algebra, one can now carry out the λ-integration, which leads to

$$E_c^{RPA} = \int_0^\infty \frac{d\omega}{2\pi} \mathrm{Tr}\{\ln[1-\chi^{KS}\nu] + \chi^{KS}\nu\}, \quad (4.24)$$

the correlation energy expression of the Adiabatic Connection Fluctuation-Dissipation Theorem in its Random Phase Approximation (ACFDT-RPA), where ν denotes the Coulomb kernel.

One of the main problems of the RPA energy expression is, that it is not bounded, this means that especially χ^{KS} (and therefore also all expressions containing χ^{KS}) depends on infinitely many wave-functions. In plane wave basis-set calculations only energies for finite basis-sets are calculated. Therefore an extrapolation scheme (also applied for MP2 calculations) is used

$$E_c(E_{cut}^\chi) = E_c^\infty + \frac{A}{(E_{cut}^\chi)^{\frac{3}{2}}}. \quad (4.25)$$

In this expression E_{cut}^χ denotes the energy cut-off for which the response function is evaluated[5]. But even when using the extrapolated value for infinite cut-off energies E_c^∞,

[5] Actually the response function is only evaluated for Kohn Sham wave-functions up to the energy E_{cut}^χ. A typical value for this parameter is about 2/3 of the total energy cut-off. For higher energies the energy cut off is not high enough to allow for a proper sampling of the wave-functions of the system, which would lead to a large basis-set bias in the calculated results.

a strong dependence of this value on the total cut off energy can be observed. Luckily, this dependence vanishes, when energy differences are investigated, which contrary to total energies converge rather quickly [83].

It is in principle possible to calculate the RPA energies self-consistently by applying an optimized effective potential (OEP) methods, but it is usually preferred (due to the high computational cost) to calculate energies using DFT wave-functions. The RPA also leads to a systematic underbinding [84, 85, 86] of systems. Ren et al. [87] have observed, that results can be improved by calculating the exchange contributions self-consistently[6] and seeing the RPA correlation energy as a correction. This point of view allows to apply the Brillouin-Theorem [88] and justifying this effect. But when looking at the derivation, this can not be justified. It seems more likely, that in this case a combination of an overbinding method (HF) and an underbinding method (RPA) leads to a cancellation of errors[7], which improves results. While this approach seems to work well for a test-set of small molecules it does not cure the inherent problems of the RPA which will be discussed in the later chapters on alkane adsorption.

As already mentioned, the RPA underestimates total (and in many cases also binding) energies by about 1/3. This can also be understood by using diagrammatic techniques, where it is obvious, that certain diagrams are missing. This can be corrected by adding second order screened exchange (SOSEX), a very costly method. Therefore also alternative approaches were considered [89, 90], which could not cure the main problems of the RPA.

Despite these problems in the area of accuracy the RPA has (besides the theoretical beauty of its derivation) many advantages. It is (contrary to DFT) a method using a truly non-local correlation energy expression, which can actually solve the so called CO-adsorption puzzle [91]. It also has a good scaling with systemsize ($\mathcal{O}(N^4)$ and makes it therefore one of the most efficient ways to treat correlation effects non-locally. It can also be used for metals, contrary to MP2, which is discussed in the next section.

Second Order Møller-Plesset Perturbation Theory(MP2)

While all the already discussed methods are variational there are also perturbative approaches to calculate ground state energies. In the many electron ground state problem this is (after its inventors C. Møller and C.S. Plesset) the so called Møller-Plesset perturbation theory (MP). It is important to mention that while variational approaches always give upper bounds for the energies this is generally not true for perturbative approaches. MP is discussed in many textbooks on theoretical chemistry and here we will follow the derivation in chapter 9 of [92].

The basic Hamiltonian is again the many body Hamiltonian discussed in previous chapters. As already discussed, the true many body wave-function will be a linear combination of the ground state Slater Determinant and excited state Slater Determinants. In MP, the Hartree-Fock system is seen as ground state, and the perturbation

[6] actually calculating Hartree-Fock energies

[7] actually the exchange repulsion within the bonding areas is reduced

is given by

$$H^{(1)} = H - H^{HF}. \tag{4.26}$$

Using now in zeroth order approximation the ground state Slater determinant Ψ_0 leads to

$$E^{(0)} = \langle \Psi_0 | H | \Psi_0 \rangle \tag{4.27}$$

which again is the Hartree Fock energy of the system.

$$E^{(1)} = \left\langle \Psi_0 | H^{(1)} | \Psi_0 \right\rangle \tag{4.28}$$

now gives the first order energy correction. By the definition of $H^{(1)}$ this term equals 0. Therefore the first contributions come from second order perturbation theory, leading to

$$E^{(2)} = \sum_J \frac{\left\langle \Psi_J | H^{(1)} | \Psi_0 \right\rangle \left\langle \Psi_0 | H^{(1)} | \Psi_J \right\rangle}{E_0^{(0)} - E_J^{(0)}}, \tag{4.29}$$

where Ψ_J denotes an excited Slater Determinant and $E_J^{(0)}$ its corresponding zeroth order energy. To evaluate this expression the first point to note is that

$$\left\langle \Psi_J | H^{(HF)} | \Psi_0 \right\rangle = 0 \tag{4.30}$$

since Ψ_J and Ψ_0 are orthogonal eigenfunctions of H^{HF}.

Therefore the remaining terms to evaluate are

$$\langle \Psi_0 | H | \Psi_0 \rangle . \tag{4.31}$$

But which Ψ_js do contribute? Due to the Brillouin's Theorem [88] single excited determinants do not contribute. Due to the structure of $\frac{1}{|r-r'|}$ and the orthonormality of the single electron wave-functions ϕ_i, higher than double excited determinants do not contribute either, which leaves double excited determinants. Now inserting those leads to the term

$$E^{(2)} = \frac{1}{4} \sum_{a,b}^{occ} \sum_{i,j}^{uocc} \frac{\langle ab||pq\rangle \langle pq||ab\rangle}{\epsilon_a + \epsilon_b - \epsilon_p - \epsilon_q}, \tag{4.32}$$

with

$$\langle ab||pq\rangle \langle pq||ab\rangle = \int d^3\mathbf{r} d^3\mathbf{r}' \frac{\phi_a^*(\mathbf{r})\phi_b^*(\mathbf{r}')\phi_p(\mathbf{r})\phi_q(\mathbf{r}')}{|\mathbf{r}-\mathbf{r}'|} - \int d^3\mathbf{r} d^3\mathbf{r}' \frac{\phi_a^*(\mathbf{r})\phi_b^*(\mathbf{r}')\phi_p(\mathbf{r}')\phi_q(\mathbf{r})}{|\mathbf{r}-\mathbf{r}'|}, \tag{4.33}$$

where ϕ_a and ϕ_b are occupied and ϕ_p and ϕ_q are unoccupied single electron orbitals with corresponding ϵ_i. Including this term in the perturbative series leads to second order Møller-Plesset perturbation theory (MP2).

While MP2 gives excellent results as far as bond-lengths and energies of large gap systems are concerned, it also has some downsides. Since MP2 is a perturbative approach, you can not get any information about the ground state density and therefore

obtaining forces on the nuclei is more difficult. Also one can not get any information about excitation spectra. The structure of equ. 4.32 also implies, that calculations are only possible for systems with a finite energy gap. For metals the missing energy gap would lead to divisions by 0 and the second order correction would diverge.

Usually MP2 calculations are carried out in a localized basis-set and only recently calculations using a plane-wave basis-set have been performed. A detailed description of the implementation of MP2 using a plane-wave basis-set can be found in [93].

Also higher order perturbation theory calculations (MP3, MP4) are possible and increase accuracy, but more sophisticated algebra is involved and evaluation of the included terms becomes more expensive. Therefore diagrammatic techniques are often preferred.

The Fourth Rung Revisited - Treating Correlation Non-Locally

In many discussions on the Jacob's Ladder the fourth rung is considered to be complete by the introduction of exact exchange, either in the form of Hartree-Fock theory or hybrid functionals. In these functionals correlation is either omitted or treated locally. Non-local treatment of correlation effects is usually achieved by using fifth rung methods, which were already discussed previously.

But when thinking about the "true" exchange-correlation energy, the Hohenberg-Kohn formulas imply, that a non-local exchange as well as a non-local correlation energy expression should be used. Within the Kohn-Sham framework this is by definition the Hartree-Fock exchange energy. The correlation energy on the other hand must be a non-local energy expression depending only on the densities $n(\mathbf{r})$ and $n(\mathbf{r}')$. While the non-local treatment of correlation effects comes naturally when using fifth rung methods things get more complicated when looking for $E_c(n(\mathbf{r}), n(\mathbf{r}'))$, even though it would be highly desirable due to a higher computational efficiency.

The only approach in this direction has been made by Dion et al. [94, 95] in their van der Waals density functional (vdW-DF). Here the correlation is split into a local and a non-local part

$$E_c(n(\mathbf{r}), n(\mathbf{r}') = E_c^0(n(\mathbf{r}) + E_c^{nl}(n(\mathbf{r}), n(\mathbf{r}')). \tag{4.34}$$

It is important to note that in this expression the short range correlation energy $E_c^0(n(\mathbf{r})$ is treated by a local expression, while $E_c^{nl}(n(\mathbf{r}), n(\mathbf{r}'))$ is a truly non-local expression

$$E_c^{nl} = \frac{1}{2} \int d^3\mathbf{r} d^3\mathbf{r}' n(\mathbf{r}) \Phi(\mathbf{r}, \mathbf{r}') n(\mathbf{r}'), \tag{4.35}$$

where $\Phi(\mathbf{r}, \mathbf{r}')$ is a given function depending upon $\mathbf{r} - \mathbf{r}'$.

The tricky part is the derivation of said $\Phi(\mathbf{r}, \mathbf{r}')$. The exact derivation is rather complicated and can be found in [96, 94, 95]. The starting point is the correlation energy expression of the ACFDT given in 4.23. It is split into a local and non-local part leading to

$$E_c^{nl} = \int_0^\infty \mathrm{Tr}\left[\ln(1 - \nu\chi^{KS}) - \ln\epsilon\right], \tag{4.36}$$

where ϵ is the approximated dielectric function. After developing the logarithm in this expression in terms of $S = 1 - \epsilon^{-1}$ and using an appropriate approximation for S leads to

$$\Phi(\mathbf{r}, \mathbf{r}') = \frac{2me^4}{\pi^2} \int_0^\infty a^2 da \int_0^\infty b^2 db W(a,b) T(\nu(a), \nu(b), \nu'(a), \nu'(b)) \tag{4.37}$$

where

$$T(w,x,y,z) = \frac{1}{2}\left[\frac{1}{w+x} + \frac{1}{y+z}\right]\left[\frac{1}{(w+y)(x+z)} + \frac{1}{(w+z)(y+x)}\right], \tag{4.38}$$

$$\begin{aligned} W(a,b) = 2[&(3-a^2)b\cos(b)\sin(a) + (3-b^2)a\cos(a)\sin(b) + \\ &+(a^2+b^2-3)\sin(a)\sin(b) - 3ab\cos(a)\cos(b)]/a^3b^3 \end{aligned} \tag{4.39}$$

and the quantities

$$\nu(y) = y^2/2h(y/d) \tag{4.40}$$

and

$$\nu'(y) = y^2/2h(y/d') \tag{4.41}$$

where

$$d = |\mathbf{r} - \mathbf{r}'| q_0(\mathbf{r}) \tag{4.42}$$

and

$$d' = |\mathbf{r} - \mathbf{r}'| q_0(\mathbf{r}'). \tag{4.43}$$

q_0 can be expressed as

$$q_0(\mathbf{r}) = \frac{\epsilon_{xc}^0 \mathbf{r}}{\epsilon_x^{LDA}(\mathbf{r})} k_F(\mathbf{r}) \tag{4.44}$$

Here k_F is the Fermi-wavevector and ϵ_{xc}^0 is a gradient corrected expression for the exchange-correlation potential and ϵ_x^{LDA} is the LDA exchange potential.

At this point it is important to note that Φ only depends on $\mathbf{r}$ and $\mathbf{r}'$ via d and d', which allows for tabulating values for different values of d and d', which speeds up computations considerably.

In the original version E_c^0 is chosen to be the LDA correlation energy and E_x is the revPBE [58] exchange energy expression. It is argued, that the revPBE GGA has no artificial van der Waals bonding energies originating from a wrong asymptotic behavior, but this choice seems a little bit arbitrary.

Various implementations of the vdW-DF exist [97, 98, 99, 100] and have already been tested, which also lead to the deficiencies of this functional. Even though van der Waals interactions are included, naturally errors are still pretty large (in the range of ??????-check) and even worse, the functionals do not show a clear trend but sometimes severely over- and sometimes severely underestimate values for atomization energies.

To cure these errors improvements have been suggested, especially by substituting E_x and E_c^0 by different functionals [101, 102, 99, 100]. This is actually a very interesting approach, because, similar to the error cancellation between exchange and correlation

energies for GGAs, it can be expected that errors between GGA-part and non-local part of the vdW-type functionals cancel out. The advantages of the latter functionals are furthermore, that they are optimized with respect to a far wider reference data-set consisting of molecules as well as solids which allows for smaller errors for a far wider class of materials than the original version.

4.4 The ideal functional?

After having discussed a large variety of different functionals there remains one last question to be answered: What is the ideal functional?

The ideal functional should

- be universally applicable
- lead to accurate energies
- be efficient (and therefore have an ideal scaling with systemsize)
- treat exchange and correlation non-locally.

The main assumption in Kohn-Sham Density Functional Theory, namely the simplified assumption of non-interacting, fully occupied electron states, implies the use of exact exchange. All the other effects must be summarized in the correlation energy. The correlation energy should as previously discussed be a non-local expression depending on the densities (or at least the occupied single particle wave-functions) only.

Finding a reasonable non-local correlation expression is the biggest remaining challenge in the framework of DFT. The discussion in this chapter has shown that every method has its applications, where it leads to great results, but only few can be used for a large number of problems. Those which are applicable to almost all problems usually show a very bad scaling behavior, which limits their application to very small systems. These problems imply, that at the time of writing one has to be very careful about the choice of functional and always consider the system under investigation.

Part II

Structure and Properties of Metal-exchanged Zeolites Studied Using Gradient-corrected and Hybrid Functionals

5 Structure and Energetics

Summary

The structural and energetic properties of purely siliceous, proton- and Cu- and Co-exchanged chabazite have been studied using periodic density-functional (DFT) calculations with both conventional gradient-corrected exchange-correlation functionals and hybrid functionals mixing exact (i.e. Hartree-Fock) and DFT exchange. Spin-polarized and fixed-moment calculations have been performed to determine the equilibrium and excited spin-configurations of the metal-exchanged chabazites. For the purely siliceous chabazite hybrid functionals predict a slightly more accurate cell volume and lattice geometry. For isolated Al/Si substitution sites gradient-corrected functionals predict that the lattice distortion induced by the substitution preserves the local tetrahedral symmetry, whereas hybrid functionals lead to a distorted Al coordination with two short and two long Al-O bonds. Hybrid functionals yield a stronger cation-framework binding that conventional functionals in metal-exchanged zeolites, they favor shorter cation-oxygen bonds and eventually also a higher coordination of the cation. Both types of functionals predict the same spin in the ground-state. The structural optimization of the excited spin-states shows that the formation of a high-spin configuration leads to a strong lattice relaxation and a weaker cation-framework bonding. For both Cu- and Co-exchanged chabazite the prediction of a preferred location of the cation in a six-membered ring of the zeolite agrees with experiment, but the energy differences between possible cation locations and the lattice distortion induced by the Al/Si substitution and the bonding of the cation depends quite significantly on the choice of the functional. All functionals predict similar energy differences for excited spin states. Spin-excitations are shown to be accompanied by significant changes in the cation coordination, which are more pronounced with hybrid functionals. The consequences on electronic spectra and chemical reactivity are analyzed in the following publications.

5.1 Introduction

During the last decades, important progress has been realized in theoretical investigations of the physicochemical properties of complex solids based on density functional theory (DFT). DFT allows to recast the intractable complexity of a many-electron system into an effective one-electron potential determined by the exchange-correlation functional. This functional describes the complex kinetic and energetic correlations between one electron and all the other electrons in the system. The form of the functional that would make the re-formulation of the many-body Schrödinger equation exact is

not known, but a hierarchy of approximations (nick-named by Perdew[103, 104] the "Jacob's ladder" of DFT) aiming to achieve step-by-step an ever increasing accuracy of the DFT predictions has been developed. The four rungs on Jacob's ladder accessible to date are (i) the local density approximation (LDA), (ii) the generalized gradient approximation (GGA), (iii) the meta-GGA introducing a dependence on the Laplacian of the electron density (i.e. the density of the kinetic energy), and (iv) hybrid functionals mixing DFT and exact (i.e. Hartree-Fock) exchange. The LDA predicts structural properties with reasonable accuracy, albeit with a certain tendency to overbind: molecular bond lengths and lattice constants are too small by a few percent, cohesive energies are overestimated. More serious failures of the LDA are pronounced overestimations of the adsorption energies of atoms or molecules on solid surfaces and within microporous materials, combined in some cases with qualitatively wrong predictions of the potential energy profiles for adsorption (presence or absence of a barrier in the entrance channel for adsorption)[105, 106] or for the adsorption site[107]. For the adsorption of saturated molecules in zeolites, LDA calculations strongly overestimate the strength of the interaction with the inner walls of the cavity, which is mediated by dispersion forces which are not described by DFT.[108, 109] GGA functionals such as the Perdew-Wang (PW91)[54] or the Perdew-Burke-Ernzerhof (PBE)[55] functionals cure the overbinding tendency of the LDA to a good extent, but do not improve the prediction of certain electronic properties such as the energy gap between the highest occupied (HOMO) and the lowest unoccupied (LUMO) eigenstate in molecules or in semiconducting and insulating solids. This problem also affects DFT predictions on the adsorption of molecular species because it leads to a too strong partial occupation of the LUMO, favoring highly coordinated adsorption configurations.[107, 110] A correct prediction of the HOMO-LUMO gap in molecules or of the band gap in solids requires, in principle, computationally very demanding techniques based on many-body theory such as GW calculations.[111, 112, 113] However, it has also been demonstrated that hybrid functionals mixing exact and DFT exchange (such as the B3LYP[114], PBE0 [72] and HSE[73, 74] functionals) not only achieve improved results for molecular and crystalline geometries and atomization energies, but also for HOMO-LUMO gaps in molecules and band gaps in solids in consistently good agreement with the computationally much more demanding GW calculations.

However, hybrid functionals do not perform equally well for all classes of materials, and there are also significant differences between different types of hybrid functionals. While the accuracy of atomization energies of small molecules calculated using the parameterized B3LYP functional (which is very popular in molecular quantum chemistry) and using the parameter-free PBE0 functional are essentially on par, for solids the picture is entirely different. Atomization energies calculated using B3LYP are less accurate than the results achieved using conventional GGA functionals (PW91, PBE) for all classes of materials, the discrepancies being largest for metals.[76] The reason for the failure of the B3LYP functional is that the exchange-correlation energy is overestimated for atomic-like and underestimated for itinerant systems, the functional also fails to reproduce the homogeneous electron gas limit.[115]. Other hybrid functionals (PBE0, HSE) perform somewhat better, but reach at best the performance of pure

GGA functionals. Functionals based on screened exchange interactions (HSE) lead to more accurate energies than those using pure Hartree-Fock exchange (PBE0). Adsorption energies of small molecules on metallic surfaces are generally overestimated by GGA calculations. Recent studies of CO adsorption using hybrid functionals have shown that the error is reduced for CO on Cu surfaces, but even increased on Rh and Pt surfaces.[110] The reason is that the broadening of the *d*-band caused by the admixture of exact exchange and the down-shift of its center of gravity overcompensates the down-shift of the HOMO of the adsorbed molecule. The performance of hybrid functionals is most problematic for magnetic systems, because the admixture of exact exchange causes a strong enhancement of the exchange-splitting between spin-up and spin-down states. For ferromagnetic Fe, for example, this leads to an enhancement of the magnetic moment[76] from a PBE value of 2.2 μ_B (in perfect agreement with experiment) to a much too high value of 2.7 μ_B. On the other hand, hybrid functionals lead to a much improved description of the properties of antiferromagnetic insulators.[116] Little is known about the relative performance of both types of functionals for solids containing isolated magnetic ions. Significant differences between pure DFT and hybrid functionals have also been found for other properties: For small molecules such as NO or CO, hybrid functionals predict shorter (and hence more realistic) bond lengths[117], but much higher (and considerably less accurate) stretching frequencies.[118]. Little is known about the influence of the choice of the functional on the vibrational eigenstates of solids. Recently, the phonon dispersion relations of the elemental semiconductors have been analyzed by Hummer *et al.*[119]. As for the small molecules, slightly lower and - for Si, Ge, and Sn - slightly more accurate lattice constants were found with the HSE functional, differences in the phonon frequencies calculated at the equilibrium lattice constants are very modest with the most accurate results achieved with the PBE functional.

It is evident that standard tests of functionals concentrating on elementary properties such as bond lengths or lattice constants, atomization energies and band gaps are only of limited help in choosing the most appropriate exchange-correlation functional for calculating the properties of complex solids such as metal-exchanged zeolites, let alone for studying the adsorption of small molecules at the active sites within the zeolite. In their purely siliceous form zeolites (i.e. microporous forms of silica) are wide gap insulators - hence the choice of a hybrid functional such as HSE predicting an accurate gap width seems to be appropriate. Zeolites can be chemically functionalized by substituting a minority of framework Si atoms by Al and compensation of the electron-deficit on the framework by introducing electron-donating extra-framework atoms such as hydrogen or metal atoms. These extra-framework particles bind to "activated" oxygen atoms close to the Al/Si substitution sites, donation of electrons to the framework formally leads to the formation of extra-framework cations with Lewis- or protons with Brønsted-acidity. Transition-metal cations with open *d*-shells carry a magnetic moment. The significant differences in the exchange splitting predicted by conventional GGA and hybrid functionals will lead to very different predictions for the position of the occupied and empty *d*-states of the cation relative to the bands of the framework, affecting the chemical reactivity of the Lewis sites. The experimental characterization

of the coordination and of the physico-chemical properties of transition-metal cations in zeolites is a very difficult task. The usefulness of X-ray diffraction (XRD) methods is limited because XRD determines only an average structure around a given crystallographic site, whether it is occupied or not.[120] A more direct information on the cation coordination is provided by spectroscopic methods (X-ray photoelectron spectroscopy of the core states of the cations, photoluminescence spectroscopy of valence states).[121, 122, 123] The reactivity of the active sites is often characterized by measuring the vibrational spectra of adsorbed probe molecules.[124, 125, 126] However, the assignment of particular spectroscopic features to particular cation locations is rather indirect - very often a reliable interpretation of the measured spectra is possible only via their comparison with theoretical calculations. However, the results of such calculations will also depend on the accuracy of the predicted molecular properties.

DFT calculations based on both conventional local and semi-local (gradient-corrected) exchange-correlation functionals[127] and on hybrid functionals have already a long tradition in zeolite research. However, because Hartree-Fock and hybrid-functional calculations on periodic systems became feasible only rather recently[117, 76], two different approaches have been developed in parallel. Calculations based on periodic models of zeolites have been performed using pure DFT (mostly GGA) functionals. Their advantage is that they permit to construct realistic models of the active sites and account for the flexibility of the zeolite framework. Recent work has demonstrated that both the adsorption energies and the vibrational eigenstates of adsorbed species show large variations correlated to the structure and activity of the acid site.[26, 128, 129]

Hybrid functionals have been used almost exclusively in calculations based on cluster models - either using finite clusters with the dangling bonds saturated by hydrogen atoms, or clusters embedded within a static model of the surrounding framework described at a lower level. Within the QM-Pot approach[130] the surrounding of the cluster is modeled using empirical interatomic forces, more advanced techniques start with a DFT calculation of the periodic system and correct the total energy by the difference between the energies of a finite cluster surrounding the active site, calculated using conventional DFT and hybrid functionals for the frozen DFT geometry.[131, 132] For both types of cluster calculations, careful tests of the convergence with respect to the cluster size are required. The available results demonstrate that both for the coordination of the extra-framework cations[133] and for the total energy[134] complete agreement with periodic calculations is not achieved even for large clusters containing more than twenty tetrahedral sites. Recent results show that for some active sites very good agreement between cluster calculations based on a QM-Pot strategy and embedded in periodic DFT calculations is achieved, whereas for other sites there is significant disagreement between both calculations.[132] A more technical problem is that in many cases periodic and cluster calculations are performed using different codes and different basis sets, leading to further questions concerning convergence.

The conventional assessment of the relative performance of GGA and hybrid functionals based on the available data is that hybrid functionals provide lower and more realistic values for the adsorption energies of molecular species in zeolites than the GGA. GGA calculations yield quite accurate vibrational eigenfrequencies for adsor-

bates and accurate values for the frequency shift relative to the gas phase (with the notable exception of CO adsorbed at monovalent Cu cations in zeolites), whereas hybrid functionals overestimate the stretching frequencies and produce smaller shifts relative to the gas phase.

In the present work we investigate the relative performance of GGA (PW91, PBE) and hybrid (PBE0, HSE) functionals at the example of Cu(I)-, Cu(II)- and Co(II)-exchanged chabazite, using periodic calculations for both types of functionals. We present detailed results for the structural properties of the purely siliceous and metal-exchanged zeolite, using different locations of the extra-framework cations and of the Al/Si substitution sites on the framework. Because hybrid functionals are known to enhance the exchange-splitting between electronic eigenstates with different spin, particular attention is paid to spin-dependent effects. In addition to calculations optimizing simultaneously all geometrical, electronic and magnetic degrees of freedom, fixed-moment calculations have been performed for excited spin-states. For some configurations it has been found that a spin-excitation induces a significant change in the coordination of the cation and a re-distribution of charge- and spin-densities involving also the zeolite framework.

Two following papers will be devoted to detailed investigations of the electronic structure and of the chemical properties of Cu(I)-, Cu(II)- and Co(II)-exchanged chabazite. The study of the electronic properties demonstrates large changes in the width of the band gap of the host materials and of the position of local cation states within the gap. The investigations include a theoretical analysis of the diffuse reflectance spectra (DRS) which have been used extensively to obtain detailed information on the cation locations in zeolites. Because the energy of the exciting radiation is often lower than the minimal energy required for the creation of electron-hole excitations, the investigation of excited spin states plays an important role in the interpretation of DRS data. The calculations for the excited states have been performed both for the frozen ground state geometry and for a geometry optimized at the excited spin-state. The combination of these results permits the determination of the excitation and emission energies for transitions between different spin-states and detailed analysis of the photoluminescence spectra. The chemical reactivity of Lewis sites in Cu- and Co-exchanged chabazite has been probed by the adsorption of NO and CO molecules and the calculation of the vibrational eigenfrequencies of the probe molecules. The adsorption of these molecules allows to test different aspects of the exchange-correlation functionals: For CO the predicted width of the HOMO-LUMO gap of the molecule, for NO the interplay of the paramagnetic moment of the molecule with the moment located on the cation is of central interest. In a previous publication we have presented a similar, but much less comprehensive investigation for NO adsorption on Cu- and Co-exchanged SAPO34 (a silico-aluminophosphate with a framework isostructural to chabazite).[118] The present work provides a more detailed analysis of the structural, electronic, and chemical properties of a wider variety of different configurations.

5.2 Functionals

In our studies we used four different functionals: The gradient corrected DFT (GGA) functionals by Perdew and Wang (PW)[54] and Perdew, Burke and Ernzerhof (PBE)[55] and the hybrid functionals PBE0[72] and HSE[73, 74] derived from the PBE functional. The PW and PBE functionals are parameter-free in the sense that the functionals are constructed such as to reproduce the density-dependent exchange-correlation energies of the homogeneous electron gas determined by quantum Monte-Carlo simulations and to comply with the sum rules and asymptotic behavior known from many-body theory. The PBE0 hybrid functional is obtained by mixing 25% exact (Hartree-Fock) exchange and 75% PBE exchange, while correlation is described at the PBE level,

$$E_{xc}^{PBE0} = \frac{1}{4}E_x^{HF} + \frac{3}{4}E_x^{PBE} + E_c^{PBE}.$$

The admixture of Hartree-Fock exchange reduces the self-interaction error inherent in DFT and increases the splitting between occupied and empty eigenstates and between majority and minority spins in spin-polarized systems. The HSE functional is a range-separated hybrid functional: the Coulomb kernel in the exchange energy is split into short- and long-range parts according to

$$\frac{1}{r} = S_\mu(r) + L_\mu(r) = \frac{erfc(\mu r)}{r} + \frac{erf(\mu r)}{r}$$

and the exchange-correlation functional is evaluated as

$$E_{xc}^{HSE} = \frac{1}{4}E_x^{HF,sr,\mu} + \frac{3}{4}E_x^{PBE,sr,\mu} + E_x^{PBE,lr,\mu} + E_c^{PBE},$$

i.e. the mixing of Hartree-Fock and DFT exchange is applied only to the short-range exchange interactions. The screening of the long-range Coulomb interaction has important computational advantages, but it also expresses the fact that the long-range exchange interactions are described quite accurately in DFT. Only the description of the short-range exchange must be improved by mixing with exact exchange. The value of the range-separation parameter μ is not fixed a priori. In the original work of Heyd, Scuseria and Ernzerhof a value of $\mu = 0.3$ Å^{-1} has been used. The influence of this parameter on the performance of the functional has been investigated by Krukau *et al.*[74] and it has been shown that the results are only weakly dependent on μ. In our present work we have used two different values, $\mu = 0.3$ Å^{-1} (this functional is designed as HSE03) and $\mu = 0.207$ Å^{-1} (HSE06) to monitor the influence of the range-separation parameter on our results.

Computational Setup

In our work we used the implementations of these functionals in the latest release of the Vienna ab-initio Simulation Package (VASP).[135, 136] VASP performs an iterative solution of the Kohn-Sham equations of DFT within a plane wave basis set

and using periodic boundary conditions. The electron-ion interaction is described by the projector augmented wave (PAW) method by Blöchl [45], as modified by Kresse and Joubert[46]. The implementation of exact (Hartree-Fock) exchange and of hybrid functionals in VASP is described in detail by Paier *et al.* [117, 76].

Calculations using the PBE and hybrid functionals use PAW potentials constructed using core wave-functions calculated the PBE functional. To investigate the (in general very modest) influence of the treatment of the ionic core, we have also performed calculations using the PW91 functional for the construction of the PAW potential and in the calculation of the valence states.

All calculations have been performed in a spin-polarized mode to account for the spin-state of the extra-framework cations and of paramagnetic adsorbates such as NO. To verify that the calculations have converged to the correct ground state spin-configuration and to explore the structure and energetics of excited spin-states, fixed moment calculations have been performed.

For all our studies we used a plane-wave energy cutoff of 400 eV, which is necessary for an accurate description of the oxygen orbitals and of the eigenstates of the extra-framework cations. During selfconsistency iterations and for the calculation of the Hellmann-Feynman forces acting on the atoms Brillouin-zone sampling was restricted to the Γ-point. This is justified for the relatively large unit cell of chabazite. For the calculations of densities of states a 2x2x2 Monkhorst-Pack k-point grid [137] and a Gaussian smearing of the eigenstates of 0.2 eV was used.

Geometry optimizations at constant volume were performed using a mixture of damped molecular dynamics, conjugate gradient and quasi-Newton algorithms as implemented in VASP, using analytical Hellmann-Feynman forces. Convergence was assumed when the forces on the atoms were smaller than 0.05 eVÅ^{-1}. The equilibrium volume of chabazite was determined by performing a series of calculations with cell volumes varying between 750 Å^3 and 850 Å^3, allowing the cell shape and the internal coordinates to relax independently. The equilibrium volume was derived from a Birch-Murnaghan fit to the total energies.

All calculations have been performed in a spin-polarized mode, using the spin-interpolation scheme of Vosko *et al.*[138]. Spin-polarized DFT calculations converge to the spin ground state. To explore also excited spin-states calculations have also been performed in a fixed-moment mode. The total magnetic moment M of a system may be constrained to a fixed value by adding the constraint by a Lagrange multiplier λ, the total energy being given by [139]

$$E(M) = min\big[E[n(\vec{r}), m(\vec{r})] + \lambda[\int_V m(\vec{r})d^3r - M]\big].$$

Here $n(\vec{r})$ and $m(\vec{r})$ represent the charge- and spin-densities of the system and physically the Lagrange-multiplier λ represents a magnetic field acting on the electrons. Alternatively, the difference in the number of electrons occupying the spin-up and spin-down eigenstates (and hence the magnetic moment M) may be constrained to a fixed value [140, 65]. This means that two different Fermi energies $E_F^{\pm}$ for both spin-directions are used and this is equivalent to the Lagrange-multiplier method if the

volume V of integration extends over the entire system, in this case $E_F^{\pm} = E_F \pm \lambda$. Here we follow the computationally less demanding approach of Williams *et al.* [140] to fix the occupation number in the two spin-channels.

To determine the energy differences between different spin states, fixed-moment calculations combined with an independent structural optimization in each spin-state have been performed. However, structural relaxations proceed on a time-scale that is much slower than that for electronic transitions. Therefore, fixed-moment calculations have also been performed with a geometry frozen at the initial state. For the calculation of vertical excitation energies, total energies for the ground state configuration and for the excited spin-state have been performed for the frozen ground state geometry. Conversely, for the calculations of emission energies the total energies of the excited and final states have been calculated for the optimized geometry of the excited spin-state. In the following paper, the use of this approach for the interpretation of photoluminescence spectra will be discussed in detail.

5.3 Structures

Chabazite is a relatively simple representative of the zeolite family whose framework belongs to the trigonal system.[1, 141] The structure can be described either in a hexagonal lattice containing 36 tetrahedral (T) sites, or in a rhombohedral lattice with 12 T sites per unit cell. The secondary building blocks of the structure are double six-membered rings (D6R's) arranged in layers with an ABC stacking sequence and linked by four-membered rings (see Fig. 5.1). Purely siliceous chabazite belongs to space group $R\bar{3}m$, all tetrahedral sites are crystallographically equivalent. The four non-equivalent oxygen atoms can be distinguished according to their location in different rings of the framework. O(1) belongs to two four-membered (4MR) and one eight-membered (8MR) ring, O(2) to one 4MR, one 6MR and one 8MR, O(3) to two 4MR and one 6MR, and O(4) belong to one 4MR and two 8MR's (see Fig. 5.1).

The location and coordination of transition-metal ions is still a matter of debate.[142] Usually the cations are assigned to well defined rings or cavities in the zeolite. The preference of cations to occupy these specific extra-framework sites is attributed to stabilizing interactions between the cation and framework oxygen atoms. Three different locations of extra-framework cations in chabazite have been considered: Position (I) is located in the center of a 6MR, the cation forming bonds to O(2) and O(3) atoms (see Fig. 5.1). Positions (IIa) and (IIb) are in the center of two different 8MR's such that the cation can form bonds with O(1) and O(4), and O(2) and O(4) atoms, respectively. In the literature[1, 141] also a location in the center of the D6R has been considered. However, as in this position access of adsorbates to the cation is hindered by the framework, this has not been considered in the present work. Also, in our work on isostructural Cu- and Co-exchanged SAPO34 [118] we have found that a cation initially placed into the center of the D6R drifts to a position within the plane of one of the 6MR's and we expect the same to occur in the framework of chabazite.

To compensate the charge of a monovalent cation, a charge-compensating Al/Si

substitution on the framework is required. For a divalent cation, two Si atoms must be replaced by Al. The Löwenstein rule postulates that Al atoms on the zeolite framework must be separated by at least one intermediate T site occupied by Si.[143] This permits two different combinations of two Al/Si substitution sites: one with both Al atoms in the same 6MR, the other with one Al atom in each of the 6MR's forming the D6R. In both cases Al atoms are located at the largest possible distance - see Fig. 5.1. In the first configuration, the two Al atoms are linked through -Al-O(3)-Si-O(2)-Si-O(3)-Al- bonds within a 6MR or through -Al-O(1)-Si-O(4)-Si-O(3)-Al- bonds to its periodically repeated image (shortest Al-Al distance about 6.4 Å in both cases), in the second through -Al-O(4)-Si-O(3)-SiO(2)-Al- bonds (Al-Al distance ∼7.3 Å) or -Al-O(3)-Si-O(2)-Si-O(1)-Al- bonds (Al-Al distance ∼6.6 Å). The cation has always been placed close to at least one of the Al atoms such that it can bind to "activated" oxygen atoms (i.e. oxygen atoms coordinated to a framework Al atom). Combining the different extra-framework locations and the positions of the Al atoms within the framework we have considered three configurations for Cu(I)-exchanged chabazite and six configurations for the Cu(II)- and Co(II)-zeolites. The position of the cation in the center of a 6MR or 8MR of course defines only the initial configuration - the stable structure is determined by the interaction of the cation with the framework (the binding to "activated" oxygen atoms close to Al being stronger than that with non-activated atoms) and by the flexibility of the zeolitic framework which allows rather strong distortions in reaction to the presence of Al/Si substitutions and to the formation of covalent cation-oxygen bonds.

5.4 Purely Siliceous and Al-doped Chabazite

SiO_2 Chabazite

Our results for purely siliceous chabazite (composition $Si_{12}O_{24}$) are compiled in Table 5.1, together with the experimental results of Smith *et al.*[144] obtained by neutron diffraction on the high-silica form of the zeolite (H-SSZ-13) and the X-ray diffraction data of Fickel and Lobo[145] on Cu-SSZ13 with a high Si/Al ratio of 12 and a Cu/T ratio of Cu/(Al+Si)∼ 0.05 (i.e. about one Cu extra-framework cation in every second unit cell). The optimization of the structure has been performed either under the experimentally observed space group $R\bar{3}m$ or without any symmetry constraint. Even if no symmetry constraint is used, the equilibrium configuration is very close to rhombohedral symmetry: the angle is unchanged, differences in the lattice constants are of the order of 0.01 Å. The results compiled in the Table 5.1 refer to full rhombohedral symmetry. The choice of the functional is most important for the volume of the unit cell. The classical GGA functionals overestimate the experimental volume by about 1.5 pct. (PW91) and 2.1 pct. (PBE). Hybrid functionals predict a cell volume in almost perfect agreement with experiment. The volume contraction is slight larger with the PBE0 functional, the screening of the exchange interaction enlarges the volume by 0.02 pct. for the more strongly screened HSE03 functional.

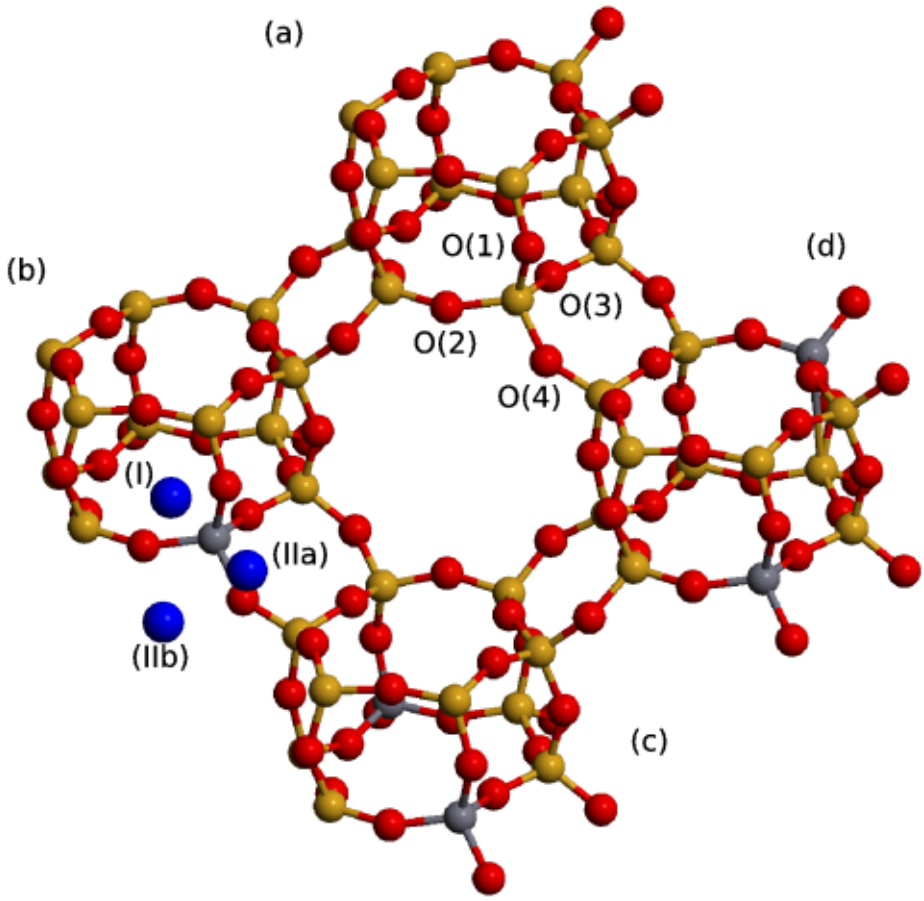

Figure 5.1: Crystal structure of chabazite. Four unit-cells with different Al occupancy are shown: The purely siliceous unit cell with the four different O-positions around a tetrahedral site occupied by Si (a), a cell with one Al-Si substitution per cell (b), two Al-Si substitutions in the same six-membered ring (c), and two Al-Si substitutions in different rings (d). O atoms are displayed in red, Si atoms in yellow and Al atoms in grey color. Possible locations of extra-framework cations are marked in blue. At site (I) the transition metal atom is located in the center of a six-membered ring, bonding to O(2) and O(3) atoms. At sites (IIa) and (IIb) the atom lies in the center of different eight-membered rings, bonding to O(1) and O(4), and to O(2) and O(4) atoms, respectively. Cf. text.

Table 5.1: Geometric data and energy gap of purely siliceous chabazite, calculated with different functionals. Lattice constants and interatomic distances are given in Å, the cell volume in Å^3, angles in deg, the width of the band gap in eV.

	PW91	PBE	PBE0	HSE03	HSE06	Exp.[a]	Exp.[b]
Unit Cell							
volume	804.45	808.94	792.86	794.64	793.32	792.32	791.5
a	9.325	9.341	9.279	9.286	9.280	9.291	
α	94.0	94.0	94.0	94.0	93.9	93.9	
Local Geometry							
Si-O(1)	1.627	1.630	1.615	1.615	1.615	1.617	1.617
Si-O(2)	1.615	1.618	1.605	1.606	1.615	1.599	1.591
Si-O(3)	1.628	1.618	1.605	1.607	1.606	1.615	1.604
Si-O(4)	1.616	1.618	1.605	1.607	1.606	1.613	1.611
∠O(1)-Si-O(2)	110.9	110.9	110.4	110.1	109.5	110.3	112.5
∠O(1)-Si-O(3)	110.2	110.2	109.7	110.0	110.3	110.2	107.0
∠O(1)-Si-O(4)	108.4	108.4	108.9	108.9	109.0	107.9	107.9
∠O(2)-Si-O(3)	108.4	108.5	108.7	108.5	108.8	109.7	108.7
∠O(2)-Si-O(4)	108.1	108.1	109.0	109.2	110.3	108.4	110.4
∠O(3)-Si-O(4)	110.9	110.8	110.3	110.1	109.0	110.2	110.2
∠Si-O(1)-Si	144.8	144.5	145.4	145.4	145.3	144.8	144.6
∠Si-O(2)-Si	151.3	151.2	151.2	151.2	151.3	149.4	153.8
∠Si-O(3)-Si	149.4	149.1	150.2	150.1	150.2	147.8	149.9
∠Si-O(4)-Si	146.2	147.0	147.3	147.3	147.5	150.5	144.9
Energy Gap							
Gap[eV]	5.5	5.5	8	7	7.3		

[a] After Ref. [144].
[b] After Ref. [145].

Interatomic distances calculated using hybrid functionals are smaller by about 0.01 Å, small changes are also found in the tetrahedral angles. It is remarkable that even the very small deviations of the O-Si-O angles from the ideal tetrahedral angle of 109.5° are well described by the calculations. Si-O-Si angles vary between 144.8° on the O(1) site and 151.3° on the O(2) site if GGA functionals are used. The bond angles around the O(1) and O(3) sites are increased by about 1.0° if hybrid functionals are used, those around the O(2) and O(4) sites remain almost unchanged.

The strongest influence of the admixture of Hartree-Fock exchange is found in the electronic spectrum. The band gap is increased from 5.5 eV (PBE) to 8.0 eV (PBE0). Screening of the exchange interactions reduces the gap to 7.0 to 7.3 eV, depending on the screening length. Details of the electronic structure will be discussed in the following paper of this series.

Al→Si Substitution and Protonated Chabazite

The substitution of a framework Si atom by Al creates a local electron-deficit which may be compensated by the introduction of a hydrogen atom forming a hydroxyl group with an oxygen atom bound to the Al site. It is usually assumed that the hydrogen atom transfers its electron to the framework such that a negatively charged framework and a positively charged proton showing Brønsted acidity are formed. Al/Si substitution and protonation induce local distortions of the framework. Because in zeolites exchanged with divalent cations one of the Al sites may be located at a certain distance from the charge-compensating cation, it is of interest to examine both effects separately.

In zeolites with a high Al/Si ratio, the substitution of a large fraction of the Si atoms by Al leads to an increase of the cell volume. Here we are interested in low-Al chabazite - in principle this would require to use a computational cell consisting of several unit cells, and an Al/Si substitution in only one 6DR. In this case the surrounding framework would limit the local expansion of the lattice. Because of the large computational effort needed for periodic calculations with hybrid functionals, we have used only a model consisting of a single unit cell. To mimic the effect of the undoped environment we have frozen the atomic volume per cell at the equilibrium value calculated for the pure SiO_2 chabazite. The comparison between the experimental data of Smith *et al.*[144] and Fickel and Lobo[145] confirms that a low exchange rate does not lead to a measurable increase of the cell volume. No symmetry constraint has been applied during relaxation.

Table 5.2 summarizes the results for the Al-O distances around the substitution sites and the distances between the activated O atoms and the nearest Si atoms. The tetrahedral symmetry around the site occupied by Al is broken, and this effect is more pronounced in calculations with hybrid functionals. Using GGA functionals, three Al-O bonds are elongated by about 0.1 Å and the fourth [Al-O(1)] by 0.12 Å, O-Si bonds remain unchanged or are slightly contracted by up to 0.02 Å. If hybrid functionals are used, two Al-O bonds are stretched by 0.15 to 0.17 Å [Al-O(1) and Al-O(3)] while the remaining two are elongated only by about 0.06 to 0.08 Å. The adjacent O(1)-Si and O(3)-Si bonds are even elongated while the O(2)-Si and O(4)-Si bonds undergo

stronger contractions. As the tetrahedral angles are very rigid, this also results in stronger changes of the Al-O-Si bond angles around the activated oxygen atoms.

If a hydroxyl group is formed at one of the activated oxygen atoms, the Al-OH bond is further stretched to about 1.86 to 1.93 Å, while the other three Al-O bonds measure about 1.70±0.01 Å. Evidently the influence of the choice of the functional is much more modest than in the non-protonated Al-chabazite. O-H bond lengths are shorter by 0.01 Å if hybrid functionals are used. Our GGA results are in good agreement with the calculations of Jeanvoine *et al.*[146] and also with unrestricted Hartree-Fock calculations reported by Corà *et al.*[147]. Corà *et al.* also claimed that calculations at the unrestricted Hartree-Fock level and DFT calculations using either hybrid or gradient-corrected functionals are in good agreement regarding the geometrical data of chabazite doped with di- or trivalent atoms, confirming a weak dependence on the treatment of exchange and correlation. The stability of the Brønsted site calculated using GGA decreases in the sequence O(1) - O(2) - O(3) - O(4). The energetic ordering is essentially the same with hybrid functionals, only a proton attached to the O(3) site is now found to be less stable than at the O(4) site.

In the present context, the important result is that the choice of the exchange-correlation functional has a rather pronounced influence on the predicted distortion of the framework around a non-compensated Al/Si substitution site. Such sites can exist in zeolites exchanged with divalent atoms and the distortion around this site can interfere with the distortion induced by the extra-framework atom.

To analyze the origin of these differences, we have performed a Bader analysis [148, 149] of the charge distribution. The Al-O interaction is predicted to be largely ionic, about two thirds of the electron deficit created by the Al/Si substitution is distributed rather evenly over the four oxygen neighbors if GGA functionals are used, the rest is spread over the more distant neighbors. In contrast, calculations performed with hybrid functionals predict the electron-deficit to be concentrated on only two oxygen atoms - those whose distance from the Al site is significantly elongated compared to the other two. An electron deficit of about 0.5 electrons is calculated for the O(1) site with the largest distance from the Al site, about 0.33 electrons for the O(3) sites, and only about 0.035 electrons on the O(2) and O(4) atoms. The stronger localization of eigenstates is caused by the admixture of Hartree-Fock exchange and is a significant aspect hybrid functionals. Similar effects appear also in metal-exchanged, but not in protonated zeolites.

5.5 Extra-framework Sites in Metal-Exchanged Chabazite

Transition-metal counter-ions compensating the electron-deficit in Al-doped zeolites are coordinated to framework oxygen atoms, preferentially to "activated" oxygen atoms bound to Al/Si substitution sites. The coordination of the metal cations is often not saturated, which means that the ions can act as adsorption sites for molecules or as

Table 5.2: Al-O distances and distances between activated oxygen atoms and Si atoms in Al-doped and protonated chabazite. For the protonated chabazite all four possible locations of the Brønsted site have been considered, energy differences are quoted relative to the energetically most favorable O(1) site (in eV). All distances are given in Å. Cf. text.

	PW91	PBE	PBE0	HSE03	HSE06	PW91	PBE	PBE0	HSE03	HSE06	PW91	PBE	PBE0	HSE03	HSE06	PW91	PBE	PBE0	HSE03	HSE06
	Al-Chabazite					O(1)-H					O(2)-H					O(3)-H					O(4)-H				
O(x)-H						0.975	0.975	0.966	0.966	0.966	0.977	0.978	0.968	0.968	0.968	0.977	0.977	0.967	0.968	0.968	0.977	0.978	0.968	0.968	0.968
Al-O(1)	1.748	1.749	1.791	1.783	1.788	1.907	1.911	1.895	1.896	1.895	1.709	1.710	1.696	1.696	1.695	1.710	1.711	1.696	1.696	1.696	1.719	1.720	1.706	1.706	1.705
O(1)-Si	1.607	1.608	1.651	1.645	1.649	1.702	1.704	1.686	1.686	1.686	1.599	1.601	1.586	1.586	1.586	1.597	1.598	1.584	1.584	1.584	1.602	1.604	1.589	1.590	1.589
Al-O(2)	1.717	1.720	1.661	1.677	1.680	1.695	1.696	1.684	1.684	1.686	1.873	1.879	1.864	1.865	1.864	1.700	1.701	1.686	1.685	1.684	1.712	1.714	1.700	1.701	1.700
O(2)-Si	1.589	1.592	1.574	1.571	1.573	1.587	1.589	1.575	1.576	1.575	1.697	1.700	1.683	1.684	1.683	1.588	1.590	1.574	1.574	1.573	1.594	1.596	1.581	1.582	1.582
Al-O(3)	1.750	1.752	1.756	1.753	1.754	1.718	1.719	1.706	1.706	1.705	1.716	1.717	1.703	1.704	1.703	1.925	1.929	1.906	1.904	1.904	1.713	1.714	1.700	1.700	1.699
O(3)-Si	1.611	1.612	1.630	1.627	1.628	1.602	1.604	1.589	1.590	1.589	1.603	1.604	1.590	1.590	1.590	1.716	1.718	1.697	1.696	1.695	1.603	1.605	1.590	1.591	1.590
Al-O(4)	1.712	1.713	1.683	1.679	1.684	1.706	1.707	1.694	1.695	1.694	1.705	1.706	1.694	1.694	1.694	1.690	1.690	1.674	1.671	1.671	1.875	1.879	1.864	1.865	1.864
O(4)-Si	1.590	1.590	1.580	1.575	1.580	1.593	1.594	1.580	1.581	1.580	1.590	1.592	1.578	1.579	1.578	1.585	1.585	1.569	1.567	1.567	1.704	1.707	1.688	1.689	1.688
ΔE[eV]						0.000	0.000	0.000	0.000	0.000	0.057	0.056	0.069	0.067	0.069	0.100	0.092	0.122	0.176	0.171	0.090	0.093	0.106	0.107	0.106

catalytically active centers. It has been demonstrated that the stability and activity of extra-framework cations varies strongly with the degree of local charge compensation: cations closely coordinated to framework Al atoms acquire an increased stability, but the activity of the cations is larger for the less stable and coordinatively unsaturated sites.[26, 108, 128, 129]

The location and coordination of Cu and Co cations in zeolites has been the subject of many experimental and theoretical studies.[120, 142, 122, 123, 150, 151, 152] Experimental investigations use X-ray diffraction, X-ray adsorption techniques (EXAFS, XANES), electron spin resonance and diffusive reflectance spectroscopies, theoretical calculations are based on DFT and quantum chemical methods applied to finite or embedded clusters, but only a very few DFT studies based on hybrid functionals for periodic systems have been published so far. In the present work our interest is focused on the influence of the choice of the functional on the geometry and energetics and the spin-state of Cu(I), Cu(II) and Co(II) cations in chabazite.

Cu-exchanged chabazite

Extra-framework Cu can be present in zeolites in the form of mono- or divalent cations. Ion-exchange using aqueous solutions of Cu(II)-sulfate or Cu(II)-acetate leads to the co-presence of copper cations in different oxidation states[153, 154], considerably complicating the experimental analysis of the Cu environment. Cu(II) can be reduced to Cu(I) in hydrogen or by auto-reduction at elevated temperatures[155], but the exact degree of reduction is difficult to assess. In the following we shall discuss first the theoretical results for both Cu(I) and Cu(II) extra-framework cations, and present the comparison with experimental data for both species together.

Structure of Cu(I) Lewis-sites in Chabazite

As already discussed in Sec.5.3, we considered three possible extra-framework locations of the Cu(I) cation, one in one of the 6MR's and the other two in two different 8MR's and with one of the tetrahedral sites in the ring occupied by Al. The calculations have been performed in a spin-polarized mode, but converged for all three configurations to a singlet (S=0) state. Fixed moment calculations have been used to verify that the triplet (S=1) state has a higher energy and to determine the energy difference between relaxed singlet and triplet states. The vertical $S_0 \rightarrow T_1$ excitation and $T_1 \rightarrow S_0$ emission energies, using the singlet- and triplet-optimized geometries, respectively, will be discussed together with the electronic properties in the following paper.

In configuration (1) with the Cu(I) cation in the 6MR the trigonal symmetry of the cation location is already broken by the Al/Si substitution (see Fig. 5.2). Upon relaxation using GGA functionals the cation drifts towards the Al site such as to form two strong bonds with one activated O(**3**) and one non-activated O(3) atom and a weaker bond to the activated O(**2**). Here and in the following we distinguish activated oxygen atoms by bold numbers, bond lengths for all configurations are summarized in Table 5.3. The distance between the cation and the O(**2**) atom is longer because the

acute angle of the Al-O(**2**)-Si bond points to the outer side of the 6MR, whereas the two Al-O(**3**)-Si and Si-O(3)-Si angles point inward. Relaxation of the configuration cannot shorten the Cu(I)-O(**2**) distance sufficiently, because of the stiffness of the tetrahedral angles between the bonds at the Al and Si sites. All other Cu(I)-O distances are longer than 3 Å, the distance between the cation and the Al atom is about 2.84 Å.

If hybrid functionals are used, the bonds between the Al site and the framework O atoms are stretched by 0.02 to 0.06 Å for the PBE0 and by 0.06 to 0.18 Å for the screened HSE03 and HSE06 functionals, respectively. The Al-Cu(I) distance is increased by 0.08 and 0.15 Å, respectively, placing the Cu(I) cation closer to the center of the ring. This allows the formation of a fourth, moderately strong bond with the O(*3*) atom on the opposite side of the ring (numbering in italics will be used for such oxygen sites). It has been argued that such a fourfold coordination of the Cu(I) cation, almost co-planar with the 6MR is preferred in many zeolites and stabilized by the interaction of $d_{x^2-y^2}$ states of Cu with O-*p* orbitals.

Tetrahedral angles are rather stiff and show little variation in dependence on the exchange-correlation functional. T-O-T angles are changed relative to the Si-O-Si angles in purely siliceous chabazite by the Al-Si substitution and the interaction with the extra-framework cation. The Al-O(**2**)-Si angle is reduced to about 132°, the Al-O(**3**)-Si angle is increased to about 156° due to the interaction with the Cu(I) cation, these values are almost identical for both types of functionals.

In configuration (2) the cation is initially located in the center of a 8MR - in this position the Cu(I)-O distances are too large to allow the formation of strong bonds to oxygen atom on both sides of the ring. Upon relaxation the cation drifts closer to the Al site, forming three strong bonds - two with activated [O(**1**) and O(**4**)] and one with a non-activated O(2) atom (see Fig. 5.3). The threefold coordination of the cation is almost co-planar with the plane of the 8MR. Both types of functionals lead to a similar cation coordination, but the Cu-O(**4**) bond is shortened by about 0.05(0.07) Å , while the Cu-O(2) bond is stretched by about 0.14(0.19) Å with hybrid functionals. Again the variations in the bond lengths are more pronounced if a screened hybrid functional is used. The T-O-T angles around the outer O framework atoms binding to Cu(I) are reduced to $\sim$ 122(126)° for Al-O(**1**)-Si (the larger value in parentheses is the result with hybrid functionals) and $\sim$ 146° for Si-O(2)-Si - the asymmetry is a consequence of the activation of the O(**1**) site. The Al-O(**4**)-Si angle remains almost identical to the value of 145° in purely siliceous chabazite.

In configuration (3) the cation is also located in a 8MR, but in contrast to configuration (2) the acute angle of the O(**2**)-Al-O(**4**) bond points to the outer side of the ring(see Fig. 5.4). The rigidity of the tetrahedral angle allows only the formation of two bonds with the activation framework oxygen atoms measuring about 2.01 and 2.04 Å and leads to a rather short Cu-Al distance of $\sim$ 2.73 Å. Hybrid functionals only lead to smaller differences in the Al-O bond lengths. The Al-O(**4**)-Cu(I)-O(**2**)-Al bonds form a slightly distorted square. The embedding of this configuration in the framework is very symmetric with GGA functionals, the Al-O(**4**)-Si and Al-O(**2**)-Si angles are both reduced to $\sim$ 138°. With a hybrid functional (PBE0) the former is further reduced to about 131°, the latter is increased to 155°, the asymmetry is somewhat

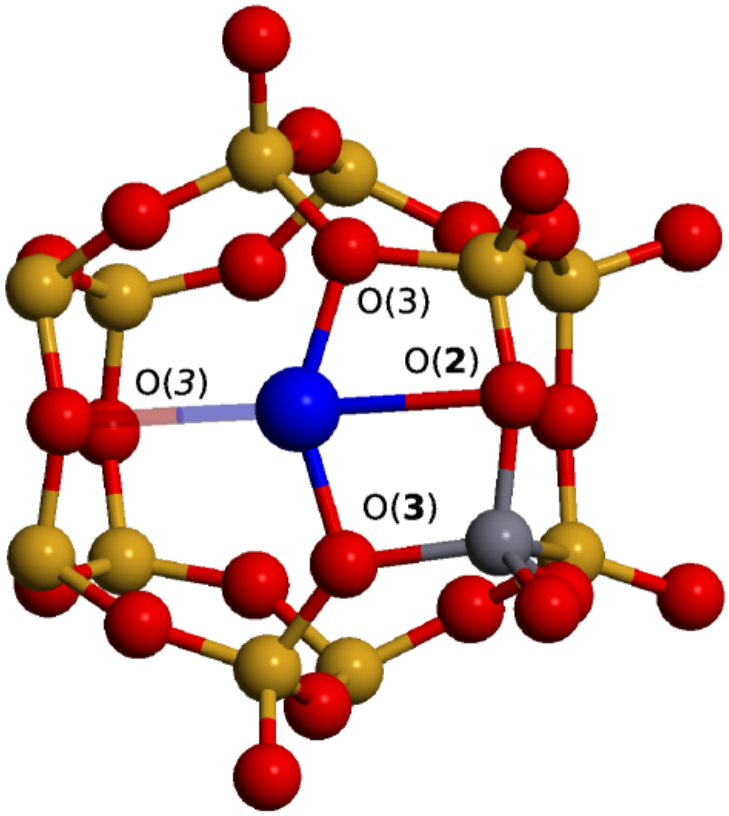

Figure 5.2: Coordination of a Cu(I) cation in a 6MR of chabazite [configuration (1)]. The extra-framework cation forms three (four) strong bonds to framework oxygen atoms if GGA (hybrid) functionals are used: two to activated O(**2**) and O(**3**) activated atoms closest to the Al-atom, one to a non-activated O(2). The fourth bond to the O(*3*) atom on the opposite side of the ring is formed only if hybrid functionals are used. The color-coding is the same as in Fig. 5.1. Only bonds around Cu(I) that are shorter than 3 Å are drawn, bonds drawn in light shading are formed only if hybrid functionals are used. Cf. text.

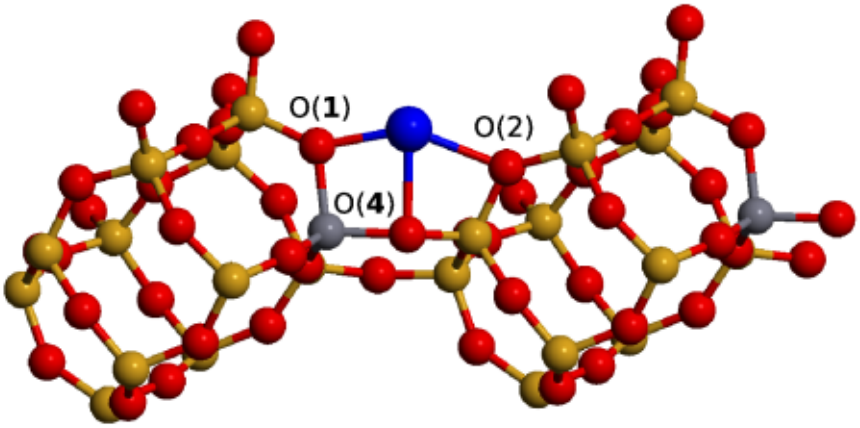

Figure 5.3: Threefold coordination of a Cu(I) cation in a 8MR of chabazite [configuration (2)] to O(**1**), O(**4**), and O(2) framework atoms. Cf. Fig. 5.2 and text.

weaker with a screened hybrid functional.

Energies of Cu(I) Lewis-sites in Chabazite

Table 5.4 lists the total energies of the Cu-exchanged zeolites, calculated relative to the neutral, but electron-deficient zeolite with one or two Al/Si substitution sites and the free neutral transition-metal atom,

$$E^{ads} = E^{TM-Chab} - E^{Chab} - E^{TM-atom}, \tag{5.1}$$

as well as the energy differences ΔE_{site} relative to the most stable configurations and the energy differences ΔE_{spin} of the first excited spin state relative to the ground state for each configuration.

The stability of the Cu(I) cation location decreases with the number of bonds between the cation and framework oxygens, i.e. from configuration (1) to (2) and (3). Hybrid functionals predict a stronger binding of the cation to the framework than GGA functionals. The location in a 8MR is disfavored by 0.35 to about 0.46 eV (GGA), and 0.29 to 0.33 eV (hybrid functionals).

Recently Solans-Monfort *et al.*[156] have investigated the structure and energetics of Cu(I) extra-framework cations located in a 6MR and in a 8MR [configuration (3)] in chabazite using periodic B3LYP calculations. For the location in the 6MR a threefold coordination of the cation with an average Cu(I)-O bond length of 2.12 Å was reported. While the average Cu(I)-O distance is comparable with our HSE results, slightly smaller differences in the bond lengths to activated and non-activated oxygens were found. In the 8MR the Cu(I) cation is bound only to two activated oxygens, but in contrast to our results for configuration (3) with two almost equal Cu(I) distances

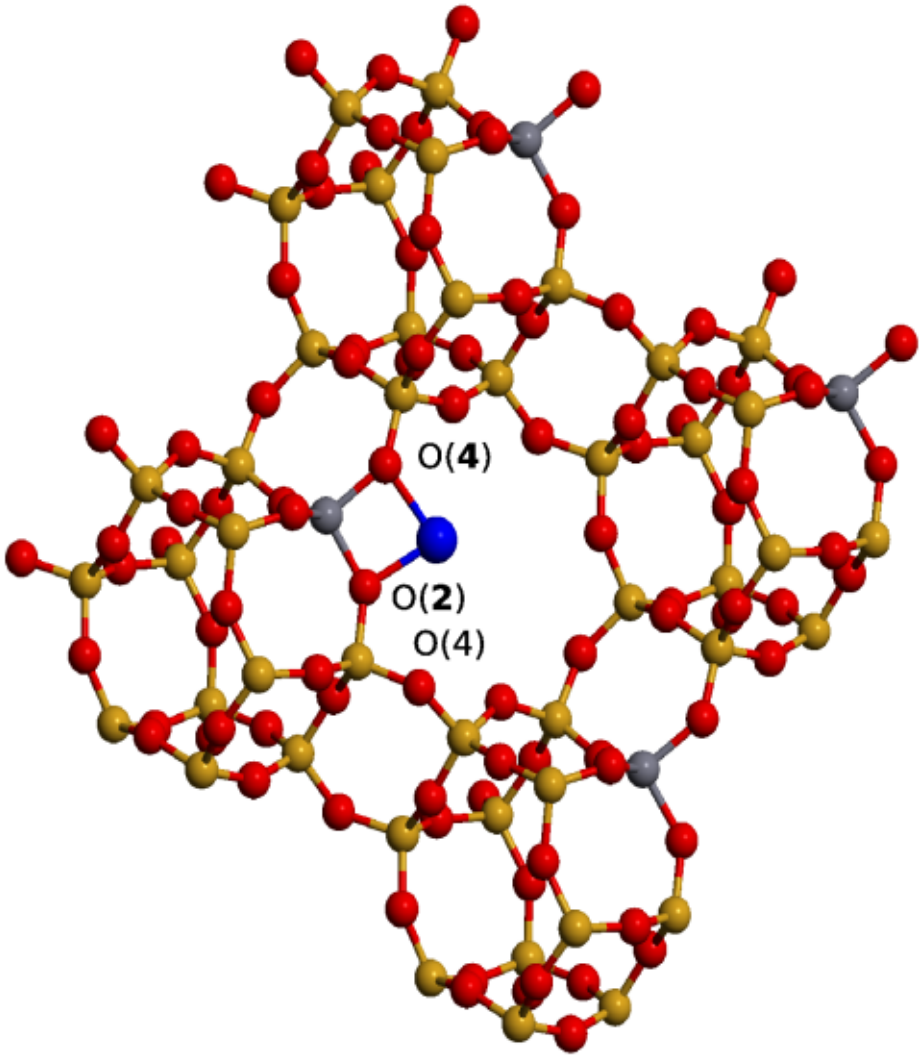

Figure 5.4: Twofold coordination of a Cu(I) cation in a 8MR of chabazite [configuration (3)], binding to activated O(**2**) and O(**2**) framework atoms. Cf. Fig. 5.2 and text.

Table 5.3: Structural data for extra-framework cations Cu(I), Cu(II) and Co(II) in chabazite, calculated for different configurations and using both GGA (PW91, PBE) and hybrid (PBE0, HSE03, HSE06) functionals. All distances are given in Å.

	Cu(I)					Cu(II)					Co(II)				
	PW91	PBE	PBE0	HSE03	HSE06	PW91	PBE	PBE0	HSE03	HSE06	PW91	PBE	PBE0	HSE03	HSE06
						Configuration 1					Configuration 1				
Cu/Co-O(**2**)						2.042	2.045	2.014	2.004	2.013	2.083	2.077	2.093	2.086	2.091
Cu/Co-O(**3**)						1.979	1.983	1.966	1.960	1.945	1.996	1.998	1.989	1.998	1.998
Cu/Co-O(3)						2.066	2.071	2.062	2.053	2.032	2.077	2.085	2.061	2.073	2.073
Cu/Co-O(***3***)						2.002	2.009	2.014	1.996	1.984	1.994	2.002	2.000	1.999	1.998
Al-O(**2**)						1.781	1.785	1.779	1.771	1.771	1.776	1.779	1.762	1.767	1.766
Al-O(**3**)						1.832	1.835	1.833	1.827	1.822	1.834	1.836	1.817	1.819	1.818
Al-Cu/Co						2.872	2.876	2.866	2.852	2.844	2.910	2.913	2.910	2.906	2.909
	Configuration 1					Configuration 2					Configuration 2				
Cu/Co-O(**2**)	2.557	2.574	2.647	2.753	2.753	2.107	2.096	1.991	1.994	1.995	2.150	2.149	2.099	2.097	2.106
Cu/Co-O(**3**)	1.897	1.899	1.936	1.957	1.957	1.903	1.899	1.898	1.899	1.899	1.915	1.922	1.936	1.941	1.935
Cu/Co-O(3)	1.947	1.950	1.995	2.026	2.026	1.948	1.944	1.925	1.926	1.927	2.016	2.025	2.016	2.018	2.012
Cu/Co-O(2)	3.093	3.089	3.159	3.049	3.049	2.482	2.631	2.395	2.385	2.388	2.156	2.157	2.179	2.189	2.187
Cu/Co-O(*3*)	3.095	3.079	2.669	2.340	2.340	3.625	3.664	3.493	3.489	3.490	3.249	3.219	3.255	3.243	3.213
Al-O(**2**)	1.738	1.741	1.717	1.717	1.717	1.790	1.794	1.785	1.785	1.785	1.770	1.771	1.761	1.764	1.762
Al-O(**3**)	1.844	1.849	1.814	1.808	1.808	1.844	1.844	1.843	1.843	1.843	1.871	1.873	1.851	1.852	1.854
Al-Cu/Co	2.834	2.842	2.927	2.992	2.992	2.782	2.770	2.764	2.767	2.767	2.860	2.864	2.851	2.852	2.853
						Configuration 3					Configuration 3				
Cu/Co-O(**1**)						2.010	2.014	1.968	1.971	1.969	1.973	1.977	1.994	1.989	1.996
Cu/Co-O(**4**)						2.001	1.998	1.896	1.898	1.893	1.934	1.933	1.934	1.944	1.935
Cu/Co-O(2)						2.196	2.208	2.119	2.129	2.133	2.192	2.188	2.165	2.163	2.160
Al-O(**1**)						1.842	1.844	1.844	1.843	1.842	1.867	1.869	1.851	1.855	1.854
Al-O(**4**)						1.796	1.801	1.809	1.811	1.808	1.808	1.811	1.792	1.789	1.790
Al-Cu/Co						2.763	2.767	2.743	2.748	2.744	2.774	2.777	2.790	2.788	2.789
	Configuration 2					Configuration 4					Configuration 4				
Cu/Co-O(**1**)	2.003	2.011	2.017	2.019	2.019	1.977	1.981	1.923	1.927	1.923	1.930	1.931	1.946	1.944	1.944
Cu/Co-O(**4**)	2.250	2.248	2.192	2.176	2.176	2.034	2.032	1.886	1.894	1.893	1.941	1.937	1.938	1.933	1.932
Cu/Co-O(2)	2.254	2.245	2.385	2.437	2.437	2.223	2.243	2.215	2.227	2.201	2.241	2.251	2.210	2.225	2.237
Al-O(**1**)	1.832	1.834	1.807	1.804	1.804	1.830	1.831	1.829	1.829	1.827	1.849	1.851	1.840	1.840	1.840
Al-O(**4**)	1.745	1.747	1.737	1.741	1.742	1.790	1.792	1.815	1.814	1.812	1.815	1.818	1.803	1.805	1.803
Al-Cu/Co	2.803	2.798	2.802	2.804	2.803	2.763	2.762	2.734	2.739	2.734	2.768	2.768	2.775	2.771	2.768
						Configuration 5					Configuration 5				
Cu/Co-O(**2**)						1.964	1.962	1.865	1.867	1.866	1.909	1.907	1.902	1.902	1.900
Cu/Co-O(**4**)						1.978	1.982	1.937	1.940	1.938	1.949	1.956	1.961	1.963	1.961
Cu/Co-O(4)						2.144	2.147	2.089	2.094	2.093	2.102	2.118	2.130	2.125	2.124
Al-O(**2**)						1.780	1.783	1.796	1.797	1.797	1.805	1.808	1.791	1.790	1.790
Al-O(**4**)						1.830	1.832	1.833	1.834	1.834	1.857	1.859	1.843	1.843	1.842
Al-Cu/Co						2.764	2.769	2.740	2.741	2.740	2.761	2.763	2.760	2.770	2.767
	Configuration 3					Configuration 6					Configuration 6				
Cu/Co-O(**2**)	2.008	2.010	2.061	2.044	2.043	1.946	1.945	1.859	1.861	1.858	1.905	1.903	1.903	1.899	1.890
Cu/Co-O(**4**)	2.037	2.037	2.037	2.040	2.041	2.015	2.022	1.976	1.980	1.979	1.970	1.980	1.977	1.986	2.001
Cu/Co-O(4)	3.292	3.280	2.719	3.012	3.013	2.131	2.140	2.068	2.072	2.078	2.054	2.066	2.063	2.082	2.121
Al-O(**2**)	1.785	1.786	1.748	1.758	1.759	1.778	1.780	1.791	1.791	1.791	1.797	1.800	1.782	1.783	1.784
Al-O(**4**)	1.775	1.776	1.772	1.766	1.766	1.830	1.831	1.834	1.834	1.833	1.858	1.859	1.849	1.848	1.844
Al-Cu/Co	2.732	2.733	2.737	2.743	2.743	2.759	2.762	2.737	2.739	2.737	2.757	2.759	2.756	2.758	2.762

Table 5.4: Binding energy E of the extra-framework Cu-atom, energy difference ΔE_{spin} of the relaxed first excited spin-state relative to the ground state, and energy difference ΔE_{site} with respect to the most stable configuration, calculated with different exchange-correlation functionals. All energies are given in eV.

		PW91	PBE	PBE0	HSE03	HSE06
Cu(I)						
Config1	E	-4.412	-4.367	-5.019	-4.992	-5.028
	ΔE^{a}_{spin}	2.788	2.738	2.538	2.726	2.573
	ΔE_{site}	0.000	0.000	0.000	0.000	0.000
Config2	E	-4.067	-4.009	-4.732	-4.702	-4.727
	ΔE^{a}_{spin}	2.327	2.281	2.130	2.299	2.135
	ΔE_{site}	0.345	0.358	0.287	0.290	0.301
Config3	E	-3.959	-3.887	-4.645	-4.663	-4.692
	ΔE^{a}_{spin}	2.164	2.124	2.042	2.212	2.055
	ΔE_{site}	0.453	0.479	0.374	0.329	0.336
Cu(II)						
Config1	E	-6.166	-6.156	-7.688	-7.407	-7.598
	ΔE^{b}_{spin}	4.553	4.486	5.091	5.192	5.088
	ΔE_{site}	0.000	0.000	0.000	0.000	0.000
Config2	e	-5.120	-5.055	-6.379	-6.192	-6.250
	ΔE^{b}_{spin}	3.632	3.584	3.978	4.011	4.105
	ΔE_{site}	0.937	0.955	1.079	1.215	1.357
Config3	E	-4.700	-4.678	-5.932	-5.651	-5.814
	ΔE^{b}_{spin}	2.961	2.901	3.141	3.258	3.133
	ΔE_{site}	1.466	1.478	1.756	1.756	1.783
Config4	E	-4.496	-4.433	-5.413	-5.373	-5.442
	ΔE^{b}_{spin}	2.824	2.765	2.839	2.975	2.857
	ΔE_{site}	1.562	1.576	2.045	2.034	2.065
Config5	E	-4.766	-4.747	-5.904	-5.463	-5.772
	ΔE^{b}_{spin}	2,950	2.896	3.023	3.027	3.017
	ΔE_{site}	1.399	1.409	1.784	1.945	1.826
Config6	E	-4.503	-4.436	-5.567	-5.360	-5.571
	ΔE^{b}_{spin}	2.785	2.724	2.912	2.881	2.895
	ΔE_{site}	1.555	1.573	1.891	2.047	1.946

[a] Total energy difference between relaxed singlet- and triplet-configurations.
[b] Total energy difference between relaxed doublet- and quadruplet-configurations.

of ~ 2.04 Å, bond lengths of 2.06 and 2.22 Å have been reported. The location in the 8MR is higher in energy by 0.36 eV than the 6MR-site, in very good agreement with our result with hybrid functionals.

Structure and Energies of Cu(I) Lewis-sites in Excited Spin-states

The creation of a spin-polarized triplet-state of a Cu(I) extra-framework cation formally requires the excitation of one electron from a $3d$ to a $4s$ state. The creation of a hole in the $3d$ band and the occupation of a much more extended $4s$ orbital leads to important changes in the coordination of the cation which are most pronounced for configuration (1) with Cu(I) in the 6MR. In the structure optimized at the triplet state, the cation binds only to the activated O(**2**) and O(**3**) atoms, with Cu-O distances of $\sim 2.04 \pm 0.02$ Å (GGA) and $\sim 2.00 \pm 0.02$ Å (hybrid functionals). The bonds to the non-activated O(3) framework oxygen are lost, the Cu-O coordination is reduced from three (respectively four with hybrid functionals) to two. The triplet-optimized structure of Cu(I) in the 6MR is shown in Fig. 5.5. Due to the lack of binding to O atoms on the other side of the ring, the Cu(I) cation also drifts away from the plane of the ring to a position pointing towards the center of the large cavity.

For Cu(I) cations in configurations (2) and (3) in an 8MR the changes in the local geometries are are similar, but less dramatic. In configuration (2) the distance from the non-activated O(2) atom is stretched beyond 2.8 Å such that the Cu-O coordination is reduced from three to two, the Cu-O(**4**) is reduced by about 0.18 Å. In configuration (3) with only two Cu-O bonds the geometry of the excited spin-state remains almost the same. The two Cu-O bonds are stretched by about 0.01 Å with GGA functionals, but contracted by 0.04 to 0.07 Å if hybrid functionals are used. Detailed information on the optimized geometries of excited spin sates may be found in Appendix A.

The total energy differences between the relaxed ground state and the relaxed first excited spin state range between about 2.7 eV [configuration (1)] and 2.1 eV [configuration (3)], they depend only weakly on the choice of the functional. Details are compiled in Table 5.4.

Structure of the Lewis Site in Cu(II) Chabazite

For the divalent extra-framework cations we have considered the same cation-locations, but for the positions of the two charge-compensating Al atoms two possibilities, one with both Al in the same 6MR and one with just one Al in each part of the D6R have been considered. The electronic ground state of the free Cu(II) cation is d^9, with one un-paired d-electron. For all configurations the spin-polarized calculations converge to a doublet (S=1/2) state. Fixed moment calculations have been performed to check that all other spin-states are higher in energy and to determine the spin excitation energies.

The relaxed configurations (1) and (2) for the Cu(II) cation in the 6MR are shown in Fig. 5.6(a,b). If the Al atoms are located at opposite sides of the same 6MR [configuration (1)], four strong Cu(II)-O bonds of about equal length of $\sim 2 \pm 0.05$ Å can

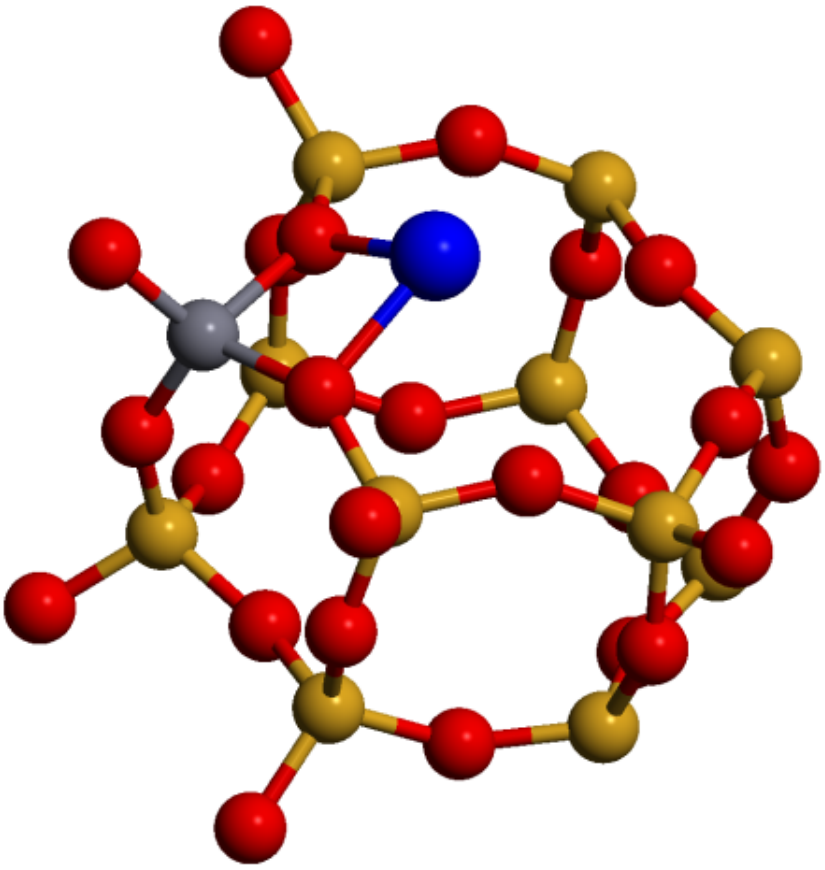

Figure 5.5: Triplet-optimized coordination of a Cu(I) cation in a 6MR of chabazite [configuration (1)]. The extra-framework cation forms only two strong bonds to activated framework oxygen atoms O(**2**) and O(**3**). Cf. Fig. 5.2 for the singlet GS-configurations and text.

be formed (see Table 5.3). Three of these bonds connect to activated oxygen atoms, the fourth to a non-activated O(3) atom. Bonding to activated oxygen atoms only at both opposite sides of the ring would require a too strong and energetically unfavorable distortion of the 6MR. Replacement of the GGA by a hybrid functional leaves the structure unchanged and induces only modest contractions of the bond lengths to activated oxygens. Due to the interaction with the cation, the three T-O-T angles around both activated and non-activated O(3) atoms are reduced from 147° to about 131 to 134°, while the T-O-T angles at the O(2) sites remain close to their value in purely siliceous chabazite.

If the second Al site is located in a different 6MR, the Cu(II) cation is also fourfold coordinated. Bonds are formed with two activated and two non-activated oxygen atoms, all located at one side of the 6MR, see Fig. 5.6(b). If GGA functionals are used the distance to the O(**2**) atom is longer by about 0.20 Å than the Cu(II)-O(**3**) bond, the difference between the bonds to the non-activated O atoms is even larger, about 0.5 Å. The difference in the bond lengths is a consequence of the topology of the 6MR with alternating orientations of the T-O-T angles. T-O-T angles around the O(3) sites are reduced to about 128° (activated) and 138° (non-activated oxygen), those around the O(2) are increased to about 161°. If hybrid functionals are used the differences in the bond-lengths are considerably reduced, see Table 5.3. Bond angles are much less affected.

In configurations (3) to (6) with the Cu(II) cation in a 8MR the position of the second Al site is of minor importance because the distance to the cation is in both cases too large to allow the formation of a bond between cation and an activated oxygen atom. As for the Cu(I) cation in configuration (2), three strong Cu(II)-O bonds, two to activated and one to a non-activated O atom can be formed. The cation-coordination shown in Figs. 5.6(c,d) is similar to that shown in Figs. 5.3 and 5.4 for the monovalent cation, albeit with some differences in the bond-lengths. In configurations (5) and(6), the divalent Cu(II) cation forms an additional third bond to a non-activated O(4) atom. Due to the stronger bonding of the divalent cation, both bonds to activated oxygen atoms measure about 2.0±0.05 Å if a GGA functional is used, they are further contracted to ∼ 1.95 Å and 1.86 Å if hybrid functionals are used in the calculations. The bond to the non-activated oxygen atom is less affected, except in configuration (6) (Cu(II) cation in position IIb, Al atoms in different rings) where the Cu(II)-O(4) distance is shorter by almost 1 Å for the divalent cation. The shorter cation-oxygen distances are also correlated to a stronger distortion of the framework. T-O-T angles around the O(**1**) atom are reduced to ∼ 121°, those around the O(2) atom to ∼ 131° for configurations (3) and (4). Even slightly larger reductions of the T-O-T angles are calculated for the activated and non-activated O(4) sites in configurations (5) and (6). Bond angles are only little affected by the choice of the functional.

Energies of the Lewis Site in Cu(II) Chabazite

The location of the Cu(II) cation in the 6MR, together with both Al atoms is by far lowest in energy (see Table 5.4). A position of the second Al atom at the opposite

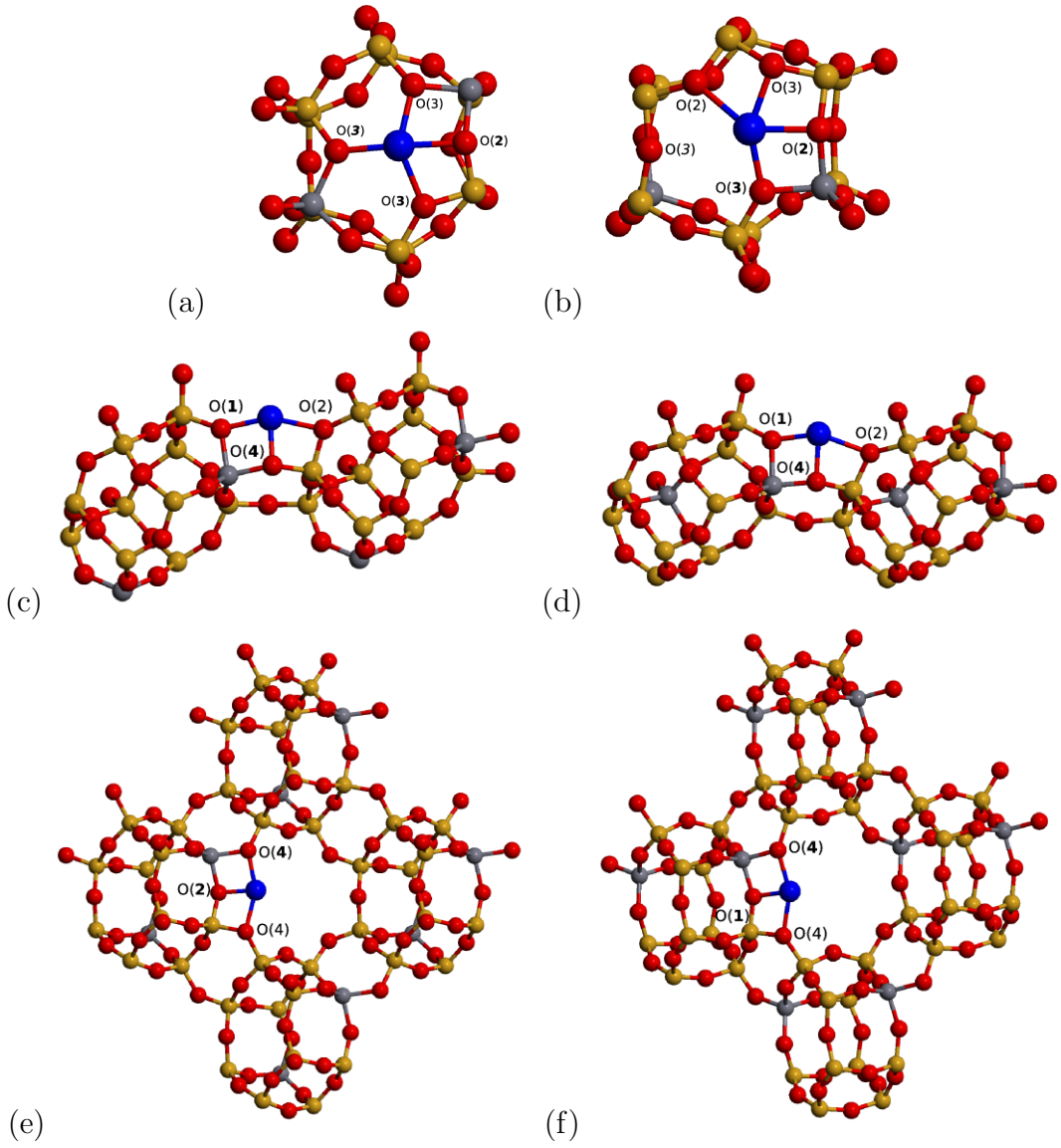

Figure 5.6: (Color Online) (a,b) Fourfold coordination of a Cu(II) cation in a 6MR of chabazite, with two Al atoms (a) and only one Al atom (b) in the 6MR [configurations (1) and (2)], respectively. (c,d) Threefold coordination of a Cu(II) cation in extra-framework site IIa [configurations (3) and (4) differ only in the location of the Al atoms]. (e,f) Threefold coordination of a Cu(II) cation in extra-framework site IIb [configurations (5) and (6)]. Cf. Fig. 5.2 and text.

side of the D6R increases the energy by almost 1 eV (and by slightly more if hybrid functionals are used). All four configurations with the Cu(II) cation in a 8MR are higher in energy by about 1.5 eV (GGA) and by 1.75 to 2.05 eV (hybrid functionals). For these positions of the cation, the location of the second Al is of lesser importance. It increases the energy by about 0.1(0.3) eV (cation location IIa) and 0.15(0.1) eV (cation location IIb), values calculated with hybrid functionals in parentheses. Because of the relatively small energy differences, the choice of the functional also influences the energetic ordering of these four cation coordinations. The screening of the exact exchange added to the hybrid functional has also a modest influence on the energy differences between the different cation-coordinations.

Structure and Energy of Cu(II) Lewis-sites in Excited Spin-states

The ground state of the Cu(II) cation in chabazite is a spin doublet (S=1/2), the first excited spin-state is a quadruplet (S=3/2). For a free cation the excitation requires the transfer of an electron from a spin-paired $3d$ to a $4s$ state, the electron configuration of the quadruplet state is $3d^8 4s^1$. For an extraframework cation in the zeolite, framework states can contribute to the spin-polarization as well. The relaxed geometry around Cu(II) in the excited spin-state in the 6MR configuration (1) with two Al atoms on opposite sides of the ring is shown in Fig. 5.7. The coordination of the cation is very similar to the triplet-relaxed state of the Cu(I) cation, binding only to the activated O(**2**) and O(**3**) atoms next to one of the Al atoms. The bonds to the activated O(**3**)atom next to the second Al site and to the non-activated O(3) atom are lost. This also leads to significant changes in the T-O-T angles around the oxygen atoms that do no longer bind to the Cu(II) cation. The Cu(II) cation also drifts away from the plane of the ring to a position pointing towards the center of the large cavity. In configuration (2) with only one Al atom in the 6MR the effect of the spin-excitation on the coordination of the cation is very similar: the Cu-O coordination is reduced from four to two, the bond lengths between the cation and the two activated framework oxygens have almost the same length, whereas in the ground state they differed by about 0.2(0.1) Å with GGA(hybrid) functionals. This more symmetric arrangement is possible because without the bonds to oxygen atoms on the other side of the ring its geometry is less distorted.

The energy of the excited spin-state is for configuration (1) higher by about 4.50 (5.1) eV than the ground state with GGA (hybrid) functionals, for configuration (2) the energy differences are smaller, about 3.6 (4.0) eV (for details see Table 5.4).

For configurations (3) to (6) with the Cu(II) cation in a 8MR the Cu-O coordination is reduced from three to two, the two remaining bonds to activated framework oxygens are stretched and more symmetric than in the spin ground state (for details, see Appendix A). For these configurations, the energy differences between the two spin states range between 2.8 (2.9) and 2.95 (3.2) eV with GGA (hybrid) functionals, detailed results are compiled in Table 5.4.

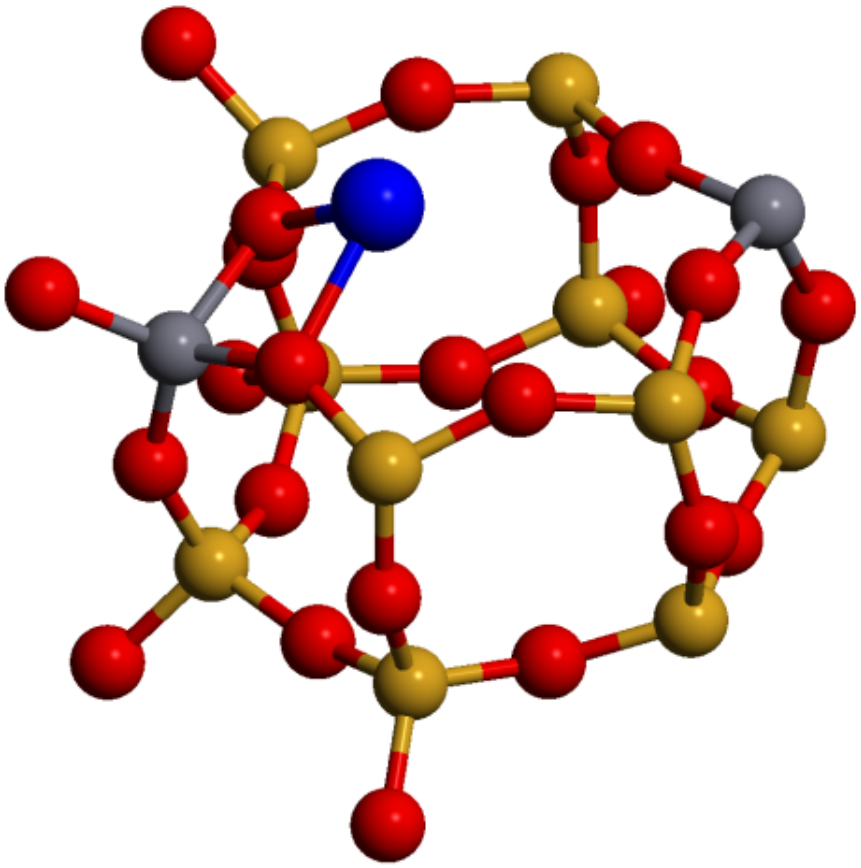

Figure 5.7: Quadruplet-optimized coordination of a Cu(II) cation in a 6MR of chabazite [configuration (1)]. The extra-framework cation forms only two strong bonds to activated framework oxygen atoms O(**2**) and O(**3**). Cf. Fig. 5.2 for the singlet GS-configuration and text.

Co(II)-exchanged Chabazite

Structure of the Lewis Site in Co(II) Chabazite

The electronic configuration of a free Co(II) cation is d^7, with three un-paired d-electrons. Correspondingly, the spin-polarized calculations for Co(II)-exchanged chabazite converge to a quadruplet (S=3/2) ground state for all six configurations. A spin of S=3/2 has also been predicted by DFT calculations[151] for Co(II)-MOR and Co(II)-FER and confirmed for Co(II)-MFI by the electron spin resonance experiments of El Malki *et al.*[152]. The spin is not localized on the Co-cation alone, but distributed over the cation and the bonding framework oxygen atoms (a more detailed discussion of electron- and spin-density distributions will be presented in the following paper).

In configuration (1) the Co(II) cation is located close to the center of the 6MR, with four about equally strong bonds to framework oxygen atoms and there are only minor differences between the GGA and hybrid functionals (see Table 5.3). The configuration is almost planar, the O-Co(II)-O bond angles are around 90°. The coordination of Co(II) cations is qualitatively similar to that of Cu(II), therefore no pictures are presented here. In configuration (2) with only one Al in the 6MR the cation drifts to the side of the ring where the Al atom is located, but remains fourfold coordinated. The two bonds with O(3) atoms measure about 1.9 and 2.0 Å, those to O(2) atoms about 2.15 Å (calculations with GGA functionals) - hence in this case the difference in the bond lengths is due to the topology of the ring and not to the state of activation of the oxygen atom. Only in calculations with hybrid functionals, the Co(II) distance to the activated O(**2**) is distinctly shorter than to the non-activated O(2).

In configurations (3) to (6) with the cation in a 8MR, three cation-oxygen bonds are formed. The two bonds to the activated framework oxygens are distinctly shorter (1.90 to 1.97 Å) than those to the third, non-activated atom (about 2.05 to 2.24 Å). The choice of the functional has only a minor influence on the cation coordination.

Energies of Co(II) Lewis Sites in Chabazite

A location of the Co(II) cation in a 6MR with two Al atoms is lower in energy by about 1 eV than in the presence of only one Al atom. A location in a 8MR is disfavored by more than 1.45 eV, the presence of a second Al in the ring causes an energy difference of about 0.4 eV for configurations (3) and (4), but only a smaller difference of about 0.1 eV for configurations (5) and (6). For a complete list of structural energy differences, see Table 5.5. Energy differences calculated with hybrid functionals are larger than those determined with GGA functionals. The energetic ordering is (1)-(2)-(3)-(5)-(4)-(6) with GGA, and (1)-(2)-(3)-(5)-(6)-(4) with hybrid functionals.

Structure and Energies of Excited Spin-States

For Co(II) cations spin-excitations can lead to the formation of a low-spin state with S=1/2 or of a high-spin-state with S=5/2. For a free cation the formal electron configuration in the low-spin state remains d^7, while in the high-spin-state a $3d$ minority

Table 5.5: Binding energy E of extra-framework Co-atoms, energy difference ΔE_{spin} between the relaxed spin ground sate and the relaxed first excited spin-state, and energy difference ΔE_{site} with respect to the most stable configuration, calculated with different exchange-correlation functionals. All energies are given in eV.

		PW91	PBE	PBE0	HSE03	HSE06
Co(II)						
Config1	E	-7.875	-7.794	-9.197	-9.144	-9.458
	$\Delta E_{spin}(Q_{3/2} \rightarrow D_{1/2})$	0.314	0.423	0.878	0.908	0.936
	$\Delta E_{spin}(Q_{3/2} \rightarrow S_{5/2})$	3.884	3.942	4.898	5.048	4.198
	ΔE_{site}	0.000	0.000	0.000	0.000	0.000
Config2	E	-6.978	-6.751	-8.234	-8.156	-8.279
	$\Delta E_{spin}(Q_{3/2} \rightarrow D_{1/2})$	0.361	0.471	0.942	1.091	0.951
	$\Delta E_{spin}(Q_{3/2} \rightarrow S_{5/2})$	3.307	3.359	3.800	3.915	3.807
	ΔE_{site}	0.885	0.896	1.034	1.056	1.046
Config3	E	-6.427	-6.340	-7.586	-7.456	-7.841
	$\Delta E_{spin}(Q_{3/2} \rightarrow D_{1/2})$	0.563	0.567	0.973	0.979	0.989
	$\Delta E_{spin}(Q_{3/2} \rightarrow S_{5/2})$	2.692	2.714	3.812	3.227	3.181
	ΔE_{site}	1.449	1.454	1.611	1.689	1.617
Config4	E	-6.042	-5.816	-7.293	-7.211	-7.337
	$\Delta E_{spin}(Q_{3/2} \rightarrow D_{1/2})$	0.519	0.540	0.950	1.100	0.960
	$\Delta E_{spin}(Q_{3/2} \rightarrow S_{5/2})$	2.363	2.395	2.796	2.916	2.799
	ΔE_{site}	1.821	1.830	1.975	2.001	1.989
Config5	E	-6.314	-6.208	-7.396	-7.345	-7.648
	$\Delta E_{spin}(Q_{3/2} \rightarrow D_{1/2})$	0.454	0.523	0.899	0.927	0.923
	$\Delta E_{spin}(Q_{3/2} \rightarrow S_{5/2})$	2.540	2.536	2.924	3.041	2.906
	ΔE_{site}	1.561	1.586	1.801	1.799	1.810
Config6	E	-6.197	-5.968	-7.407	-7.321	-7.414
	$\Delta E_{spin}(Q_{3/2} \rightarrow D_{1/2})$	0.478	0.513	0.928	1.084	0.916
	$\Delta E_{spin}(Q_{3/2} \rightarrow S_{5/2})$	2.524	2.539	2.831	2.831	2.973
	ΔE_{site}	1.666	1.679	1.861	1.891	1.911

electron has to be promoted to a 4*s* state. Consequently, larger changes in the energetics and cation coordination are expected in the excited high-spin state.

We discuss the low-spin state with S=1/2 first. In configurations (1) and (2) the Co(II) cation remains fourfold coordinated. In configuration (1) the two Cu-O bonds to activated oxygen are contracted by 0.17(0.12) Å for O(**2**) and 0.05(0.05) Å for O(**3**) in calculations with GGA (hybrid) functionals. The bond lengths to non-activated O atoms remain almost unchanged. In configuration (2) the bonds to the activated O(**2**) and the non-activated O(3) atoms are contracted while the bond to the activated O(**3**) remains unchanged and the distance to the O(2) atom is even increased. The energy difference between the relaxed spin-states is small, about 0.3 to 0.4 eV with GGA and 1.0 eV with hybrid functionals (all energy differences are compiled in Table 5.5).

For configurations (3) to (6) with the Co(II) in an 8MR relaxation effects in the low-spin state are modest. The cation remains threefold coordinated, only moderate changes in the Cu-O bond lengths are predicted with GGA functionals while with hybrid functionals we find a contraction of the distances to activated and/or non-activated oxygens (details are given in Appendix A). The relaxed energy difference relative to the spin ground state varies around 0.5 eV with GGA and around 1.0 eV with hybrid functionals (see Table 5.5).

Much larger changes relative to the ground state are found for the high-spin (S=5/2) state. In configuration (1) the Co(II) cation remains fourfold coordinated, but all four Cu-O bonds are stretched to 2.05 to 2.32 Å (1.97 to 2.26 Å) with GGA (hybrid) functionals. In configuration (2) the cation is only threefold coordinated in the high-spin state, the bond to the O(2) atom is broken. The remaining three bonds are stretched to 2.13 (2.19) Å on average, depending on the type of functional. The energy difference is about 3.9 (4.9) eV for configuration (1) and 3.3 (3.8) eV for configuration (2), calculated with GGA (hybrid) functionals. For configurations (3) to (6) the energy differences range between 2.35 and 2.70 (2.8 and 3.2) eV.

5.6 Comparison with experiment

Structure of Purely Siliceous Chabazite

For purely siliceous chabazite we have found that hybrid functionals predict a lower volume of the unit cell and shorter Si-O bond lengths in slightly better agreement with experiment.[144, 145]. Upon Al/Si substitution GGA functionals predict an almost uniform expansion of all four bonds around the tetrahedral site. In contrast, hybrid functionals predict a stronger expansion of two Al-O bonds and a more modest one of the two remaining bonds. However, as the substitution breaks the rhombohedral symmetry and as the average Al-O bond length is almost the same, XRD experiments are not able to discriminate between these two cases.

Structure of Lewis Sites: Comparisons with XRD and XAS data

According to the XRD experiments of Fickel and Lobo[145] Cu-cations occupy a location just outside the plane of a 6MR, symmetrically coordinated to three oxygen atoms in the ring at a distance of 2.21 Å. The high-silica sample (Si/Al∼12) on which the diffraction has been performed has a Cu/Al ratio of 0.35, which suggests that the oxidation state is Cu(II), but no attempt has been made to determine the oxidation state. Korhonen *et al.*[157] have performed an EXAFS analysis of the Cu(II) coordination in chabazite (using a sample very similar to that on which the XRD study has been performed) and report a coordination number of 3.2 and an average Cu-O distance of 1.93 Å. The mismatch with the XRD data has been attributed to a displacement of the Cu-cation from the center of the 6MR. The threefold coordination of Cu(II) cations agrees with the interpretation of earlier ESR data.[158].

The preference for a location in a 6MR agrees with our calculations for both the Cu(I) and Cu(II) cations. For the Cu(I) cation, the average Cu-O distance is 2.13 Å (PW, PBE) and 2.19 Å (PBE0) and 2.24 Å (HSE03). For the Cu(II) cation in configuration (1) (i.e. with two Al atoms in the same ring) the coordination is fourfold, the average Cu(II)-O distance is 2.01 Å using both types of functionals. For a Cu(II) cation in configuration (2) the coordination is threefold, the average Cu-O distance is 1.99 Å (PBE) and 1.94 Å (PBE0, HSE03), respectively.

Comparison of theory and experiment is hence difficult. For the high-silica chabazite it seems to be rather unlikely that two Al atoms are present in the same ring - configuration (2) will be more frequent than (1). In this configuration the calculated coordination number and average Cu-O distance are in good agreement with experiment, with hybrid functionals leading to a lower and hence slightly more accurate Cu-O bond length.

An early XRD experiment for Co(II)-chabazite has been presented by Calligaris *et al.*[159] for natural and dehydrated chabazite. The sample has a very high Al/Si ratio of nearly 1/2 and contains 1.7 Co atoms per unit cell plus 0.4 Na atoms. Co atoms where assigned to Site I in a 6MR, site II in an 8MR and also to site III in the center of the D6R. Due to the high content in Al the average bond lengths between the tetrahedral atoms and oxygen are increased by about 0.03 Å, while the tetrahedral bond angles undergo only a very modest change. The T-O-T angles are in reasonable agreement with our results for Cu(II)- or Co(II)-exchanged chabazite: angles around O(3) sites are decreased to 133°, those around the O(2) sites are increased to about 173° (but note that a different nomenclature has been used for the oxygen sites). The Co(II) cations have been assigned to positions of threefold (in the center of a 6MR) or twofold (in the 8MR) symmetry. This assumption leads to rather high Co-O distances: three Co-O bonds with 2.25 A in the 6MR, two bonds of 2.38 Å and one with 2.62 Å in the 8MR. These values are much larger than our results calculated for the off-symmetry locations of the Co(II) cation [2.06 Å for the fourfold coordinated cation in a 6MR, configuration (2); 2.04 Å for the threefold coordinated cation in a 8MR, configuration (4)]. Of the 1.7 Co atoms per unit cell about 0.76 are assigned to site I in a 6MR, 0.48 to site II in a 8MR, and 0.43 to site III in the center of the D6R (this site has not been

included in the present study). The comparison illustrates the difficulties hampering a detailed analysis of the XRD data, but also confirms the predicted preference for a cation location in a 6MR.

5.7 Conclusions

We have investigated the structure and energetics of purely siliceous, Al-substituted, and transition-metal exchanged chabazite, using periodic density-functional calculations with conventional semilocal (gradient-corrected) and hybrid exchange correlation functionals. The results can be summarized as follows:

(1) For purely siliceous chabazite hybrid functionals predict a cell volume by 1.5 to 2 pct smaller than GGA functionals, in almost perfect agreement with experiment. The volume contraction parallels a slight decrease of the Si-O bond lengths by about 0.01 Å. Si-O-Si bond angles around the O(1) and O(3) sites are increased by about 1°.

(2) The bond lengths around a Al/Si substitution sites are uniformly expanded by about 0.1 Å in calculations with GGA functionals, while hybrid functionals predict a violation of the local tetrahedral symmetry: Al-O(1) and Al-O(3) bonds are expanded by about 0.16 Å, those to the O(2) and O(4) atoms only by about 0.07 Å, bond lengths between the oxygens and the next Si atoms are also different.

(3) The geometric difference reflects different distributions of the electron deficit around the Al site: with GGA functionals we find that about 2/3 of the missing electronic charge is distributed over the four oxygen neighbors, the rest is spread out over the framework. With hybrid functionals the largest electron deficit of 0.5 and 0.33 electrons is found on the O(1) and O(3) sites, smaller deficits of 0.033 electrons on the O(2) and O(4). The stronger localization of the charge deficit is caused by the admixture of Hartree-Fock exchange in the hybrid functionals. Similar effects are also found in metal-exchanged chabazite where the charge on the framework is formally compensated by electrons transferred from the metal atoms.

(4) For Cu(I) cations located in a coplanar off-center position within the 6MR a threefold coordination to framework oxygens is found with GGA functionals, while hybrid functionals predict a fourfold coordination in a location closer to the center of the ring. Cations in a 8MR are three- or twofold coordinated to oxygen atoms. In these cases both functionals predict nearly the same geometries, far removed from the center of the 8MR. Hybrid functionals predict a stronger bonding of the cation to the framework than GGA functionals, a location in the 6MR is always favored over a position in a 8MR. A location close to the center of the hexagonal prism is found to be unstable, the cation drifts towards the plane of the 6MR containing the Al atom.

(5) The ground state of a Cu(I) cation is a singlet. A triplet state is higher in energy by up to 2.8 eV, the energy difference being slightly higher with GGA functionals. For the high-spin state of the cation located in the 6MR both functionals predict an only twofold coordination of the cation which also moves from the plane of the 6MR towards the center of the large cavity. Relaxation effects are less pronounced for the locations in a 8MR.

(6) For a divalent Cu(II) cation the binding to the framework is much stronger. A cation located in a 6MR is always fourfold coordinated, whether one or two Al atoms are located in the 6MR, and also independent of the choice of the functional. Hybrid functionals only predict slightly shorter Al-O bonds. Cu(II) cations in a 8MR are always threefold coordinated, bonds to activated oxygen atoms are shorter by 0.05 to 0.15 Å if calculated with hybrid functionals. The energetically most favorable position is in a 6MR with two Al atoms, a location in a ring with only one Al is disfavored by about 1 eV. Positions in a 8MR are higher in energy by about 1.5 eV. If hybrid functionals are used, these energy differences increase by 0.3 to 0.5 eV.

(7) For a Cu(II) cation the spin ground state is S=1/2, the excited state has S=3/2. The relaxed geometry of the quadruplet state is very similar to that of the triplet state of the Cu(I), with only two Cu(II)-O bonds for a position in the 6MR. Relaxation effects are less dramatic for cations in a 8MR. The energy difference between both spin states ranges between 4.5 (5.1) eV for configuration (1) (6MR with two Al) and 2.8(2.9) eV for configuration (6) (8MR with one Al), calculated with GGA (hybrid) functionals.

(8) Bonding to the framework is even stronger for a Co(II) cation. In a 6MR with two Al atoms the Co(II) cation is located almost in the center of the ring. If only one Al atom is present it drifts towards the substitution site, but remains fourfold coordinated. In a position off the center of a 8MR, the Co(II) cation is always threefold coordinated. Differences in the Co(II)-O bond lengths calculated with both types of functionals are much smaller than for Cu(II). Energy differences between cation locations are comparable to Cu(II). Hybrid functionals yield energy differences larger by about 0.2 eV than GGA.

(9) For a Co(II) cation the ground state is S=3/2. For an excited low-spin state with S=1/2 a cation in a 6MR remains fourfold coordinated, but the distances to activated O atoms are contracted. Threefold coordination is also preserved for a location in a 8MR. The energy differences between the ground state and the excited low-spin state are modest, ranging between 0.3 and 0.5 (1.0 and 1.9) eV with GGA (hybrid) functionals. Formation of an excited high-spin state with S=5/2 requires a much larger energy between 2.5 and 3.9 (2.8 and 5.0) eV with GGA (hybrid) functionals. The larger energy differences go parallel with larger relaxation effects. In configuration (1) a high-spin Co(II) cation remains fourfold coordinated, but in configuration (2) the coordination is reduced to threefold.

The predicted preference for a location of Cu and Co cations in a 6MR agrees with experimental observation and earlier calculations. However, the calculations indicate that the cation location has lower symmetry than inferred from XRD (or rather assumed in the interpretation of the XRD data) - this applies especially for location in a 6MR where only one Al/Si substitution site exists. These configurations predominate in high-silica chabazite. The average Cu-O distances calculated for Cu(II)-chabazite are in better agreement with experiment when hybrid functionals are used in the calculations. Hybrid functionals also describe the overall geometry of the siliceous framework somewhat better. However, they also indicate a stronger distortion of the framework around Al/Si site where no charge-compensating cation is present in the

immediate vicinity. We have shown that the stronger distortion of the framework is correlated to a stronger localization of the charge-deficit created by the substitution. The stronger localization of the eigenstates associated with framework substitution and/or extraframework cations is a characteristic feature of hybrid functionals. Together with the increased energy difference between occupied and empty eigenstates and between majority and minority spin states these effects dominate the electronic structure to be discussed in the following paper.

6 Electronic Structure and Photoluminescence Spectra

Summary

The influence of the choice of the exchange-correlation functional (semilocal gradient corrected or hybrid functionals) on the electronic properties of metal-exchanged zeolites has been investigated for Cu- and Co-exchanged chabazite. The admixture of exact exchange in hybrid functionals increases the fundamental gap of purely siliceous chabazite, leading to better agreement with experiment and many-body perturbation theory. For the metal-exchanged chabazite the increased exchange splitting strongly influences the position of the cation-states relative to the framework bands - in general, gradient-corrected functional locate the occupied cation states close to the valence-band maximum of the framework, while hybrid functionals shift the occupied cation states to larger binding energies and the empty states to higher energies within the fundamental gap. The photoluminescence spectra have been analyzed using fixed-moment total-energy calculations for excited spin-states in structurally relaxed and frozen geometries. The geometrical relaxation of the excited states leads to large differences in excitation and emission energies which are more pronounced in calculations using hybrid functionals. Due to the stronger relaxation effects calculated with hybrid functionals the large differences in the electronic spectra calculated with both types of functionals are not fully reflected in the photoluminescence spectra.

6.1 Introduction

In the preceding chapter (hereafter referred to as I) we have analyzed in detail the influence of the choice of an exchange-correlation functional [semilocal gradient-corrected (GGA) or hybrid functional] on the structural properties of purely siliceous and transition-metal exchanged chabazite predicted by density-functional calculations. We have shown that for the pure SiO_2 zeolite hybrid functionals (the PBE0[72] or HSE[73, 74] functionals) predict a slightly lower volume and shorter Si-O bond lengths in better agreement with experiment than semilocal gradient-corrected functionals (the PBE[55] and the PW[54] functionals). More significant differences were found in the local environment of the extraframework cations and of the Al/Si substitution sites in Cu(I)-, Cu(II)-, and Co(II)-exchanged chabazite. Around an isolated Al/Si substitution site, the conventional functionals predict a uniform expansion of the tetrahedral environment (uniform elongation of all four Al-O bonds) and a uniform distribution of the

electron deficit on all surrounding framework oxygens. Hybrid functionals predict a stronger stretching of two Al-O bonds and a smaller one of the two remaining Al-O bonds, accompanied by a localization of the electron deficit on the two oxygen atoms with stretched bonds to the Al site. For all three extraframework cations both types of functionals predict a preferred location of the cation in an almost coplanar off-symmetry position within a six-membered ring (6MR) of the chabazite structure. For the Cu(I) cation GGA functionals predict a threefold, hybrid functionals a fourfold coordination by framework oxygens. For the divalent Cu(II) and Co(II) cations the coordination is always fourfold, but hybrid functionals predict stronger bonds to the activated oxygen atoms next to an Al site. Locations of the cation in an eight-membered ring (8MR) are always two- or threefold coordinated, independent of the choice of a functional, but energetically disfavored by about 0.35 to 0.45 eV (0.29 to 0.37 eV) with GGA (hybrid) functionals. For the Cu(II) cation the energy differences measure up to 1.5 eV with GGA, with hybrid functionals the energetic penalty increases by 0.3 to 0.5 eV.

Spin-polarized density-functional calculations have been used to determine the ground-state, fixed-moment calculations have been used to determine the structure and energies of excited spin states. Cu(I)-chabazite has a singlet ground-state, the triplet state is higher in energy by up to 2.8 eV, depending on the configuration. This energy difference is slightly higher with GGA than with hybrid functionals. An important result is that in the structurally relaxed triplet state a Cu(I) cation in a 6MR is only twofold coordinated. For Cu(II)-chabazite the ground state has spin as S=1/2, the excited spin state S=3/2. Again for the location within a 6MR the coordination is reduced to two oxygen atoms in the excited state, while for locations in a 8MR the changes in the local structure is less dramatic. This is also reflected in the spin-dependent difference in the total energy, which is much larger for Cu(II) in a 6MR than in an 8MR.

The ground-state of a Co(II) cation in chabazite has spin S=3/2. A Co(II) cation is fourfold coordinated in a 6MR and threefold in a 8MR, energy differences are of the same order of magnitude than for Cu(II). The lowest excited state is a low-spin state with S=1/2, higher in energy by 0.3 to 0.5 eV (0.9 to 1.0 eV) with GGA (hybrid) functionals. In the low-spin state the coordination of the Co(II) cation remains unchanged. A high-spin state with S=5/2 is higher in energy by 2.4 to 3.9 eV (2.8 to 5.0 eV) with GGA (hybrid) functionals, changes in the coordination are smaller than for the Cu(II) cation - in the high-spin state essentially all Co-O bonds are stretched, but not broken.

These results demonstrate that the influence of the choice of the exchange-correlation functional is more pronounced for the spin-state of the cation and its local coordination than for the structure of the zeolitic framework. An even increased importance of the choice of the functional is expected for the electronic structure. It is well known that density-functional calculations seriously underestimate the width of the fundamental gap in semiconductors and insulators. For SiO_2 polymorphs early density functional calculations predicted a gap width varying between 5.5 eV for β-quartz and 6.8 eV for β-cristobalite, with an almost linear variation as a function of the volume per formula unit.[160] More recent calculations[161] report gaps of 5.79 eV, 5.53 eV, 5.33 eV for α-

quartz, α- and β-cristobalite, invalidating the pronounced volume dependence reported in earlier work. A very similar width of the gap of 5.6 eV has also been reported in density-functional calculations for amorphous silica.[162] These values are much lower than those measured in experiment. From photoconductivity measurements on polycrystalline SiO_2 a gap width of 8.9 eV was derived[163], while for amorphous silica films a value of 9.3 eV has been reported.[164] Hartree-Fock calculations on the other hand largely overestimate the width of the gap, with values ranging between 16.9 eV for α-quartz and 16.2 eV for amorphous silica.[162] More accurate determinations of the gap width require many-body perturbation (GW) calculations.[111, 112] Because of the complexity of GW calculations, most applications to silica use approximate versions of the theory with model dielectric functions. Ramos *et al.*[165] have calculated gaps between 10.16 and 10.31 eV for different structural variants of β-cristobalite,, Martin-Ramos *et al.*[162] reported GW gaps of 9.4 eV and 9.3 eV for α-quartz and amorphous silica, Umari *et al.*[166] a GW gap of 8.5 eV for vitreous silica.

For zeolites information on their electronic structure is rather scarce, because most theoretical studies have concentrated on their structures and chemical reactivities. Early density functional calculations[167] predicted a gap width of 5.5 eV for mordenite, Hartree-Fock cluster calculations[168] values of about 10 eV for protonated sodalite. For structures as complex as those of zeolites, GW calculations would be computationally very demanding. However, extended comparisons of GW calculations with hybrid-functional calculations for a wide range of semiconductors and insulators have demonstrated[113] have demonstrated that the gaps calculated with a screened hybrid functional[73] are in consistently good agreement with the most sophisticated GW calculations. Hence we expect that calculations with hybrid functionals will also yield improved values for the energy gap of the purely siliceous chabazite.

However, for transition-metal exchanged zeolites this is not the entire story. The divalent Cu(II) and Co(II) cations carry a paramagnetic moment. The exchange-splitting between majority- and minority-spin states and the gap between the occupied and empty metal *d*-states will determine the position of the energy levels of the cation relative to the bands of the framework and hence be of crucial importance for determining the chemical reactivity of the active sites in the zeolite. Hybrid functionals are known to predict a much larger exchange-splitting than conventional GGA functionals, even for the same value of the spin of the cation.

The electronic state of cations in metal-exchanged zeolites may be probed using various photoluminescence spectroscopies [diffuse reflectance spectroscopy (DRS) covering the range from the ultraviolet (UV) across the visible (vis) range to the near infrared (NIR),....]. [121, 122, 123, 169, 124, 170, 171] The measured spectra proved to be sensitive to the environment of the extra-framework cation and have been widely used to characterize their locations. However, the assignment of particular features in the spectra to particular locations of the cations turned out to be difficult. Traditionally, cations were attributed to different possible extraframework locations on the basis of the comparison of the dominant DRS emission bands with the energies of the electronic eigenstates of the cation in the ligand field of the surrounding framework oxygens, calculated for optimized cluster models representing the surrounding of the

cation.[122, 123, 142] The basic assumption behind this approach is that the creation of an excited state of the cation does not affect its coordination to the framework - hence the energies measured in absorption and emission spectra should be the same.

Lamberti *et al.*[121] were the first to point out that the difference in the measured emission and adsorption energies reflects changes in the environment of the cation. Adsorption peaks reflect excitation processes from the ground state to an excited state. Because electronic processes are much faster than ionic re-arrangements, the equilibrium geometry of the ground state is conserved in the excited state. The lifetime of the excited state is long enough for the excited state to relax its structure before a transition back to the ground state occurs, accompanied by the emission of radiation. Therefore vertical excitation energies have to be calculated as the energy difference between the lowest excited state and the ground state at the ground-state optimized structure. Conversely, vertical emission energies are calculated as the energy difference between the excited state and the ground state, calculated for the excited-state optimized geometry. Therefore, the difference between the excitation and emission energies is just the sum of the energies gained by relaxing the excited state from the frozen ground state geometry to its equilibrium structure, and the ground state from the frozen excited state geometry back to equilibrium (see also Scheme I). Nachtigall *et al.*[150] seem to have been the first to realize, following the suggestion of Lamberti *et al.*[121] that the coordination of a cation may be significantly different in the ground and excited states and to present calculations which account for the relaxation of the excited-state geometries and for the differences in the excitation and emission energies.

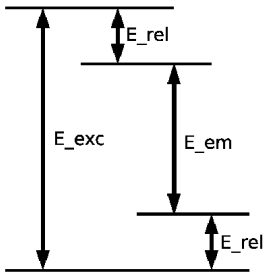

Scheme I: Schematic energy diagram for excitation and emission energies between different spin states of extra-framework cations.

One has to emphasize that the two approaches to a theoretical interpretation of the DRS spectra are fundamentally different. The first is based on a frozen ground-state geometry and determines the energies of the DRS bands (which are supposed to be identical in emission and adsorption) in terms of differences between one-electron energies. In the second approach the geometry is also assumed to remain unchanged

during the excitation or emission process, but it is admitted that the system remains long enough in the excited electronic state to relax its geometry before the transition back to the electronic ground state takes place. In addition, total-energy differences and not differences in one-electron eigenvalues are used to derive the energies of the DRS bands. Here we shall examine both methods, but with the essential difference that the electronic spectrum has been calculated not only for a cluster, but for the complete periodic structure of the zeolite.

In the following we will first present the electronic spectra of purely siliceous chabazite, followed by a detailed analysis of the electronic densities of states of the transition-metal exchanged chabazites in their ground- and excited spin-states. Our results demonstrate that GGA and hybrid functionals lead to very different results for the location of the cation *d*- and *s*-states relative to the energy bands of the framework and significant differences in the spin-density distributions. This will be followed by the analysis of the DRS spectra measured in emission and absorption, using both the conventional framework of one-electron excitations at a fixed lattice geometry and the assignment of the peaks in the measured DRS spectra to total energy differences between ground and excited states proposed by Nachtigall *et al.*.[150].

The significant differences in the eigenstates of the cations, depending on the choice of the exchange-correlation functional, will of course be of consequence for their chemical reactivities. The following and last paper of this series will be devoted to the calculations of the adsorption and of the vibrational properties of CO and NO probe molecules.

6.2 Functionals and Computational Setup

In our calculations we have used five different exchange-correlation functionals: (i) The PBE[55] and PW[54] functionals developed by Perdew *et al.* in the generalized gradient approximation (GGA). Both functionals are parameter-free in the sense that all parameters are derived from sum-rules, asymptotic limits etc. known from many-body theory, no adjustment to data from experiment or higher-level quantum-chemical calculations has been made. (ii) The hybrid functionals PBE0[72], HSE03[73] and HSE06[74] mixing 75 pct. density-functional and 25 pct. exact (Hartree-Fock) exchange, while treating correlation within the GGA. In the PBE0 functional the full Coulomb-kernel has been used in the Hartree-Fock exchange energy, while in the HSE functionals a screened Coulomb-interaction with different screening lengths has been introduced.

The calculations have been performed using the Vienna ab-initio simulation package VASP[135, 136] which performs a variational solution of the Kohn-Sham equations of density-functional theory (DFT). Unconstrained DFT calculations always converge to the ground state. For the calculation of excited spin-states we have used a fixed-moment method.[139] Selfconsistent DFT calculations for excited states with the same spin as in the ground state are not possible. For the transition-metal cations considered in this study the creation of an excited high-spin state involves the excitation of a 3*d*-

electron in a spin-down state to a $4s$ state with spin up. Because the exchange-splitting of the $4s$ state is always much smaller than the energy difference between $3d$ and $4s$ states, the spin-dependent contribution to the total-energy difference will be much smaller than the contribution from the $3d \rightarrow 4s$ transfer. For all technical details we refer to I.

6.3 Electronic Spectrum of Purely Siliceous Chabazite

The electronic density of states of purely siliceous chabazite is shown in Fig. 6.1. The electronic spectrum of chabazite is very similar to that of other, more densely packed polymorphs of SiO_2 (quartz, cristobalite, coesite,...)[160, 161, 162, 165]. The upper part of the valence band (about 4.5 eV wide) is of pure O-p character, it is separated by a small internal gap from the lower part (about 5.5 eV wide) with a stronger contribution from Si. A narrow band at $\sim$ 18 eV below the valence band edge is predominantly of O-s character. The conduction band consists mostly of Si states, emphasizing the ionic character of the material.

The indirect band gap of SiO_2 chabazite calculated using GGA functionals is 5.5 eV (PBE or PW91), to be compared with 5.79 eV (α-quartz), 5.53 eV (α-cristobalite), and 5.32 eV (β-cristobalite)[161] from calculations using the same type of functionals. Admixture of exact exchange increases the width of the gap to 8.0 eV (PBE0), screening of the exchange interactions (with the HSE03 or HSE06 functional) reduces the gap to 7.0 to 7.3 eV, depending on the screening length. The gap predicted with hybrid functionals is slightly lower than the result of recent GW calculations for crystalline and amorphous silicas of 9.3–9.4 eV (Ref. [162]) or 10.1–10.3 eV (Ref. [165]), depending on the GW-variant adopted in the calculations. No GW calculations and no experimental values for the band gap of zeolites are available so far. However, the comparison with the results for other SiO_2 polymorphs suggest that even with hybrid functionals the predicted band gap for chabazite is about 1 eV to narrow.

6.4 Electronic Spectrum of TM-exchanged Zeolites

The chemical reactivity of extra-framework transition-metal cations in zeolites is determined by the position of the electronic eigenstates of the cation with respect to the valence band of the zeolite framework, which in turn depends on the hybridization of the d-states of the cation with O-p states. Although it is current practice to consider the charge-transfer between the extra-framework metal atom and the framework to be complete, such that the system consists of a cation with the full positive ionic charge and a negatively charged framework on which all T-O bonds are saturated, the analysis of the electronic structure suggests only a partial charge transfer. This has consequences on the binding between cation and framework and also on the chemical reactivity of the Lewis site. In the following we analyze the electronic properties by calculating the electronic density of states, by performing a Bader analysis[148, 149]

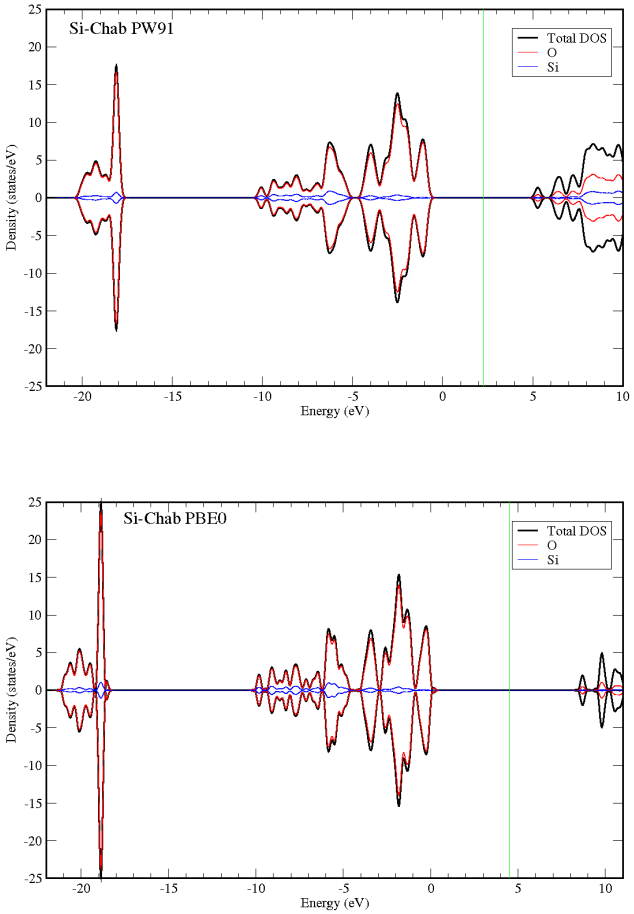

Figure 6.1: Electronic density of states of purely siliceous chabazite using GGA [(a), here PW91] and hybrid functionals [(b), here PBE0]. Black - total DOS, red and blue - partial DOS of O and Si, respectively.

Table 6.1: Width of the energy gap between the highest occupied Cu-d states and the lowest conduction-band state in Cu(I)-chabazite (in eV), for configurations (1) to (3), calculated with different exchange-correlation functionals.

Cu(I)	PW91	PBE	PBE0	HSE03	HSE06
Config1	3.16	3.14	5.72	4.52	4.80
Config2	2.27	2.25	4.94	3.80	4.08
Config3	1.65	1.72	4.67	3.50	3.79

of the local charges and studying the local electron- and spin-density distributions. In addition, we present a detailed analysis of the electronic spectra of excited spin-states derived from fixed moment calculations.

Cu(I)-chabazite

Ground state - spin singlet

For Cu(I)-chabazite the occupied 3d-states of the monovalent cation form a narrow band just above the valence band of the framework. However, the Cu-3d states also undergo a certain degree of hybridization with framework states belonging to the upper part of the valence band. The empty s-states are rather delocalized and spread out over a range of energies at the bottom of the conduction band (see - Fig. 6.2). This result is almost independent of the choice of the functional and of the location of the cation, except for the width of the gap between the highest occupied Cu-d state and the lower edge of the conduction band with a modest admixture of Cu-s states which varies for a cation in a 6MR between 3.2 eV (PBE) and 5.7 eV (PBE0). Compared to a Cu(I) cation located in a 6MR, a location in a 8MR only shows a tendency to a more bimodal character of the d-band, due to the lower coordination number of the cation, and narrower energy gaps between the 3d states and the conduction band minimum. The gaps calculated with all five functionals for all three configurations of Cu(I)-chabazite are summarized in Table 6.1.

The degree of hybridization between cation- and framework-states influences the charges on cation and framework. A Bader analysis[148, 149] shows that the charge on the cation is lower than the formal ionic charge of +1, varying between 0.70 and 0.75 if GGA functionals are used, and between 0.76 and 0.80 for hybrid functionals, see Table 6.2. The charge is lower for the more stable cation location in the 6MR. The analysis shows that the delocalized 4s electron of the Cu atom is largely, but not completely transferred to the zeolite framework.

A calculation of the difference-electron density (charge-distribution on the metal-exchanged chabazite minus charge-distributions on the neutral Al-chabazite and the neutral transition-metal atom, calculated at the frozen geometry of the metal-exchanged zeolite) shows the nature of the charge-redistribution - see Fig. 6.3 for a cation in a

(a)

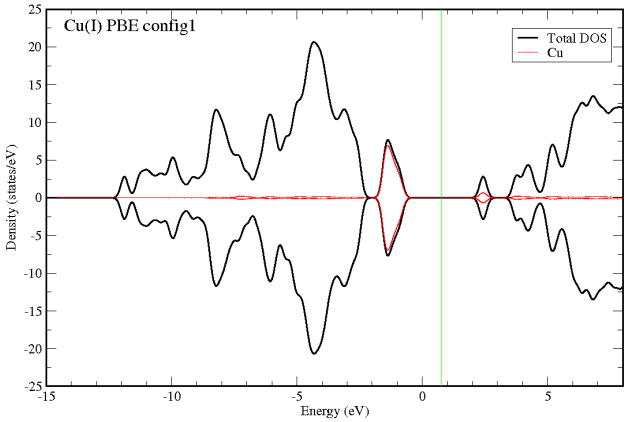

(b)

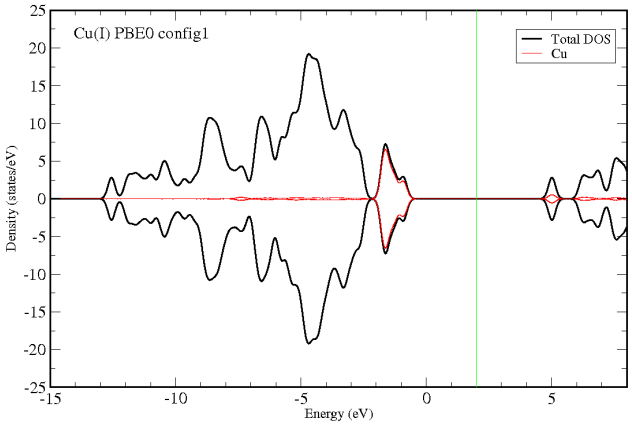

Figure 6.2: Electronic density of states (DOS) of Cu(I)-chabazite (total DOS and local DOS on the Cu-sites) in the S=0 ground state - calculated for configuration (1) with the cation in a 6MR containing two Al atoms, using the PBE (a) and the PBE0 (b) functionals, respectively. Cf. text.

Table 6.2: Charges on Cu(I) and Cu(II) extra-framework cations in chabazite, calculated using different exchange-correlation functionals as determined by a Bader analysis.

	PW91	PBE	PBE0	HSE03	HSE06
Cu(I)					
Config. (1)	0.700	0.703	0.758	0.763	0.764
Config. (2)	0.733	0.732	0.784	0.787	0.789
Config. (3)	0.751	0.753	0.793	0.797	0.800
Cu(II)					
Config. (1)	1.116	1.128	1.316	1.317	1.322
Config. (2)	1.067	1.069	1.291	1.285	1.294
Config. (3)	1.043	1.050	1.316	1.311	1.322
Config. (4)	1.001	1.004	1.305	1.299	1.306
Config. (5)	0.996	1.050	1.312	1.309	1.312
Config. (6)	1.056	1.059	1.309	1.303	1.312
Co(II)					
Config. (1)	1.315	1.322	1.487	1.488	1.493
Config. (2)	1.280	1.293	1.463	1.477	1.441
Config. (3)	1.292	1.288	1.499	1.497	1.501
Config. (4)	1.240	1.244	1.487	1.482	1.474
Config. (5)	1.254	1.263	1.478	1.475	1.479
Config. (6)	1.256	1.267	1.475	1.473	1.484

8MR. The Cu(I) site is electron-depleted, electrons are transferred to the activated oxygen atoms. Calculations using a GGA functional (here PBE) predict the transferred charge to be rather delocalized and distributed over all activated atoms, predominantly to those forming a strong bond to the Cu(I) cation. Calculations using hybrid functional show a stronger localization of the charge on the framework, the largest negative charge is concentrated on the O(**1**) atom forming the shortest Cu-O bond. The bonding oxygen atoms are also polarized, charge is accumulated in *p*-states extending perpendicular to the plane of the 8MR.

Excited state - spin triplet

The formation of a state with spin S=1 (spin-triplet) requires the excitation of a spin-down Cu-3*d* electron to a spin-up Cu-4*s* state. The formation of a hole in the Cu-3*d* band and the occupation of a much more extended Cu-4*s* state lead to a change in the coordination of the cation (as discussed in detail in I) and to a profound modification of the electronic spectrum. The densities of states for the geometrically relaxed S=1 state of the Cu(I) cation in configuration (1), calculated using the PBE and HSE03 functionals and the fixed-moment approach are shown in Fig. 6.4. Note that in fixed-moment calculations the difference in the Fermi-energies of spin-up and spin-down electrons is adjusted such as to produce the desired magnetic moment (for details, see I). The spin-polarized 3*d*-states now overlap with the valence band of the zeolite framework. Whereas GGA calculations predict the Cu-3*d* states to be located close to the valence-band maximum (VBM), and an empty 3*d*-state just above the Fermi level for spin-down electrons, hybrid functionals locate the occupied Cu-3*d* states at larger binding energies close to the center of the O-*p* band and the empty minority Cu-3*d* state is located about 2.5 eV above the upper edge of the valence band. A spin-polarized Cu-4*s* state is located in the upper half of the band gap between occupied and empty framework state, the Fermi energy for spin-up electrons is located between the two spin-polarized Cu-4*s* states. The partial occupation of the spatially much more extended Cu-4*s* state is responsible for the low coordination (only two Cu-O bonds) of the Cu(I)-cation in the triplet state.

The delocalized character of the spin-distribution of Cu(I)-chabazite in the triplet state [configuration (1)], calculated using the PBE functional is shown in Fig. 6.5. The figure shows an extended spin-distribution of mixed Cu-4*s* and Cu-3*d* character at the cation and spin-polarized O-*p* states on the two activated oxygen atoms forming strong bonds with 3*d*-states of the cation.

It is important to note that the exchange-splitting of the 4*s*-state is modest in comparison of the 3*d*-band. Hence a change in the spin-orientation of the 4*s* electron (leading to the formation of an excited singlet state) will require only an excitation energy which is much smaller than that for the $3d \rightarrow 4s$ excitation.

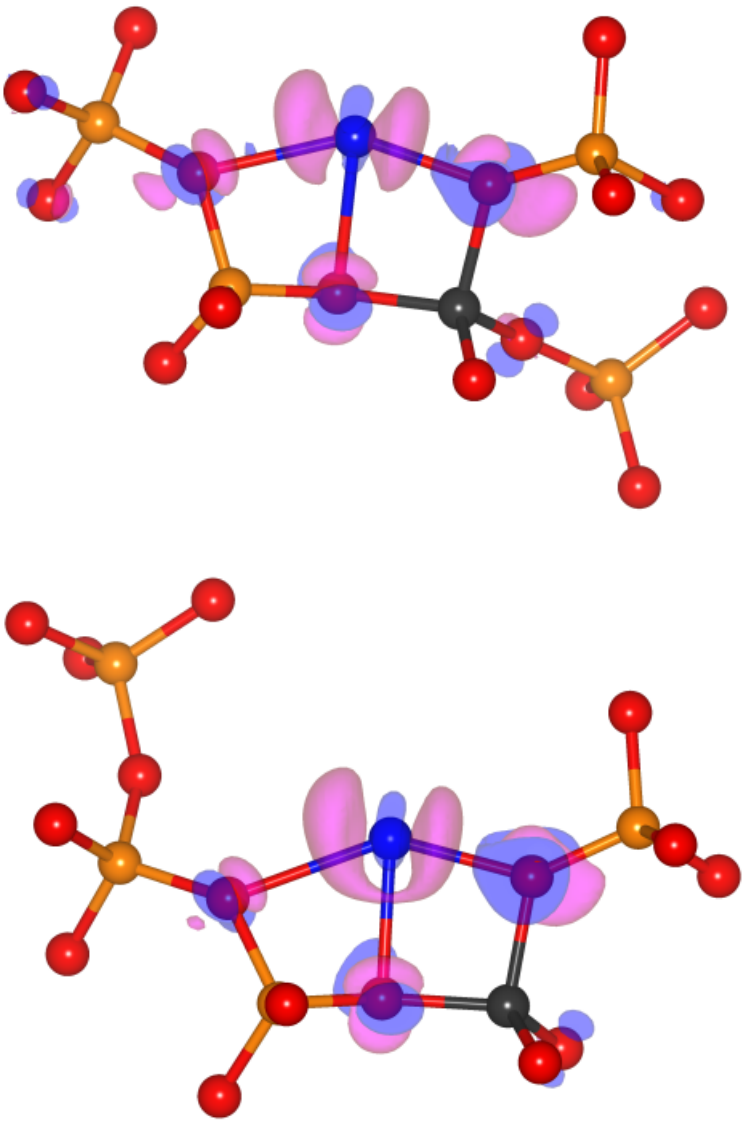

(a)

(b)

Figure 6.3: Difference-electron density around a Cu(I) cation located in a 8MR of chabazite [configuration (2)], calculated using the PBE (a) and PBE0 (b) functionals. Blue (light) constant-density surfaces surround electron-depleted regions, red surfaces regions of increased electron density. Contour values are $5{\times}10^{-3}$ electrons/Å^3.

(a)

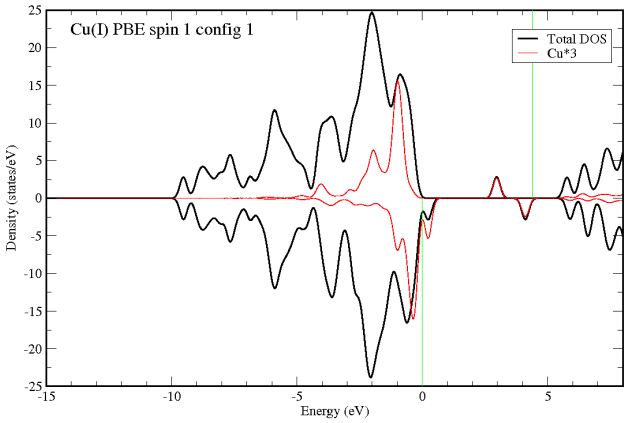

(b)

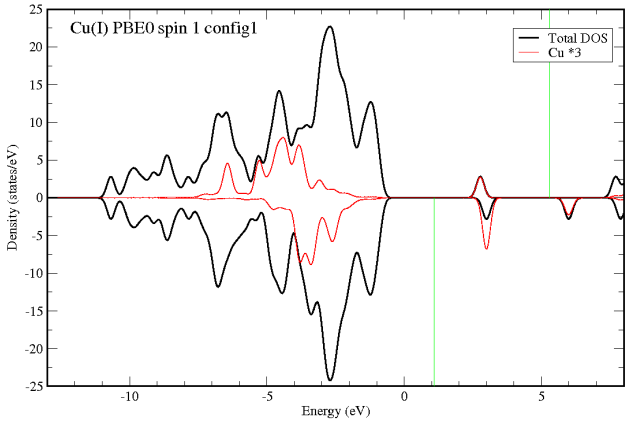

Figure 6.4: Electronic density of states (DOS) of Cu(I)-chabazite (total DOS and local DOS on the Cu-sites) in the excited state with S=1 ground state - calculated for configuration (1) with the cation in a 6MR containing two Al atoms, using the fixed-moment method and the PBE (a) and the PBE0 (b) functionals, respectively. Note that the fixed-moment method enforces the occupation of the majority $4s$ state and the formation of a hole in the minority $3d$ states and hence leads to different Fermi energies for spin-up and spin-down states as marked by the vertical lines. Cf. text.

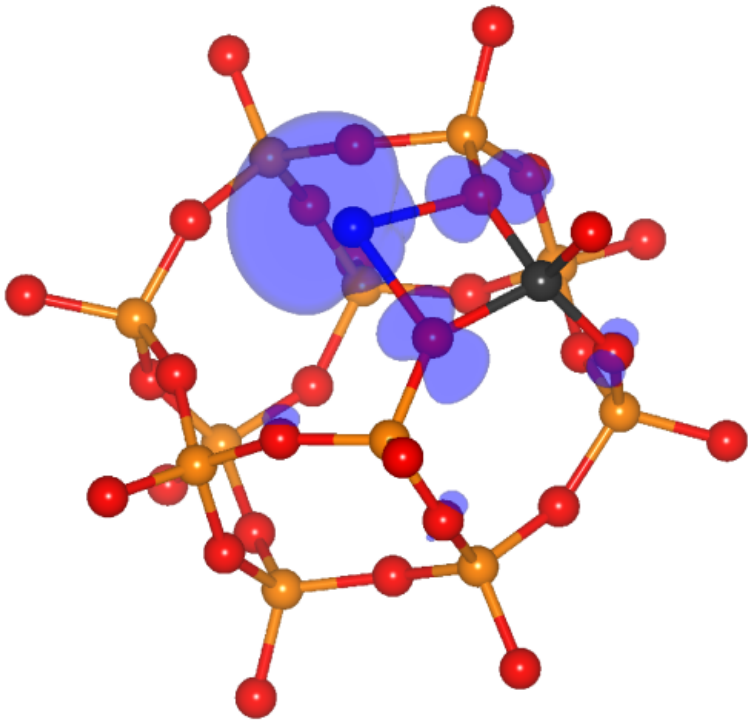

Figure 6.5: Spin-density distribution around a Cu(I) cation in the excited high-spin (triplet) state, located in a 8MR of chabazite [configuration (3)], calculated using the PBE functionals. Constant-density surfaces surround the atoms carrying a magnetic moment. Contour values are $5{\times}10^{-3}$ electrons/Å^3.

Cu(II)-chabazite

Ground state - spin doublet

For an extra-framework Cu particle compensating the electron deficit of two Al/Si substitutions on the framework, the formal ionic charge is 2+, the electron configuration is $3d^9$. The unpaired $3d$-electron has a spin of S=1/2 which is also the spin of the Cu(II)-chabazite system in its ground state. Although the geometries optimized with both types of functionals display only minor differences, the electronic spectra are very different. As an example the total DOS and the partial DOS on the Cu-site calculated with the PBE, PBE0 and HSE03 functionals are shown for configuration (3) of Cu(II)-chabazite in Fig. 6.6.

Calculations with a conventional GGA functional predict a relatively narrow, weakly spin-polarized Cu-3d band overlapping with the upper part of the valence band of the zeolite framework. A very weak spin-polarization is also induced on the framework. The broadening of the Cu-3d states of the isolated cation to a narrow band arises from the hybridization with framework O-2p states, forming bonding Cu-3d–O-2p states. The majority Cu(II)-3d states are fully occupied, the minority band is shifted to slightly lower binding energies such that a hole state distributed over cation and framework is located at the upper edge of the valence band. The empty Cu-4s state is located approximately in the center of the band gap. The exact location of the empty Cu-4s state for all configurations, calculated with different functionals is listed in Table 6.3. The weaker bonding of the Cu(II) cation located in a 8MR is reflected in a much lower distance of the Cu-s state from the VBM.

Calculations with the PBE0 hybrid functional show that the admixture of exact exchange leads to (i) an increased exchange splitting (as measured by the different positions of the center of gravity of the majority and minority 3d-states) and (ii) an increased splitting between occupied and empty d-states, resulting in a shift of the occupied Cu-3d states to larger binding energies close to the center of the valence band of the framework and of the empty Cu-3d and 4s states to energies farther above the valence-band edge [see Fig. 6.6(b)]. As a result, the empty minority 3d-states are now separated from the VBM by a gap of about 1.1 to 3.4 eV, the empty Cu-4s states are located 3.7 eV [configuration (6)] to 6.9 eV [configuration(1)] above the valence-band edge (detailed values are listed in Table 6.3). The screening of exact exchange in the HSE03 and HSE06 functionals reduces the gap between occupied and empty eigenstates, the empty minority 3d-states are now positioned closer to the VBM, the energies of the Cu-4s states are about 1 eV lower than calculated with the PBE0 functional.

A Bader analysis of the charge state of the extra-framework Cu(II) cation yields a positive charge of about +1 if GGA functionals are used, and of +1.3 with hybrid functionals. These charges are almost independent of the coordination of the extra-framework cation, for details see Table 6.2. The character of the non-spin-compensated states close to the Fermi-edge determines the spin-density distribution. Fig. 6.7 shows the spin-density in Cu(II)-chabazite [configuration (3)] as calculated with PBE and

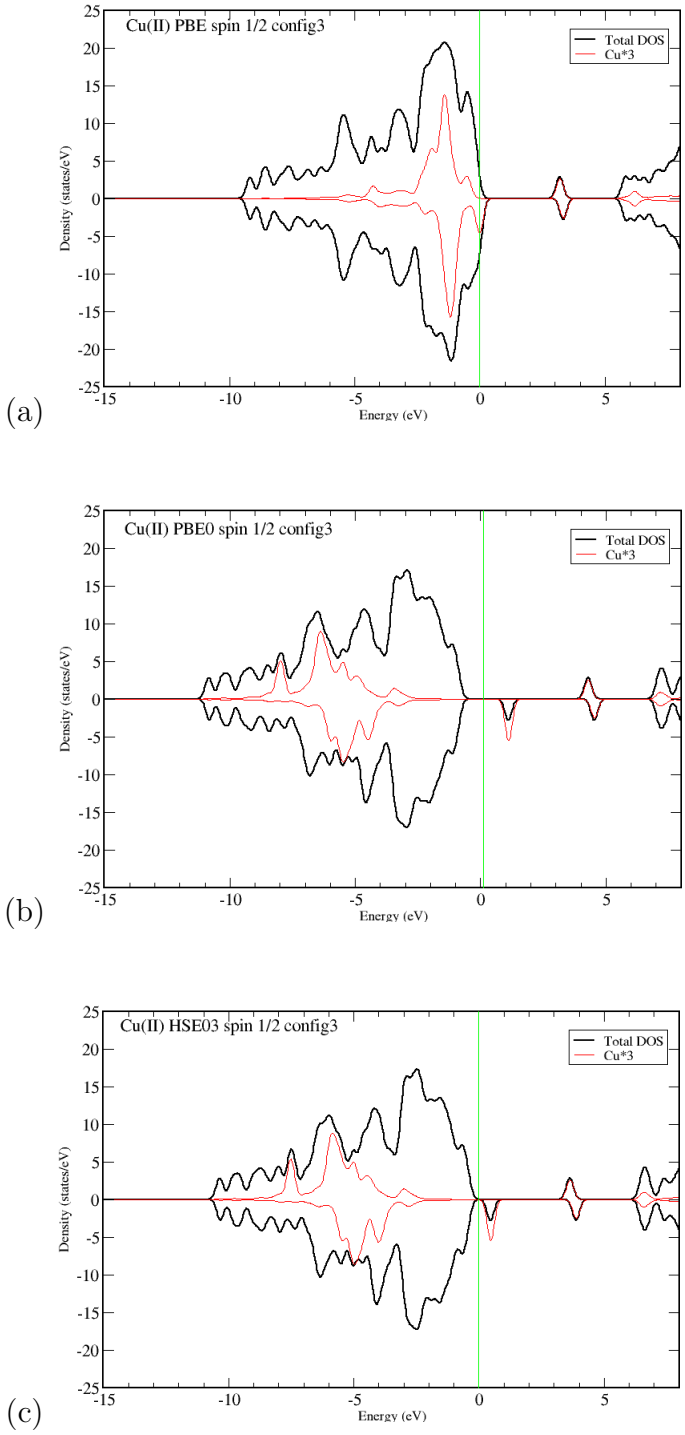

Figure 6.6: Electronic density of states (DOS) of Cu(II)-chabazite (total DOS and local DOS on the Cu-sites) - configuration (3) with the cation in a 8MR containing two Al atoms. The calculations have been performed using the PBE (a), PBE0 (b), and HSE03 (c) functionals. For better visualization, the partial Cu-DOS has been multiplied by a factor of three. Cf. text.

Table 6.3: Width of the energy gap between the valence-band maximum (VBM) and the empty Cu-3d and Cu-4s states located in the gap of Cu(II)-chabazite (in eV), for configurations (1) to (6), calculated with different exchange-correlation functionals.

	PW91	PBE	PBE0	HSE03	HSE06
VBM →	3d				
Config1	0.55	0.31	3.37	2.20	2.51
Config2	0.14	0.14	2.94	1.56	1.86
Config3	0.24	0.24	2.18	1.03	1.35
Config4	0.04	0.03	1.71	0.51	0.89
Config5	0.23	0.01	1.62	0.51	0.80
Config6	0.02	0.12	1.14	0.10	1.36
VBM →	4s				
Config1	4.46	4.40	6.95	5.84	6.12
Config2	4.11	4.01	6.42	4.95	5.24
Config3	3.22	3.16	5.17	4.03	4.33
Config4	3.09	3.00	4.55	3.49	3.78
Config5	2.51	2.56	4.09	3.02	3.29
Config6	2.52	2.49	3.72	2.96	3.29

HSE03 functionals. The spin-densities reflect the bonding eigenstate formed by Cu-d and O-p states, which is of a more localized character if a hybrid functional is used (note the spin-polarization of the O-atoms next to the second Al framework site which is not directly connected to the cation).

The important result of the foregoing analysis is that GGA calculations predict a non-zero DOS of Cu-3d states at the Fermi level, whereas with hybrid functionals the highest occupied Cu-3d-states are located about 2.5 eV below E_F and the lowest empty Cu-3d states about 0.1 to 3.4 eV above E_F, depending on the cation location and the screening of the exchange-correlation functional. As a consequence, the predicted chemical reactivity and adsorption capacity of a Cu(II)-cation will be much lower if hybrid functionals are used in the calculations.

Excited state - spin quadruplet

The formation of an excited high-spin state of Cu(II)-chabazite with S=3/2 formally requires the excitation of a spin-down electron to an empty spin-up state. However, because even in calculations with a conventional GGA functional, the occupied spin-down states of the Cu(II) cation have comparable or even larger binding energies than the highest framework states, the excitation proceeds not by the promotion of a spin-down Cu-3d electron, but by the creation of a hole in the spin-down bands of the framework. The DOS of the structurally relaxed high-spin state of Cu(II)-chabazite,

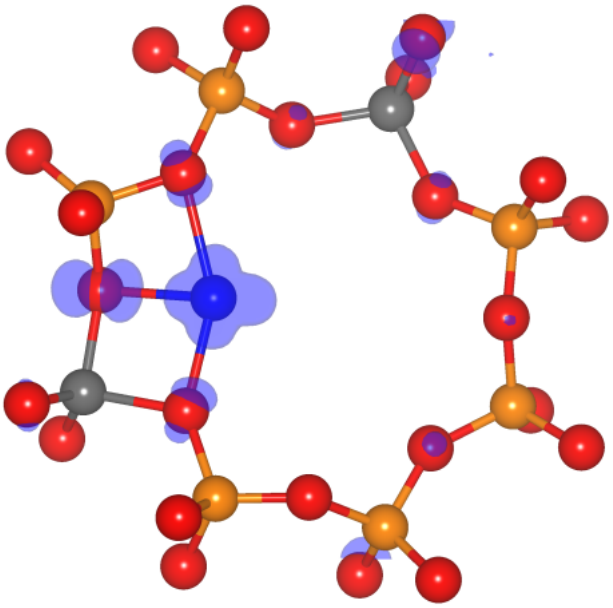

(a)

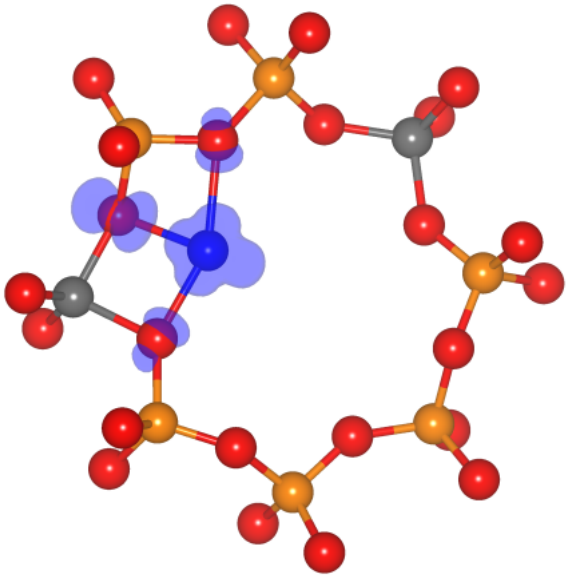

(b)

Figure 6.7: Spin-densities in Cu(II)-chabazite [configuration (3)], calculated with PBE (a) and HSE03 (b) functionals. The spin-density reflects the character of the bonding eigenstates consisting of a linear combination of Cu-*d* and O-*p* states located on the bonding oxygen framework sites. Spin-densities calculated with conventional and hybrid functionals are very similar, but also demonstrate a more de-localized character of the eigenstates calculated with conventional functionals.

calculated using the fixed-moment approach and the PBE and HSE03 functionals are shown in Fig. 6.8.

Irrespective of the cation configuration and of the choice of the functional, the total spin of S=3/2 is carried by an occupied Cu-4*s* spin-up state, and two holes in the spin-down a Cu-3*d* and framework valence states. The DOS for different cation locations and calculated using different functionals differ (i) in the position of the Cu-*d* states relative to the framework states, and (ii) the splitting between empty and occupied spin-down states. With conventional GGA functionals the spin-down Fermi level lies in a region of a high DOS of hybridized Cu-*d* and framework states, the spin-up Fermi-level lies in the gap between the spin-up and spin-down Cu-*s* states. With hybrid functionals, the empty spin-down framework state is separated by a small gap (or a deep DOS minimum) from the occupied states, the empty Cu-*d* states is shifted to higher energies in the gap.

The three components of the S=3/2 spin-distributions are shown in Fig. 6.9 at the example of configuration (1) and calculations with the HSE03 functional. The spin density distribution consists of (i) the occupied spin-up Cu-*s* state, (ii) the empty Cu-*d* spin-down state and (iii) the empty spin-down framework state. Even in calculations with a hybrid functional (which tend to produce more localized eigenstates) we find that the spin contributed by the hole in the valence band of the framework is very delocalized and distributed over many oxygen atoms.

An excited doublet state is created if the occupied 4*s*-state conserves the spin of the spin-down 3*d*-state. The excited doublet state will be higher in energy than the S=3/2 state by an energy roughly proportional to the exchange-splitting of the 4*s* state.

Co(II)-chabazite

Ground state - spin quadruplet

A Co(II)-cation with the formal charge 2+ has electron configuration d^7 and spin S=3/2. This is also the ground state for Co(II)-chabazite in all six configurations. As the coordination of the extra-framework Co(II) cations in chabazite is very similar to that of the divalent Cu(II) cations, the main differences in the electronic spectra arise from the increased exchange splitting. Fig. 6.10 shows as an example the electronic DOS for configuration (1) as calculated with the PBE, PBE0 and HSE06 functionals.

PBE calculations predict a fully occupied majority Co-*d* band located at the upper edge of the valence band of the framework. The minority states are split into a broad band centered at the Fermi level and a narrower band located within the energy gap. The Fermi level is located in a region with a high DOS of minority states. Calculations with the PBE0 hybrid functional predict a shift of the occupied majority Co-*d* states to higher binding energies and a splitting of about 3 to 5 eV between the occupied and empty minority states, depending on the location of the cation. The Fermi level is now located in the wide gap between the occupied bonding and empty antibonding states. With a screened hybrid functional the empty Co-*d* states are located at lower energies within the gap.

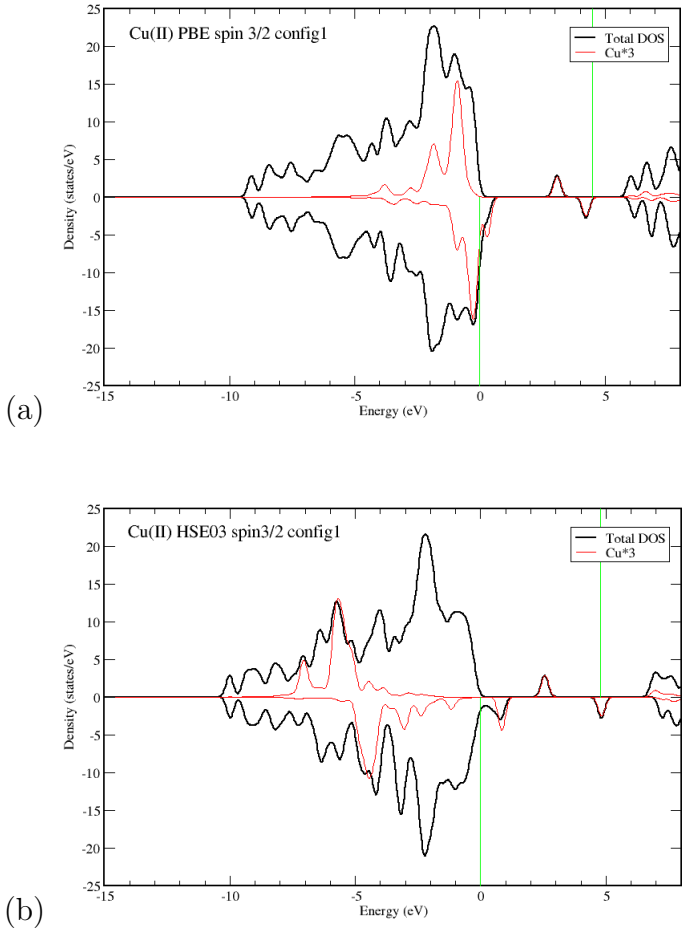

Figure 6.8: Electronic density of states (total DOS and local DOS) of Cu(II)-exchanged chabazite in the high-spin state with S=3/2 - configuration (1) with the cation in a 6MR containing two Al atoms. The calculations have been performed using the fixed-moment method and the PBE (a) and HSE03 (b) functionals. For better visualization, the partial Cu-DOS has been multiplied by a factor of three. Cf. text.

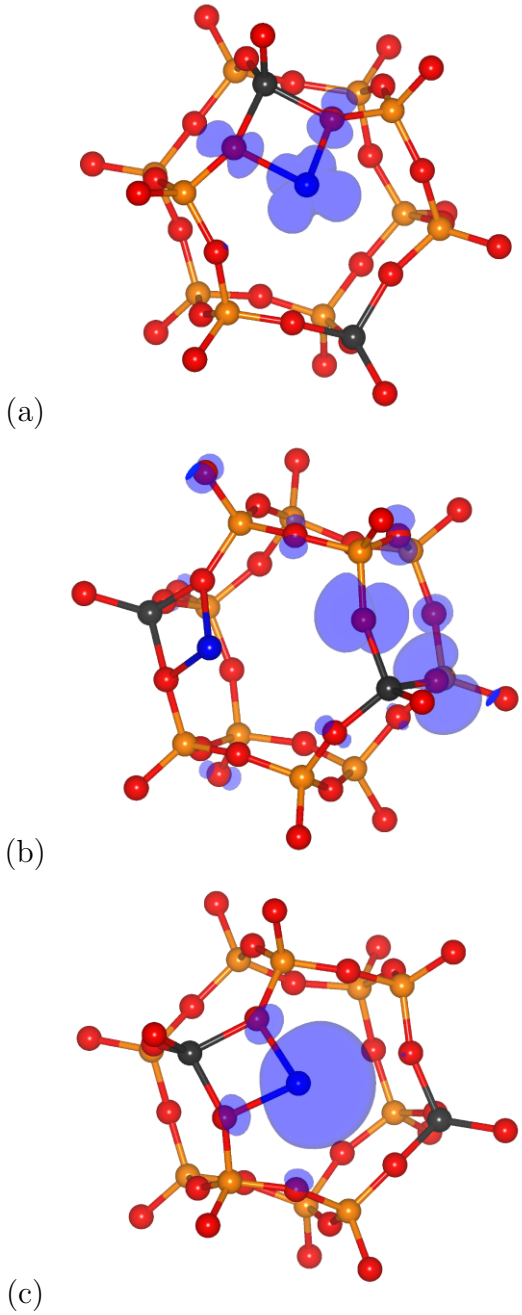

Figure 6.9: Contributions to the spin-density distribution around a Cu(II) cation located in a 6MR of chabazite [configuration (1)] in the high-spin state, located in a 6MR of chabazite [configuration (1)], calculated using the HSE03 functional. (a) Spin-density of the empty Cu-3*d* spin-down state, (b) spin-density of the empty spin-down framework state, and (c) spin density of the occupied spin-up Cu-4*s* state. Blue (light) constant-density surfaces are shown for a density of $5{\times}10^{-3}$ electrons/Å^3.

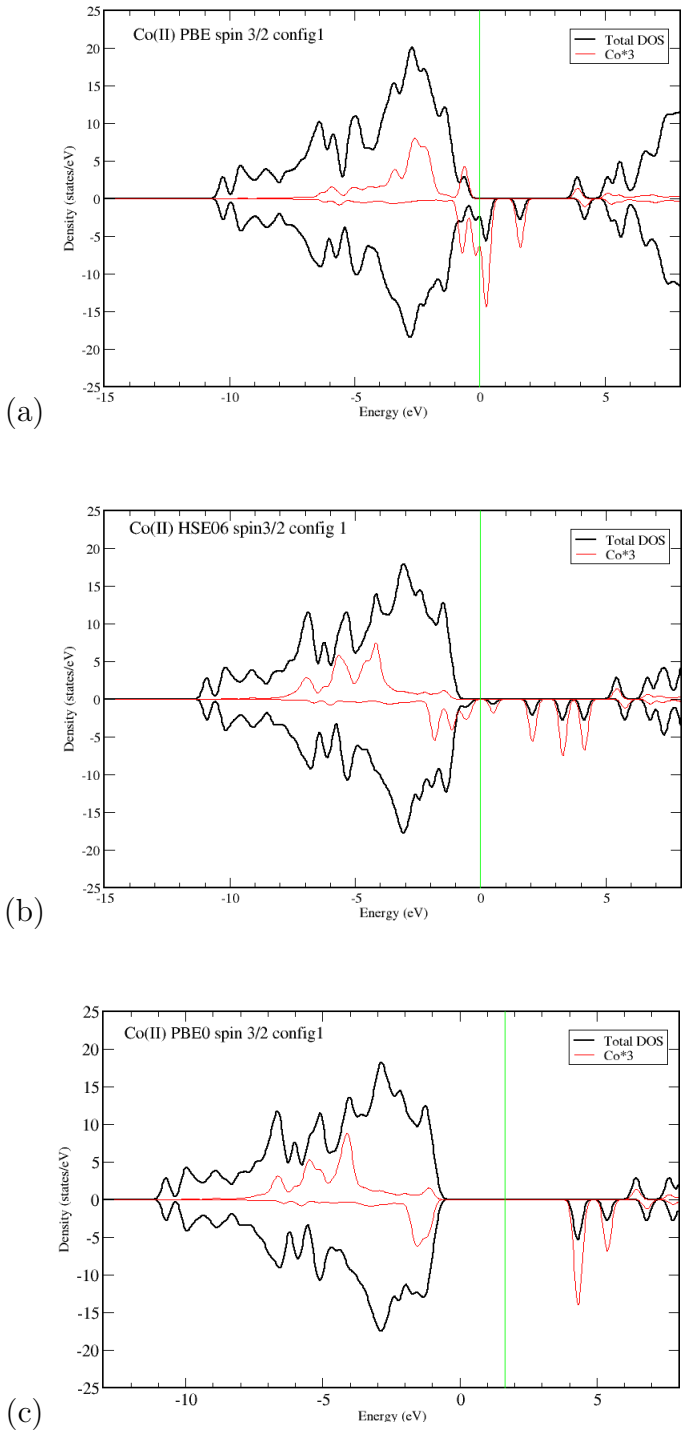

Figure 6.10: Electronic density of states (DOS) of Co(II)-chabazite (total DOS and local DOS on the Cu-sites) - configuration (1) with the cation in a 6MR containing two Al atoms. The calculations have been performed using the PBE (a), HSE06 (b) and the PBE0 (c)functionals. For better visualization, the partial Cu-DOS has been multiplied by a factor of three. Cf. text.

Calculations with GGA functionals predict also only a modest variation of the DOS with the location of the cation: independent of the configuration the highest occupied majority Co-*d* state is always close to the upper edge of the framework band, and the band of minority states overlaps with the Fermi level. In contrast, the location of the cation states with respect to the framework varies appreciably in calculations with PBE0 functional. For configuration (1) the highest occupied majority and minority Co-*d* states coincide with the edge of the valence band of the zeolite framework. In configuration (2) (with only one Al in the 6MR) the highest occupied Co-*d* states are about 1 eV below the VBM, in configurations (3) to (6) with the cation in a 8MR the energy difference increases to about 2 eV. As the gap between the occupied and empty Co-*d* minority states is about the same in all six configurations, the gap between the VBM and the lowest empty Co-*d* in the gap is reduced accordingly.

The Bader analysis yields an effective charge of about +1.3 (GGA) and +1.5 (hybrid functionals) for the cation, see Table 6.2 for details. The charge-redistribution is illustrated in Fig. 6.11. Not only is charge transferred from the cation to the surrounding framework oxygen atoms, both the *d*-states of the cation and the *p*-states of the oxygen atoms are polarized. On the cation the positive charge leads to an increased electron density close to the nucleus and to a charge depletion at larger distances. On the oxygen atoms charge is transferred between different *p* states, increasing the overlap with the cation *d*-states and promoting a stronger bonding of the cation to the framework.

Thus we find that hybrid functionals influence the two divalent cations in chabazite to a very different extent. In Cu(II)-chabazite the splitting of the *d*-states in the field of the ligands leads to a vanishing DOS of *d*-states close to the Fermi level and hence to a reduced reactivity of the Lewis-site if hybrid functionals are used. In Co(II)-chabazite the change in the DOS caused by the admixture of exact exchange is generally the same, but because also the exchange splitting is increased, occupied minority *d*-states are found at the upper edge of the valence band. Hence we expect the influence of the choice of the functional on the chemical reactivity of the Lewis site to be less pronounced.

The spin-densities introduced by the two transition-metal cations are also quite different. Whereas for Cu(II) all bonding oxygen atoms on the framework are spin-polarized to some degree, for Co(II) the spin is much more localized on the cation. This is illustrated in Fig. 6.12 which shows that only the oxygen atom forming the strongest bond to the cation is weakly spin-polarized.

Excited low- and high-spin states

An excited low-spin state with S=1/2 (singlet) of the Co(II) cation can be formed by transferring the electron occupying the highest spin-up Co-*d* state into the empty spin-down state with the lowest energy. In the DOS calculated with GGA functionals (see Fig. 6.10) the minority Co-*d* band overlaps with the Fermi level, a low-spin state hence has only modest energy difference relative to the S=3/2 ground state of 0.3 to 0.6 eV. Calculations with hybrid functionals predict a location of the lowest empty minority Co-*d* states at energies between 0.5 and 5 eV above the VBM (depending

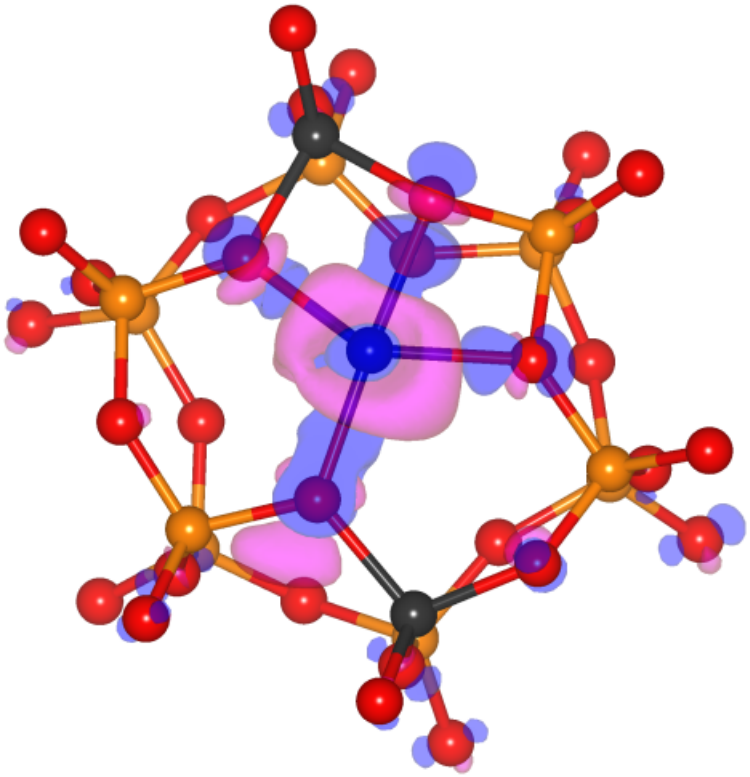

Figure 6.11: Difference-electron density around a Co(II) cation located in a 6MR of chabazite with two Al atoms [configuration(1)]. Blue (light) constant-density surfaces surround electron-depleted regions, red surfaces regions of increased electron density. Contour values are 5×10^{-3} electrons/Å^3.

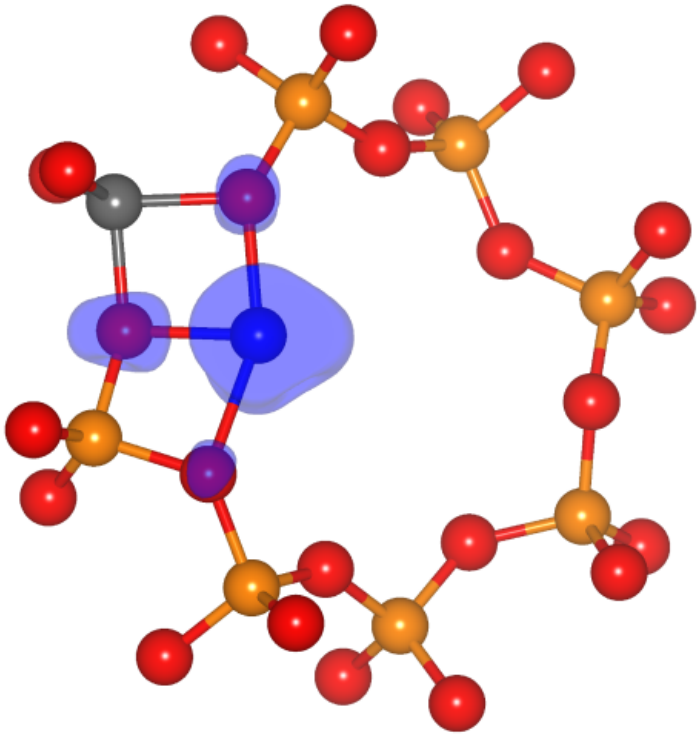

Figure 6.12: Spin-densities in Co(II)-chabazite [configuration (5)], calculated with the PBE functional. The spin-density is concentrated on the cation, the almost spherical spin-density contour shows that different *d*-orbital contribute to the spin-polarized eigenstate. Contour values are 5×10^{-3} electrons/Å^3.

strongly on the screening of the exchange kernel), but still modest energy differences of the relaxed S=1/2 state relative to the ground state of about 1 eV (for details, see I). This suggests strong electronic relaxation effects. Like for all excited spin-states, the calculations for the low-spin state of Co(II)-chabazite have been performed using the fixed-moment method. However, in contrast to the other excited spin states where different Fermi energies for spin-up and spin-down states are required to achieve the chosen total spin moment, for the S=1/2 state of Co(II)-chabazite the calculations converge to a metastable spin configuration with a common Fermi energy for spin-up and spin-down states. The DOS shown in Fig. 6.13 demonstrates that for GGA functionals this is achieved by an almost rigid shift of the majority Co-3*d* states to lower binding energies such that the highest state is now unoccupied, and a shift of the minority Co-3*d* states to larger binding energies such that now three and not only two states are occupied. The shift of the majority Co-3*d* band significantly reduces its hybridization with the framework states. Calculations with hybrid functionals show a similar picture, but the majority Co-3*d* states are shifted by a much larger amount, placing both occupied majority and minority Co-states at the upper edge of the valence band of the framework. GGA calculations locate the empty Co-3*d* states just above the Fermi energy, hybrid functionals predict a gap of about 4 eV between the VBM and the empty states.

The formation of an excited high-spin state with S=5/2 requires the transfer of a spin-down electron into a spin-up state - which can be only a Co-4*s* state. The DOS calculated with the fixed-moment method is shown in Fig. 6.14. Calculations with GGA functionals predict shifts of the majority and minority Co-3*d* bands in opposite directions such that the fully occupied majority states are located at the center of the chabazite valence band, whereas the only occupied minority state is located at the VBM, with the empty Co-3*d* states immediately above the Fermi energy and the occupied Co-4*s* state 3.8 eV above. Because hybrid functionals predict a strongly increased splitting of occupied and empty states, the occupied majority Co-3*d* states fall almost at the bottom of the valence band, the single occupied minority Co-3*d* state close to the center of the band is strongly broadened by hybridization with the framework. The empty minority states form a narrow band separated from the VBM. The drastic changes in the electronic structure reflect the large energy difference between the high-spin and the ground state (see I for details).

6.5 Photoluminescence Spectroscopy of Electronic Excitations

The energy of the excited photons used in photoluminescence or diffuse reflectance experiments on transition-metal exchanged zeolites lies in the ultraviolet (UV), visible (vis), or near-infrared (NIR) range. This is usually much lower than the width of the energy gap of the purely siliceous host lattice. In this case the electronic transitions related to the photoluminescence energies measured in adsorption or emission must occur

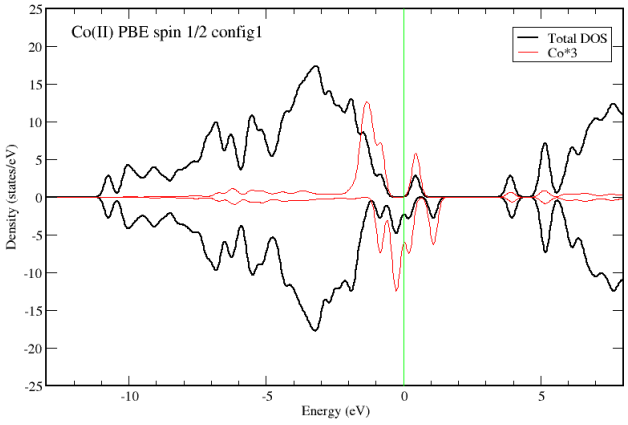

(a)

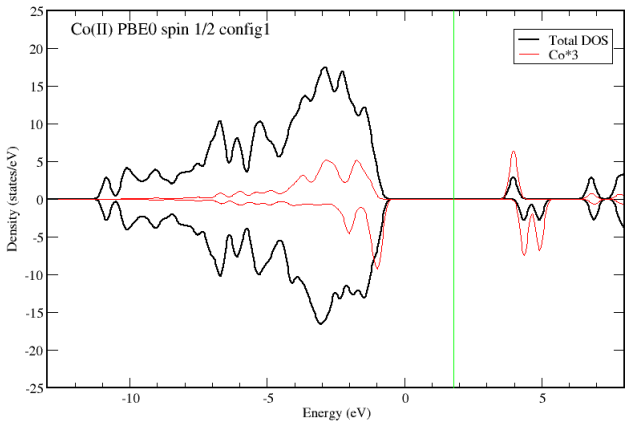

(b)

Figure 6.13: Electronic density of states (DOS) of Co(II)-chabazite (total DOS and local DOS on the Cu-sites) in the low-spin state with S=1/2 for configuration (1) with the cation in a 6MR containing two Al atoms. The calculations have been performed using the PBE (a) and the PBE0 (b) functionals. For better visualization, the partial Cu-DOS has been multiplied by a factor of three. Cf. text.

(a)

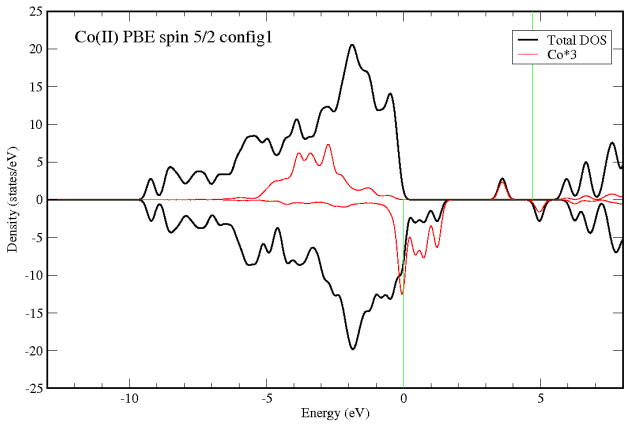

(b)

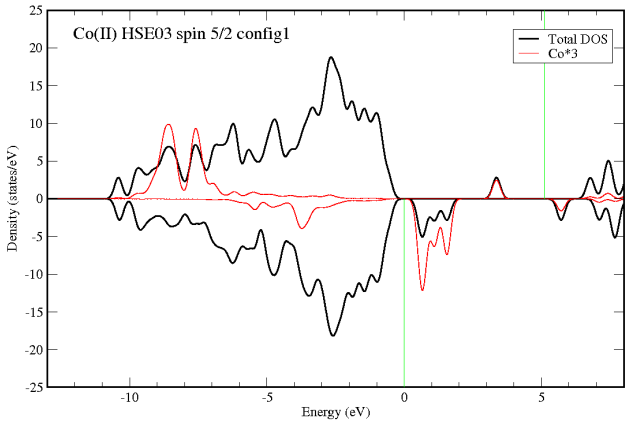

Figure 6.14: Electronic density of states (DOS) of Co(II)-chabazite (total DOS and local DOS on the Cu-sites) in the high-spin state with S=5/2 for configuration (1) with the cation in a 6MR containing two Al atoms. The calculations have been performed using the fixed moment method and the PBE (a) and the HSE03 (b) functionals. The different Fermi energies for majority and minority states are marked by the vertical lines. For better visualization, the partial Cu-DOS has been multiplied by a factor of three. Cf. text.

between the ground state and empty eigenstates within the gap created by the presence of the extraframework cation. Theoretical calculations of the photoluminescence energies are usually based on cluster calculations of the splitting of the d-states of the cation in the ligand-field of the surrounding oxygen framework atoms.[122, 123, 142] Within our approach based on periodic band-structure calculations this corresponds to the calculation of differences between one-electron energies of empty and occupied eigenstates. In both cases the underlying assumption is that the excitation does not induce a relaxation of the electronic and/or atomic structure, i.e. that Koopmans theorem applies. A consequence of this assumption is that the same energies should be measured in both excitation (absorption) and emission. An important difference between both approaches is, however, that ligand field theory admits only $d-d$ transitions between eigenstates of the cation whereas band theory considers the energy of the cation-states relative to the framework bands and the possibility that a charge-transfer transition from a framework oxygen to the cation may occur at an even lower energy.

Lamberti *et al.*[121] seem to have been the first to point our that the measured absorption and emission wavelengths can be significantly different. They explained the observed difference by changes in the first coordination shell of the extraframework cation. Following this suggestion Nachtigall *et al.* [150] performed calculations of excitation and emission energies accounting for the electronic and structural relaxation of Cu(I)-ZSM5 in the singlet ground state and in the excited triplet state. In the following we shall present a comparative discussion of both approaches applied to the interpretation of the photoluminescence data of Cu- and Co-exchanged chabazite.

DRS spectrum of Cu(I)-Chabazite

DRS UV-vis spectra for Cu(I)-chabazite have been reported by Dědeček *et al.*[172]. The experiment was performed on Cu(II)-exchanged chabazite reduced in hydrogen or carbon monoxide and it was estimated that 90% of the Cu cations are in the monovalent state. Two different Cu(I) emission bands with intensity maxima at 2.48 eV (500 nm) and 2.29 eV (540 nm) have been reported. Only the band at higher energy was detected at low Cu(I) loading, it was attributed to three-coordinated cations located in the 6MR, while the emission band at lower energy was assigned to cations located in a 8MR. This assignment is also supported by the observation that the presence of large co-cations (Cs^+, Ca^{2+}) blocking the site in the 6MR eliminates the band at 2.48 eV. However, it has to be emphasized that the energies of the emission bands were determined by fitting two Gaussian bands to a broad, slightly asymmetric emission spectrum. The width of both Gaussians is larger than the separation of the two bands.

Our calculations of the electronic structure of Cu(I)-chabazite have demonstrated that, independent of the location of the cation and of the choice of the exchange-correlation functional, both the fully occupied Cu-3d states and the empty Cu-4s state are located within the energy gap of purely siliceous chabazite. Cation location and functional influence only the energy difference for the $3d \rightarrow 4s$ excitation which varies between 3.3 eV [configuration(1) in the 6MR] and 2.2 eV [configuration (3) in a 8MR] in calculations with the PBE functional, and between 5.8 eV and 4.8 eV

for the same configurations with the PBE0 hybrid functional (for a complete list of all energy differences, see Table 6.1). These transition energies are much larger than those observed experimentally, and in I we have also shown that the cation coordination (especially of a cation located in the 6MR) chances significantly in the triplet state created by the $3d \rightarrow 4s$ excitation.

Following Nachtigall *et al.*[150] vertical $S_0 \rightarrow T_1$ excitation energies were calculated as the energy-difference between the triplet and singlet states at singlet-optimized structures. Vertical $T_1 \rightarrow S_0$ emission energies are determined by the energy difference between triplet and singlet states, calculated at triplet-optimized geometries. Our results are compiled in Table 6.4. The results may be summarized as follows: (i) Excitation energies are always much higher than emission energies. The difference is largest for the Cu(I) cation in the 6MR which is fourfold coordinated in the ground state, but only twofold coordinated in the excited state. It is much lower for configurations (2) and (3) with the cation in a 8MR were the excitation induces only a modest change in the local geometry. (ii) The choice of the functional has only a modest influence on the calculated excitation and emission energies. In this respect the Cu(I)-cation seems to be a special case, because the spin-densities associated with the unpaired electron in the $4s$ state are rather delocalized. (iii) Excitation energies vary between 2.20 eV and 3.60 eV (PBE), and 2.22 eV and 3.52 eV (PBE0) - the highest excitation energy is calculated for the cation located in the 6MR. (iv) The emission energies predicted by our calculations range between 2.07 and 2.16 eV (GGA) and 1.96 and 2.00 eV (hybrid functionals). The emission energies are only slightly larger for configurations (1) and (2) than for configuration (3), because the larger energy difference between the relaxed spin-states of the cation located in the 6MR is compensated by larger relaxation effects. (v) Although the calculated emission energies are lower by about 0.3 eV than the experimental values, the comparison demonstrates that both electronic and structural relaxation must be considered in the theoretical interpretation of the photoluminescence data.

The DRS spectra of Cu(I)-chabazite may be compared with those of other Cu-exchanged zeolites. For Cu(I)-ZSM5 Lamberti *et al.*[121] reported the existence of two predominant emission peaks at 2.53 eV and 2.32 eV and two excitation bands at 4.13 eV and 4.84 eV. In agreement with the assignment of Dědeček *et al.* for Cu(I)-chabazite, the high-energy bands (both emission and excitation) were attributed to three-coordinated Cu(I) cations, and the low-energy bands to two-coordinated species. For the same zeolite Dědeček *et al.*[173] reported emission bands centered at 2.58 eV and 2.29 eV, assigned to Cu(I) cations adjacent to two and one Al on tetrahedral sites, respectively. Nachtigall *et al.*[150, 174] have calculated the transition energies for the singlet-triplet transitions (at singlet-optimized geometries) and the triplet-singlet transitions (at triplet-optimized geometries) for various DFT-optimized cluster models of cation sites in Cu(I)-ZSM5, using the B3LYP hybrid functional. Emission energies varying between 1.88 and 2.34 eV, and excitation energies between 2.10 and 3.72 eV were reported. For the excitation energies a pronounced correlation with the number of Cu-O bonds exists - the highest excitation energies were found for cations coordinated to three to four framework oxygens. No such correlation exists for the emission

Table 6.4: Excitation and emission energies [in eV] between the ground state and the lowest excited spin state in Cu(I)- and Cu(II)-chabazite. Cf. text

	PW91	PBE	PBE0	HSE03	HSE06
Cu(I)-$S_0 \rightarrow T_1$					
Config 1	3.64	3.60	3.52	3.81	3.67
Config 2	2.81	2.77	2.50	2.62	2.46
Config 3	2.24	2.20	2.22	2.31	2.15
Cu(I)-$T_1 \rightarrow S_0$					
Config 1	2.15	2.11	1.97	1.99	1.99
Config 2	2.16	2.12	1.99	2.00	2.01
Config 3	2.11	2.07	1.96	1.98	1.97
Cu(II)-$D_{1/2} \rightarrow Q_{3/2}$					
Config 1	4.90	4.86	6.17	6.30	6.40
Config 2	4.38	4.27	5.60	5.54	5.41
Config 3	3.49	3.45	4.60	4.64	4.57
Config 4	3.31	3.24	4.16	4.18	4.18
Config 5	3.97	3.96	4.50	4.44	4.51
Config 6	3.48	3.43	4.51	4.43	4.49
Cu(II)-$Q_{3/2} \rightarrow D_{1/2}$					
Config 1	2.61	2.60	2.16	2.22	2.17
Config 2	2.63	2.60	2.17	2.29	2.26
Config 3	2.67	2.62	2.15	2.21	2.17
Config 4	2.56	2.51	2.12	2.18	2.17
Config 5	2.50	2.46	2.05	2.19	2.10
Config 6	2.44	2.39	2.01	2.07	2.04

energies. These conclusions are also supported by our results, and the calculated emission energies are also lower than experiment (especially those calculated with hybrid functionals because the admixture of Hartree-Fock exchange increases the exchange splitting and favors the formation of high-spin states).

Nachtigall *et al.* argued that the measured excitation energies represent the excited $3d^9 4s^1$-singlet state (which cannot be determined by a fixed-moment method). An estimated energy of 0.2 to 0.3 eV for the singlet-triplet splitting would lead to full agreement of the emission energies calculated in the GGA with experiment. For the hybrid functionals a slightly larger energy of 0.3 to 0.4 eV is required - this agrees with the larger exchange-splitting of the $4s$ state induced by the addition of exact exchange. In summary both types of functionals seem to perform equally well.

DRS spectra of Cu(II)-Chabazite

Korhonen *et al.*[157] have reported DRS spectra for Cu(II)-chabazite showing broad maxima at 1.49 eV (assigned to $d - d$ transitions) and about 5.88 eV (attributed to electron transfer from oxygen to Cu). A similar spectrum has been reported by Groothaert *et al.*[175] for Cu(II)-ZSM5 with a low Cu/Al ratio, and by Smeets *et al.*[176] for a variety of Cu-exchanged zeolites (faujasite, mordenite, ferrierite, ..). DRS bands in the energy range around 1.5 eV and assigned to $d - d$ transitions have also been reported for other Cu(II) zeolites (MFI, Y, X, faujasite, mordenite).[142, 123] The bands around 1.5 eV were de-convoluted into a set of three bands with maxima in the energy ranges 1.29 - 1.55 eV, 1.51 - 1.70 eV, and 1.82 - 1.91 eV assigned, on the basis of cluster calculations, to various cation configurations in a 6MR of the zeolite containing a different number of Al atoms. In the energy range between the bands assigned to $d - d$ and charge-transfer transitions after calcination in O_2 an intense feature assigned to an oxygen-bridged di-cooper cluster was reported. However, the possibility of the formation of cluster cations was not considered here.

In the electronic DOS calculated using a conventional GGA functional the Cu-3d states are located close to the Fermi level, with the highest unoccupied minority state located just above E_F. For all cation locations, a $d - d$ transition, from the highest occupied majority to the lowest empty minority state (and hence changing the sign, but not the magnitude of the spin) is possible with an excitation energy of between 0.05 and 0.5 eV. Calculations with a PBE0 hybrid functional predict a different picture: the admixture of Hartree-Fock exchange induces a splitting of 3 to 4 eV between the occupied and empty minority Cu-3d states, placing the highest occupied state at about 2 eV below the valence band maximum and the empty Cu-d state at 1.5 to 2.5 eV above. In this case the lowest possible excitation energy for an electronic transition is from a framework state at the valence band edge to the empty Cu-d state, i.e. for a charge-transfer transition from a framework oxygen atom to the Cu(II)-cation which is reduced to Cu(I). Depending on the cation location the difference in the one-electron energies vary between 1.1 eV [configuration (6) in a 8MR] and 3.4 eV [configuration (1) in the 6MR], for details see Table 6.3. Screened hybrid functionals (HSE03 and HSE06) reduce the distance between the VBM and the empty Cu(II)-3d state to 0.5 to 2.5 eV (see Table 6.3). Hence screened hybrid functionals predict for the most probable configurations (1) and (2)transition energies in good agreement with the photoluminescence data, although the transitions are assigned to O $\rightarrow$ Cu charge transfer and not to direct $d - d$ transitions. Admittedly, this interpretation neglects electronic as well as structural relaxations, but this seems to be legitimate for these low transition energies.

The DRS maximum at about 5.9 eV may be assigned to transitions to a high-spin state with S=3/2. The energies of the DRS excitation and emission bands are determined by the vertical $D_{1/2} \rightarrow Q_{3/2}$ transition energies at the doublet-optimized structures, and of the emission energies for the vertical $Q_{3/2} \rightarrow D_{1/2}$ transitions at the quadruplet-optimized geometries. We find larger differences between the excitation and emission energies and, especially for cations in the 6MR [configurations (1) and (2)],

also a pronounced influence of the choice of the functional (see Table 6.4). Excitation energies calculated using hybrid functional range between 4.5 and 6.3 eV, they are larger by $\sim$ 0.50 to $\sim$ 1.50 eV than those calculated using GGA functionals. In contrast, emission energies are lower if calculated using hybrid functionals (2.05 to 2.2 eV), compared to 2.4 to 2.6 eV with conventional GGA functionals. For both types of functionals we find only a weak dependence of the emission energies on the cation location. This reflects the fact that structural relaxations in the excited high-spin state are much more pronounced with hybrid functionals. Compared to Cu(I)-chabazite, excitation energies are strongly increased by up to 2.6 eV (especially those calculated using hybrid functionals), while emission energies are increased by much smaller amounts. As for Cu(I) we note a strong dependence of the excitation energies on the coordination of the cation, whereas the emission energies depend much less on the cation configuration.

The excitation energies for the most stable configurations 81) and 82) calculated using hybrid functionals for the S=1/2 $\rightarrow$ S=3/2 transition are in good agreement with the DRS maxima reported by Korhonen *et al.*[157]. The excitation involves a transfer of an electron from the valence band of the chabazite framework to the spin-polarized Cu-4*s* state - hence the assignment of the DRS maximum to a charge-transfer excitation is confirmed by our calculations. GGA functionals predict excitation energies which are about 1 eV lower than experiment, in line with the general trend of DFT to underestimate electronic excitation energies.

DRS Spectra of Co(II)-Chabazite

DRS measurements in the visible range have been performed by Dědeček *et al.*[177]. The spectrum consists of a broad, asymmetric band extending between 14000 cm^{-1} and 22000 cm^{-1} which can be de-convoluted into five Gaussians centered at 14800 cm^{-1} (1.84 eV), 15200 cm^{-1} (1.89 eV), 17200 cm^{-1} (2.13 eV), 19200 cm^{-1} (2.38 eV) and 20700 cm^{-1} (2.57 eV). Dědeček and co-workers have also reported DRS-vis spectra for a number of other Co-exchanged zeolites: mordenite [178], ZSM5[179], ferrierite[124, 169], beta[170]. The DRS bands cover the same energy range, they have been de-convoluted into a series of Gaussian. The lowest emission band has been attributed to Co(II) cations located in α-sites (cation coordinated to four oxygens at the wall of a channel formed by 10MR's), the bands at medium energies to β-sites (cations located in deformed 6MR's), those with the highest energies to γ sites (cation in complex "boat-shaped" sites).

The energies for spin excitations visible as adsorption or emission peaks in the photoluminescence spectra have been calculated as the total energy differences (relative to the quadruplet state with S=3/2 for doublet (S=1/2) and sextet (S=5/2) states at the frozen geometry of the quadruplet relaxed state. Energies for emission peaks have been calculated as the energy difference between the doublet and quadruplet states with the doublet-relaxed geometry and between the sextet and quadruplet states at the sextet-relaxed geometry. Results are compiled in Table 6.5.

For the transition to or from a low-spin state differences in excitation and emission

energies are modest, reflecting the very small changes in the cation coordination. With a PBE functional we calculate excitation energies between about 0.55 and 0.77 eV and emission energies between about 0.25 and 0.52 eV. A PBE0 functional yields excitation energies between 0.95 and 1.08 eV, and emission energies between 0.87 and 0.92 eV. DRS adsorption bands in the range from 0.77 to 1.11 eV have been reported for various Co-exchanged zeolites.[122, 178]. These energies correspond rather well to the excitation energies for low-spin states calculated using hybrid functionals. However, it has also been pointed out that the interpretation of the experimental spectra in this range is difficult because of the overlap with absorption bands of framework OH groups.

The assignment of the bands in the visible range is more difficult. Excitation energies calculated using hybrid functionals are much larger than those derived in the GGA, while emission energies are higher if the GGA is used. This reflects the stronger relaxation effects discussed in I. The emission energies calculated using GGA functionals for the high-spin state with S=5/2 range for configurations (2) to (6) between 2.44 and 1.92 eV, in good agreement with the DRS data.[177] Only for configuration (1) with two Al atoms in the 6MR occupied by the cation a much too high emission energy is calculated. This would mean that although the configuration (1) is the energetically most favorable one, it is not or only rarely realized in a low-Al chabazite with Al/Si=11. Calculations with hybrid functionals produce too low emission energies for configurations (2) to (6). This reflects the preference for high-spin states characteristic for hybrid functionals. Only for configuration (1) an even higher emission energy is calculated.

6.6 Discussion

We have presented a detailed investigation of the influence of the choice of an exchange-correlation functional (conventional gradient-corrected or hybrid functional) on the electronic structure of purely siliceous and metal-exchanged chabazite in the ground-state and in excited spin-states. The results have been used to interpret the photoluminescence (diffuse reflectance) spectra measured for the metal-exchanged chabazite which have been widely used to determine the cation locations in the zeolite. In this analysis we have used two very different approaches. In analogy to ligand-field theory of the eigenvalue spectra of the cations in the field of the coordinating oxygen atoms we have compared the measured photoluminescence peaks with the eigenvalue spectrum of $3d$ and $4s$ states of the transition-metal cation bound in the periodic model zeolite - this approach assumes that upon excitation the system undergoes neither an electronic nor a structural relaxation. Alternatively, the excitation and emission energies have been confronted with total energy differences between excited spin states which fully account for electronic and structural relaxation.

For the purely siliceous zeolite the admixture of Hartree-Fock exchange in hybrid functionals leads to an increase of the predicted width of the fundamental gap from 5.5 eV (PBE, PW91) to 8.0 eV (PBE0 functional). A screening of the exchange kernel

Table 6.5: Excitation and emission energies [in eV] between the ground state and the excited spin states in Co(II)-chabazite. Cf. text

	PW91	PBE	PBE0	HSE03	HSE06
Co(II)-$Q_{3/2}$ →$D_{1/2}$					
Config 1	0.45	0.55	0.98	1.15	1.02
Config 2	0.70	0.77	1.08	1.24	1.10
Config 3	0.58	0.61	1.03	1.19	1.03
Config 4	0.54	0.64	1.00	1.14	1.01
Config 5	0.47	0.56	0.95	1.11	0.95
Config 6	0.52	0.55	0.98	1.13	0.96
Co(II)-$D_{1/2}$ → $Q_{3/2}$					
Config 1	0.20	0.26	0.78	0.75	0.80
Config 2	0.18	0.25	0.79	0.79	0.78
Config 3	0.51	0.52	0.92	0.82	0.93
Config 4	0.47	0.51	0.91	0.91	0.91
Config 5	0.45	0.47	0.87	0.76	0.87
Config 6	0.43	0.48	0.87	0.88	0.89
Co(II)-$Q_{3/2}$ → $S_{5/2}$					
Config 1	4.31	4.66	5.91	6.06	5.48
Config 2	4.05	4.09	5.23	5.47	5.01
Config 3	3.21	3.21	4.30	4.37	4.27
Config 4	3.01	3.04	4.44	4.56	4.41
Config 5	3.23	3.08	4.11	4.26	4.23
Config 6	3.31	3.33	4.55	4.67	4.24
Co(II)-$S_{5/2}$ → $Q_{3/2}$					
Config 1	3.29	3.28	4.39	4.36	4.39
Config 2	2.46	2.44	1.43	1.49	1.05
Config 3	2.36	2.29	1.68	1.67	1.63
Config 4	2.08	2.02	1.33	1.19	1.15
Config 5	2.14	2.06	1.18	1.20	1.13
Config 6	1.99	1.94	0.90	1.02	0.90

(such as in the HSE03 or HSE06 functionals) leads to a smaller gap of 7.0 to 7.3 eV, depending on the screening length. Even with the PBE0 functional the width of the gap is still lower by at least 1 eV than measured experimentally or derived from many-body perturbation theory for other SiO_2 polymorphs.

For Cu(I)-chabazite the width of the gap between the highest occupied and the lowest empty eigenstates of the zeolitic framework remains unchanged. The occupied Cu-3d states of the non-magnetic cation are located just above the valence band maximum, the empty Cu-4s states below the conduction-band minimum, both hybridize weakly with framework states. The $3d - 4s$ gap is much larger if calculated with hybrid functionals, and much larger for a cation coordinated by three or four oxygen atoms in a 6MR than for a cation more loosely bound to an Al-site in a 8MR. In an excited spin-state with S=1/2 a Cu-3d electron is promoted to a 4s state. The choice of the functional strongly influences the relative position of the partially occupied Cu-3d states to the framework bands. GGA functionals predict both majority and minority Cu-3d states to be located close to the Fermi energy which falls in a range of a non-zero minority DOS. Hybrid functionals predict the occupied Cu-3d states to be located at higher binding energies, close to the center of the valence band of the framework. The empty minority Cu-3d state is separated by a gap of several eV from the VBM, at only slightly lower energy than the occupied Cu-4s state. The spin-density distribution is more localized with hybrid functionals. For Cu(I)-chabazite the electronic excitations probed by DRS necessarily involve a promotion of an electron from the fully occupied Cu-3d to a 4s state. Even with GGA functionals, the energy difference between these eigenstates calculated for the ground-state is substantially larger than the energies of the DRS emission bands. Excitation energies have been calculated as energy differences between triplet and singlet states at singlet-optimized geometries, emission energies as triplet-singlet energy differences at singlet-optimized structures. The emission energies calculated using GGA functionals are larger by about 0.15 eV than those derived using hybrid functionals and in slightly better agreement with experiment (but still lower than experiment). The dependence of the calculated emission energies on the cation location is much weaker than that of the excitation energies, and this is well understood in terms of relaxation effects caused by the much larger spatial extension of the Cu-4s states. Full agreement with experiment is found if a modest energy for the triplet-singlet excitation of the 4s state is added.

A Cu(II)-cation in chabazite is paramagnetic with spin S=1/2. The electronic structure of Cu(II)-chabazite in its ground state is rather similar to that of Cu(I)-chabazite in the excited spin-state. The major difference is that with hybrid functionals the occupied Cu-3d states are shifted to even larger binding energies. As the exchange-splitting remains almost the same, the position of the empty Cu-3d state is generally closer to the VBM of the framework. The energy of the empty Cu-3d state depends rather sensitively on the screening of the exchange kernel and on the cation location. For the fourfold coordinated position in the 6MR the energy of the empty 3d-state is about 3 eV above the VBM, for cations in a 8MR it is only 1 to 2 eV (PBE0, screening of the exchange interaction leads to a further down-shift). The Cu-4s state is located close to the conduction-band minimum, varying with the bond-strength between cation

and framework. In the excited state with S=3/2, three contributions to the magnetic moment have been identified: from a hole in the Cu-3d state, from the occupied Cu-4s state and from a hole in the valence band of the framework. The photoluminescence spectrum shows broad maxima around 1.5 eV assigned to $d-d$ transitions and at 5.9 eV (attributed to oxygen-Cu charge transfer). The low-energy DRS peak can be assigned to transitions to the empty Cu-3d state whose location relative to the VBM depends very sensitively on the choice of the functional and the cation location. Best agreement with experiment is achieved with a screened hybrid functional (HSE03) locating the empty Cu-3d state at 1.56 eV for a cation bound to a single Al atom in a 6MR. For the energetically even more favorable cation location in a 6MR with two Al/Si substitution sites the calculated emission energy is 2.2 eV, it corresponds to the less intense high-energy part of the measured emission peak. Lower energies are calculated for cation locations in a 8MR. The character of the transition, however, depends on the choice of the functional. While the GGA result is compatible with a $d-d$ transition (albeit at a too low energy), the position of the occupied Cu-3d states calculated with a hybrid functional excludes this interpretation - only for framework states at the VBM an excitation energy in agreement with experiment is found. Hence the low-energy peak must also be interpreted as a O→Cu-3d charge-transfer transition.

For the high-energy DRS band of Cu(II)-chabazite the measured adsorption energies are also in quite reasonable agreement with the calculated energies of the Cu-4s state. However, the transition from a localized Cu-3d or an O-2p framework state to a much more extended 4s states causes quite strong structural relaxations such that the excitation energies must be calculated as the total energy difference between doublet and quadruplet states, calculated at a frozen doublet structure, and the emission energies at the energy differences at the relaxed quadruplet geometry. The excitation energies calculated with a hybrid functional (HSE03) range between 6.30 eV (cation in a 6MR with two Al) and 4.2 eV (cation in a 6MR), they change only weakly for a screened hybrid functional. Excitations calculated with a GGA functional are too low. The charge-transfer character of the excitation is much more pronounced with a hybrid functional. Because of the pronounced structural relaxations, emission energies are much lower and rather insensitive to the cation location. Altogether only hybrid functionals permit a quantitatively accurate interpretation of the measured photoluminescence spectra.

For a Co(II)-cation in chabazite with S=3/2 in the ground state GGA functionals predict a Co-3d minority band overlapping with the Fermi level, the center of gravity of the majority states is shifted to higher binding energies but there is still an appreciable majority DOS close to E_F. With hybrid functionals the both the full majority band and the occupied minority Co-3d states are shifted to higher binding energies, the empty minority Co-3d states lie in the upper half of the energy gap close to the Co-4s states. For Co(II)-chabazite both low- and high-spin excited states exist. The low-spin state is metastable with a small energy difference, the electronic spectrum is similar to that of the ground state, with small shifts of majority and minority DOS's in opposite directions. Formation of a high-spin state requires the occupation of the spin-up Co-4s state by an electron transferred from the highest Co-3d minority state. The electronic

spectra calculated using GGA and hybrid functional differ mainly in the position of the occupied Co-3*d* states, while they agree regarding the location of the empty minority Co-3*d* states in the lower part of the gap.

The excitation energies to the low-spin state calculated with hybrid functionals (HSE03) range between 1.1 and 1.2 eV, emission energies are lower by about 0.3 eV. These values agree rather well with the measured DRS bands in the range from 0.8 to 1.1 eV reported for various Co-exchanged zeolites. However, this energy range is not covered by the experiments on Co(II)-chabazite. With GGA functionals, the energies for the low-spin transitions are rather well approximated by the difference in the one-electron energies of the highest occupied majority and the lowest empty minority Co-3*d* state in the ground state with S=3/2. Hybrid functionals, however, predict a wide gap between these states, much larger than that of the measured DRS energies. In this case our calculations have shown that in the low-spin state the DOS is very different from that in the ground state.

The emission energies from the high-spin state calculated using conventional GGA functionals, varying between 2.0 eV [configuration (6)], 2.46 eV [configuration (2)] and 3.3 eV [configuration (1)] agree reasonably well with the measured DRS bands, except for configuration (1). However, at the low Al/Si substitution rate, the simultaneous presence of two Al atoms in the same 6MR will be rather rare, this configuration will hence contribute to the experimental spectrum with only very low intensity. The emission energies calculated with hybrid functionals are too low, due to very strong relaxation effects leading to differences of up to 3.6 eV between excitation and emission energies.

6.7 Conclusions

We have presented a detailed analysis of the electronic spectra of transition-metal exchanged chabazites in the ground and excited states. The mixing of DFT and exact exchange in hybrid functionals not only increases the fundamental gap in the eigenstates of the zeolite framework, it also strongly affects the position of the occupied and empty eigenstates of the extraframework cation relative to the framework bands. The admixture of exact exchange increases the exchange-splitting and the energy difference between occupied and empty states. These effects are most pronounced in Cu(II)-chabazite where GGA functionals predict a location of the Cu-3*d* states close to the VBM, while with hybrid functionals the occupied 3*d*-states are shifted to much higher binding energies. These changes are expected to influence the chemical reactivity of the cation. Similar effects are observed also in Co(II)-chabazite, but here at least the 3*d*-minority states are found close to the VBM such that the influence of the functional on the calculated adsorption properties will be less pronounced.

The analysis of the DRS spectra highlights two important effects: (i) The strong structural relaxation in excited electronic states leads to substantial differences in the excitation and emission energies. (ii) Calculations based on the full periodic structure of the zeolite allow to asses the relative importance of intra-ionic excitations between

eigenstates of the cation split in the ligand field of the surrounding cations and charge-transfer excitation between framework and cation states.

For Cu(I)-chabazite calculations both hybrid and GGA functionals accounting for the relaxation of the excited state lead to good agreement with experiment if a small correction for the triplet-singlet splitting in the excited state is added. For the Cu(II)-chabazite the low-energy DRS bands are assigned to $d-d$ transitions, the high-energy bands to charge-transfer excitations - in both cases best agreement with experiment is found with screened hybrid functionals. For Co(II)-chabazite the low-spin excitation energies calculated using hybrid functionals are in good agreement with the DRS adsorption bands in the range around 1 eV reported for other Co(II)-exchanged zeolites (no data are available for chabazite). For the DRS bands at higher energies between 1.8 and 2.6 eV emission energies calculated in the GGA yield best agreement with experiment. In this case hybrid functionals produce too low emission energies because the relaxation effects in the excited high-spin state seem to be overestimated. Larger DRS energies are calculated for cation locations in the 6MR of the chabazite structure, with larger values for two Al/Si substitution sites in the same ring.

7 Energetics and Vibrational Spectroscopy of Adsorbates

Summary

The influence of the exchange-correlation functional (semilocal gradient corrected or hybrid functional) on density-functional studies of the adsorption of CO and NO in Cu- and Co-exchanged chabazite has been investigated, extending the studies of the structural and electronic properties of these materials (see F. Göltl and J. Hafner, preceding papers of this issue) and including for comparison carbonyls and nitrosyls of Cu and Co. Hybrid functionals predict much lower adsorption energies than conventional semilocal functionals, in better agreement with experiment as far as data are available for comparison. The calculated adsorption energies show a strong linear correlation with the stability of the cation sites. For Cu(I)-chabazite the calculated adsorption energies span almost the interval between the adsorption energies calculated for pure neutral and positively charged Cu-carbonyls and nitrosyls. For divalent Cu(II) and Co(II) the adsorption energies at cations in chabazite are much lower than the metal-molecule binding energies in the free carbonyls or nitrosyl, especially for the most stable cation location in a six-membered ring of the chabazite structure. For the stretching modes of adsorbed CO only hybrid functionals reproduce the blue-shift of the frequency reported for all Cu(I)- and Co(II)-zeolites. For Cu(II)-chabazite both types of functionals predict a blue-shift, the larger value calculated with hybrid functionals being in better agreement with observation. For NO adsorbed on Cu(I)-chabazite all functionals produce a red-shift, the smaller value derived with hybrid functionals being in better agreement with experiment. For NO adsorbed in Cu(II)- and Co(II)-chabazite gradient-corrected functionals produce the best agreement with experiment for cations located in a six-membered ring. Semilocal functionals tend to underestimate the frequencies, while hybrid functionals tend to overestimate. The decisive factors determining the influence of the functionals are the larger HOMO-LUMO gap and the larger band-gap of the zeolite host, as well as the larger exchange-splitting of the cation eigenstates predicted with hybrid functionals. For Co(II)-chabazite the tendency to overestimate the exchange-splitting and to stabilize a high-spin state lead to better results with semilocal functionals. Finally, a comprehensive discussion of the influence of the exchange-correlation functional on the physico-chemical properties of these complex systems, based all three papers of this series is presented.

7.1 Introduction

It is well known that the accuracy of materials properties calculated using density functional theory (DFT) depends critically on the choice of an exchange-correlation functional. In the preceding papers of this series[109] (hereafter referred to as I and II) we have analyzed in detail the structural, electronic and magnetic properties of transition-metal exchanged chabazite derived from calculations using semilocal gradient-corrected (GGA) or hybrid functionals. In I we have shown that for the pure SiO_2 zeolite hybrid functionals (the PBE0[72] or HSE[73, 74] functionals) predict a slightly lower volume and shorter Si-O bond lengths in better agreement with experiment than semilocal gradient-corrected functionals (the PBE[55] and the PW[54] functionals). More significant differences were found in the local environment of the extraframework cations and of the Al/Si substitution sites in Cu(I)-, Cu(II)-, and Co(II)-exchanged chabazite. For all three extraframework cations both types of functionals predict that a location of the cation in an almost coplanar position within a six-membered ring (6MR) of the chabazite structure is preferred over a position with the larger eight-membered ring (8MR). Hybrid functionals yield a stronger binding between cation and framework. Fixed-moment calculations have been used to investigate the structure and energetics of excited spin states. Strong structural relaxations are predicted for the excited states, which are even more pronounced with hybrid functionals.

The admixture of exact (i.e. Hartree-Fock) exchange in hybrid functionals also affects the electronic structure very strongly, as shown in II. The fundamental energy gap in the electronic spectrum of the zeolitic framework is increased. For the metal-exchanged systems both the exchange-splitting and the gap between occupied and empty cation-states is increased. This leads to significant changes in the electronic structure, especially for the systems with divalent cations: Whereas GGA functionals place both the occupied and empty $3d$-states of the cation close to the valence-band maximum (VBM), hybrid functional shift the occupied states to higher binding energies and the empty states to higher energies within the gap. These effects are even more pronounced in excited high-spin states. The electronic eigenstates of extraframework cations are often probed using diffuse reflectance spectroscopy (DRS). We have demonstrated that the analysis of excited spin-states provides the key to an improved understanding of the measured DRS spectra. The strong relaxation of the excited states leads to large differences between excitation and emission energies. For Cu(I)-chabazite the GGA-calculated emission energies are in slightly better agreement with experiment. For Cu(II)-chabazite the GGA results agree with the assignment of the low-energy DRS peak to $d - d$ transitions (albeit at a too low energy), whereas the position of the occupied $3d$ states at large binding energies calculated with hybrid functionals excludes such an interpretation and suggests that the peak arises from a charge-transfer transition from a framework oxygen to the cation. For the high-energy DRS peak both types of functionals agree on a charge-transfer excitation, with the hybrid functionals leading to better agreement with experiment. For Co(II)-chabazite the transitions to an excited low-spin state calculated with hybrid functionals correspond rather well to a low-energy DRS peak measured in other Co(II)-zeolites (no data

in this range are available for chabazite), while the DRS peaks in the visible range can be assigned to the emission from a high-spin state calculated in the GGA. Due to too strong relaxation effects hybrid functionals predict in this case too low emission energies.

The strong dependence of the position of the $3d$ states on the choice of the functional also suggests pronounced differences in the chemical reactivities of the extraframework cations. One of the techniques used most frequently to characterize the reactivity of cations in zeolites is infrared (IR) spectroscopy of adsorbed probe molecules, especially CO[180, 181] and NO.[182] The interpretation of the data on Cu-carbonyl complexes in zeolites has been controversial for some time. Now it is well established that the most stable complexes of CO are formed with monovalent Cu(I) cations[180, 23, 183], whereas Cu(II)-carbonyls are very unstable.[184, 185] It has even been argued that Cu(II) cations are too weak acids to bind CO even at low temperatures.[186] The experimentally observed stretching frequencies of CO adsorbed on Cu(I) zeolites are blue-shifted with respect to 2143 cm^{-1} for gas-phase CO. The measured frequencies are only very weakly sensitive to the zeolite type and cation site: 2157 cm^{-1} in Cu(I)-ZSM5 [187, 188, 189], 2160 and 2140 cm^{-1} in Cu(I)-Y [187, 190], 2157 - 2159 cm $^{-1}$ in Cu(I)-FER and Cu(I)-MFI [189, 183], 2159 and 2153 cm^{-1} in Cu(I)-BEA [23]. Significantly higher stretching frequencies of 2221 and 2198 cm^{-1} were assigned to CO adsorbed on Cu(II) cation in a BEA zeolite[23]. Broclawik *et al.*[188] assigned a mode at 2200 cm^{-1} to Cu(II) in ZSM5. Similar blue-shifted CO frequencies were reported for Co(II)-exchanged zeolites: 2204 cm^{-1} in Co(II)-ZSM5 and Co(II)-FER [191], 2205 and 2191 cm^{-1} in Co(II)-MOR[126]. In mordenite, the higher frequency was assigned to CO adsorbed Co(II)-cations in α-sites, the lower to adsorption complexes in β-sites.

The origin of the striking difference in the adsorption capacity of Cu(I)- and Cu(II)-exchanged zeolites and of the blue-shift of the stretching frequency of CO adsorbed on transition-metal exchanged zeolites is still disputed. The binding between CO and the cation consists of three contributions: (i) the electrostatic interaction of the molecule with the charged cation, (ii) donation of electrons from the highest occupied (HOMO) 5σ orbital of CO to the cation, and (iii) back-donation from d-states of the cation to the lowest unoccupied (LUMO) $2\pi^\star$ orbital of CO. Because of the at least partial antibonding character of both HOMO and LUMO, both σ-donation and $\pi^\star$ back-donation weaken the bonding and promote a red-shift. The observed frequency shift depends on the balance between the three different bonding contributions. However, many attempts to explain the blue-shift by DFT calculations turned out to be unsuccessful.[188, 192, 133] Therefore an alternative explanation was proposed by Nachtigall *et al.*[192, 133, 193, 194], suggesting that the blue-shift is caused by the interaction of the CO molecule with the opposite wall of the zeolite cavity. However, because a possible CO-framework interaction is based on dispersion forces, the argument cannot be supported by DFT calculations. Nachtigall *et al.*[192, 133, 193, 194] have used an scaling relation between stretching frequencies and C-O bond length (based on coupled-cluster calculations on model compounds) to derive frequencies reproducing the observed blue-shift. In addition it was argued that the structural models have to be large enough to include interactions of the adsorbed CO with framework

atoms on the opposite side of the cavity. Here we want to investigate an alternative reason for the failure of DFT calculations. It is well known that DFT calculations based on conventional local or semilocal exchange-correlation functionals strongly underestimate not only the energy gap in insulating compounds, but also the HOMO-LUMO gap of molecules. One of the reason of the red-shift predicted by DFT calculations is hence that the too small HOMO-LUMO gap results in an overestimation of $\pi^\star$ back-donation. It has been demonstrated that the same effect also leads to the prediction of a wrong adsorption site for CO on the surfaces of some transition metals and that this can be at least partially corrected by using a hybrid functional predicting a more accurate HOMO-LUMO gap.[110] For CO adsorbed in Cu(I)-exchanged zeolites, embedded cluster calculations using hybrid functionals for the quantum-mechanical part of the calculations have been presented.[193, 194] These calculations demonstrate that hybrid functionals yield lower (and hence more realistic) adsorption energies, but frequencies were derived only using the scaling approach.

Large differences have also been observed between Cu(I)-NO and Cu(II)-NO adducts in zeolites. In contrast to CO, preferential adsorption of NO on Cu(II) cations has been reported.[184, 195] The stretching frequency of the NO molecule is red-shifted compared to the value of 1876 cm^{-1} in gas-phase NO in Cu(I)- and blue-shifted in Cu(II)-adducts: 1809 cm^{-1} for Cu(I) and 1905 cm^{-1} for Cu(II) in ZSM5 [188], 1802 and 1813 cm^{-1} for Cu(I) and 1905 and 1912 cm^{-1} for Cu(II) in BEA [23]. Rather complex IR spectra have been reported for Co(II)-exchanged zeolites. It has been demonstrated that due to the high adsorption capacity of Co(II)-cations di- and even trinitrosyl species can be formed in addition to Co(II)-NO adducts. There is now general agreement that the eigenmodes in the range from 1930 to 1980 cm^{-1} can be attributed to mononitrosyls. The stretching modes are centered around 1940 cm^{-1} in Co(II)-ZSM5[196], 1935 cm^{-1} in Co(II)-FER[124], and 1940 cm^{-1} in Co(II)-MOR[126]. Hence we note again a weak dependence of the stretching frequency on the zeolite type and on the location of the cation, although the width of the spectra suggests some modest variation with the extraframework position.

The free NO molecule differs from CO by the partial occupation of the $\pi^\star$ state and the formation of a paramagnetic moment. The location of the $\pi^\star$ state at the Fermi-level facilitates $\pi^\star$-back-donation - this helps to understand the red-shift for adsorption on a monovalent and non-magnetic cation. For the adsorption at the divalent cations, the situation is more complex because of the interplay of the magnetism of adsorbate and cation. If as a consequence of a larger exchange-splitting the *d*-states of the cation are shifted to larger binding energies, donation from the antibonding $\pi^\star$ state is possible. The depletion of the antibonding state contributes to the observed blue-shift of the stretching mode, but also reduces the magnetic moment of the adsorbate. Embedded cluster calculations for NO-adsorption in Cu(I)-zeolites, using both GGA and hybrid functionals for treating the central cluster around the cation, have been present by Pulido and Nachtigall[132]. Hybrid functionals yield lower adsorption energies and higher stretching frequencies than GGA functionals, with those derived using the GGA being in better agreement with experiment. However, with hybrid functionals endothermic heats of formation are calculated for dinitrosyls, although the

IR data suggest that such species exist in Cu(I)-chabazite. A comprehensive investigation of NO adsorption in Co(II)-exchanged CHA, MOR and FER, based on periodic calculations at the GGA level, has been performed by Georgieva *et al.*.[151] It has been shown that the vibrational eigenfrequencies of mono- and dinitrosyls are predicted with good accuracy (although showing a slight tendency to an underestimation if anharmonic corrections are taken into account). On the other hand, the energies of formation are probably too exothermic, evidence for the formation of trinitrosyl species exists for Co(II)-ZSM5, but hardly for Co(II)-MOR and Co(II)-FER. For Cu- and Co-exchanged SAPO34 (which is isostructural to CHA) Uzunova *et al.*[118] have performed a comparative investigation of the adsorption and vibrational properties of NO. It was shown that GGA functionals provide more accurate stretching frequencies, whereas hybrid functionals yield more accurate heats of adsorption.

In the present work we compare the performance of GGA and hybrid functionals in predicting the structure, energetics and vibrational properties of CO and NO adsorbed in Cu(I)-, Cu(II)-, and Co(II)-chabazite. The investigations are based on the cations locations determined in I, and the chemical reactivities of the extraframework sites are discussed in relation to the electronic spectra presented in II. Our calculations include the isolated carbonyls and nitrosyls of Cu and Co in different charge states. This permits to asses the influence of the zeolite surrounding on the physico-chemical properties of the cations.

7.2 Functionals and computational setup

In our calculations we have used the gradient-corrected semilocal PBE[55] and PW91[54] functionals and three hybrid functionals: PBE0[72], HSE03[73] and HSE06[74]. The PBE0 functional mixes 3/4 of DFT exchange with 1/4 exact (i.e. Hartree-Fock) exchange, the HSE03 and HSE06 functionals use screened exchange with different screening lengths. The calculations have been performed using the Vienna ab-initio simulation package VASP[135, 136] which performs a variational solution of the Kohn-Sham equations of DFT. All calculations have been performed in a spin-polarized mode, excited spin-states have been treated in a fixed-moment method. For all details we refer to I. The additional aspect in this work is the calculation of the vibrational frequencies of the adsorbate. Harmonic eigenfrequencies can be calculated using the classical equations of motion and the force constants derived using the "direct" method described by Kresse *et al.*[197]. Alternatively, anharmonic stretching frequencies may be calculated by numerically integrating the one-dimensional Schrödinger equation for the vibrating diatomic molecule using the program ANHARM developed by Ugliengo.[198, 199] The one-dimensional potential-energy surface has been determined by varying the bond-length of the molecule from -0.2 Å to +0.3 Å of the experimental value, keeping its center of gravity fixed. For the CO and NO molecules, the classical and quantum-mechanical eigenmodes show only negligible differences, but the anharmonic corrections are important to assess the accuracy of the competing approaches.

The calculations are based on the locations of the extraframework cation derived in

I. For monovalent Cu(I) three different locations, one in a 6MR and two in a 8MR, with the charge-compensating Al/Si substitution in the immediate vicinity have been used. For the divalent Cu(II) and Co(II) cation two variants of the same locations have been used, one with two Al in the same ring and the second with only one Al in the same ring and the other at larger distance. The electronic structures and the photoluminescence spectra of all configurations have been presented in II.

7.3 Gas-phase carbonyls and nitrosyls

We start by summarizing the results for the CO and NO molecules and for the carbonyls and nitrosyls with Cu and Co in different charge states. The calculations have been performed for the isolated molecules placed into the center of a large cubic box measuring 12 Å. Fixed-moment calculations have been performed for carbonyls and nitrosyls to determine the spin ground state. To achieve reliable results for the relaxed bond lengths and stretching frequencies, the convergence criteria for total energies and electronic eigenvalues had to be sharpened to 1×10^{-7} eV. It also has to be emphasized that an increased cut-off energy of 700 eV could produce slightly more accurate results for the isolated gas-phase species.[118] However, such large basis sets are computationally prohibitively expensive for zeolites. A cut-off energy of 400 eV, such as used in the preceding papers and in the present work offers a tractable compromise between computational effort and accuracy.

The results for CO and NO molecules (see Table 7.1) already illustrate the difficulty to identify an optimal functional. Both types of functionals slightly overestimate the bond-lengths, with hybrid functionals producing more accurate results. GGA underestimates and hybrid functionals overestimate the stretching frequency for CO, the absolute error being larger with hybrid functionals. For NO GGA leads to frequencies in very good agreement with experiment, while hybrid functionals yield too high frequencies. Calculated molecular binding energies are of comparable accuracy, because errors for molecules and free atoms largely compensate. Hybrid functionals produce a much wider and more accurate HOMO-LUMO ($\sigma - \pi^\star$) gap for CO. For the paramagnetic NO molecule the energy difference between the singly occupied molecular $\pi^\star$ orbital (SOMO) and the σ state depends only weakly on the choice of the functional, whereas the the SOMO-LUMO gap depends critically on the exchange-splitting and is therefore much larger with hybrid functionals.

It must also be emphasized that the calculations with PW91 and PBE functionals have been performed with slightly different PAW potentials using the same functionals also for the calculation of the frozen core states. For CO this leads to negligible differences in bond-lengths and stretching frequencies, but for NO the frequencies calculated with PBE are higher by about 20 cm^{-1} than those derived with PW91. Calculations with hybrid functionals are all based on the same PAW potential, independent of the screening of the excact exchange contribution. For the gas-phase molecules the screening influences the width of the HOMO-LUMO gap, but not the bond-length or the stretching mode.

Table 7.1: Bond lengths R (in Å), anharmonic stretching frequencies ν (in cm^{-1} (harmonic frequencies are given in parentheses) , molecular binding energy E_{bind} (in eV), and HOMO-LUMO gap E_g (in eV) of CO and NO, calculated using different exchange-correlation functionals.

Functional	PW91	PBE	PBE0	HSE03	HSE06	expt.
CO						
R_{C-O}	1.142	1.144	1.132	1.132	1.132	1.128[a]
ν_{C-O}	2107	2106	2201	2202	2204	2143[a],2141[b]
	(2133)	(2132)	(2225)	(2226)	(2229)	
E_{bind}	11.80	11.53	11.24	10.93	10.93	11.45[c]
E_g(HOMO-LUMO)	6.93	6.91	9.93	8.80	9.12	
NO						
R_{N-O}	1.169	1.172	1.157	1.157	1.157	1.151[d],1.148[e]
ν_{N-O}	1878	1899	2025	2024	2027	1876[d],1903[e]
	(1904)	(1928)	(2052)	(2050)	(2053)	
E_{bind}	7.48	7.15	5.92	6.18	6.12	6.63[f]
E_g(SOMO-LUMO)	0.13	0.23	3.60	2.45	2.77	
E_g(SOMO-σ)	6.57	6.48	5.57	6.56	6.57	

[a] Ref. [200], [b] Ref. [201], [c] Ref. [202], [d] Ref. [203], [e] Ref. [204], [f] Ref. [58]

TM-carbonyls

Our results for the TM carbonyls are summarized in Tables 7.2 and 7.3. The bond dissociation energy E_{bond} has been calculated relative to the ground state of the isolated metal atom or ion and the ground state of the molecule. For Cu-carbonyls both types of functionals predict a S=0 ground state for negative and positive charge (i.e. at an even number of valence electrons), and an S=1/2 ground state for the neutral carbonyl. We also find the same bent geometries with Cu-C-O angles of 131° and 143° for negative and neutral Cu-carbonyls, and a linear configuration at positive charge.

GGA functionals predict elongated C-O bond-lengths and strongly red-shifted C-O stretching frequencies compared to the gas-phase molecule for negative and neutral carbonyls, while at positive charge the bond-length is slightly contracted and the stretching-mode blue-shifted. With hybrid functionals the C-O bond lengths are reduced and the Cu-C distances increased compared to GGA functionals. This reflects the weaker binding between metal and molecule calculated with hybrid functionals. C-O stretching frequencies are higher with hybrid functionals, agreement with the measured stretching frequencies[201] is better with the GGA for $[CuCO]^-$, with hybrid functionals for CuCO, while the absolute error is about the same for $[CuCO]^+$ (underestimation with GGA, overestimation with hybrid functionals). The important point, however, is the frequency shift relative to gas-phase CO for which both types of functionals produce comparable results [for the positive species the blue-shift compared to the gas-phase is increased from +71 cm^{-1} (GGA-PBE) to +93 cm^{-1} (hybrid

functional-PBE0)]. Using both types of functionals, the variation of the frequency with the charge is somewhat stronger than linear, slightly larger than found experimentally. The bond-dissociation energy (calculated relative to the isolated molecule and the free atom or cation, respectively) is much larger for the positively charged than for the neutral species. Calculations using hybrid functionals yield a dissociation energy reduced by about 20 to 30 pct. compared to the GGA. For $[CuCO]^+$ Meyer *et al.*[205] have measured a bond dissociation energy of 1.54 eV which is even lower than the value calculated with hybrid functionals.

For Co-carbonyls we find a spin of S=1 for positively or negatively charged species and S=1/2 for the neutral complex, independent of the choice of the functional. The spin-state indicates that for the neutral and positively charged species the formation of the carbonyl bond leads to $4s$ to $3d$ promotion, the electronic configuration of the Co(I) cation is d^8, that of the neutral atom is d^9. Similar results have been reported by Pilme *et al.*[206] for a series of carbonyls of $3d$ transition metals. No $4s$ to $3d$ promotion occurs for the negatively charged carbonyl were the electronic configuration of Co is d^8s^2. A linear geometry is predicted for all charge states and functionals. Using GGA functional we find elongated C-O bond lengths and strongly red-shifted C-O stretching frequencies for negative and neutral Co-carbonyls, while both remain almost unchanged for the positively charged complex. With hybrid functionals we calculate reduced C-O and increased Co-C distances compared to GGA functionals and higher C-O stretching frequencies. For a positive charge of the Co-carbonyl the stretching mode is now blue-shifted by about 49 cm^{-1}, we also find a stronger variation of the frequency with the charge of the carbonyl. Agreement with experiment[207] is best in the GGA for a negative charge, while for the neutral and positive Co-carbonyl GGA under- and hybrid functionals overestimate the frequency. The bond-dissociation energy calculated with hybrid functionals is only about half the value derived in the GGA, leading to significantly improved agreement with experiment. The influence of the charge state on the dissociation energy is much less pronounced than for Cu-carbonyls.

The most important factor influencing the molecular bond length and stretching frequency is the charge on the metal atom. For a negatively charged or neutral carbonyl back-donation to the antibonding $\pi^\star$ LUMO dominates over σ-donation, resulting in a pronounced red-shift of the stretching mode. For the positively charged species σ donation becomes dominant and produces a blue-shift of the stretching mode. Hybrid functionals yield a larger blue-shift leading to better agreement with experiment for $[CuCO]^+$, whereas for $[CoCO]^+$ the experimental value lies between the values derived with both types of functionals.

The differences between Cu- and Co-carbonyls may be understood in terms of the differences in the filling of the $3d$ states. For Co with a partially filled $3d$-shell the $\sigma - e_g$ and $\pi^\star - t_{2g}$ interactions favor a straight molecular geometry and the formation of a strong, predominantly covalent Co-CO bond, irrespective of the charge state. For Cu with a filled $3d$-shell the hybridization between $3d$ and $4s$ states is of foremost importance for understanding the bonding mechanism. The interaction of the molecular eigenstates with the $4s - 3d$ hybrid state leads to the formation of a bent geometry for

Table 7.2: C-O and C-Cu bond lengths R_{C-O} and R_{Cu-C} (in Å), Cu-C-O angle $\angle_{Cu-C-O}$ (in deg), bond-dissociation energy E_{bond} (in eV), anharmonic C-O stretching frequencies ν_{C-O} (in cm^{-1}, harmonic values are given in parentheses), frequency shift $\Delta\nu$ relative to gas-phase CO, and spin S of negative, neutral and positively charged Cu carbonyls, calculated using different exchange-correlation functionals. ΔE_{spin} is the energy difference to the lowest excited spin-state.

	PW91	PBE	PBE0	HSE03	HSE06	expt.
CuCO S=1/2						
R_{C-O}	1.163	1.164	1.148	1.148	1.148	
ν_{C-O}	1943(1968)	1937(1962)	2044(2070)	2039(2065)	2042(2068)	2030[a]
$\Delta\nu_{CO}$	-164	-169	-157	-163	-162	-111
R_{Cu-C}	1.859	1.857	1.893	1.895	1.896	
∠ Cu-C-O	142.4	142.6	142.2	141.3	141.4	
E_{bond}	0.984	0.984	0.619	0.598	0.578	
ΔE_{spin}	4.217	4.127	3.507	3.527	3.515	
$CuCO^-$ S=0						
R_{C-O}	1.190	1.199	1.169	1.170	1.170	
ν_{C-O}	1747(1774)	1741(1768)	1872(1903)	1866(1896)	1869(1900)	1746[a]
$\Delta\nu_{CO}$	-360	-365	-329	-336	-335	-395
R_{Cu-C}	1.990	1.984	2.050	2.055	2.056	
∠ Cu-C-O	121.0	121.8	120.4	120.2	120.2	
ΔE_{spin}	0.765	0.734	0.524	0.498	0.477	
$CuCO^+$ S=0						
R_{C-O}	1.136	1.137	1.122	1.123	1.123	
ν_{C-O}	2178(2201)	2173(2196)	2294(2316)	2291(2313)	2295(2317)	2234[a]
$\Delta\nu_{CO}$	71	67	93	89	91	93
R_{Cu-C}	1.813	1.813	1.854	1.854	1.855	
∠ Cu-C-O	179.7	179.7	178.9	179.9	179.8	
E_{bond}	2.300	2.276	1.854	1.817	1.808	1.54[b]
ΔE_{spin}	3.785	3.699	3.294	3.298	3.301	

[a]Ref. [201], [b] Ref. [205].

Table 7.3: C-O and C-Co bond lengths R_{C-O} and R_{Co-C} (in Å), Co-C-O angle $\angle_{Co-C-O}$ (in deg), bond-dissociation energy E_{bond} (in eV), anharmonic C-O stretching frequencies ν_{C-O} (in cm^{-1}, harmonic values are given in parentheses), frequency shift $\Delta\nu$ relative to gas-phase CO, and spin S of negative, neutral and positively charged Co carbonyls, calculated using different exchange-correlation functionals. ΔE_{spin} is the energy difference to the lowest excited spin-state.

	PW91	PBE	PBE0	HSE03	HSE06	expt.
CoCO S=1/2						
R_{C-O}	1.175	1.176	1.157	1.157	1.157	
ν_{C-O}	1940(1960)	1937(1957)	1999(2019)	2006(2026)	2008(2028)	1974[a]
$\Delta\nu_{CO}$	-167	-169	-203	-196	-196	-167
R_{Co-C}	1.668	1.668	1.691	1.689	1.689	
∠ Cu-C-O	179.9	180.0	180.0	179.9	179.9	
E_{bond}	2.367	2.262	1.044	1.038	1.018	
ΔE_{spin}	1.005	0.925	0.205	-0.017	0.203	
$CoCO^-$ S=1						
R_{C-O}	1.190	1.191	1.174	1.176	1.176	
ν_{C-O}	1817(1838)	1803(1824)	1856(1872)	1856(1874)	1856(1873)	1820[a]
$\Delta\nu_{CO}$	-290	-303	-346	-346	-348	-321
R_{Co-C}	1.702	1.703	1.717	1.717	1.716	
∠ Co-C-O	178.4	180.0	179.8	180.0	179.9	
ΔE_{spin}	0.060	0.205	0.213	0.206	0.217	
$CoCO^+$ S=1						
R_{C-O}	1.144	1.146	1.128	1.129	1.129	
ν_{C-O}	2117(2140)	2113(2136)	2245(2267)	2243(2265)	2245(2268)	2165[a]
$\Delta\nu_O$	10	7	43	41	41	+24
R_{Co-C}	1.790	1.792	1.843	1.835	1.845	
∠ Co-C-O	179.8	179.7	179.9	179.9	179.7	
E_{bond}	2.783	2.527	1.453	1.435	1.431	
ΔE_{spin}	0.570	0.704	0.806	0.807	0.808	

[a] Ref. [207]

the negative and neutral carbonyl, while for $[CuCO]^+$ a linear geometry is predicted because the $4s-3d$ hybridization opens the $3d$-shell and enables σ donation and the formation of a covalent bond. This is also the reason that the bond dissociation energy is very low for the neutral carbonyl and much larger for the positively charged species.

TM-nitrosyls

Our results for Cu- and Co-nitrosyls are summarized in Tables 7.4 and 7.5. For the Cu-nitrosyls carrying negative or positive charges calculations with both types of functionals predict a spin of S=1/2 in the ground-state. Independent of the charge-state and the choice of the functional, the Cu-nitrosyls are bent, the Cu-N-O angle varying between $\sim 120°$ for the negatively and $\sim 133°$ for the positively charged species. For the neutral Cu-nitrosyl GGA calculations predict that the spins of the metal atom and of the molecule compensate each other, resulting in zero spin for the nitrosyl. In contrast, with hybrid functionals the spins are aligned, resulting in S=1 for the nitrosyl.

However, the S=0 state is only slightly higher in energy. For $[CuNO]^-$ and CuNO GGA predicts a pronounced elongation of the N-O bond length, accompanied by a strong red-shift of the stretching frequency. For $[CuNO]^+$ we find a modest contraction of the molecular bond, resulting in a very small blue-shift of the stretching mode compared to NO in the gas phase. Together we find an almost linear variation of the stretching frequency with the charge of the nitrosyl.

For the negatively and positively charged species where all calculations predict a S=1/2 ground state, hybrid functionals yield a reduced N-O and an increased Cu-N distance, reflecting a weaker binding between metal and molecule. Compared to the gas phase molecule, in $[CuNO]^-$ the molecular bond is elongated, the stretching frequency strongly red-shifted. In $[CuNO]^+$ the bond length is contracted, the frequency is blue-shifted. For the neutral species in the S=1 ground state the N-O bond length and stretching frequency are slightly larger than in the S=0 state predicted with GGA functionals. Hence in this case the stretching mode does not follow a linear dependence on the charge. Screening of the exact exchange in the hybrid functional has only a very modest influence upon the results. The anharmonicity of the stretching mode is only modest, varying between ~ 20 cm^{-1} or negative and ~ 26 cm^{-1} for positive charge, using all functionals.

For neutral CuNO the frequencies calculated in the GGA are in reasonable agreement with the experimental value of 1602 cm^{-1} (Ref. [208, 209]), while hybrid functionals overestimate the stretching frequency by about 70 cm^{-1}. For $[CuNO]^+$ the GGA result is again in good agreement with experiment, while hybrid functionals lead to an overestimation of about 150 cm^{-1}. However, only with hybrid functionals the calculations predict for $[CuNO]^+$ a blue-shift of the stretching frequency as found in experiment.[208, 209].

For $[CuNO]^+$ micro-calorimetric measurements of the bond dissociation energy have been performed.[210] The experimental value of 1.13 eV is lower by about 0.2 eV than our calculations with hybrid functionals and only about half the GGA value. Koszinowksi *et al.* also presented results from coupled cluster theory (1.02 eV) and using the B3LYP[114] hybrid functional (1.17 eV).

The results for Co-nitrosyls display some significant differences. Again we find using both types of functionals the same S=1/2 ground state for the charged species, and for the neutral nitrosyl a S=0 ground state using the GGA, while hybrid functional predict a S=1 ground state to be slightly lower in energy than S=0. The calculated spins suggest that in all cases formation of the nitrosyl leads to a $4s$ to $3d$ promotion on the Co atom or ion. At negative charge, the electron configuration is d^{10}, the spin of the nitrosyl is contributed by the paramagnetic molecule. At positive charge, the electron configuration is d^8, the spins of the anion and the molecule partially compensate such that a spin or S=1/2 results for the nitrosyl. For the neutral species the electron configuration of Co is d^9. With hybrid functionals the localized spin densities on atom and molecule are aligned, whereas in the GGA with a more delocalized charge density the spin of the nitrosyl is quenched.

GGA functionals predict for $[CoNO]^-$ a bent configuration with a Co-N-O angle of about 158° and a linear geometry for CoNO and $[CoNO]^+$. For the negative and

Table 7.4: N-O and N-Cu bond lengths R_{N-O} and R_{Cu-N} (in Å), Cu-N-O angle $\angle_{Cu-N-O}$(in deg), bond-dissociation energy E_{bond}(in eV), anharmonic N-O stretching frequencies ν_{N-O} (in cm^{-1}, harmonic values are given in parentheses), frequency shift $\Delta\nu$ relative to gas-phase NO, and spin S of negative, neutral and positively charged Cu nitrosyls in their spin ground-state, calculated using different exchange-correlation functionals. For the neutral nitrosyl where GGA and hybrid functionals lead to different predictions for the equilibrium spin ΔE_{spin} is list the energy difference relative to the ground state, for charged nitrosyls the energy difference to the first excited spin state is given.

	PW91	PBE	PBE0	HSE03	HSE06	
CuNO S=0						
R_{N-O}	1.193	1.195	1.194	1.194	1.195	
ν_{N-O}	1621(1649)	1663(1692)	1699(1726)	1698(1726)	1699(1726)	1602(1587)[a]
$\Delta\nu_{NO}$	-257	-236	-326	-326	-328	-276(-291)
R_{Cu-N}	1.864	1.864	1.860	1.862	1.861	
∠ Cu-N-O	120.1	120.0	121.6	121.7	121.7	
E_{bond}	1.539	1.457				
ΔE_{spin}	0.	0.	0.048	0.042	0.050	
CuNO S=1						
R_{N-O}	1.211	1.213	1.203	1.203	1.203	
ν_{N-O}	1591(1616)	1607(1634)	1677(1701)	1675(1670)	1675(1699)	1602(1587)[a]
$\Delta\nu_{NO}$	-287	-292	-348	-349	-352	-276(-291)
R_{Cu-N}	1.808	1.809	1.831	1.834	1.834	
∠ Cu-N-O	131.7	131.4	129.7	129.2	129.1	
E_{bond}			0.879	0.888	0.860	
ΔE_{spin}	0.248	0.192	0.	0.	0.	
$CuNO^-$ S=1/2						
R_{N-O}	1.247	1.247	1.235	1.236	1.235	
ν_{N-O}	1395(1419)	1407(1433)	1523(1546)	1515(1537)	1522(1544)	
$\Delta\nu_{NO}$	-483	-492	-502	-509	-505	
R_{Cu-N}	1.879	1.881	1.898	1.901	1.901	
∠ Cu-N-O	120.1	119.8	121.7	121.3	121.6	
ΔE_{spin}	0.494	0.462	0.176	0.184	0.180	
$CuNO^+$ S=1/2						
R_{N-O}	1.156	1.159	1.146	1.146	1.146	
ν_{N-O}	1878(1906)	1898(1928)	2058(2086)	2052(2080)	2060(2088)	1907[a]
$\Delta\nu_{NO}$	0	-1	33	28	33	29
R_{Cu-N}	1.841	1.841	1.885	1.887	1.887	
∠ Cu-N-O	131.1	131.4	133.0	132.7	133.0	
E_{bond}	2.173	1.948	1.369	1.359	1.347	1.13[b]
ΔE_{spin}	3.741	3.591	3.079	3.083	3.090	

[a] Ref. [208, 209]. Where two values are quoted, the higher frequency refers to nitrosyls embedded in a neon matrix, the lower value to embedding in argon.
[b] Ref. [210].

neutral Co-nitrosyl we find an expansion of the N-O bond length and a red-shifted stretching frequency, whereas for positive $[CoNO]^+$ the bond length is contracted and the stretching mode blue-shifted by more than 100 cm^{-1}. The frequency shifts predicted in the GGA are in reasonably good agreement with experiment, irrespective of the charge.

The influence of the choice of the functional is very different from that found for Cu-nitrosyls. With hybrid functionals we calculate bent geometries with Co-N-O angles of 127° and 138° for negative and neutral Co-nitrosyls, and a straight geometry only for the positively charged species. For $[CoNO]^-$ we find a slightly increased N-O bond length and a strongly increased Co-N distance, and an N-O stretching frequency which is comparable or even lower (with screened functionals) than calculated with GGA functionals. For neutral CoNO the N-O distance is almost the same using both functionals (but remember the difference in the spin), the elongation of the Co-N distance is less dramatic, the stretching frequency is about 50 cm^{-1} lower than calculated in the GGA. Only for $[CoNO]^+$ the effect of the functional is the same as for Cu-nitrosyl: the N-O distance is slightly reduced, the Co-N distance increased, the stretching mode is blue-shifted. Compared to experiment, the stretching frequencies calculated using hybrid functionals are in agreement with experiment for the negative, too low for the neutral, and too high for the positive species. The variation of the stretching frequency with the charge of the nitrosyl is approximately linear with the GGA, but not with hybrid functionals. The shift of the stretching frequency compared to gas-phase NO is predicted more accurately using GGA functionals. Hybrid functionals overestimate $\Delta\nu$ for negative and neutral Co-nitrosyls and underestimate it for the positive species.

7.4 Adsorption of CO in Cu- and Co-exchanged chabazite

In the following we present our results for the adsorption of CO in Cu- and Co-exchanged chabazite. We will discuss the change in the geometry of the cation-sites induced by the adsorption, as well as the influence of the zeolite environment on the adsorption capacity of the cation by comparing the results with the properties of the isolated carbonyls. In our calculations we have considered cation sites close to the center of the 6MR and within the larger 8MR (in the literature comparable sites in other zeolites have often been referred to as type I and type II, respectively).[211] For divalent cations for each case a configuration with two Al/Si substitution sites in the same ring at close proximity, and one with only one Al in the same ring and the second at larger distance have been considered. All details of the relaxed configurations have been described in I. The adsorption energies have been calculated relative to the clean, metal-exchanged zeolite and the gas-phase molecule. We begin with CO in Cu(I)-chabazite.

Table 7.5: N-O and N-Co bond lengths R_{N-O} and R_{Co-N} (in Å), Co-N-O angle $\angle_{Co-N-O}$(in deg), bond-dissociation energy E_{bond}(in eV), anharmonic N-O stretching frequencies ν_{N-O} (in cm^{-1}, harmonic values are given in parentheses), frequency shift $\Delta\nu$ relative to gas-phase NO, and spin S of negative, neutral and positively charged Co nitrosyls in their spin ground-state, calculated using different exchange-correlation functionals. For the neutral nitrosyl where GGA and hybrid functionals lead to different predictions for the equilibrium spin ΔE_{spin} is list the energy difference relative to the ground state, for charged nitrosyls the energy difference to the first excited spin state is given.

	PW91	PBE	PBE0	HSE03	HSE06	
CoNO S=0						
R_{N-O}	1.190	1.191	1.199	1.200	1.200	
ν_{N-O}	1804(1821)	1825(1843)	1749(1773)	1744(1770)	1738(1763)	1794(1761)[a]
$\Delta\nu_{NO}$	-74	-74	-276	-280	-289	-84(-117)
R_{Co-N}	1.565	1.565	1.741	1.742	1.742	
∠ Cu-N-O	180.0	179.8	138.4	138.2	138.1	
E_{bond}	3.091	2.857				
ΔE_{spin}	0.	0	0.004	0.010	0.003	
CoNO S=1						
R_{N-O}	1.197	1.199	1.194	1.194	1.194	
ν_{N-O}	1673(1697)	1692(1718)	1753(1781)	1746(1773)	1752(1779)	1794(1761)[a]
$\Delta\nu_{NO}$	-205	-207	-272	-278	-275	-84(-117)
R_{Cu-N}	1.664	1.665	1.778	1.778	1.779	
∠ Cu-N-O	141.9	142.2	135.1	134.4	134.4	
E_{bond}			1.293	1.305	1.289	
ΔE_{spin}	0.380	0.286	0.	0.	0.	
$CoNO^-$ S=1/2						
R_{N-O}	1.221	1.221	1.230	1.230	1.230	
ν_{N-O}	1586(1606)	1602(1623)	1578(1603)	1532(1561)	1521(1545)	1568[a]
$\Delta\nu_{NO}$	-292	-297	-447	-492	-506	-310
R_{Co-N}	1.599	1.600	1.846	1.847	1.848	
∠ Co-N-O	157.9	158.0	125.7	126.2	126.7	
ΔE_{spin}	0.441	0.324	0.322	0.329	0.307	
$CoNO^+$ S=1/2						
R_{N-O}	1.150	1.154	1.149	1.149	1.149	
ν_{N-O}	1989(2005)	2013(2037)	2042(2065)	2041(2065)	2041(2065)	1958[a]
$\Delta\nu_{NO}$	111	114	17	17	14	80
R_{Co-N}	1.633	1.635	1.676	1.675	1.677	
∠ Co-N-O	180.0	179.6	179.8	179.9	179.8	
E_{bond}	4.199	4.397	2.102	2.115	2.094	
ΔE_{spin}	1.027	0.942	0.279	0.283	0.276	

[a] Ref. [208, 209]. Where two values are quoted, the higher frequency refers to nitrosyls embedded in a neon matrix, the lower value to embedding in argon.

CO adsorbed on Cu(I)-chabazite

Structure and energetics

Our results for CO adsorption in Cu(I)-chabazite are summarized in Table 7.6. CO molecules bind strongly to Cu(I)-cations in chabazite in an almost linear geometry. The ground state is a singlet, as for pure Cu(I)-chabazite. The adsorption energy increases with decreasing stability of the cation location, with GGA functionals from about 1.6 eV (configuration 1, Cu in 6MR) to 2.2 eV (configuration 3, Cu in 8MR), and with hybrid functionals from about 1.3 eV to 1.6 eV for the same configurations. These adsorption energies are much larger than for the isolated neutral CuCO carbonyl, but lower than for $[CuCO]^+$. No experimental data are available for CO in Cu(I)-chabazite. For CO adsorption in Cu(I)-ZSM5 Kuroda *et al.*[183] reported from micro-calorimetric measurements an initial heat of adsorption of 0.98 eV, decreasing slightly at higher coverage. A higher value of 1.35 eV at 303 K was reported by Reed *et al.*[212] for Cu(I)-MFI. Davidová *et al.*[211] have used the B3LYP functional and an embedded cluster approach to determine the adsorption energy of CO in Cu(I)-MFI zeolite and the bond dissociation energy of $[CuCO]^+$. Both for zeolite adsorption (E_{ads} = 1.14 eV and 1.44 eV for adsorption by Cu(I) in type I and type II sites, respectively) and for the charged carbonyl (E_{bond}=1.54 eV) their values are lower than ours. A similar approach, based on both B3LYP and PBE functionals has been applied by Rejmak *et al.*[194] to CO in Cu(I)-faujasites. For Cu(I) cations interacting with a single Al atom heats of adsorption of 1.24(0.80) eV and 1.89(1.23) eV were derived using PBE(B3LYP) for cation locations in a 6MR or 8MR, respectively. Hence both the present periodic and the cluster approach agree on a weaker binding by the cation embedded in the zeolites and on a weaker adsorption by cations in a 6MR and in a larger ring. The difference in the absolute values can be attributed to the different hybrid functionals and to the use of rather small clusters with only six or seven tetrahedral sites for the quantum-mechanical part of the calculations. In any case the comparison shows that hybrid functionals lead to much more accurate adsorption energies.

The strong binding of the adsorbate weakens the binding of the cation to the framework. In configuration 1 Cu(I) is threefold (fourfold) coordinated to oxygen atoms of the framework in calculations with GGA (hybrid) functionals (for details, see I). Upon adsorption of CO only the two bonds to the activated O(**3**) and O(**2**) atoms next to Al (as in the preceding papers we use the convention to designate activated oxygen atoms by bold numbers) are preserved, and they are stretched by 0.1 to 0.15 Å with GGA and by up to about 0.1 Å with hybrid functionals. The Cu(I) cation moves from a position almost coplanar with the 6MR to a position above the ring. The Al-Cu distance is slightly reduced. Hence adsorption of a CO molecule induces a change in the cation location similar to that caused by a spin-excitation (see I for details). Similarly, in configuration 2 in a 8MR the Cu(I)-O coordination is reduced from three to two, only the bonds to the activated O(**1**) and O(**4**) atoms are conserved. They are even slightly contracted, while the Al-Cu distance is slightly increased (using both types of functionals). In configuration 3 the Cu(I) cation remains two-fold coordinated

Table 7.6: Structure, energetics, and stretching frequencies of CO adsorbed at an extraframework Cu(I) cation in chabazite, calculated for different cation-locations and using different exchange-correlation functionals. Distances are given in Å, angles in deg, adsorption energies in eV/molecule, and frequencies in cm^{-1}. The calculated frequencies include anharmonic corrections, harmonic frequencies are given in parentheses. $\Delta\nu$ gives the frequency shift relative to CO in the gas phase.

	PW91	PBE	PBE0	HSE03	HSE06
	Configuration 1				
C-O	1.148	1.150	1.133	1.133	1.134
Cu-C	1.771	1.772	1.791	1.790	1.790
∠Cu-C-O	178.3	177.6	178.0	178.1	178.9
Cu-O(**2**)	2.045	2.064	2.072	2.063	2.070
Cu-O(**3**)	2.012	2.005	2.019	2.026	2.023
Cu-O(3)	3.009	2.989	2.887	2.929	2.878
Cu-O(*3*)	3.009	2.999	2.887	2.929	2.878
Al-Cu	2.789	2.788	2.775	2.780	2.782
E_{ads}	1.623	1.595	1.295	1.313	1.301
ν_{C-O}	2105(2124)	2103(2122)	2212(2232)	2211(2231)	2214(2234)
$\Delta\nu$	-3	-8	2	2	4
	Configuration 2				
C-O	1.148	1.149	1.133	1.133	1.132
Cu-C	1.769	1.769	1.786	1.787	1.786
∠Cu-C-O	175.0	175.6	174.3	174.1	174.8
Cu-O(**1**)	1.979	1.984	1.985	1.979	1.981
Cu-O(**4**)	2.067	2.069	2.069	2.081	2.075
Cu-O(2)	3.072	3.100	3.068	3.009	3.049
Al-Cu	2.836	2.845	2.822	2.823	2.820
E_{ads}	1.997	2.009	1.620	1.600	1.587
ν_{C-O}	2107(2127)	2105(2124)	2218(2238)	2216(2236)	2220(2240)
$\Delta\nu$	-1	-6	8	7	10
	Configuration 3				
C-O	1.148	1.150	1.133	1.134	1.133
Cu-C	1.176	1.766	1.785	1.783	1.783
∠Cu-C-O	178.7	178.3	176.1	176.3	176.8
Cu-O(**2**)	2.027	2.029	2.032	2.030	2.028
Cu-O(**4**)	2.012	2.014	2.018	2.022	2.021
Cu-O(4)	3.188	3.146	2.958	2.985	2.999
Al-Cu	2.811	2.812	2.807	2.805	2.802
E_{ads}	2.183	2.202	1.646	1.619	1.611
ν_{C-O}	2103(2122)	2104(2123)	2213(2233)	2231(2211)	2215(2235)
$\Delta\nu$	-5	-7	3	2	5

to activated O(**2**) and O(**4**) atoms, Cu-O and Al-Cu distances are slightly increased. The analysis of the changes in the geometry shows that the lower adsorption energies in configurations 1 and 2 are at least partially due to a loss of energy arising from the geometric distortion of the cation coordination.

Stretching frequencies

As the C-O bond length is almost unchanged compared to the gas-phase molecule, we also calculate almost unchanged stretching frequencies. With GGA we find a very small red-shift between -1 and -8 cm^{-1}, with hybrid functionals a weak blue-shift between 2 and 10 cm^{-1} of the C-O stretching frequency compared to gas-phase CO. The absolute value of the frequency is overestimated by about 70 cm^{-1} with hybrid functionals, and underestimated by about 40 cm^{-1} in the GGA. The frequency is also found to be almost independent of the cation-location. Experimentally, stretching modes cluster around 2157$\pm$4 cm^{-1}, blue-shifted by about 14 cm^{-1}, for CO adsorbed in many different zeolites (see Introduction). Hence, while the blue-shift is predicted only by hybrid functionals, GGA under- and hybrid functionals overestimate the frequency, with a larger absolute value in the later case.

For CO bound to Cu(I)-cations in faujasite Rejmak *et al.*[194] have calculated harmonic stretching frequencies using the PBE and B3LYP functionals. For cations in a 6MR bound to a single Al atom they reported frequencies of 2122 cm^{-1} (red-shifted by -11 cm^{-1} corresponding to the gas-phase) using PBE, and 2223 cm^{-1} (blue-shifted by 5 cm^{-1}) using B3LYP. In their work the lower stretching frequencies around 2140 cm^{-1} measured in faujasite and some other zeolites were assigned to adsorption at cations bound to two Al in close proximity. Hence in agreement with our results the weak blue-shift reported for CO adsorbed in Cu(I)-zeolites is reproduced with hybrid functionals, but not in the GGA.

Bonding and electronic structure

The adsorption of CO also leads to significant changes in the electronic structure of Cu(I)-chabazite. Fig. 7.1 shows the charge flow around the cation induced by CO adsorption. The difference electron density is calculated between the CO-Cu(I)-chabazite complex on one hand and the Cu(I)-chabazite before adsorption (but deformed to the relaxed geometry in the adsorption complex) and the isolated CO molecule (with the C-O distance of the adsorbed molecule). Charge is withdrawn from the Cu-O and C-O bonds and transferred to the Cu-C bonding region, reflecting the formation of a covalent bond between the CO molecule and the cation, in contrast to the predominantly ionic Cu-framework bonding before adsorption. The result is almost identical with GGA and hybrid functionals. Since the $3d$-shell of Cu is completely filled, the formation of a covalent bond is enabled only by a $4s - 3d$ hybridization. The opening of the $3d$ shell also permits a weak σ-donation. The partial occupation of the $4s$ states is also seen in the large spatial extension of the Cu-C bond charge, it also explains the close similarity of the structural changes upon CO adsorption and spin-excitation.

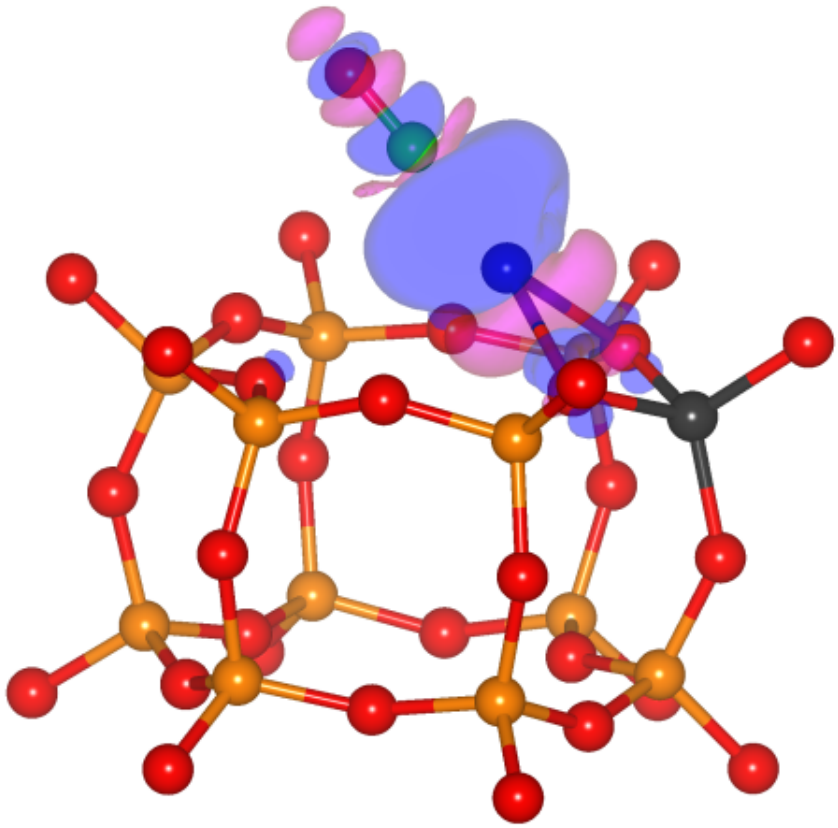

Figure 7.1: Charge-flow induced by the adsorption of a CO molecule on an extraframework Cu(I) cation located in a 6MR of chabazite (configuration 1). C atoms are displayed in green, Si in orange, O in red, Cu in blue and Al in dark grey. Red constant-density surfaces surround electron-depleted regions and blue surfaces surround regions of increased electron density. Contour values are 2.5×10^3 electrons/Å^3. For a more detailed discussion c.f. text.

The charge-rearrangement upon adsorption is also reflected in the electronic spectrum. Independent of the choice of the functional before CO adsorption the Cu-3d states form a narrow band just above the valence band maximum (VBM) of the chabazite host, the 4s state is located below the conduction band minimum. Both 3d and 4s states hybridize weekly with framework states (see Fig. 2 in II). Upon adsorption the 3d states are shifted below the VBM, they hybridize with both the molecular orbitals and the zeolite framework (see Fig. 7.2). With GGA functionals the shift of the Cu-3d band upon CO adsorption is almost the same as calculated for the excited spin-state with S=3/2 were one electron was promoted from 3d to 4s [see Fig. 4(a) in II], but there no hole is created in the hybridized $3d-4s$ band. The d-band shift upon adsorption is almost the same with hybrid functionals, but in this case spin-excitation causes a much larger shift to higher binding energies combined with a large exchange-splitting [see Fig. 4(b) in II].

The σ-HOMO and the $\pi^\star$-LUMO of the CO molecule interact most strongly with the cation states. The balance between σ-donation and $\pi^\star$ back-donation can be quantified by performing a Bader analysis [148, 149] of the charges on cation and molecule. Irrespective of the choice of the functional we calculate a positive charge of 0.82±0.01 on the cation, enhanced in the GGA by 0.07 to 0.12 compared to clean Cu(I)-chabazite and with hybrid functionals by 0.02 to 0.06. The largest increase is found for cations located in a 6MR. On the adsorbed CO molecule we find a negative charge of -0.07 ± 0.005 in the GGA and a smaller negative charge of about -0.03 with hybrid functionals. Hence $\pi^\star$ back-donation is slightly larger than σ-donation, but electrons are also transferred from the cation to the bonding framework oxygens. The dominant $\pi^\star$ back-donation correlates with the red-shift of the stretching mode found in the GGA.

Hence the analysis of the electronic DOS suggests that the CO-Cu(I)-chabazite bonding is almost the same with both types of functionals. The reason is that the admixture of exact exchange increases both the HOMO-LUMO gap of the molecule and the band gap of the Cu(I)-zeolite by a similar amount (the widening of the band gap is even slightly larger). The calculated differences in the shift of the stretching mode arise from the larger HOMO-LUMO ($\sigma-\pi^\star$) gap with hybrid functionals which reduces the possible amount of $\pi^\star$ back-donation.

CO adsorbed on Cu(II)-chabazite

Structure and energetics

For the adsorption of CO at extraframework Cu(II) cations our calculations predict a very strong dependence of the adsorption energy on the cation location. For the by far energetically most favorable position of the cation in a 6MR with two Al (configuration 1), only a very low adsorption energy of ~ 0.46(~ 0.27) eV is calculated with PBE (PBE0) functionals. If only one Al atom exists in the same 6MR (configuration 2), the adsorption energy increases to more than twice of this value (see Table 7.7). For the less favorable locations in a 8MR with two or one Al (configurations 3 to 6) adsorption energies comparable to those calculated for monovalent Cu(I) cations are calculated.

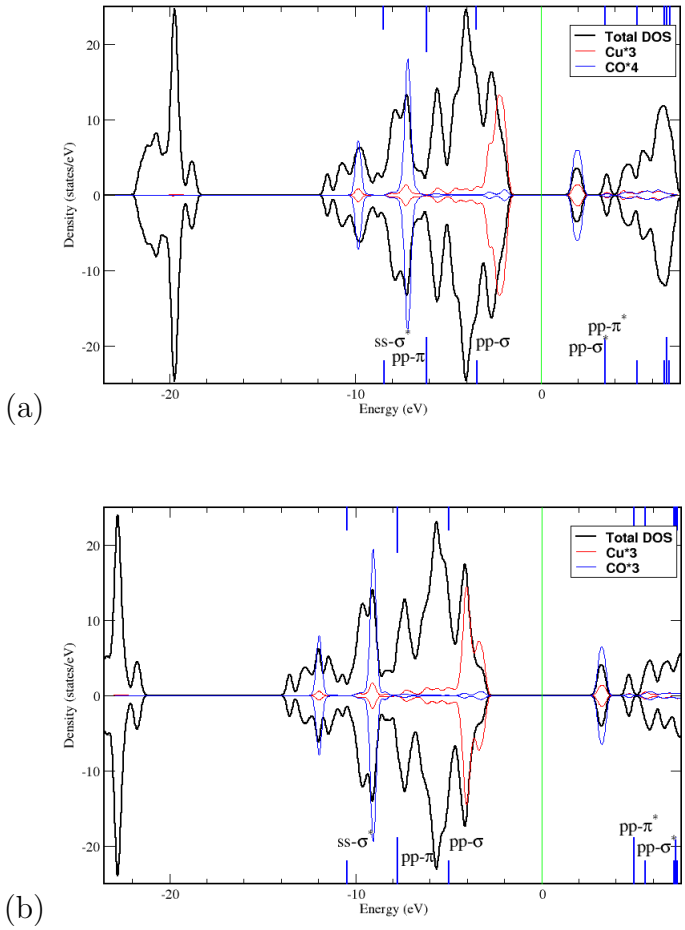

Figure 7.2: Total and local DOS of Cu(I)-chabazite in configuration 1 after CO-adsorption, compared to the MO-scheme of gas-phase CO for (a) PBE and (b) PBE0. The local Cu-DOS (red) is multiplied by a factor of three, the local CO-DOS by a factor of 4 for reasons of better visualization. Energies are measured relative to the Fermi level. C.f. text.

Table 7.7: Structure, energetics, and stretching frequencies of CO adsorbed at an extraframework Cu(II) cation in chabazite, calculated for different cation-locations and using different exchange-correlation functionals. Distances are given in Å, angles in deg, adsorption energies in eV/molecule, and frequencies in cm^{-1}. The calculated frequencies include anharmonic corrections, harmonic frequencies are given in parentheses. $\Delta\nu$ gives the frequency shift relative to CO in the gas phase.

	PW91	PBE	PBE0	HSE03	HSE06		PW91	PBE	PBE0	HSE03	HSE06
	Configuration 1						Configuration 4				
C-O	1.138	1.140	1.126	1.125	1.125	C-O	1.140	1.142	1.119	1.120	1.119
Cu-C	1.917	1.916	2.327	2.328	2.326	Cu-C	1.834	1.826	1.965	1.964	1.965
∠Cu-C-O	174.3	174.6	166.4	171.3	171.3	∠Cu-C-O	173.5	175.1	170.1	170.9	170.7
Cu-O(**2**)	2.047	2.057	2.047	2.042	2.041	Cu-O(**1**)	1.980	1.984	1.945	1.945	1.944
Cu-O(**3**)	2.009	2.001	1.968	1.980	1.979	Cu-O(**4**)	1.985	1.983	1.895	1.893	1.892
Cu-O(3)	2.862	2.927	2.078	2.073	2.072	Cu-O(2)	2.671	2.715	2.276	2.304	2.292
Cu-O(***3***)	2.038	2.050	2.035	2.032	2.031						
Al-Cu	2.923	2.924	2.870	2.874	2.872	Al-Cu	2.834	2.840	2.784	2.785	2.784
E_{ads}	0.475	0.456	0.270	0.310	0.248	E_{ads}	1.559	1.586	1.425	1.434	1.397
ν_{C-O}	2136(2153)	2137(2148)	2259(2282)	2262(2285)	2264(2288)	ν_{C-O}	2121(2143)	2099(2128)	2320(2343)	2318(2340)	2321(2344)
$\Delta\nu$	28	26	49	53	54	$\Delta\nu$	13	-12	110	109	111
	Configuration 2						Configuration 5				
C-O	1.140	1.141	1.123	1.123	1.123	C-O	1.145	1.144	1.120	1.120	1.119
Cu-C	1.871	1.872	1.990	1.989	1.989	Cu-C	1.793	1.809	1.962	1.959	1.969
∠Cu-C-O	178.1	179.1	175.9	175.8	175.4	∠Cu-C-O	177.0	176.5	176.1	176.4	176.1
Cu-O(**2**)	2.054	2.045	1.961	1.960	1.958	Cu-O(**2**)	2.035	1.954	1.854	1.857	1.862
Cu-O(**3**)	2.006	2.010	1.919	1.922	1.919	Cu-O(**4**)	1.960	2.028	2.004	1.995	1.993
Cu-O(3)	2.116	2.121	1.993	1.999	1.994	Cu-O(4)	3.253	2.995	2.296	2.303	2.223
Cu-O(*3*)	3.895	3.891	3.795	3.767	3.765						
Al-Cu	2.791	2.798	2.743	2.742	2.741	Al-Cu	2.801	2.801	2.768	2.776	2.777
E_{ads}	0.994	1.012	0.793	0.931	0.773	E_{ads}	1.539	1.543	1.423	1.475	1.305
ν_{C-O}	2128(2151)	2129(2153)	2287(2310)	2287(2310)	2290(2313)	ν_{C-O}	2084(2098)	2102(2113)	2315(2337)	2314(2337)	2315(2337)
$\Delta\nu$	20	18	77	78	80	$\Delta\nu$	-24	-9	105	105	105
	Configuration 3						Configuration6				
C-O	1.139	1.140	1.120	1.120	1.120	C-O	1.141	1.142	1.121	1.121	1.119
Cu-C	1.839	1.838	1.963	1.962	1.966	Cu-C	1.823	1.825	1.973	1.973	1.975
∠Cu-C-O	170.5	170.4	167.7	168.8	168.2	∠Cu-C-O	178.0	178.0	176.0	176.1	176.0
Cu-O(**1**)	2.014	2.018	2.000	2.000	2.006	Cu-O(**2**)	1.949	1.947	1.878	1.877	1.875
Cu-O(**4**)	1.960	1.961	1.884	1.887	1.891	Cu-O(**4**)	2.039	2.042	1.997	2.001	1.994
Cu-O(2)	2.730	2.751	2.295	2.286	2.239	Cu-O(4)	2.684	2.677	2.083	2.095	2.094
Al-Cu	2.809	2.811	2.776	2.779	2.780	Al-Cu	2.817	2.816	2.801	2.805	2.801
E_{ads}	1.562	1.560	1.407	1.417	1.390	E_{ads}	1.606	1.608	1.425	1.593	1.443
ν_{C-O}	2132(2148)	2127(2145)	2318(2341)	2316(2339)	2319(2341)	ν_{C-O}	2121(2143)	2121(2144)	2312(2335)	2309(2332)	2312(2335)
$\Delta\nu$	24	16	108	107	109	$\Delta\nu$	13	10	102	100	102

The only slightly lower adsorption energies calculated with hybrid functionals correlate with a stronger cation-zeolite interaction.

No experimental heats of adsorption for CO in Cu(II)-chabazite are available. The large differences in the adsorption energies calculated for Cu(II) cations correlate with the pronounced heterogeneity of Cu(II) locations in Cu(II)-BEA reported by Kefirov *et al.*[23] from temperature-programmed desorption experiments showing desorption peaks spread over the temperature range from 400 to 700 K.

The remarkably low adsorption capacity of Cu(I) in configurations 1 and 2 correlates not only with a strong binding between cation and framework, but also - in contrast to the results for Cu(I) - with only modest or minimal changes of the cation coordination upon adsorption. In both configurations Cu(II) is fourfold coordinated to framework oxygens (see I for details). Calculations within the GGA show that only the distance to the non-activated O(3) atom is stretched to about 2.9 Å and the Cu(II)-Al distance increased by 0.05 Å, while with hybrid functionals all four Cu(II)-O bonds are preserved (they are stretched by at most 0.03 Å or even reduced) and the Cu(II)-Al distance remains unchanged. In configuration 2 there are three strong and one intermediate Cu(II)-O bonds. The three strong bonds are preserved, the weaker one to a non-activated oxygen is broken. The Cu(II)-Al distance remains almost unchanged. The Cu(II)-C distance is much larger in calculations with hybrid functionals, it is larger for cations in a 6MR than in a 8MR, in analogy with the low adsorption energy.

In configurations 3 to 6 the cation interacts with the framework through three strong bonds with oxygen atoms (two activated and one non-activated). Upon CO adsorption the distances to the activated oxygens are unchanged on average, but that to the non-activated O atoms is increased by at least 0.5 Å and the Cu(II)-Al distance by about 0.05 Å within the GGA. With hybrid functionals the distance to the non-activated oxygen is stretched only by at most 0.2 Å or less.

The C-O bond length is reduced compared to the gas-phase, the contraction is more pronounced with hybrid functionals. However, the C-O bond length of the molecule adsorbed in Cu(II)-chabazite is larger than in a positively charged isolated $[CuCo]^+$ carbonyl. The Cu-C-O angle is very close to 180°, the very small deviations from an exactly linear geometry are mostly due to weak steric effects (Pauli repulsion from the framework). The Cu-C distance is increased compared to the carbonyl, in accordance with an adsorption energy which is much lower than the bond-dissociation energy in the isolated species. This effect is most pronounced in configuration 1.

Stretching frequencies

The contracted C-O distances should be reflected in a blue-shift of the stretching mode. Within the GGA we calculate stretching frequencies around 2125 cm^{-1}, only slightly blue-shifted compared to the gas-phase or even slightly red-shifted for some cation sites. Using hybrid functionals we calculate stretching frequencies between about 2260 cm^{-1} for the most stable configuration 1 and to about 2315 cm^{-1} for configurations 3 to 6, blue-shifted by 50 to 100 cm^{-1} compared to the gas-phase. The stronger blue-shift is in much better agreement with frequencies shifted by 55 to 78 cm^{-1} in Cu(II)-BEA

[23] and by 57 cm^{-1} in Cu(II)-ZSM5 [188]. The absolute values of the frequencies are underestimated in the GGA and overestimated with hybrid functionals, with deviations from experiment of about the same magnitude.

Bonding and electronic structure

Fig. 7.3 shows the difference-electron densities (charge flow) for CO adsorbed at Cu(II) cations in configurations 1 and 5. The picture is qualitatively very similar to that for CO adsorption at monovalent Cu(I), but the charge-accumulation in the Cu-C bonding region is much less pronounced, especially for configuration 1. Charge is withdrawn from both atoms of the molecule and from the cation and accumulated in the C-O and C-Cu bonds. For the weak adsorption in configuration 1, the charges on the framework oxygens are almost unchanged, whereas for the strong-binding configuration 5 we also find additional charge on the framework.

In the ground state the CO-Cu(II)-chabazite has a spin of S=1/2, as the zeolite before adsorption. Due to the incompletely filled $3d$ shell, the states are shifted to larger binding energies compared to Cu(I)-chabazite. The d-band shift and the exchange-splitting are much more pronounced with hybrid functionals, see Fig. 6 in II. The DOS of the minority states calculated in the GGA overlaps with the Fermi level, whereas with hybrid functionals the highest occupied Cu-$3d$ states are found at binding energies of 2.5 eV or more and the empty minority state is separated by a narrow gap (whose width is influenced by the screening of exact exchange) from the VBM. The Cu-$4s$ states are located approximately in the center of the gap. As for Cu(I), adsorption of CO leads to an increased $3d-4s$ hybridization. The interaction between the $3d-4s$ hybrids of the cation and the σ state of the molecule is by far most important, see Fig. 7.4. The strength of the interaction depends significantly on the choice of the functional and the cation site. Within the GGA for all cation locations occupied and empty $3d$ states are located close to the Fermi energy, at energies that are higher than the σ-level of CO. This limits the amount of σ-donation and explains the very small blue-shift of the stretching mode. With hybrid functionals the occupied cation states are shifted to higher binding energies, the shift increases with larger spin. This facilitates σ-donation and explains the large blue-shift of the CO stretching modes.

Again a Bader analysis of the local charges is helpful in quantifying these effects. For a Cu(II) cation in a 6MR the effective charge (see Table II in II) is almost unchanged upon adsorption, but the adsorbed CO molecule acquires a positive charge of about 0.06 for both types of functionals. Electrons are also transferred to framework oxygens. The slight excess of σ-donation explains the blue-shift of the stretching mode. In contrast for a cation in a 8MR (configuration 3) the charge on the cation is reduced from 1.05(1.32) to 0.97(1.26) with PBE(PBE0) functionals due to a transfer of 0.03(0.13) electrons from the adsorbed molecule. The difference between these values shows that in the GGA electrons are transferred to the molecular and molecule-framework bonds, while with hybrid functionals electrons are also transferred to the framework (see Fig. 7.1). The stronger depletion of the molecular σ-state explains the stronger blue-shift of the stretching mode calculated with hybrid functionals, the electron transfer

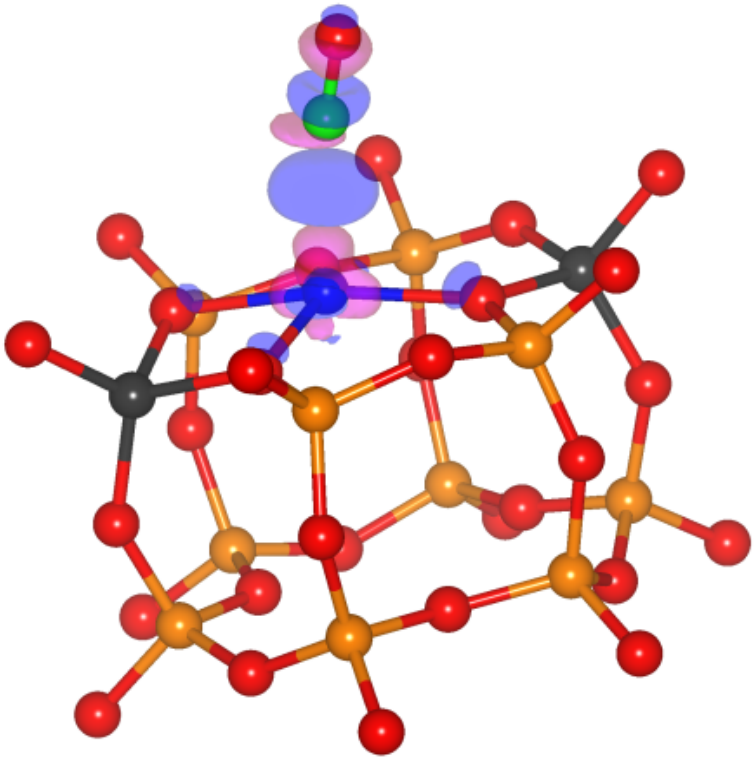

(a)

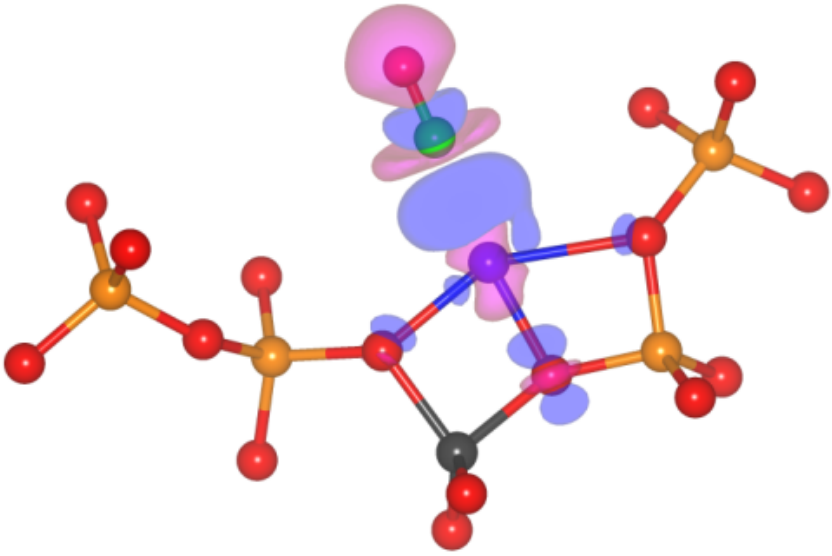

(b)

Figure 7.3: Charge-flow upon CO adsorption on a Cu(II)-cation in chabazite, calculated for configurations 1 (a) and configuration 5 (b). For the explanation of symbols, cf. Fig. 7.1.

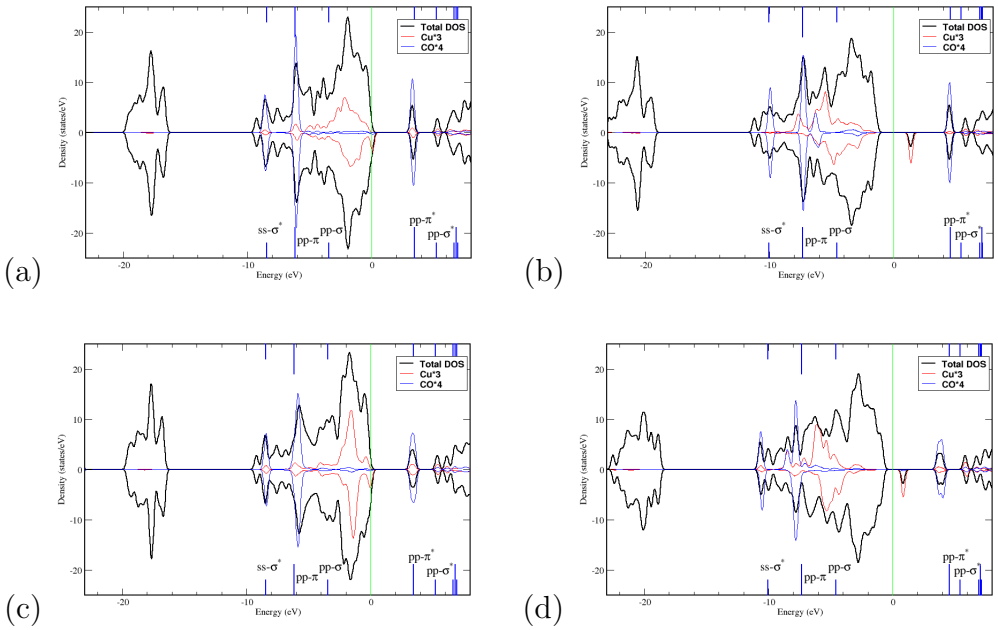

Figure 7.4: Total and local electronic DOS of CO-Cu(II)-chabazite in configurations 1 (a,b) and 3 (c,d), calculated using the PBE (left) and HSE06 (right) functionals. Partial Cu DOS (red) is multiplied by a factor of three, partial CO DOS by a factor of 4 for reasons of better visualization. For discussion c.f. text.

to the framework shows a stronger binding of the cation with hybrid functionals.

The dependence of the adsorption energy on cation location is particularly pronounced with hybrid functionals. Comparison of the DOS calculated with the screened HSE06 functional for configurations 1 and 3 (see Fig. 7.4) shows in the former case a clear splitting of the bonding and antibonding states derived from the σ level, with the center of gravity at about the same energy than the molecular eigenstates. In contrast for configuration 3 the σ states are strongly broadened and shifted to larger binding energies.

CO adsorbed on Co(II)-chabazite

According to Hund's rule a free Co(II) cation has spin S=3/2, and this is also the ground state for Co(II)-chabazite in all six configurations, independent of the choice of the functional. However, GGA calculations predict an excited low-spin state with S=1/2 at energies increased by only 0.3 to 0.6 eV (see I for details). With hybrid functionals the spin-dependent energies differences are increased to about 1 eV. The formation of a low-spin state implies the transfer of an electron from the fully occupied $3d$ majority to the minority band. As in the GGA the lowest empty minority state is

located immediately above the VBM, this immediately explains a low spin-excitation energy. With hybrid functionals the lowest empty $3d$ states is located at energies of 0.5 to 5 eV above the VBM (depending strongly on an eventual screening of the exchange operator), high excitation energies imply very structural relaxation effects (as discussed in detail in I and II).

The formation of a hole in the $3d$ majority band favors the formation of a strong CO-Co(II) bond as it facilitates electron donation from the molecular σ state to the $3d$ states of the cation. In this respect the formation of a low-spin state has an influence similar to $3d-4s$ hybridization. Indeed our calculations show that within the GGA adsorption of CO induces a transition to a low-spin state with S=1/2 for all configurations (except configuration 1), whereas hybrid functionals predict that the spin-state S=3/2 remains unchanged. There are no experiments determining the spin-state of CO-Co(II)-chabazite, but for Co(II)-ZSM5 a spin-crossover from S=3/2 to S=1/2 induced by CO adsorption has been derived from electron paramagnetic resonance (EPR) experiments.[213]

The bonding properties are significantly different in both spin states. This is illustrated in Fig. 7.5 showing the charge-flow induced by CO adsorption at a Co(II) cation in a 8MR (configuration 3), calculated within the GGA (using the PBE functional) and using a screened hybrid functional (HSE03). The transition to a low-spin state predicted in the GGA is accompanied by an extended charge redistribution: (i) Electrons are withdrawn from the framework oxygens bonding to the cation. (ii) Around the Co(II) cation the electron density is generally reduced, but we also find an accumulation of charge in the d_σ states binding to the molecular σ state. (iii) The intramolecular $pp\sigma$ bond is weakened. (iv) Bonding charge is accumulated between the C atom and the Co(II) cation. With a hybrid functional, where adsorption leaves the spin-state unchanged, charge is redistributed only between cation and adsorbate. Electrons are withdrawn from both the C and O atoms, but the intramolecular bond is even strengthened. Electrons are transferred to both the cation and to the bonding region between cation and CO molecule. The pronounced differences in the charge distributions also suggest significant differences in the structure, energetics and vibrational properties of the cation-adsorbate complex.

Structure and energetics

Our results for CO adsorption on Co(II)-chabazite are summarized in Table 7.8. Compared to the divalent Cu(II) cation we find some interesting differences. For a cation located in a 6MR (configurations 1 and 2) Co(II) binds CO more strongly than Cu(II), irrespective of the choice of the functional. For a location in a larger 8MR (configurations 3 to 6), similar adsorption energies are calculated for Co(II) and Cu(II) in the GGA whereas hybrid functionals predict a weaker binding by Co(II) than by Cu(II).

In a 6MR a Co(II) cation is fourfold coordinated by framework oxygens at distances around 2 Å. If only one Al exists in the ring the Co(II)-O bonds are re-arranged while preserving the fourfold coordination (see I for details). Upon CO adsorption the cation is still fourfold coordinated in a ring with two Al, only one of the bonds is stretched

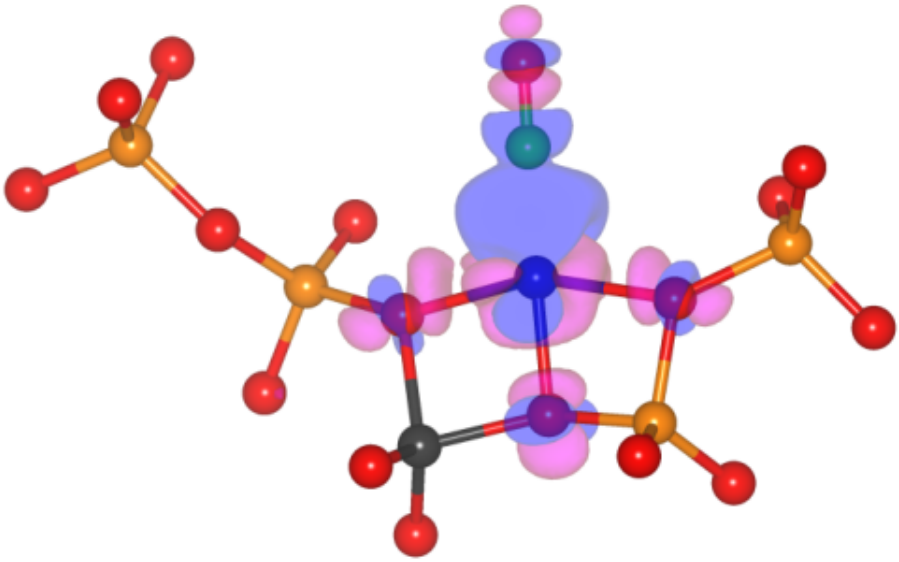

(a)

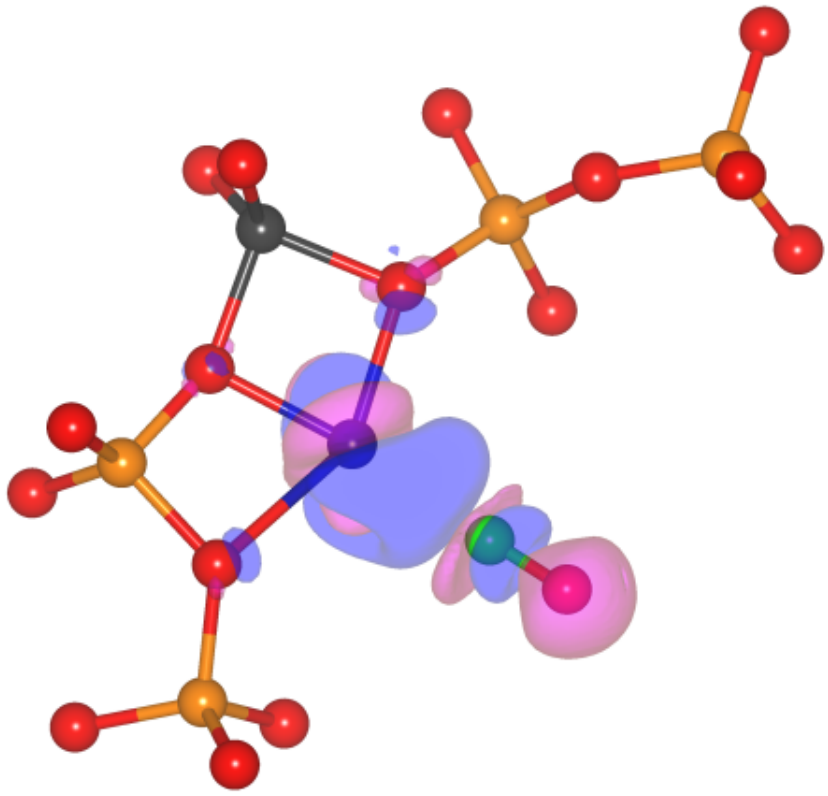

(b)

Figure 7.5: Charge-flow (difference electron densities) for CO adsorption on Co(II)-chabazite, for a cation located in a 8MR (configuration 3). Part (a) shows the result calculated with the PBE functional, with spin S=1/2. Part (b) shows the results derived using a screened hybrid functional (HSE03) - in this case the spin state is S=3/2 as before adsorption of CO. For the explanation of symbols, see Fig. 7.1. C.f. text.

Table 7.8: Spin, structure, energetics, and stretching frequencies of CO adsorbed at an extraframework Co(II) cation in chabazite, calculated for different cation-locations and using different exchange-correlation functionals. Distances are given in Å, angles in deg, adsorption energies in eV/molecule, and frequencies in cm^{-1}. The calculated frequencies include anharmonic corrections, harmonic frequencies are given in parentheses. $\Delta\nu$ gives the frequency shift relative to CO in the gas phase.

	PW91	PBE	PBE0	HSE03	HSE06		PW91	PBE	PBE0	HSE03	HSE06
	Configuration 1						Configuration 4				
S	3/2	3/2	3/2	3/2	3/2	S	1/2	1/2	3/2	3/2	3/2
C-O	1.145	1.145	1.125	1.124	1.124	C-O	1.145	1.148	1.120	1.121	1.121
Co-C	1.885	1.890	2.059	2.053	2.058	Co-C	1.782	1.781	2.055	2.055	2.064
∠Co-C-O	175.3	175.6	176.9	175.5	175.5	∠Co-C-O	171.8	171.6	174.3	174.7	174.9
Co-O(**2**)	2.333	2.347	2.280	2.233	2.230	Co-O(**1**)	1.905	1.901	1.957	1.956	1.966
Co-O(**3**)	2.014	2.016	2.016	2.025	2.025	Co-O(**4**)	1.907	1.905	1.947	1.945	1.942
Co-O(3)	2.097	2.100	2.089	2.125	2.128	Co-O(2)	2.127	2.107	2.304	2.326	2.309
Co-O(***3***)	2.010	2.018	2.019	2.017	2.017						
Al-Cu	3.042	3.050	3.006	2.989	2.988	Al-Co	2.800	2.806	2.808	2.818	2.820
E_{ads}	1.109	0.985	0.712	0.681	0.665	E_{ads}	1.866	1.826	1.214	1.218	1.187
ν_{C-O}	2078(2102)	2081(2106)	2266(2290)	2264(2289)	2268(2292)	ν_{C-O}	2081(2103)	2083(2102)	2310(2324)	2301(2324)	2303(2326)
$\Delta\nu$	-29	-25	65	62	64	$\Delta\nu$	-26	-23	109	99	99
	Configuration 2						Configuration 5				
S	1/2	1/2	3/2	3/2	3/2	S	1/2	1/2	3/2	3/2	3/2
C-O	1.150	1.151	1.123	1.123	1.123	C-O	1.148	1.149	1.121	1.121	1.121
Co-C	1.775	1.778	2.045	2.043	2.046	Co-C	1.777	1.777	2.043	2.044	2.040
∠Co-C-O	173.1	172.6	176.8	177.1	176.8	∠Co-C-O	177.8	178.0	176.6	176.9	176.9
Co-O(**2**)	1.916	1.915	2.003	2.028	2.028	Co-O(**2**)	1.872	1.872	1.931	1.928	1.925
Co-O(**3**)	1.901	1.909	1.943	1.943	1.944	Co-O(**4**)	1.935	1.941	1.985	1.984	1.982
Co-O(3)	1.956	1.963	2.011	2.013	2.012	Co-O(4)	2.046	2.058	2.263	2.260	2.265
Co-O(*3*)	3.901	3.900	3.780	3.732	3.733						
Al-Co	2.743	2.750	2.792	2.789	2.790	Al-Co	2.773	2.774	2.793	2.800	2.798
E_{ads}	1.226	1.125	0.757	0.768	0.756	E_{ads}	1.803	1.666	1.145	1.140	1.333
ν_{C-O}	2067(2089)	2066(2088)	2279(2302)	2277(2301)	2281(2304)	ν_{C-O}	2076(2098)	2081(2103)	2275(2313)	2298(2322)	2302(2326)
$\Delta\nu$	-40	-40	78	75	77	$\Delta\nu$	-31	-25	74	96	98
	Configuration 3						Configuration 6				
S	1/2	1/2	3/2	3/2	3/2	S	1/2	1/2	3/2	3/2	3/2
C-O	1.146	1.148	1.121	1.122	1.121	C-O	1.149	1.149	1.121	1.121	1.121
Co-C	1.782	1.782	2.058	2.055	2.058	Co-C	1.776	1.779	2.048	2.048	2.052
∠Co-C-O	172.6	172.8	172.6	172.2	172.7	∠Co-C-O	177.9	177.0	178.1	177.8	178.0
Co-O(**1**)	1.947	1.953	2.037	2.037	2.036	Co-O(**2**)	1.868	1.868	1.941	1.939	1.936
Co-O(**4**)	1.911	1.913	1.939	1.938	1.941	Co-O(**4**)	1.922	1.949	1.989	1.992	1.990
Co-O(2)	2.100	2.102	2.275	2.275	2.264	Co-O(4)	1.987	2.011	2.136	2.149	2.150
Al-Co	2.773	2.775	2.823	2.820	2.819	Al-Co	2.810	2.806	2.826	2.827	2.825
E_{ads}	1.661	1.534	1.152	1.213	1.121	E_{ads}	2.067	1.873	1.178	1.189	1.126
ν_{C-O}	2039(2063)	2036(2058)	2301(2325)	2297(2321)	2302(2325)	ν_{C-O}	2081(2102)	2083(2104)	2310(2336)	2298(2321)	2300(2323)
$\Delta\nu$	-68	-70	100	95	98	$\Delta\nu$	-26	-23	109	96	96

to about 2.3 Å. In a ring with only one Al, the coordination is reduced to three. In configurations 3 to 6 the cation is always threefold coordinated, with the third bond to a non-activated oxygen slightly longer than the two to activated atoms. Here the change of the cation-coordination depends strongly on the choice of the functional: in the GGA all three Co(II)-O bonds are slightly elongated, with hybrid functionals the bond to the non-activated oxygen atom is always contracted by about 0.1 Å while the bonds to the activated oxygens remain unchanged or are also slightly reduced. Hence the adsorption energies and geometries reflect the different spin states of the CO-Co(II)-chabazite complexes. The elongation of the Co(II)-CO distances in particular is clearly correlated to the charge redistribution discussed above.

The choice of the functional also strongly influences the geometry of the adsorbate. In the GGA the C-O bond lengths are increased compared to both the free molecule and to the positively charged carbonyl, while with hybrid functionals they are slightly reduced. The Co-C distance is increased compared to the free Co-carbonyl for configuration 1 (by $\sim$ 0.1 Å in the GGA and by $\sim$ 0.2 Å with hybrid functionals). For configurations 2 to 6 the GGA predicts an almost unchanged Co-C distance while with hybrid functionals an elongation by about 0.2 Å is calculated. The Co-C-O angle is almost straight, only for a cation location in a 6MR a very modest canting of the molecule relative to the Co-C bond is calculated, which is larger in the GGA.

Stretching frequencies

The changes in the C-O bond lengths are also reflected in the stretching frequencies. With hybrid functionals we calculate a blue-shift increasing from about +63 cm^{-1} for configuration 1 to +100 to +110 cm^{-1} for configurations 3 to 6. In the GGA we find a red-shift of at least -25 cm^{-1}. For Co(II)-ZSM5 Góra-Marek *et al.*[191] reported a single stretching mode at 2204 cm^{-1}, blue-shifted by +61 cm^{-1}, for Co(II)-mordenite Gutierrez *et al.*[214] found two distinct stretching modes, at 2205 cm^{-1} (blue-shifted by +61 cm^{-1}) and assigned to α-sites (in a 6MR), and at 2191 cm^{-1} (shifted by +48cm^{-1}) and assigned to cations in β-sites (in a 8MR). The small differences between the two different zeolites different cation locations suggest that similar frequencies can be expected also for Co(II) chabazite. The blue-shift found experimentally is reproduced only with hybrid functionals, and for the most stable location in a 6MR the calculated shift is in good agreement with experiment. For the absolute values of the frequencies we find a strong underestimation by about -120 cm^{-1} in the GGA, while hybrid functional overestimate by about 60 to 80 cm^{-1}.

The stretching frequencies are also influenced by the spin-state. If we calculate the frequencies using the PBE0 functional for the excited low-spin-state with S=1/2, we find for configurations 1 to 6 frequencies of 2236(32), 2230(26), 2268(64), 2270(66), 2258(54), 2257(53) cm^{-1}, respectively (frequency shifts relative to gas-phase CO are given in parentheses). The reduced blue-shift is in better agreement with the experiment on other Co(II)-zeolites and the error in the absolute values is also strongly reduced. This is another hint that CO induces a spin-crossover to a low-spin state in Co(II)-zeolites.

Bonding and electronic structure

Fig. 7.6 shows the total and local electronic DOS of Co(II)-chabazite in configuration 3, calculated using different functionals and for different spin states (fixed moment calculation) before and after CO adsorption. Formation of an excited low-spin states is achieved by shifting the $3d$ majority DOS to lower and the minority DOS to lower binding energies. Because hybrid functionals produce a much larger splitting between occupied and empty states, the empty $3d$ states are located around the center of the fundamental gap of the zeolite and the occupied states lie at least 2.5 eV below the VBM, for both high and low spin. In contrast in the GGA both occupied and empty states are distributed close to the Fermi level. The graphs demonstrate that adsorbate bonding proceeds in both cases by σ-donation to the cation. In the high-spin states the position of the $3d$ states at higher binding energies facilitates σ-donation, especially with hybrid functionals. In the GGA a low-spin state is favored through a small shift of the both majority and minority states to higher binding energies.

Summary - CO adsorption

The results described in the preceding section reveal some common trends. The adsorption energy decreases almost linearly with increasing stability of the cation location. The binding energy to the cation embedded in the zeolite is always much lower than the binding energy in a positively charged free carbonyl. Only for Cu(I)-chabazite the binding energy calculated for the least stable configuration approaches the value in the free carbonyl. For Cu cations the trend is summarized in Fig. 7.7(a). For Cu(I) the data collected within the GGA and using hybrid functionals follow a common trend, in this case the adsorption energy calculated with hybrid functionals is always significantly lower and in better agreement with experiment.

In contrast, for Cu(II) the adsorption energies calculated using both types of functionals cover almost the same range, but we note a large difference in the cation stability. The adsorption energies calculated in the GGA continue the trend seen for Cu(I)-chabazite, while with hybrid functionals the decrease of the adsorption energies with increasing stability of the cation sitting is less pronounced. Still, the difference in the adsorption energies is largest for the most stable cation locations where we calculate very low adsorption energies with both types of functionals. For locations of the Cu(II) cation in a 8MR we find adsorption energies around 1.5 eV, only slightly lower with hybrid functionals than in the GGA and of the same order of magnitude than for Cu(I). The screening of exact exchange in the hybrid functionals plays only a minor role for the adsorption energies. This means that the observed instability of Cu(II)-carbonyls is reproduced with both types of functionals, but only for cation locations in a 6MR, not for less stable sites in the larger 8MR.

The situation is more complex for adsorption in Co(II)-chabazite, where in addition to the different stability of the possible framework locations the differences in the spin-excitation energies play an important role. Cation stability increases by about 1.2 to 1.4 eV with hybrid functionals, spin-excitation energies by 0.4 to 0.5 eV, adsorption

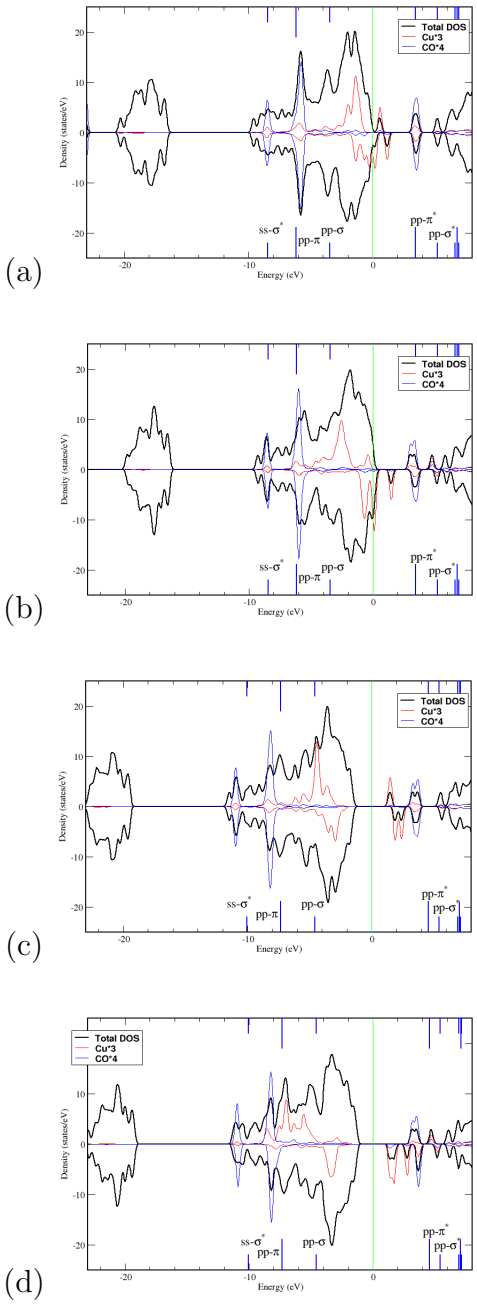

Figure 7.6: Total and local DOS for Co(II)-chabazite in configuration 3 before (left) and after CO-adsorption (right), compared to the molecular eigenstates of CO. Panels (a,b) show the results calculated with PBE functionals for spin S=1/2 (a) and S=3/2 (b). Panels (c,d) presents the results derived using the screened hybrid functional HSE06 for spin S=1/2 (c) and S=3/2 (d). The local Cu DOS (red) is multiplied by a factor of three, the local CO DOS by a factor of 4 for reasons of better visualization. C.f. text.

energies decrease by 0.3 to 0.6 eV - in this case the difference is largest for the least stable cation sites. CO adsorption is predicted to induce a high-spin to low-spin (from S=3/2 before to S=1/2 after adsorption) in the GGA, but not with hybrid functionals. Still, the correlation between adsorption energy and cation stability follows roughly the same linear trend with both functionals. The spin-crossover induced in the GGA for configurations 2 to 6 leads to slightly larger adsorption energies.

For CO adsorbed on Cu(I)-chabazite only hybrid functionals produce the blue-shift of the C-O stretching mode found experimentally for other Cu(I)-zeolites. For CO-Cu(II)-chabazite both types of functionals predict a blue-shift, but the larger shift calculated with hybrid functional is in better agreement with observations. For CO-Co(II)-chabazite only hybrid functionals yield the blue-shift found in other Co(II)-zeolites and in the isostructural Co(II)-SAPO34, while a red-shift is predicted in the GGA. However, for the high-spin state found with hybrid functionals the blue-shift is overestimated. Better agreement of the calculated frequency shift with experiment is found in fixed-moment calculations for the low-spin state. The absolute values of the frequencies however, are always much larger with hybrid functionals than in the GGA. The absolute value of the error is larger with hybrid functionals for Cu(I), about equal for Cu(II), and smaller for Co(II)-chabazite.

We have already mentioned that for carbonyls the stretching frequency of adsorbed CO varies approximately linear with the charge of the transition metal. It has been argued that this relation may be used to estimate the effective charge of the cation in the zeolite. In II we have used a Bader analysis[148, 149] to determine the cation charge - we are hence able to verify whether this relation holds. For Cu(I)-chabazite charges of about 0.73 and 0.78 have been derived using a Bader analysis in the GGA and using hybrid functionals, respectively. Comparison of the calculated frequency with that determined by linear interpolation of the stretching frequency as a function of the charge of the carbonyl leads to an estimated cation charge of about 0.57 and 0.68, respectively. For Cu(II)-chabazite the Bader analysis suggests charges of about 1.05 (1.31) with GGA (hybrid) functionals, averaged over all configurations. The comparison with the interpolated frequencies of the carbonyls yields significantly lower values of 0.82(0.86). Higher average charges on the cation of about 1.27 (1.48) are calculated for Co(II)-chabazite, extrapolation of the frequencies calculated for Co-carbonyl yields lower charges of 0.79(1.15).

For all investigated species, from gas-phase CO over the neutral and charged carbonyls to CO adsorbed in the zeolite we find a roughly linear dependence of the stretching frequency on the C-O distance, see Fig. 7.8. This holds in the GGA as well as with hybrid functionals. Only if the charged carbonyls are included, the frequency ranges calculated in the GGA and with hybrid functionals overlap. This demonstrates that the distance-frequency correlation has some universal character within DFT which remains unchanged if, as in hybrid functionals, a certain fraction of exact exchange is mixed to the DFT functional.

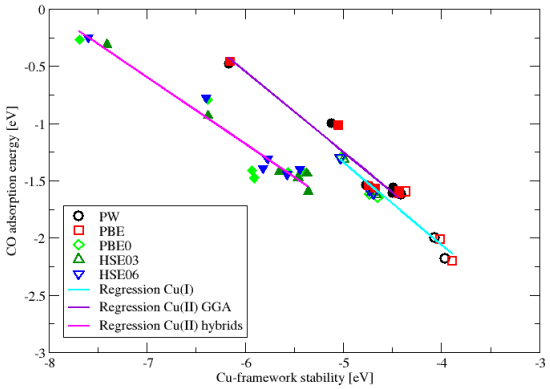

(a)

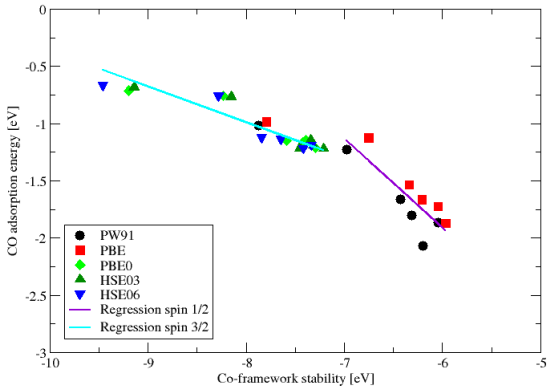

(b)

Figure 7.7: CO adsorption energy E_{ads} versus binding energy between cation and framework E_{cation}: (a) for Cu(I)- (open symbols) and Cu(II)-chabazite (full symbols) and (b) for Co(II)-chabazite, calculated using different functionals (see the color code given in the inset). Cf. text.

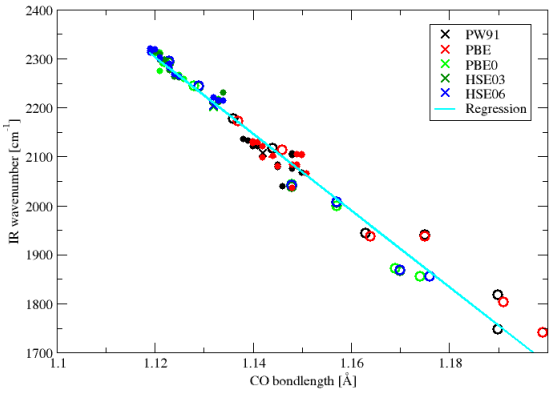

Figure 7.8: Correlation between C-O bond length R_{C-O} and stretching frequency ν_{C-O} for the gas-phase molecule (crosses), neutral and charged Cu- and Co-carbonyls (open circles) and CO adsorbed in Cu(I)-, Cu(II)- and Co(II)-exchanged chabazite (full dots), calculated using different exchange-correlation functionals (see the color-code given in in the inset). The straight lines show the linear correlation determined via a least-square fitting. Cf. text.

7.5 Adsorption of NO

For the adsorption of CO in transition-metal exchanged chabazite we have found that the dominant binding mechanism is electron donation from the molecular σ state to the d_σ states of the cation. Back-donation to the empty $\pi^\star$ states of the molecule plays only a minor role, and is even less important with hybrid functionals because of the increased HOMO-LUMO ($\sigma - \pi^\star$) gap. In addition, the larger exchange splitting of the cation states predicted by hybrid functionals plays an important role - this is most evident for Co(II)-chabazite where a spin-crossover to a low-spin state, induced by CO adsorption, is predicted in the GGA for most configurations while with hybrid functionals the high-spin state remains preferred.

This facet of the bonding mechanism can be studied in even more detail by investigating the adsorption of NO. In the NO molecule the antibonding $\pi^\star$ state is partially occupied by one electron. As the partially occupied state is pinned at the Fermi level, electrons can be donated or accepted by the $\pi^\star$ state. Due to the presence of an unpaired electron the NO molecule is paramagnetic. The molecular magnetic moment can combine in different ways with the moment of the cation - the magnetic moment of the adsorption complex in the zeolite can be either reduced or enhanced. Because of the tendency of hybrid functionals to favor high-spin states we expect a significant influence of the choice of the functional on the spin-density of the adsorption complex.

Another important difference is the formation of a bent geometry in nitrosyls and

NO adsorption complexes, in contrast to the straight geometry found for CO. Because the partially occupied $\pi^\star$ state is rather close in energy to the d_σ states, but their interaction is symmetry-forbidden at a linear geometry, a reduced Cu(Co)-N-O angle is favored.

NO adsorbed on Cu(I)-chabazite

Structure and energetics

Our results for the adsorption of NO on Cu(I)-chabazite are summarized in Table 7.9. The adsorption energy of NO in Cu(I)-chabazite varies in the GGA between 1.3 eV for a cation in a 6MR and 1.9 eV for a location in a 8MR, with hybrid functionals the adsorption energies are reduced to 0.9 to 1.2 eV. The adsorption energies are lower than the bond-dissociation energy in a free charged $[CuNO]^+$ nitrosyl. No experimental results are available for Cu(I)-chabazite, but for NO in Cu(I)-MFI Gervasini *et al.* [215] measured an heat of adsorption at 303 K of 1.05 eV. Davidová *et al.*[211] determined using the B3LYP functional for cluster models of NO in Cu(I)-MFI adsorption energies of 0.9 eV for a cation in a 6MR and 1.25 eV for a location in larger ring

After NO adsorption the Cu(I) cation is always coordinated to only two activated framework oxygens. This means that for configurations 1 and 2 the Cu(I)-O coordination is reduced, the low adsorption energy results at least partially from the adsorption-induced deformation of the cation coordination. Cu(I)-O bond lengths are elongated, but less than upon CO adsorption. Cu-N distances are smaller than Cu-C distances by about 0.01 Å. The influence of the choice of a functional on the cation coordination is very modest.

N-O bond-lengths are increased compared to the free molecule, whereas in free, charged $[CuNO]^+$ they are almost unchanged. Cu(I)-N distances are slightly increased compared to the free, charged nitrosyl in configuration 1, but are identical for configurations 2 and 3. The Cu-N-O angle is also the same in the free nitrosyl and in the adsorption complex in the zeolite.

Stretching frequencies

To the elongation of the N-O distances corresponds a pronounced red-shift of the N-O stretching frequency of about -90 cm^{-1} in the GGA and -80 cm^{-1} using hybrid functionals. This is in contrast to the blue-shift calculated for $[CuNO]^+$ with hybrid functionals. For NO-Cu(I)-chabazite no experimental information is available, but for NO in Cu(I)-ZSM5 Broclawik *et al.*[188] reported a stretching frequency of 1809 cm^{-1}, red-shifted by -67 cm^{-1}. The results for NO in Cu(I)-chabazite may also be compared with those for NO in Cu(I)-SAPO34 - the framework of this aluminosilicate is isostructural to that of chabazite. The experimental[216, 217] stretching frequency is 1805 cm^{-1}, red-shifted by -73 cm^{-1}. The periodic DFT calculations of Uzunova *et al.*[118] determined a red-shift of about -105 cm^{-1} in the GGA, and of -80 cm^{-1} with the unscreened hybrid functional. Given the small variation of the frequency

Table 7.9: Structure, energetics, and stretching frequencies of NO adsorbed at an extraframework Cu(I) cation in chabazite, calculated for different cation-locations and using different exchange-correlation functionals. Distances are given in Å, angles in deg, adsorption energies in eV/molecule, and frequencies in cm^{-1}. The calculated frequencies include anharmonic corrections, harmonic frequencies are given in parentheses. $\Delta\nu$ gives the frequency shift relative to NO in the gas phase.

	PW91	PBE	PBE0	HSE03	HSE06
	Configuration 1				
N-O	1.183	1.185	1.164	1.165	1.164
Cu-N	1.762	1.764	1.781	1.781	1.782
∠Cu-N-O	144.6	143.7	144.0	143.4	143.8
Cu-O(**2**)	2.035	2.030	2.041	2.035	2.035
Cu-O(**3**)	1.991	1.997	1.997	2.003	2.004
Cu-O(3)	2.915	2.950	2.901	2.936	2.940
Cu-O(*3*)	3.821	3.756	3.194	3.222	3.222
Al-Cu	2.772	2.776	2.742	2.747	2.749
E_{ads}	1.298	1.279	0.875	0.895	0.887
ν_{N-O}	1782(1805)	1800(1825)	1949(1976)	1945(1972)	1950(1977)
$\Delta\nu$	-96	-88	-76	-79	-77
	Configuration 2				
N-O	1.183	1.185	1.164	1.164	1.164
Cu-N	1.758	1.759	1.779	1.777	1.776
∠Cu-N-O	144.2	144.5	139.0	139.5	141.5
Cu-O(**1**)	1.964	1.968	1.960	1.960	1.962
Cu-O(**4**)	2.043	2.042	2.050	2.050	2.051
Cu-O(2)	3.045	3.022	2.887	2.910	2.949
Al-Cu	2.820	2.822	2.790	2.792	2.793
E_{ads}	1.709	1.690	1.169	1.176	1.159
ν_{N-O}	1785(1808)	1805(1831)	1945(1972)	1941(1969)	1950(1977)
$\Delta\nu$	-93	-83	-80	-83	-77
	Configuration 3				
N-O	1.183	1.184	1.164	1.165	1.164
Cu-N	1.755	1.754	1.775	1.773	1.773
∠Cu-N-O	148.4	150.3	145.6	146.1	146.7
Cu-O(**2**)	2.016	2.013	2.009	2.012	2.011
Cu-O(**4**)	1.992	1.997	1.999	1.999	1.998
Cu-O(4)	3.135	3.135	3.122	3.020	3.022
Al-Cu	2.796	2.797	2.781	2.782	2.781
E_{ads}	1.876	1.882	1.254	1.219	1.197
ν_{N-0}	1789(1811)	1814(1839)	1950(1977)	1947(1974)	1953(1979)
$\Delta\nu$	-89	-74	-75	-77	-74

with the host material it seems to be legitimate to expect similar values for Cu(I)-chabazite. This would mean that the absolute value of the frequencies calculated in the GGA are definitely more accurate, although the smaller red-shift resulting from hybrid-functionals could be somewhat closer to experiment.

Electronic structure and bonding

The electronic density of states (see Fig. 7.9 for cation location as in configuration 1, the DOS before NO adsorption is given in Fig.2 of II) reflects the bonding mechanism and the broken symmetry of the Cu(I)-NO complex. The spin of the adsorption complex is S=1/2, contributed by the paramagnetic molecule. A significant exchange splitting is found for the electronic eigenstates localized on the adsorbate, but it is almost absent on the cation. The dominant interaction is between the partially occupied $\pi^\star$ state and the hybridized $3d-4s$ band of the cation. Due to the bent geometry the rotational symmetry of the $\pi^\star$ state is broken, we now have to distinguish between $\pi^\star$ states lying in the Cu(I)-N-O plane and extending perpendicular to it, with the Fermi level falling between the two states. The spin of the NO molecule is conserved. In addition we note a weak interaction of the molecular σ state with the cation $3d$ states. The Cu-$3d$ states which lye above the VBM before adsorption are now merged with the highest framework states and broadened. The main difference between the GGA and hybrid functionals is much larger gap between the occupied and empty spin-polarized $\pi^\star$-states

The charge-flow graph presented in Fig. 7.10 shows the important role of intramolecular re-hybridization. Due to the broken rotational symmetry the degeneracy of the $\pi^\star$ states is lifted, the occupied $\pi^\star$ states extend perpendicular to the Cu-N-O plane. Electrons from both molecule and cation contribute to form a covalent Cu-N bond.

A Bader analysis has been used to determine the local charges of cation and adsorbate. For the cation we calculate an average positive charge of 0.92 ± 0.005 in the GGA and 0.915 ± 0.006 with hybrid functionals, increased from average values of 0.73 and 0.78 before adsorption. The difference corresponds to a negative charge on the molecule of -0.202 ± 0.005 and -0.148 ± 0.01 in the GGA and with hybrid functionals and hence to an increased occupation of the $\pi^\star$ state explaining the red-shift of the stretching mode.

NO adsorbed on Cu(II)-chabazite

Our results for NO adsorption on Cu(II)-chabazite are compiled in Table 7.10. Irrespective of the location of the cation and of the choice of the functional, the ground-state is always a singlet, S=0. This means that that the magnetic moments of the molecule and of the divalent cation compensate each other. How the spin-compensation is achieved, however, depends on the choice of the functional. Within the GGA where electrons are rather localized, the entire adsorption complex is completely non-magnetic. With hybrid functionals electrons are more localized and non-vanishing spin-densities of opposite sign are found on both the molecule and the cation, as illustrated in Fig. 7.11.

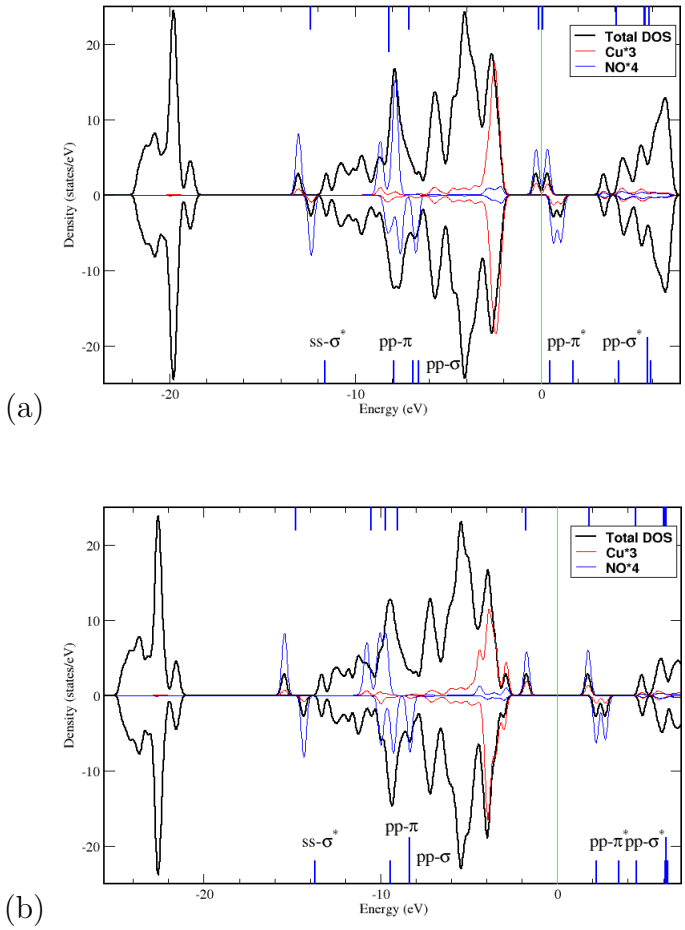

Figure 7.9: Total and local electronic DOS for NO adsorbed on Cu(I)-chabazite in configuration 1, calculated using the PBE (a) and PBE0 (b) functionals, compared to the molecular orbital scheme of the free NO molecule. Partial Cu DOS (red) is multiplied by a factor of three, partial NO DOS by a factor of 4 for reasons of better visualization. For discussion c.f. text.

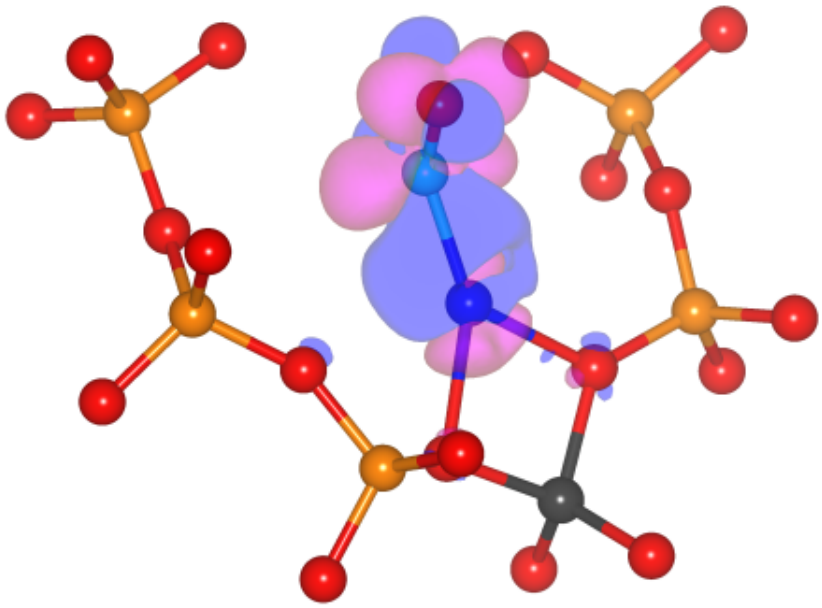

Figure 7.10: Charge-flow (difference electron density) induced by NO adsorption on Cu(I)-chabazite, configuration 2. Electrons flow from the molecular $\pi^\star$-state extending within the Cu(I)-N-O plane to states extending perpendicular to the planes. On the Cu(I)-cation the d_σ state is electron-depleted. Electrons from both the cation and the adsorbate contribute to the formation of a Cu(I)-N bond. For explanation of symbols, see Fig. 7.1. C.f. text.

Table 7.10: Structure, energetics, and stretching frequencies of NO adsorbed at an extraframework Cu(II) cation in chabazite, calculated for different cation-locations and using different exchange-correlation functionals. Distances are given in Å, angles in deg, adsorption energies in eV/molecule, and frequencies in cm^{-1}. The calculated frequencies include anharmonic corrections, harmonic frequencies are given in parentheses. $\Delta\nu$ gives the frequency shift relative to NO in the gas phase.

	PW91	PBE	PBE0	HSE03	HSE06		PW91	PBE	PBE0	HSE03	HSE06
	Configuration 1						Configuration 4				
N-O	1.146	1.149	1.137	1.137	1.137	N-O	1.143	1.146	1.132	1.132	1.134
Cu-N	1.857	1.858	2.036	2.038	2.050	Cu-N	1.732	1.735	1.891	1.890	1.913
∠Cu-N-O	131.8	131.8	127.1	126.9	127.6	∠Cu-N-O	156.4	152.9	135.1	135.3	132.3
Cu-O(**2**)	2.066	2.071	1.987	1.992	1.989	Cu-O(**1**)	1.889	1.892	1.914	1.917	1.921
Cu-O(**3**)	2.019	2.024	1.987	2.005	2.004	Cu-O(**4**)	1.963	1.973	1.923	1.924	1.927
Cu-O(3)	2.866	2.871	2.767	2.753	2.743	Cu-O(2)	2.802	2.710	2.340	2.344	2.289
Cu-O(*3*)	1.970	1.974	1.951	1.951	1.947						
Al-Cu	2.926	2.933	2.878	2.876	2.877	Al-Cu	2.791	2.789	2.756	2.761	2.760
E_{ads}	1.130	1.001	0.269	0.295	0.228	E_{ads}	2.027	1.931	1.322	1.343	1.305
ν_{N-O}	1908(1921)	1929(1942)	2064(2106)	2060(2101)	2075(2103)	ν_{N-O}	1957(1980)	1975(2001)	2104(2130)	2102(2146)	2115(2143)
$\Delta\nu$	30	41	39	36	48	$\Delta\nu$	79	87	79	78	88
	Configuration 2						Configuration 5				
N-O	1.147	1.150	1.138	1.138	1.137	N-O	1.146	1.151	1.140	1.118	1.140
Cu-N	1.797	1.797	1.960	1.956	1.972	Cu-N	1.717	1.715	1.955	1.711	1.974
∠Cu-N-O	136.9	137.0	131.3	131.3	131.6	∠Cu-N-O	170.2	166.1	127.2	171.1	125.8
Cu-O(**2**)	2.087	2.087	2.005	2.004	2.007	Cu-O(**2**)	1.923	1.930	1.890	1.900	1.887
Cu-O(**3**)	1.930	1.934	1.880	1.883	1.881	Cu-O(**4**)	1.923	1.916	1.996	1.897	2.004
Cu-O(3)	2.030	2.035	1.981	1.986	1.981	Cu-O(4)	3.102	3.107	2.128	3.034	2.147
Cu-O(*3*)	3.883	3.886	3.727	3.692	3.681						
Al-Cu	2.767	2.770	2.715	2.709	2.715	Al-Cu	2.767	2.767	2.779	2.745	2.782
E_{ads}	1.491	1.419	0.643	0.790	0.627	E_{ads}	1.999	1.857	1.148	1.279	1.101
ν_{N-O}	1907(1929)	1929(1952)	2070(2112)	2069(2108)	2085(2113)	ν_{N-O}	1965(1989)	1971(1990)	2069(2096)	2198(2227)	2072(2099)
$\Delta\nu$	29	41	45	45	58	$\Delta\nu$	87	83	44	174	45
	Configuration 3						Configuration 6				
N-O	1.146	1.147	1.127	1.128	1.135	N-O	1.143	1.146	1.138	1.139	1.137
Cu-N	1.763	1.760	1.830	1.831	1.885	Cu-N	1.730	1.724	1.957	1.965	1.963
∠Cu-N-O	141.0	142.2	138.9	137.8	134.3	∠Cu-N-O	164.8	168.5	128.9	129.4	128.9
Cu-O(**1**)	1.935	1.928	1.924	1.932	1.949	Cu-O(**2**)	1.936	1.933	1.906	1.911	1.903
Cu-O(**4**)	1.968	1.965	1.920	1.924	1.919	Cu-O(**4**)	1.920	1.927	1.966	1.964	1.963
Cu-O(2)	2.901	2.887	2.748	2.715	2.748	Cu-O(4)	2.854	2.958	2.056	2.052	2.060
Al-Cu	2.802	2.798	2.756	2.758	2.755	Al-Cu	2.792	2.780	2.783	2.788	2.779
E_{ads}	2.174	2.114	1.285	1.316	1.289	E_{ads}	2.152	2.116	1.324	1.330	1.318
ν_{N-O}	1927(1954)	1954(1989)	2104(2154)	2099(2141)	2095(2123)	ν_{N-O}	1963(1980)	1990(2014)	2080(2111)	2072(2104)	2083(2111)
$\Delta\nu$	49	66	79	75	68	$\Delta\nu$	85	102	55	48	56

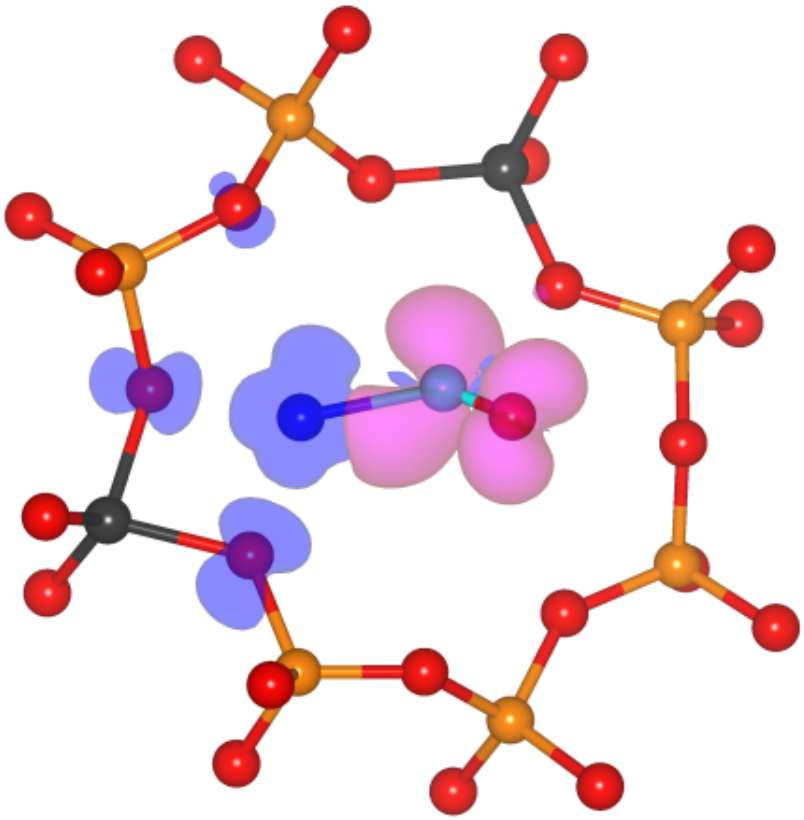

Figure 7.11: Spin densities for NO adsorbed to Cu(II)-chabazite, configuration 3, calculated using PBE0. N atoms are displayed in cyan, Si in orange, O in red, TM in blue and Al in dark grey. Red constant-density surfaces surround regions of spin-down and blue surfaces surround regions of spin up electron density. Contour values are 2.5×10^3 electrons/Å^3. C.f. text.

A negative spin-density is found on the molecule, it has the symmetry of a $pp\pi$ state extending in the Cu-N-O plane. A positive, more delocalized spin-density with $pd\sigma$ character is located on the cation and the two bonding framework oxygens. These differences are also reflected in the structural, energetic and dynamical properties of the adsorption complexes.

Structure and energetics

The adsorption energy of NO in Cu(II)-chabazite varies strongly with cation location and functional. Within the GGA, we calculate a much higher adsorption energy for NO than for CO a cation located in a 6MR, whereas with hybrid functionals a very weak adsorption is predicted for both NO and CO. However, even within the GGA, the adsorption energy for NO is still somewhat higher in Cu(I)- than in Cu(II)-chabazite.

This means that the preferred bonding of NO to Cu(II), in contrast to CO binding much more strongly to Cu(I), is not reproduced with any of the functionals as long as the cation resides in a 6MR. Only for cations located in a 8MR (configurations 3 to 6) we find a higher adsorption energy for NO than for CO, irrespective of the functional.

After NO adsorption a Cu(II) cation in a 6MR is threefold coordinated to framework oxygens. The Cu(II)-O distances are shorter than after CO adsorption. Cu-N distances are also much shorter than Cu-C distances, especially in configuration 1. These differences are more pronounced with hybrid functionals. In configurations 3 to 6 the cation-oxygen coordination is only twofold, with Cu-O distances that are shorter than before NO adsorption and after CO adsorption.

N-O distances are reduced compared to the free molecule. The Cu-N-O angles depend strongly on the cation location and the choice of the functional. For a cation in a 6MR the angle measures about 130°, it is slightly lower with hybrid functionals than in the GGA. For configurations 3 to 6, the Cu-N-O angle varies between 140° and 170°. With hybrid functionals we find that two very different adsorption geometries [one with a strongly bent Cu-N-O angle of less than 130°, a large Cu-N distance and three (two strong and one intermediate) Cu-O bonds, and a nearly linear geometry combined with much shorter Cu-N and N-O distances and only two Cu-O bonds shorter than 2.7 Å] are very close in energy - this is most evident in configuration 5 where we find a bent geometry with the PBE0 and HSE06 functionals and an almost linear geometry (which is very close to that found in the GGA) with the HSE03 functional. With PBE0 and HSE06 the bent geometries are lower in energy by 52 meV and 13 meV, respectively. For the remaining configurations, the bent geometry is always preferred with hybrid functionals, although the difference between the geometries found in the GGA and with hybrid functionals is not as pronounced as for configuration 5.

Stretching frequencies

Because of the reduced N-O distances, a blue-shift of the stretching mode could be expected. Within the GGA we calculate frequencies of 1908(1907) cm^{-1}, blue-shifted by 30(29) cm^{-1} for configurations 1(2) with the PW91 functional and $\nu_{N-O} = 1929 cm^{-1}$, $\Delta\nu = 41 cm^{-1}$ using PBE. For configurations 3 to 6 the blue-shift increases to up to 100 cm^{-1}. With hybrid functionals we find stretching frequencies of 2064(2070) cm^{-1}, blue-shifted by 39(45) cm^{-1} in configurations 1(2) using PBE0. In configurations 5 and 6 where we find large differences in the Cu-N-O angles in dependence on the functional, larger blue-shifts are found in the GGA. This is in contrast to the results for CO adsorption where hybrid functionals lead to much larger blue-shifts than the GGA. The nearly straight geometries which are stable or at least metastable with hybrid functionals lead to stretching frequencies which are at least 120 cm^{-1} higher than those for the bent geometries.

For NO adsorbed in Cu(II)-ZSM5 Broclawik *et al.*[188] report a stretching frequency of 1905 cm^{-1}, blue-shifted by 29 cm^{-1} in contrast to the pronounced red-shift experienced by NO molecules adsorbed on Cu(I) cations in the same zeolite. Kefirov *et al.*[23] assigned IR bands at 1905 and 1912 cm^{-1} to NO adsorbed on isolated Cu(II) cations

in BEA. Hadjiivanov and Dimitrov[195] reported a stretching frequency of 1888 cm^{-1}, assigned to a Cu(II)-NO nitrosyl which decomposes easily upon heating. If we expect similar N-O stretching frequencies for NO in Cu(II)-chabazite, we have to conclude that agreement with experiments is best for NO adsorbed on cations in a 6MR and calculations within the GGA.

Electronic structure and bonding

The different magnetic states of the adsorbate complex predicted in the GGA and by calculations using hybrid functionals appear clearly in the electronic DOS, see Fig. 7.12 and compare with Fig. 6 of II for the DOS before adsorption. In the GGA the entire system is predicted to be non-magnetic. The hybridization of the $\pi^\star$ state of NO with the $3d$ band of the Cu-cation quenches the spin-polarization of both. Empty antibonding states are found in a narrow band just above the Fermi level, the bonding states extend over a wide energy interval. Due to the adsorption the cation states are shifted to higher binding energies. The deeper σ and π states also hybridize with the $3d$ states, this interaction is stronger for the σ states which are shifted to higher binding energies. The broken symmetry due to the bent Cu(II)-N-O angle is reflected by the splitting of the π states.

The DOS calculated with hybrid functionals shows a clear signature of spin-polarization, with opposite signs of the exchange splitting on the cation and on the molecule. Only the minority $3d$ states of the cation hybridize with the $\pi^\star$ of the same spin direction. The bonding hybrids are concentrated just below the Fermi energy, whereas in the GGA they are spread to higher binding energies - this explains the large difference in the adsorption energies calculated with both types of functionals.

It is also interesting to examine the differences in the electronic spectra for the energetically nearly degenerate straight and bent geometries found with hybrid functionals for cation locations in an 8MR. Fig. 7.13 shows the DOS calculated with the PBE0 functional for configuration 5 where the stable solution has a Cu-N-O angle of 127°. Again only the spin-down σ-states hybridize with the spin-down $3d$ states. The different geometries of the adsorption complexes is reflected in the $3d$ band and in the molecular states. The bonding-antibonding splitting of the peaks derived from the $\pi^\star$ states is slightly larger for a bent geometry, contributing to its higher stability.

The charge-flow induced by NO adsorption influences also the zeolite framework. This effect is most pronounced in the GGA, see Fig. 7.14 for cations located in a 6MR and a 8MR with two Al atoms. The $\pi^\star$ orbital of the adsorbed NO is electron-depleted, electronic states centered on the cation are re-hybridized to form a strong covalent Cu(II)-NO bond. A Bader analysis shows a positive charge on the molecule, decreasing in the GGA from about 0.17 in configuration 1 to 0.12 in configuration 6, while with hybrid functionals we find a trend in the opposite direction with a charge increasing from about 0.16 for a cation in a 6MR to 0.29 for a site in a 8MR with a single Al atom. The decreased occupation of the $\pi^\star$ states correlates with the blue-shift of the stretching mode. In contrast, the charge on the cation is only weakly affected by NO adsorption. In the GGA the charge is unchanged or slightly increased by at

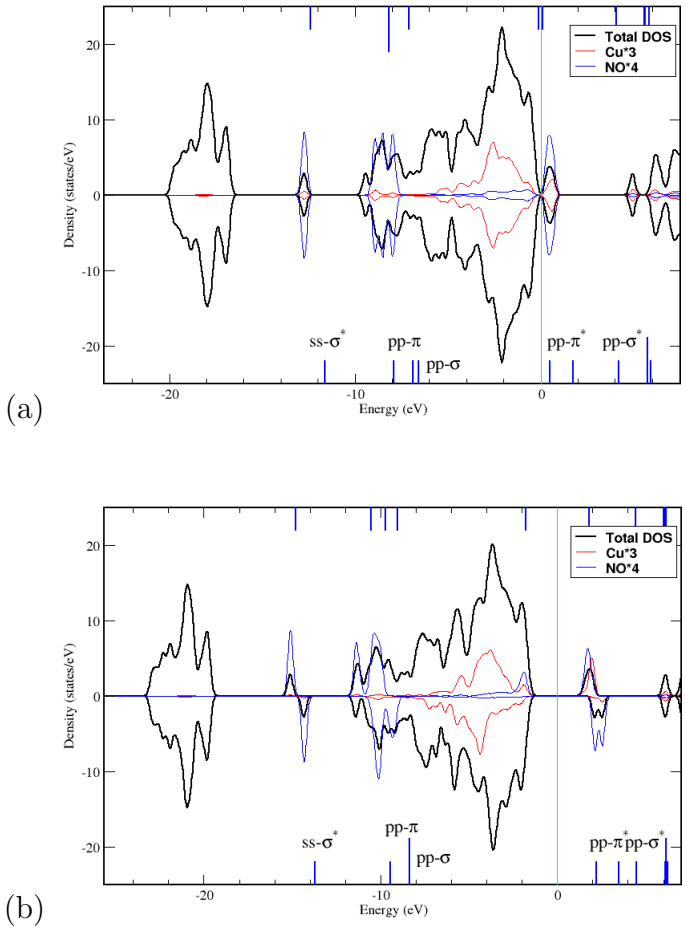

Figure 7.12: Total and local DOS for NO adsorbed in Cu(II)-chabazite in configuration 1, calculated using (a) PBE and (b) PBE0 functionals. Note that while both functionals predict zero spin for the Cu(II)-NO adsorption complex, with PBE spin-polarization is found to be completely absent while with the PBE0 hybrid functional molecule and cation cary non-vanishing spins of opposite sign. Partial Cu DOS (red) is multiplied by a factor of three, partial NO DOS by a factor of 4 for reasons of better visualization. C.f. text.

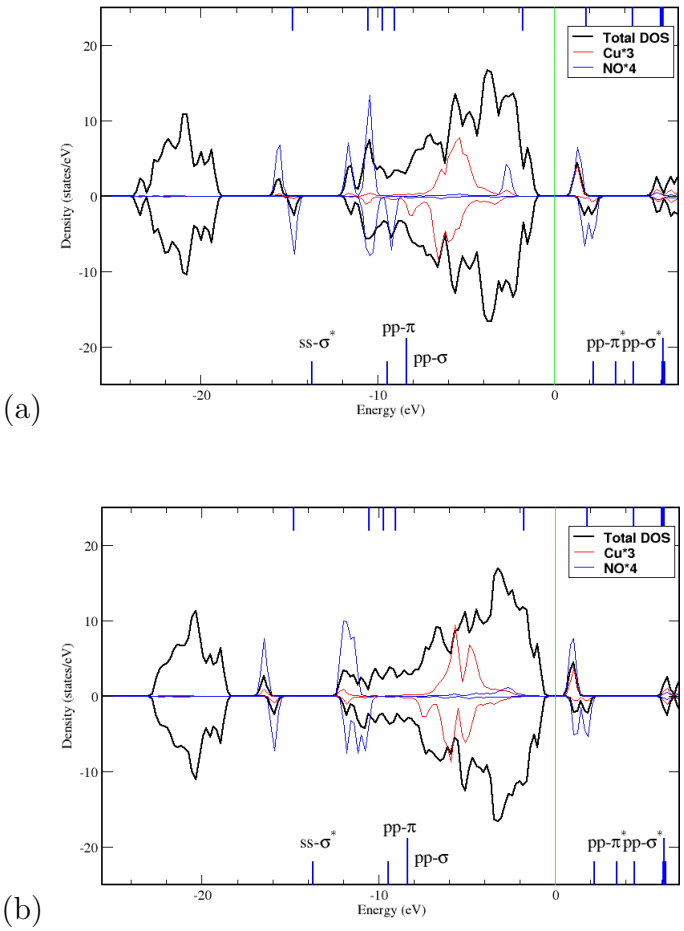

Figure 7.13: Total and local DOS for NO adsorbed in Cu(II)-chabazite in configuration 5, calculated using the PBE0 functional for a bent (a) and a straight (b) Cu-N-O angle. Note molecule and cation carry non-vanishing spins of opposite sign. Partial Cu DOS (red) is multiplied by a factor of three, partial NO DOS by a factor of 4 for reasons of better visualization. C.f. text.

most 0.08, with hybrid functionals we calculate effective charges reduced by 0.06 to 0.18. This means that electrons are also transferred to the framework (as also shown in Fig. 7.14).

The positive charge of the NO molecule induces a polarization of the activated O atom located on the opposite side of the 8MR and leads to an electrostatic interaction between molecule and framework. Hence in this configuration we find an example for the interaction of the adsorbate with the opposite wall of the zeolite cavity, which was proposed by Nachtigall *et al.*[192, 133, 193, 194] as an explanation for the observed blue-shift of the stretching frequency. However, it must be emphasized that such a polarization of the framework depends (i) on a substantial charge-transfer from the adsorbate to the cation and (ii) on a special geometry bringing the charged molecule close enough to an activated (and thus highly polarizable) oxygen atom. It is also clear that this effect is not of decisive importance for the blue-shift of the stretching mode.

The electron-transfer is also important for the understanding of the reduction of Cu(II) cations to Cu(I) when NO is desorbed at elevated temperatures, as reported by Hadjiivanov and Dimitrov[182]. It has been argued that desorption leads to the formation of an NO^+ ion capable of interacting with the framework and adsorbed NO molecules.

NO adsorbed on Co(II)-chabazite

For CO we have found that within the GGA adsorption induces a transition within the CO-Co(II) complex to a low-spin state with S=1/2 (except for configuration 1 where the cation interacts most strongly with the framework), while with hybrid functionals the high-spin state with S=3/2 remains preferred. For NO adsorption the situation is even more complex because the spin of the molecule can combine in different ways with that of the cation. Our calculations show that within the GGA low- and high-spin states of the NO-Co(II) adsorption complex are energetically almost degenerate. With the PW91 functional a low-spin state is the ground state for configurations 2, 5, and 6, with the PBE functional a low-spin ground state is found only for configuration 6. For all other configurations and with hybrid functionals for all six cation locations we find a spin of S=1 in the ground state. A spin of S=1 for the NO-Co(II) complex results from opposite spin orientations on the Co(II) cation with S=3/2 and on the paramagnetic molecule with S=1/2. A singlet state means that NO adsorption induces a high-spin to low-spin transition of the cation whose remaining spin is oriented antiparallel to that of the molecule. The spin-density distribution is illustrated for both cases in Fig. 7.15.

Structure and energetics

GGA and hybrid functionals yield very different results for the adsorption energies, especially for a cation location in a 6MR. Within the GGA the strength of adsorption increases with decreasing stability of the cation location, from E_{ads}= 1.92(1.77) eV in configuration 1 for PW91(PBE) to E_{ads}=2.95(2.74) eV in configuration 6. With hybrid functionals NO molecules bind only very weakly to cations in a 6MR, with adsorption

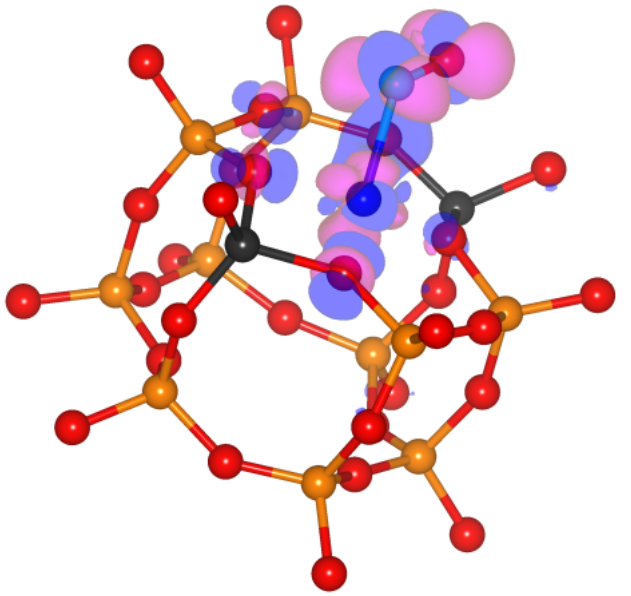

(a)

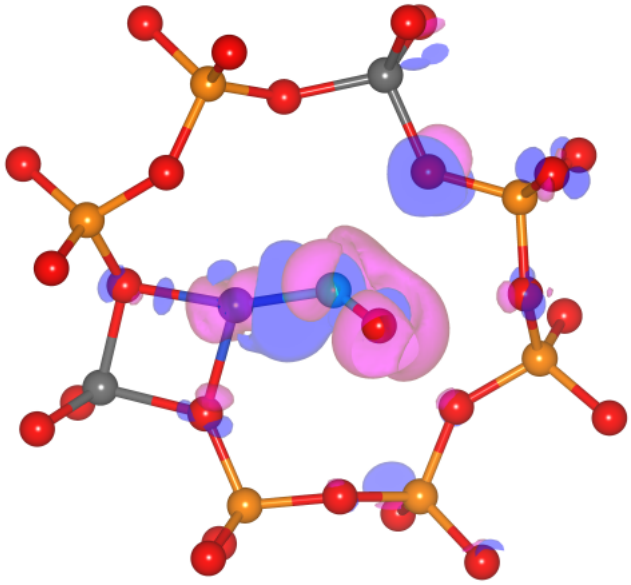

(b)

Figure 7.14: Charge-flow induced by NO adsorption to Cu(II)-chabazite for a cation in configuration 1 (a) and configuration 3 (b), calculated using the PBE functional. For the explanation of symbols, see Fig. 7.1. C.f. text.

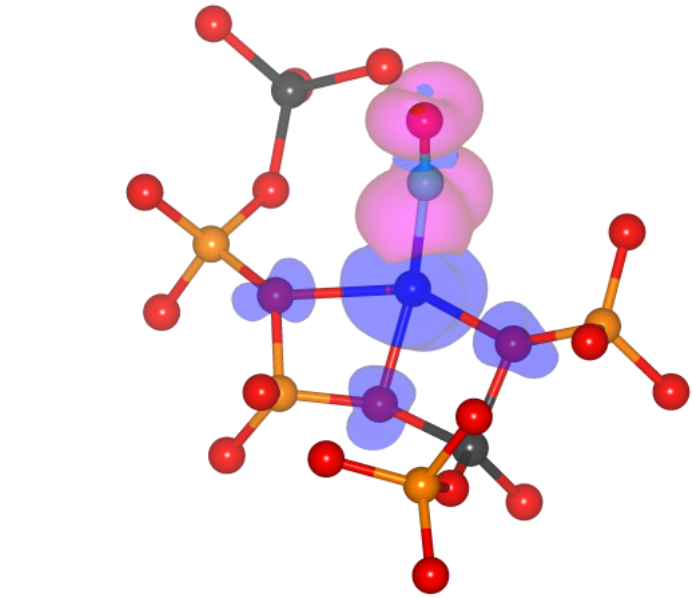

(a)

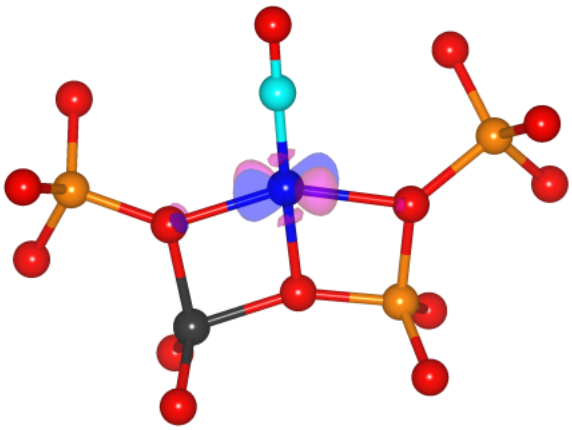

(b)

Figure 7.15: Spin-density distributions for the NO-Co(II) adsorption complex in chabazite. (a) Co(II) in configuration 3, calculated using HSE03, spin-triplet. Note the opposite spin orientations on cation and framework and on the adsorbed molecule. (b) Co(II) in configuration 6, calculated using the PBE, spin-singlet. For the explanation of symbols, see Fig. 7.11. C.f. text.

Table 7.11: Structure, energetics, and stretching frequencies of NO adsorbed at an extraframework Co(II) cation in chabazite, calculated for different cation-locations and using different exchange-correlation functionals. Distances are given in Å, angles in deg, adsorption energies in eV/molecule, and frequencies in cm^{-1}. The calculated frequencies include anharmonic corrections, harmonic frequencies are given in parentheses. $\Delta\nu$ gives the frequency shift relative to NO in the gas phase.

	PW91	PBE	PBE0	HSE03	HSE06		PW91	PBE	PBE0	HSE03	HSE06
	Configuration 1						Configuration 4				
N-O	1.157	1.160	1.149	1.149	1.149	N-O	1.151	1.154	1.135	1.135	1.135
Co-N	1.684	1.681	1.991	1.983	1.985	Co-N	1.673	1.677	1.772	1.766	1.773
∠Co-N-O	164.2	164.8	126.4	127.7	128.1	∠Co-N-O	168.7	168.7	165.5	166.2	165.9
Co-O(**2**)	2.137	2.145	2.240	2.234	2.255	Co-O(**1**)	1.918	1.924	1.973	1.971	1.973
Co-O(**3**)	2.031	2.030	2.012	2.018	2.010	Co-O(**4**)	1.935	1.937	1.932	1.930	1.934
Co-O(3)	2.133	2.131	2.078	2.087	2.077	Co-O(2)	2.514	2.513	2.333	2.347	2.326
Co-O(*3*)	2.114	2.130	2.022	2.021	2.020						
Al-Co	2.970	2.974	2.989	2.985	2.986	Al-Co	2.812	2.818	2.822	2.822	2.820
E_{ads}	1.921	1.773	0.653	0.652	0.636	E_{ads}	2.836	2.696	1.281	1.310	1.262
ν_{N-O}	1925(1947)	1945(1970)	2028(2058)	2023(2054)	2030(2060)	ν_{N-O}	1942(1964)	1964(1987)	2112(2141)	2110(2138)	2113(2141)
$\Delta\nu$	47	57	3	-1	3	$\Delta\nu$	64	76	87	86	86
	Configuration 2						Configuration 5				
N-O	1.161	1.159	1.143	1.143	1.143	N-O	1.154	1.157	1.138	1.138	1.138
Co-N	1.643	1.685	1.817	1.805	1.813	Co-N	1.631	1.674	1.763	1.758	1.761
∠Co-N-O	158.8	166.1	157.9	159.0	158.7	∠Co-N-O	177.3	173.5	173.2	173.6	173.9
Co-O(**2**)	1.909	2.074	2.123	2.123	2.123	Co-O(**2**)	1.838	1.920	1.907	1.906	1.904
Co-O(**3**)	1.883	1.976	1.944	1.947	1.947	Co-O(**4**)	1.973	1.970	2.016	2.009	2.009
Co-O(3)	1.944	2.039	2.027	2.028	2.028	Co-O(4)	2.072	2.346	2.216	2.216	2.222
Co-O(*3*)	3.818	3.644	3.540	3.535	3.529						
Al-Co	2.740	2.851	2.855	2.857	2.856	Al-Co	2.791	2.808	2.813	2.817	2.816
E_{ads}	2.068	1.999	0.708	0.721	0.696	E_{ads}	2.716	2.515	1.216	1.230	1.205
ν_{N-O}	1909(1930)	1950(1975)	2063(2093)	2058(2088)	2064(2094)	ν_{N-O}	1968(1986)	1955(1979)	2104(2133)	2097(2124)	2100(2127)
$\Delta\nu$	31	62	38	34	37	$\Delta\nu$	90	67	79	73	73
	Configuration 3						Configuration 6				
N-O	1.150	1.152	1.135	1.135	1.135	N-O	1.150	1.156	1.135	1.136	1.136
Co-N	1.682	1.687	1.779	1.773	1.780	Co-N	1.679	1.633	1.755	1.751	1.758
∠Co-N-O	163.4	163.4	162.4	163.2	163.2	∠Co-N-O	177.6	178.0	176.4	176.5	176.4
Co-O(**1**)	1.960	1.966	2.031	2.026	2.028	Co-O(**2**)	1.917	1.845	1.905	1.905	1.908
Co-O(**4**)	1.957	1.955	1.934	1.941	1.939	Co-O(**4**)	1.978	1.973	2.020	2.021	2.026
Co-O(2)	2.367	2.366	2.263	2.243	2.250	Co-O(4)	2.323	2.044	2.209	2.217	2.186
Al-Co	2.811	2.814	2.822	2.818	2.819	Al-Co	2.843	2.828	2.840	2.841	2.844
E_{ads}	2.627	2.487	1.238	1.297	1.194	E_{ads}	2.947	2.743	1.263	1.301	1.322
ν_{N-O}	1953(1976)	1974(2000)	2120(2151)	2112(2141)	2114(2143)	ν_{N-O}	1951(1973)	1976(1992)	2111(2138)	2108(2135)	2109(2137)
$\Delta\nu$	75	86	95	88	87	$\Delta\nu$	73	88	86	84	82

energies of only 0.65 eV if two, and about 0.70 eV if only one Al is present in the ring. NO is more strongly adsorbed at cations in a 8MR, with only a weak dependence of the adsorption energies on geometric details. With PBE0 the energies vary only between 1.22 eV in configuration 5 and 1.28 eV in configuration 4. Details are summarized in Table 7.11. With both types of functionals the adsorption energy is much lower than the bond dissociation energy in neutral or positively charged Co-nitrosyls.

The low adsorption capacity of cations in a 6MR is again related to their strong binding to the framework. In configuration 1 the fourfold coordination of Co(II) remains unchanged upon adsorption, the average Co(II)-O distance increases only from 2.04(2.04) to 2.10(2.09) with PBE(PBE0). The most important difference between GGA and hybrid functionals is the much lower Co(II)-N-O angle and the larger Co(II)-N distance. Compared to the charged nitrosyl, the Co-N distance increases only by 0.05 Å in the GGA, but by 0.32 Å with hybrid functionals. For charged $[CoNO]^+$ both types of functionals predict a linear geometry, a bending comparable to that calculated with hybrid functionals in Co(II) chabazite is found only for the neutral nitrosyl. However, whereas in the neutral nitrosyl the bent geometry is combined with a strongly stretched N-O distance, it is slightly contracted in the NO-Co(II)-chabazite complex In configuration 2 NO adsorption leads to a reduction of the Co(II)-O bonds from four to three, combined with a contraction of the Co-O, Co-N and N-O distances, the Co-N-O angles are now almost the same in the GGA and with hybrid functionals.

The very low adsorption energies calculated with hybrid functionals (especially for cations located in a 6MR) suggest that the reactivity of the cation is too low to allow the formation of di- or trinitrosyl species. In contrast, multiple adsorption of NO in various Co(II)-zeolites has been found in the GGA calculations of Georgieva *et al.*[151], as suggested by infrared spectroscopy.

In configurations 3 to 6 (i.e. in a 8MR) the Co(II) cation before adsorption is connected to two activated oxygens, with a third weaker bond to a non-activated oxygen. This coordination remains essentially unchanged in the NO-Co(II)-chabazite complex. The strong Co-O bonds are slightly, the weak bonds more strongly stretched. The difference between strong and weaker bonds is more substantial within the GGA. Only for the configurations where the GGA predicts a S=0 ground-state, the cation remains threefold coordinated by framework oxygens. Adsorption at cations in these locations induces a contraction of the N-O bond-lengths. Within the GGA the contraction is comparable to that found in the free charged $[CoNO]^+$ nitrosyl, while with hybrid functionals adsorption at the Co(II) cation in chabazite induces a much more pronounced contraction than in the free, charged nitrosyl. The Co-N-O angle is about 165° in configurations 3 and 4, and around 175° in configurations 5 and 6, with both types of functionals.

Stretching frequencies

Using the PBE functional we calculate stretching frequencies of 1945(1950) cm^{-1}, blue-shifted by 57(62) cm^{-1} in configurations 1(2). For these configurations hybrid functionals (PBE0) yield in configuration 1 a frequency of 2028 cm^{-1} almost identical

to that in the gas-phase molecule, while for configuration 2 we find a value of 2063 cm^{-1}, blue-shifted by 38 cm^{-1}. The difference between the two configurations is evidently related to the different Co-N-O angles. In configurations 3 to 6, the GGA predicts blue-shifts between 75 and 90 cm^{-1}, hybrid functionals yield almost identical values of $\Delta\nu = 73 - 95$ cm^{-1}.

No experimental results are available for NO in Co(II)-chabazite. For Co(II)-MOR[126] experimental frequencies of 1940 and 1952 cm^{-1} (blue-shifted by 64 and 76 cm^{-1}), for Co(II)-FER[124] of 1935 cm^{-1} (blue-shifted by 59 cm^{-1}), and for Co(II)-ZSM5[196] of 1940 and 1957 cm^{-1} (blue-shifted by 64 and 81 cm^{-1}) were reported for adsorbed mononitrosyls. Where two modes could be discriminated, the lower one was assigned to the more stable cation location (see Georgieva *et al.*[151] for a detailed discussion). The weak dependence on the zeolite-type is again remarkable. Our results for Co(II) in a 6MR, calculated in the GGA, are in excellent agreement with the experimental values while hybrid functionals yield too large absolute values and too modest blue-shifts. For Co(II) sites in a 8MR the GGA predicts only slightly increased stretching frequencies, still in reasonable agreement with experiment. Stretching frequencies calculated with hybrid functionals are further increased, increasing disagreement with experiment.

The stretching frequencies calculated in the GGA are in good agreement with the results of Georgieva *et al.*[151] who extended the investigations to include di- and trinitrosyls formed in various zeolites. The results demonstrate that the good agreement with experiment achieved in the GGA holds also for multiple adsorption of NO.

Electronic structure and bonding

The electronic DOS of Co(II)-chabazite is characterized by a full Co-3d majority and a partially filled minority band. With hybrid functionals we find a wide gap between occupied and empty Co-3d minority states, which is absent in the GGA, for details we refer to II (see in particular Fig. 10). In the GGA the NO-$\pi^\star$ states hybridize strongly with the Co-3d minority states, see Fig. 7.16. Due to the nearly straight geometry, the interaction is strongest with the d_π states of the cation. No appreciable interaction is seen with the Co-majority states, in agreement with the spin-densities shown in Fig. 7.15. With hybrid functionals we find a strongly bent geometry. In the DOS this is reflected by a stronger interaction of the $\pi^\star$ states with the d_σ states of the cation. Occupied bonding and empty antibonding $3d - \pi^\star$ combinations are separated for both types of functionals by a gap of about 2.5 eV. While with hybrid functionals the bonding states are located just below the Fermi level, in the GGA they are found at binding energies of about 1.5 eV - this explains the larger adsorption energy calculated in the GGA. Cation locations in 6MR and 8MR's differ by a shift of the 3d states to larger binding energies, which is much more pronounced with hybrid functionals. The higher binding energies of the 3d states reduce their hybridization with the $\pi^\star$ states, this leads to the much lower adsorption energies calculated with hybrid functionals.

A Bader analysis of the local charges shows that adsorption induces only a minimal charge transfer. The charge on the cation remains within ± 0.01 the same, except for configuration 1 in the GGA where we calculate an increase by 0.06. With hybrid

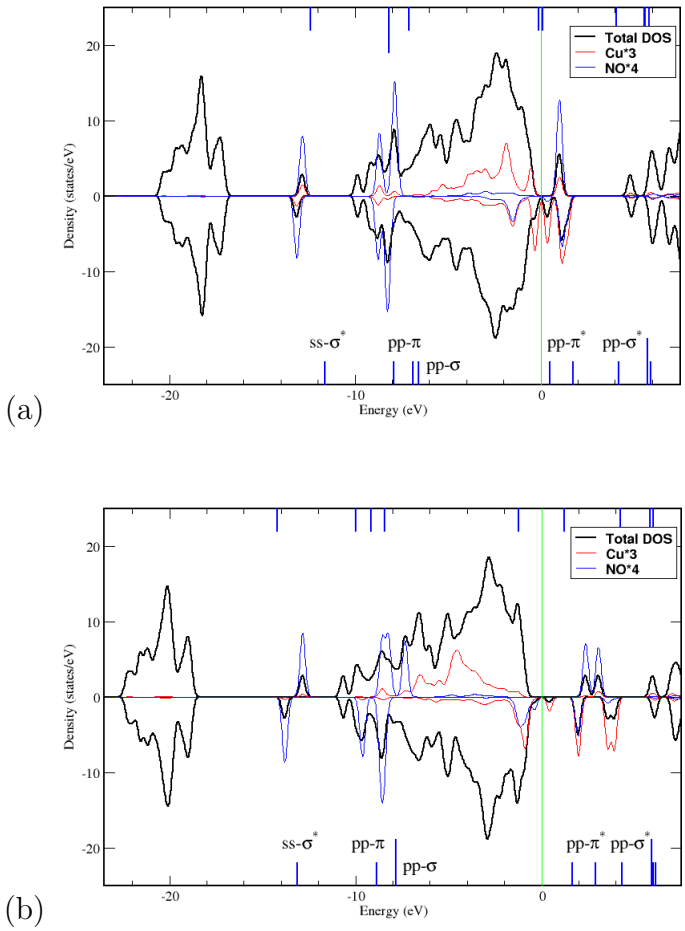

Figure 7.16: Total and local electronic DOS for NO-Co(II)-chabazite in configuration 1, calculated using (a) PBE and (b) HSE03 functionals. Partial Co DOS (red) is multiplied by a factor of three, partial NO DOS by a factor of 4 for reasons of better visualization. Cf. text.

functionals we find a slight depletion of the $\pi^\star$ states of NO varying between 0.03 and 0.08 electrons and smaller changes in both directions in the GGA. This means that for NO-Co(II) chabazite the change in the N-O stretching frequencies is due mainly to an internal charge-re-arrangement within the molecule.

Summary NO adsorption

The influence of the choice of an exchange-correlation functional is different for NO adsorption than found for CO. The reason is the interplay between the magnetic moments of cation and molecule and the fact that the partially occupied $\pi^\star$ state is pinned at the Fermi level. The adsorption complex of NO in Cu(I) has a spin of S=1/2 (as free $[CuNO]^+$), the adsorption energy is about the same as the bond dissociation energy in the neutral nitrosyl and much lower than in the charged species. The ground state of NO-Cu(II)-chabazite is a singlet, but while the GGA predicts a total absence of spin-polarization, hybrid functionals predict localized spin densities with opposite sign on cation and molecule. For a cation location in a 6MR the GGA predicts a modest reduction of the adsorption energy, while we calculate a drastic decrease with hybrid functionals. For the less stable cation sites in a 8MR, however, the adsorption energy calculated with both types of functionals is comparable or even larger than for Cu(I). This means that the reported selective adsorption on Cu(II) [in contrast to CO which is reported to attach preferentially to Cu(I)] is not found with either functional.

For NO in Co(II)-chabazite we calculate a spin of S=1, again arising from localized spins with opposite orientations on cation and molecule. Within the GGA singlet and triplet states are energetically almost degenerate. This is similar to the situation in the neutral Co-nitrosyl, where GGA predicts S=0 and hybrid functionals S=1. Within the GGA we calculate large adsorption energies, intermediate between the bond dissociation energies calculated for the neutral and the positively charged Co-nitrosyl. Adsorption energies calculated with hybrid functionals are generally lower, the difference is most pronounced for cations located in a 6MR. For these sites the adsorption energies are again intermediate between those of the neutral and charged nitrosyls, while for the less stable sites in a 8MR they approach the larger values of the neutral nitrosyl. As for CO adsorption we find a strong dependence the adsorption energy on the stability of the cation location, see Fig. 7.17. The much stronger binding between the Cu(II) cation and the framework leads to much lower adsorption energies. In contrast to our results for CO adsorption, for Cu(II) chabazite the same linear correlation holds in the GGA and for hybrid functionals. For both monovalent and divalent Cu-cations we find only a small overlap of the adsorption energies calculated with the two different types of functionals. This is even more pronounced for Co(II)-chabazite, were the lowest adsorption energy calculated in the GGA for the most stable configuration is still larger than the highest adsorption energy found with hybrid functionals for the least stable cation site. With both types of functionals the slope of the linear dependence of the adsorption energies is nearly the same, but those calculated with hybrid functionals are shifted by about 0.5 eV to lower values.

For NO in Cu(I)-chabazite both types of functionals predict a red-shift of the N-

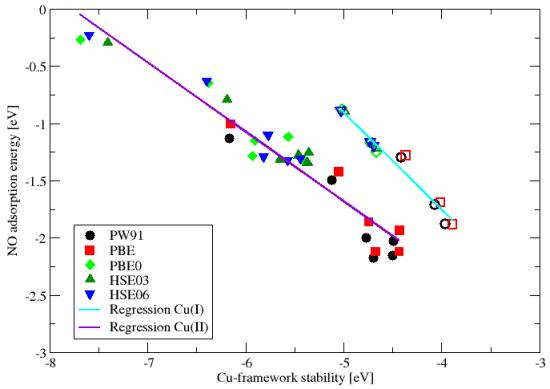

(a)

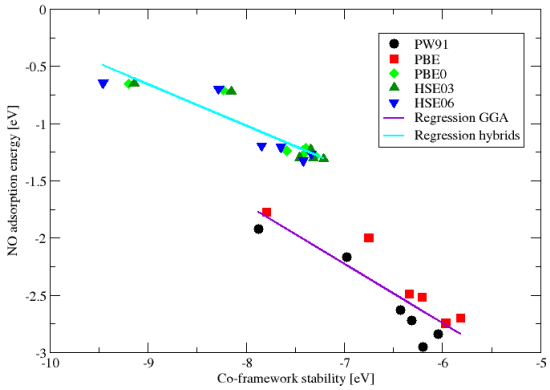

(b)

Figure 7.17: NO adsorption energy E_{ads} versus binding energy between cation and framework E_{cation} for (a) Cu(I)- (open symbols) and Cu(II)-chabazite (closed symbols) and (b) Co(II)-chabazite, calculated using different functionals. The color-code is defined in the inset). Cf. text.

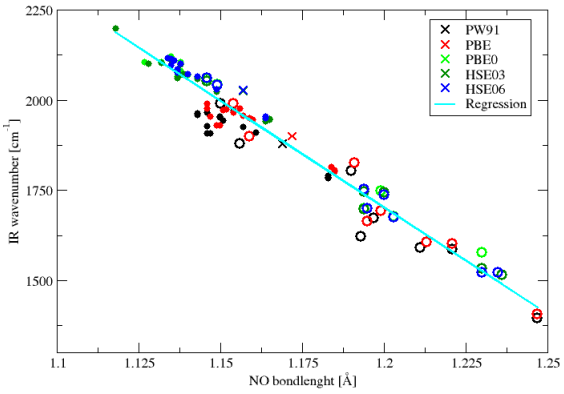

Figure 7.18: Correlation between N-O bond length R_{N-O} and stretching frequency ν_{N-O} for the gas-phase molecule (crosses), neutral and charged Cu- and Co-nitrosyls (open circles) and NO adsorbed in Cu(I)-, Cu(II)- and Co(II)-exchanged chabazite (full dots). Results calculated with the PBE functional are shown in red, those calculated with the PBE0 hybrid functional in blue. The straight lines show the linear correlation determined via a least-square fitting. Cf. text.

O stretching mode almost independent of cation location, the lower shift found with hybrid functionals being in better agreement with the experiments on other Cu(I)-zeolites and on Cu(I)-SAPO34. For NO in Cu(II)-chabazite the best agreement with the modest blue-shift reported for other Cu(II)-zeolites is found in the GGA and for cations located in a 6MR. For cations in a 8MR too large blue-shifts are calculated with both types of functionals. Similarly, for NO in Co(II)-chabazite best agreement with the experimental values estimated from other zeolites is found in the GGA for cations in a 6MR. For these cation sites reasonable blue-shifts but too large absolute values are also found with hybrid functionals, but one has to remember that these functionals predict only a very weak adsorption by divalent cation in these sites. For Co(II) in a 8MR all functionals predict too large blue-shifts. As for CO the calculated stretching frequencies follow a linear variation with the calculated N-O bond length, including also gas-phase NO and the neutral and charged nitrosyls.

7.6 Discussion and conclusion

The aim of this study was to explore the influence of the choice of an exchange-correlation functional on the calculations of the structural, energetic, magnetic, and chemical properties of a complex system at the example of a transition-metal exchanged zeolite. Our results can be briefly summarized as follows:

(1) For the zeolite host, hybrid functionals predict a slightly more accurate cell volume and Si-O distance than the GGA.
(2) Structural changes and charge re-arrangments caused by Al/Si substitution and the introduction of extra-framework cations are more localized if the calculations are performed with hybrid functionals.
(3) Hybrid functionals predict a much stronger binding of the cation to the framework. The most stable location of all cations is in an off-symmetry position within a 6MR. Structural energy differences of cation sites in a 8MR are smaller with hybrid functionals for monovalent Cu(I), but larger for divalent Cu(II) and Co(II).
(4) In the ground state the spin of the metal-exchanged zeolite is always the same as predicted by Hund's rule for the free cation.
(5) The formation of an excited spin-state leads to strong structural relaxations. As a rule, cation coordination to framework oxygens is reduced in the excited state. Spin-dependent energy differences are smaller with hybrid functionals for Cu(I), but larger for Cu(II) and Co(II). For Co(II)-chabazite the first excited spin-state is a low-spin state with S=1/2, an excited high-spin state with S=5/2 has much higher energy.
(6) Hybrid functionals predict a much wider band gap for the purely siliceous zeolite in much better agreement with the experimental results for other SiO_2 polymorphs.
(7) The admixture of exact exchange in hybrid functionals increases the exchange-splitting and the energy difference between occupied and empty eigenstates of the extra-framework cation. Generally the GGA predicts a location of the $3d$-states close to the Fermi energy, while with hybrid functionals the occupied states are shifted to higher binding energies and the empty states to higher energies within the zeolite band gap.
(8) Diffuse reflectance spectroscopy (DRS) probes excited electronic states at energies that are substantially lower than the fundamental band gap of the zeolite host. The strong structural relaxation in excited states leads to large differences between excitation and emission energies measured in DRS, calculated at the frozen geometry of the initial state.
(9) For Cu(I)-chabazite calculations with both hybrid functionals and in the GGA lead to reasonable agreement with experiment if the relaxation of the excited triplet state is taken into account.
(10) For Cu(II)-chabazite the low-energy DRS bands have been tentatively assigned to $d - d$ transitions, the high-energy bands to charge-transfer excitations. The interpretation of the low-energy peak is compatible with our results obtained in the GGA, but with hybrid functionals it can be assigned only to O→Cu-$3d$ charge-transfer excitations. The position of the high-energy peak agrees quite well with the excitation energies of the quadruplet state calculated at a frozen ground-state geometry and with screened hybrid functionals. Excitation energies calculated in the GGA are too low.
(11) For Co(II)-chabazite the excitation energies calculated with screened hybrid functionals for the low-spin state agrees quite well with DRS band measured for other Co(II) zeolites. Emission energies from the high-spin state calculated in the GGA agree quite well with the measured DRS bands, while too strong relaxation effects lead to too low emission energies in calculations with hybrid functionals.

(12) It is difficult to establish a correlation between cation location and DRS energies because the width of the measured DRS bands is comparable with the calculated site-dependent differences in the excitation or emission energies. A quantitative interpretation of the peak-shapes would require assumptions on the relative populations of the different sites, which depend on the production and thermal history of the sample.
(13) Adsorption energies for CO and NO molecules in metal-exchanged chabazite show a strong, essentially linear correlation with the stability of the cation location. Adsorption energies calculated with hybrid functionals are always much lower and - as far as experimental data are available - more realistic than those derived in the GGA.
(14) The adsorption energies calculated for Cu(I)-chabazite span essentially the same range as between nearly neutral and positively charged Cu-carbonyl or nitrosyl. This holds for both types of functionals. For Cu(II)-chabazite the adsorption energies calculated for the most stable cation location are much lower than for the corresponding neutral species in the gas-phase, those determined for the least stable cation site reach for NO the values calculated for $[CuNO]^+$ but remain below the corresponding value for CO adsorption. Again the trend is the same for both types of functionals.
(15) Adsorption energies calculated for Co(II)-chabazite are much lower than for the free carbonyl or nitrosyl. For Co-exchanged chabazite the impact of the functional on the adsorption energy is largest because of the strong exchange splitting in the S=3/2 state. GGA functionals predict that CO adsorption induces a spin-crossover transition to a low-spin state with S=1/2 in all but the most stable configuration with Co(II) in a 6MR with two Al atoms. For NO adsorption both spin states are nearly degenerate in the GGA. Hybrid functionals predict that the high-spin state is conserved.
(16) Hybrid functionals predict a short molecular bond-length of the adsorbed species and larger distance from the cation than the GGA. Adsorption-induced distortions of the cation-framework coordination are larger with hybrid functionals - this is important for understanding the very low adsorption capacity of the divalent cations in their most stable sites, especially with hybrid functionals.
(17) Using both types of functionals we find the same linear correlation between molecular bond-length and stretching frequency, including also the charged and neutral carbonyls and nitrosyls and the gas phase molecules. Hybrid functionals predict shorter bond-lengths and significantly higher frequencies than the GGA.
(18) For CO adsorbed in Cu(I)- and Co(II)-chabazite only hybrid functionals predict the blue-shift of the stretching mode observed in other zeolites and in isotructural metal-exchanged SAPO34. For Cu(II) both types of functionals predict a blue-shift, the larger value calculated with hybrid functionals being in better agreement with experiment. Absolute values are underestimated in the GGA and overestimated with hybrid functionals, the absolute error being larger with hybrid functionals for Cu(I), of the same order for Cu(II), and smaller for Co(II).
(19) For NO adsorption on Cu(I)-chabazite the GGA-calculated frequencies are more accurate, but the smaller red-shift derived with hybrid functionals is in better agreement with observation. For NO in Cu(II)- and Co(II)-chabazite agreement is best in the GGA and for cations in a 6MR.
(20) The dependence of the stretching frequency on the cation location is very small for

both molecular species in Cu(I)-chabazite. A stronger site-dependence is found with hybrid functionals for CO and NO in Cu(II)-chabazite, but the blue-shift is too large for cations in a 8MR. For CO-Co(II)-chabazite (where only hybrid functionals yield a blue-shift), the predicted shift is too large for cations in a 8MR. For NO adsorption the GGA-calculated frequencies are larger by about 20 to 25 cm^{-1} for cations in a 8MR, this difference is of the same order of magnitude than reported for Co(II)-MOR and Co(II)-ZSM5.

Hence we conclude that in most cases hybrid functionals produce more accurate results for structural and electronic properties and for the adsorption energies of molecular species in metal-exchanged zeolites. In particular, only hybrid functionals correctly predict a blue-shift for the stretching mode of adsorbed CO. In this case the improved performance of hybrid functionals can be attributed to a more accurate HOMO-LUMO gap of the molecule and a more accurate band-gap of the zeolite host. However, the results obtained with hybrid functionals are less accurate for systems with larger spins, because the admixture of exact exchange leads to a too large exchange splitting and too large gaps between occupied and empty cation states and because hybrid functionals tend to favor high-spin states. This is most evident in the calculated energies of the DRS bands, the adsorption energies and the vibrational properties of adsorbates in Co(II)-chabazite.

Hybrid functionals also produce vibrational frequencies which are systematically too high for all systems investigated here - molecules, carbonyls and nitrosyls, and molecules adsorbed in the zeolite. This difficulty is often ignored by simply downscaling the calculated frequencies.

Part III

Alkane Adsorption in Chabazite - Modeling van der Waals interactions

8 Na-exchanged chabazite

Summary

The importance of dispersion forces for the correct description of the adsorption of short alkanes in Na-exchanged and purely siliceous chabazite has been investigated at different levels of theory: (i) Standard density-functional calculations using the PBE exchange-correlation functional in the generalized gradient approximation (GGA), (ii) dispersion corrections based on empirical force fields according to Grimme [J. Phys. Chem. **109**, 3067 (2005) - PBE-d], (iii) calculations based on the van der Waals density functional proposed by Dion et al. [Phys. Rev. Lett. **92**, 246401 (2004) - vdW-DF], and (iv) using the random phase approximation (RPA) in combination with the adiabatic-connection fluctuation-dissipation theorem (RPA-ACFDT), using wave-functions calculated at the DFT and Hartree-Fock (HF) levels. A full relaxation of the adsorbate-zeolite complex was performed at the PBE, PBE-d and vdW-DF levels. RPA and RPA-HF energies were calculated for the optimized configurations. A critical analysis of the results shows that the most accurate description is achieved at the RPA level with HF exchange energies, while both PBE-d and vdW-DF overestimate the strength of the interaction with the acid site.

8.1 Introduction

Zeolite catalysts are widely used in industry to catalyze hydrocarbon conversion reactions such as cracking, isomerization and dehydrogenation. In most applications the Brønsted acidity of the protonated zeolite is used to activate the hydrocarbon molecule and the geometric constraints of the pore structure are used to direct the selectivity of the process [218], but studies suggest that the switch to Lewis acid sites like extra-framework Na atoms affects the selectivity and reaction rate of alkanes [219]. An understanding of the adsorption of alkanes is fundamental to the description of the conversion process at an atomistic level. At low alkane partial pressures and low temperatures the adsorption of alkanes at Brønsted or Lewis acid sites is usually favored. The interaction occurs via polarization-induced forces as the positive charge of the acid site induces a dipole in the hydrocarbon molecule [220]. However, experiments have demonstrated that the van der Waals interaction of the alkanes with the inner wall of the zeolite cavities accounts for the greater part of the heat of adsorption. [221, 222, 223, 224]. Experimental investigations found that the direct interaction between alkanes and Brønsted or Lewis acid sites is relatively weak ($\sim 10 - 12$ kJ/mol) and of similar strength in different types of zeolites. The strength of the interaction of

the methyl and methylene groups of the alkane with the oxygen atoms of the zeolite lattice increases with increasing chain length of the alkane and was found to depend on the framework density [225, 223] and on the size and curvature of the pores [226]. For a given alkane the heat of adsorption increases with the density of the framework (which is inversely proportional to the diameter of the cavities). For a given zeolite, the heat of adsorption increases almost linearly with chain length for small alkanes, but the rate of increase per additional CH_2-group becomes less steep as the size of the molecule reaches the pore size of the zeolite [223].

Molecular dynamics simulations based on empirical force fields [10, 227] have been successful in elucidating the sorption properties of alkanes in zeolites. Ab-initio calculations based on quantum mechanical calculations, however, encounter difficulties in describing the van der Waals (vdW) interactions promoting the interactions between the saturated hydrocarbon molecules and the oxygen atoms of the zeolitic framework. DFT calculations describe the bonding between the hydrocarbon and the acid sites quite well [108], but fail to account for the vdW forces. Within quantum chemistry a hierarchy of methods capable of describing dynamical correlation effects [and hence to account for van der Waals (vdW) or dispersion forces] have been developed. Already the simplest quantum-chemical method for electron correlation, second-order Møller-Plesset perturbation theory (MP2) describes dispersion forces quite well, but even its most efficient implementations [228] do not allow the investigation of large systems required for studying adsorption in zeolites or other mesoporous materials. To resolve this deficiency, Tuma and Sauer [229] have proposed a hybrid MP2-DFT method which combines MP2 calculations for a cluster surrounding the acid site with DFT calculations for a large system with periodic boundary conditions. In this hybrid approach, the total energy is given by that of the periodic system, calculated at the DFT level and corrected for the difference of the total energy of the cluster calculated at the MP2 and DFT levels of theory. The MP2 part of the calculations accounts for the dispersion forces, but elaborate studies of convergence with respect to cluster size and basis set convergence are required to achieve quantitatively reliable results.

Here we follow another approach. Density-functional calculations have been performed using the exchange-correlation functional proposed by Perdew, Burke and Ernzerhof (PBE) [55] in the generalized gradient approximation (GGA). Post-DFT corrections designed to account for dispersion forces at three different levels of theory have been applied to study the adsorption of short alkanes in purely siliceous and Na-exchanged zeolites. At the lowest level dispersion corrections are described by the empirical force field proposed by Grimme [66]. Although the corrections are semi-empirical (the force-field parameters are determined by comparison with high-level quantum-chemical calculations for a large molecular training set), its easy implementation and low computational costs made it the method of choice in many studies. At the second level, the vdW forces arising from long-range nonlocal electronic correlations are described by a functional proposed by Dion et al. [94, 95]. This functional is composed by the exchange part of an appropriately chosen GGA functional plus a properly constructed a non-local correlation term. This non-local term was constructed by using a simplifying approximation to the dielectric function in the Random Phase Ap-

proximation (RPA). Finally, correlation energies can be calculated with high accuracy using the RPA in connection with the Adiabatic-Connection Fluctuation-Dissipation Theorem (RPA-ACFDT)[80, 81, 82]. This high level method uses the Hartree-Fock (HF) expression for the exchange energy and a non-local correlation term which depends on the polarizability of the system. Even though absolute errors in atomization energies are still large, the errors cancel out when investigating adsorption energies. There have been some efforts to correct for the limitations of the RPA by including second-order exchange interactions between the electrons[230], but compared to the additional computational effort the improvement of the calculated total energies is quite modest. Ren et al.[87] suggested a simple but very effective way to improve the accuracy of adsorption energies calculated using the RPA by just calculating the exchange part of the RPA self-consistently.

Here we use all four levels of theory to investigate the adsorption of short alkanes in purely siliceous and in Na-exchanged chabazite. Our paper is organized as follows. In Sec. 8.2 we review very briefly the theoretical foundations, in Sec. 8.3 we summarize the computational set-up. Sec. 8.4 describes the results for the structure of the zeolite and the local structure of the acid sites, Sec. 8.5 summarizes our results for the structure and energetics of the adsorbate-zeolite complexes, Sec. 8.6 critically analyzes the results and we summarize in Sec. 8.7.

8.2 Theoretical

In Kohn-Sham density functional theory (DFT) total energies are calculated through the minimization of the functional

$$E^{KS}[n] = T[n] + \int d\mathbf{r} V^{ext}(\mathbf{r}) n(\mathbf{r}) + E^{Hartree}[n] + E^{xc}[n]$$

with respect to the electron density $n(\mathbf{r})$. While the kinetic energy $T[n]$, the interaction energy between electrons, the external potential V^{ext} and the Hartree self interaction energy $E^{Hartree}[n]$ are well defined, the form of the exchange-correlation functional E^{xc} which would make this relation exact is not known. This leaves room for a hierarchy of approximations nicknamed by Perdew et al. [47] the "Jacob's ladder" of DFT.

At the lowest level E^{xc} depends only on the local density (LDA), while at the second a dependence on the local density-gradient (generalized gradient approximation - GGA) and at the third in addition a dependence on the Laplacian of the density (or the kinetic energy density - meta-GGA) are introduced. The fourth level is represented by hybrid functionals mixing local (DFT) and non-local (HF) exchange, but using the semi-local correlation functionals from the GGA. All these approximations to not account for non-local correlations and hence cannot describe dispersion forces. Only at the fifth level charge fluctuations and non-local correlations are taken into account, permitting to describe vdW forces.

At the lowest level of our calculations, we used the GGA functional proposed by Perdew, Burke and Ernzerhof ([55]). The GGA corrects the overestimation of the

binding energy characteristic for the GGA. It correctly describes the weak specific interaction between a hydrocarbon molecule and an acid site [108], but it cannot account for the interaction of the molecule with the zeolite wall - for this part of the interaction dispersion corrections are required.

Semi-empirical dispersion corrections

vdW interactions are long-ranged dynamical dipole-dipole interactions, their contribution to the total energy can be described as

$$E^{disp} = s_6 \sum_{i=1}^{N_{at}-1} \sum_{j=i+1}^{N_{at}} \frac{C_6^{ij}}{R_{ij}^6}$$

where N_{at} denotes the total number of atoms, R_{ij} the distance between atoms i and j, and C_6^{ij} is a parameter determining the strength of the pairwise interactions. s_6 is a scaling factor specific for the exchange-correlation functional used in the DFT calculations. This simple form has inspired various attempts to create force fields modeling the long-range correlation effects neglected in the DFT. One of the most popular approaches is the PBE-d approach by Grimme et. al. [66]. Here the C_6^{ij} parameters for a pair of atoms are defined as $\sqrt{C_6^i C_6^j}$ and the C_6^i parameters have been optimized to describe the bonding properties of element i in a large set of molecular systems. A cutoff function is used, on one hand to prevent too strong interactions between neighboring atoms and on the other hand to restrict computational requirements for long range interactions in solids. The scaling factor s_6 accounts for the differences between different GGA functionals. Here we have used the parameters tabulated by Grimme[66] for the PBE functional. Very recently, the PBE-d approach has been implemented in a plane-wave DFT code by Bučko et al.[70] and applied to calculate the structures and binding energies of a large number of solids where dispersion forces play an important role.

vdW functionals

Dion et al. (Ref. [94, 95]) attempted to construct an exchange-correlation functional designed to account also for the long-range non-local correlation effects giving rise to dispersion forces. The vdW-DF functional is given by

$$E_{xc}[n] = E_x^{GGA} + E_c[n],$$

i.e. it consists of an appropriately chosen exchange functional in the GGA, and a novel non-local correlation functional. First, it has been noted that certain GGA functionals yield a certain amount of "vdW bonding" (e.g. in rare-gas dimers) from the exchange contribution alone - which is found to be incorrect when compared with HF calculations[231]. Therefore it was suggested to use the revised PBE (revPBE)

functional [58] which minimizes these spurious attractive interactions. Second, the correlation functional is separated into a short- and a long-range part,

$$E_c[n] = E_c^0[n] + E_c^{nl}[n].$$

The local short-range term $E_c^0[n]$ is treated in the LDA approximation, which implicitly uses the correct dielectric function. The derivation of the non-local long-range part of the correlation functional starts from the adiabatic connection formula[80, 81, 82] and uses an approximate form of the coupling constant integration (which is exact in homogeneous electron gas regime) and an approximate dielectric function ϵ in the single pole form[94, 95, 231]. The dielectric function is fully nonlocal and satisfies the known limits, sum rules, and invariance conditions, the pole position is scaled to yield the exact electron-gas ground state energy, including the appropriate gradient corrections. The final non-local correlation functional has the form

$$E_c^{nl} = \frac{1}{2}\int d\mathbf{r}d\mathbf{r}' n(\mathbf{r})\Phi(\mathbf{r},\mathbf{r}')n(\mathbf{r}'),$$

where the kernel $\Phi(\mathbf{r},\mathbf{r}')$ is a function of the electron densities and their gradients at sites $\mathbf{r}$ and $\mathbf{r}'$ - for all details we refer to Dion et al.[94, 95]. An overview of recent applications of the vdW-DF functional has been presented by Langreth et al.[231].

Most applications of the vdW-DF functionals are non-selfconsistent, the approach has been used to determine post-DFT corrections to the total energy at a fixed geometry. For the calculation of the Hellmann-Feynman forces used for a structural optimization of the system, a selfconsistent version of the vdW-DF scheme is required. In a selfconsistent version[232] non-locality appears also in the exchange-correlation potential in the Kohn-Sham equations

$$V_c^{nl}(\mathbf{r}) = \delta E_c^{nl}[n]/\delta n(\mathbf{r}).$$

Adiabatic connection formula and random phase approximation

Within adiabatic connection fluctuation-dissipation theory (AC-FDT)[80, 81, 82] the total energy of a system is written as the sum of the kinetic energy T_{KS} of the non-interacting Kohn-Sham (KS) system, the energy E_{el-ion} of the interaction of the electrons with the ions and the electron-electron interaction energy E_{Hxc} consisting of the Hartree, exchange and correlation contributions. E_{Hxc} is given by the integral over the expectation value of the electron-electron interaction operator V_{ee} while adiabatically switching from the KS system of noninteracting electrons ($\lambda = 0$) to the system with the full Coulomb interaction between the electrons ($\lambda = 1$),

$$E = T_{KS} + E_{el-ion} + \int_0^1 d\lambda \langle \Psi(\lambda) \mid V_{ee} \mid \Psi(\lambda)\rangle.$$

For the noninteracting KS system the ground state can be described by a single Slater determinant, $\Psi^{KS} = S(\{\psi_i^{KS}\}$. Using the fluctuation-dissipation theorem, E_{Hxc} can be expressed using the frequency-dependent dielectric function as[233]

$$E_{Hxc} = E_H[n] + E_x[\{\Psi_i^{KS}\}] - \int_0^1 \int_0^\infty \frac{d\omega}{2\pi} Tr\left\{\nu[\chi^\lambda(i\omega) - \chi^{KS}(i\omega)]\right\}$$

where χ^λ and χ^{KS} are the response function of "λ-interacting" system and the Kohn-Sham system of independent electrons, related through the Dyson equation

$$\chi^\lambda(\mathbf{q}) = \chi^{KS}(\mathbf{q}) + \chi^{KS}(\mathbf{q})[\lambda\nu(\mathbf{q}) + f_{xc}^\lambda(\mathbf{q}, i\omega)]\chi^\lambda(\mathbf{q}),$$

where ν and f_{xc}^λ are the Coulomb and exchange-correlation kernels.

The Random Phase Approximation (RPA) is defined by setting $f_{xc}^\lambda = 0$. After performing the coupling constant integration E_{Hxc} is given by

$$E_{Hxc} = E_H[n] + E_x[\{\Psi_i^{KS}\}] - \int_0^\infty \frac{d\omega}{2\pi} Tr\left\{ln[1 - \nu\chi^{KS}(i\omega)] + \nu\chi^{KS}(i\omega)]\right\},$$

the form it is evaluated in actual calculations.

The total energy without the RPA correlation energy is given by the Hartree-Fock total energy expression evaluated with KS orbitals and is therefore called the exact exchange energy. The KS response function χ^{KS} at imaginary frequencies can be evaluated using the expression of Adler[234] and Wiser [235]. An actual calculation of the RPA correlation energy proceeds by the following steps: (i) DFT calculation with the PBE exchange-correlation functional and a plane-wave cutoff energy E_{cut}, (ii) determination of all occupied and empty eigenstates within the space spanned by the basis set constructed by exact diagonalization of the KS Hamiltonian, (iii) calculation of the non-interacting response function χ^{KS} from the KS orbitals and evaluation of the RPA correlation energy.

There is no evident method of choice to calculate the KS orbitals (LDA, GGA or hybrid functionals). For molecules Furche[236] and Fuchs and Gonze[237], for adsorbates on solid surfaces Ren et al.[87] and Schimka et al.[91] have demonstrated that RPA adsorption energies and adsorption-energy differences are rather insensitive to the chosen starting point.

In principle the exact exchange energy and the RPA correlation energy must be calculated using the same set of KS orbitals. Recently it has been proposed, however, that a selfconsistent calculation of the Hartree-Fock energy might improve adsorption energies for weakly bonded regimes[87]. We have examined this approach which will be referred to as (RPA-HF).

The ACFDT-RPA method has been applied to jellium and jellium surfaces for more than forty years, but realistic molecular and solid-state systems have been investigated only recently - for a more complete account we refer to the recent work of Harl and Kresse[83]. In particular, very recent work[91] has demonstrated that the RPA permits to solve some long-standing problems in the description of molecular adsorbates on the surfaces of close-packed late transition-metals. Only an accurate evaluation of the correlation energy permits a correct prediction of the stable adsorption site. Extensions beyond the RPA level, including second-order screened exchange interactions between the electrons have recently been considered by Grüneis et al.[230] - however, these

corrections require a too high computational effort to be applied to systems as complex as a zeolite.

8.3 Computational setup

All results were calculated using the latest release of the Vienna Ab-Initio Simulation Package [135, 136], which is a plane-wave code based upon the PAW method [45, 46] for describing the electron-ion interaction. The calculation of exact exchange energies is described in Refs. [75, 76] and the method for the calculation of the response function is explained in Refs. [238, 113]. The selfconsistent calculations using the vdW-DFT functional were performed as described by Gulans [97]. For all calculations we used a cut-off energy of 400 eV and only one k-point centered at the Γ-point of the unit cell. Careful convergence checks have demonstrated that higher cut-off energies and larger k-point sets leave the results largely unchanged. The PBE-d long-range cutoff was set to 18 Å, but results did not seem to be especially sensitive to this parameter. RPA calculations were performed using PBE wave-functions. For the calculation of the adiabatic coupling integral we chose a maximum energy of $E^{\chi}_{cut} = 200$ eV and extrapolated to E^{∞}_{c} in the way described in Ref. [83], which seems sufficient for our calculations.

Structures were relaxed using a combination of a quasi Newtonian algorithm, damped molecular dynamics and a conjugate gradient algorithm. We considered the structures to be converged when the forces were smaller than 0.015 eV/Å. This is more accurate than most other calculations in similar systems, but due to the flat potential energy surface close to the minimum we considered this to be necessary. For an alkane adsorbed in the cavity of a zeolite there are many local energy minima corresponding to different, but energetically almost degenerate configurations. To systematically explore configuration space, we started with the adsorption of methane and subsequently substituted one hydrogen atom by a CH_3-group and relaxed the structure to obtain ethane adsorption energies. The procedure was repeated by substituting another hydrogen atom. The same approach was applied for transition from ethane to propane. The structures described in the following are those with lowest total energies.

8.4 Structure of zeolite and acid sites

In this work we investigated the adsorption of short alkanes in purely siliceous and Na-exchanged chabazite, because experimental results for the heat of adsorption are available for the Na-exchanged zeolite[239]. Chabazite is a microporous silicate (zeolite) with a rhombohedral unit cell (space group symmetry $R\overline{3}m$) consisting of twelve tetrahedral sites occupied by silicon atoms coordinated by four oxygen atoms. These tetrahedrons are linked via oxygen atoms, forming a double six-membered ring structure. The dominant interaction in chabazite is the covalent bonding between silicon and oxygen atoms, van der Waals interactions do not play an important role in stabiliz-

ing the chabazite structure. Recently, the PBE-d approach has been applied by Bučko et al. to optimize the structure. The calculated lattice constants are a=9.35(9.34) Å, the rhombohedral angle α =94.1(94.1) °, the bulk modulus B=68(72) GPa at the PBE(PBE-d) levels of theory, to be compared with the experimental values a=9.29 Å, $\alpha = 93.9°$ (Ref. [240]), B=62 GPa (Ref. [241]).

To create a Lewis acid site, one of the Si atoms of the framework must be replaced by an Al atom and a monovalent cation must be placed into one of the possible extra-framework sites. In chabazite, all tetrahedral sites are crystallographically equivalent. The Na atom has been placed initially into three possible high-symmetry extra-framework sites (see Fig. 8.1), but upon relaxation they move to less symmetric positions. In configuration (1), the atom is initially located in the center of an eight-membered ring, in configuration (2) in the center of a six-membered ring, and in configuration (3) next to an edge shared by two of the four-membered rings linking the constituent double six-membered rings of the chabazite structure such that the atom is located approximately above the center of both rings. These positions correspond to the extra-framework positions SIII, SI, and SIII′, respectively, classified by Smith et al.[144].

Formally, the cation-framework interaction is dominated by the electrostatic interactions between the negatively charged zeolite framework and a positively charged Na-atom, but the influence of vdW corrections is found to be non-negligible. Figure 8.2 shows the relaxed local structure around the Na sites, calculated using the PBE, PBE-d and vdW-DF methods. In all configurations the Na atom binds preferentially to "activated" oxygen atoms located next to the Al atoms, while the bonds to other oxygen atoms in the ring are elongated. In configuration (1) where the Na atom is initially located in the center of the eight-membered ring, upon relaxation the ad-atom drifts away from the center of the ring. The average length of the three short Na-O bonds is 2.41 Å at the PBE and PBE-d levels and 2.44 Å using the vdW-DF functional. In configuration (2) the Na atoms remains closer to the center of the six-membered ring, but the difference between the shortest and longest Na-O distance is still about 0.5 Å. In this configuration the dispersion corrections influence the geometry of the acid site in different ways: while, compared to the PBE results, the three shortest Na-O bonds shrink on average from 2.48 Å to 2.41 Å using the PBE-d method, the vdW-DF functional predicts only a contraction to 2.44 Å. An increase of the average length of the three longer Na-O bonds from 2.78 Å to 2.83(2.91) Å is calculated at the PBE-d(vdW-DF) level. For configuration (3) the influence of the dispersion forces is different: On average both PBE-d and vdW-DF predict a modest contraction of the three strongest Na-O bonds by 0.03 Å on average, but the vdW-DF functional predicts the formation of a fourth short bond with the O(4) atom [see Fig. 8.2(c)]. In general we find that the relaxed vdW-DF geometry is closer to the PBE results because in addition to the attractive medium- and long-range interactions described by the Grimme force fields, the vdW functional includes also a short-range repulsive interaction.

The dispersion corrections also influence the energetic ordering of the extra-framework sites. While in the PBE and vdW-DF approaches, configuration (1) is energetically preferred by 6.8(5.6) kJ/mol and 32.8(32.7) kJ/mol over configurations (2) and (3),

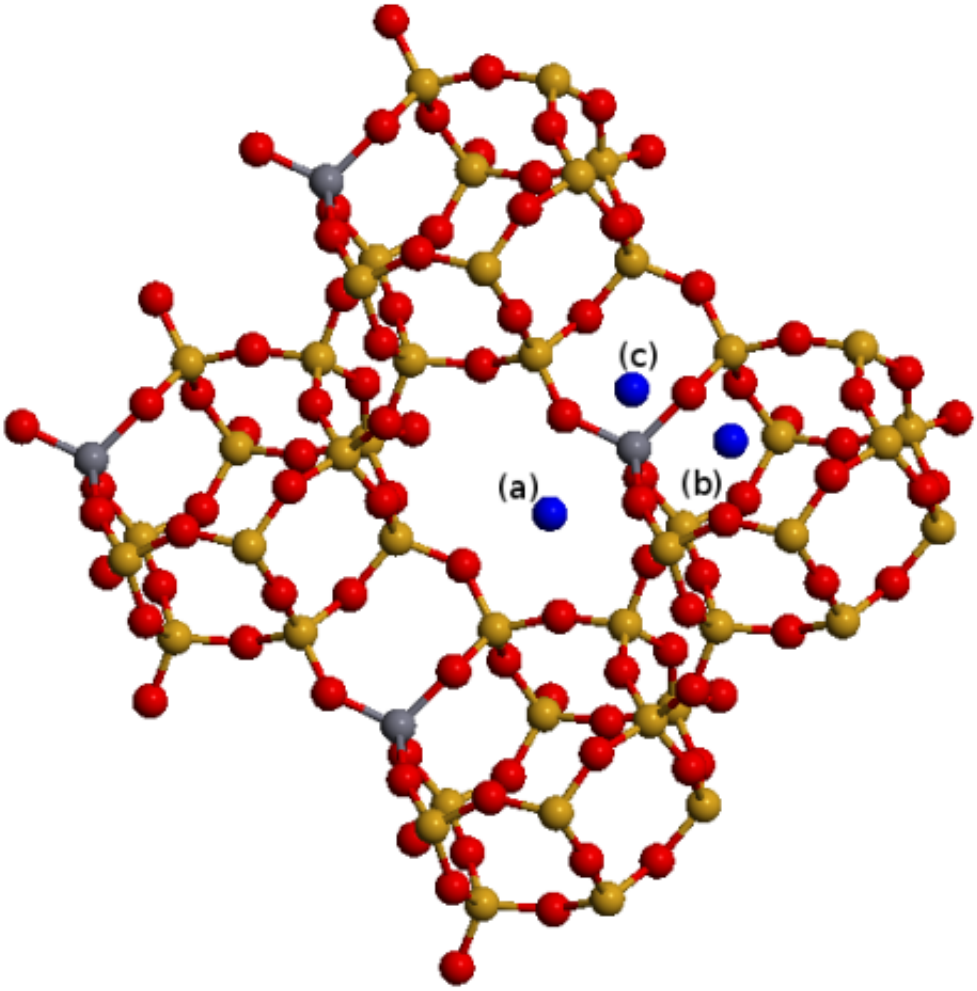

Figure 8.1: Extra-framework positions chosen for the location of the Na atoms in chabazite. In configuration (1) the Na-atom sits in the eight-membered ring (a), in configuration (2) in a six-membered ring (b), and in configuration 3 close to the edge shared by two four-membered rings. Si atoms are shown in yellow, O atoms in red. Al/Si substitutions are marked in grey, Na atoms in blue.

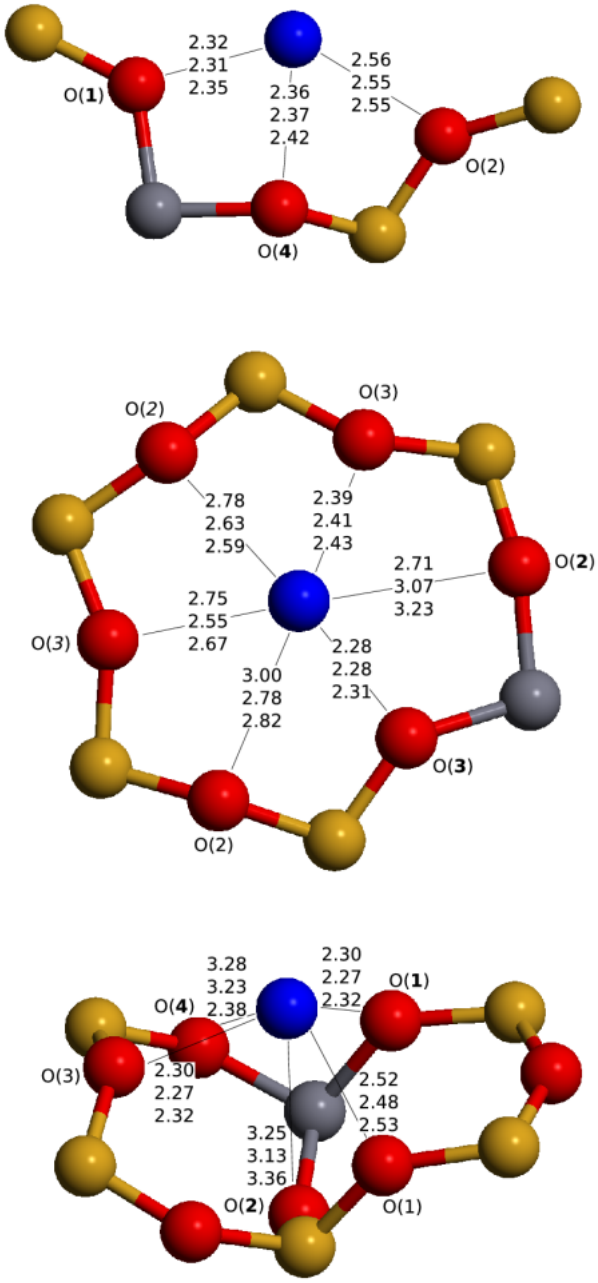

Figure 8.2: Relaxed structures around the extra-framework Na atoms in chabazite in configurations (1) to (3) (from top to bottom). Si atoms are shown in yellow, the Al atom in grey, oxygen atoms in red. The numbers give the distances (in Å) between the Na atom and the surrounding oxygen atoms of the framework, calculated in the PBE (top), PBE-d (middle) and vdW-DF (bottom) approximations.

the PBE-d method predicts configuration (2) to be lower in energy by 8.0 kJ/mol than (1) and 27.6 kJ/mol than (3).

8.5 Alkane adsorption

An alkane molecule located in the cavity interacts with the zeolite through two distinctly different mechanism: (i) A weak specific interaction between a terminal methyl group and the extra-framework cation, arising from the polarization of the molecule by the charged cation, and (ii) a van der Waals interaction between the other terminal methyl group and the methylene groups with the framework. The contribution of the vdW coupling depends crucially on the geometry of the inner wall of the zeolite. Our calculations at the PBE, PBE-d, and vdW-DF levels of theory have been performed self-consistently, resulting in fully optimized structures and energies. Within the ACFDT-RPA approach selfconsistent calculations and structure optimizations are excluded by a prohibitively high computational cost. In these cases we have performed non-selfconsistent calculations using the geometries optimized at the PBE, PBE-d and vdW-DF levels.

Calculations at the PBE, PBE-d and vdW-DF levels

The adsorption energies and the geometrical data of the adsorption complexes formed by methane, ethane, and propane in purely siliceous and Na-exchanged chabazite are summarized in Tables 8.1 to 8.3. We begin by discussing the results for purely siliceous chabazite.

Purely siliceous chabazite

In purely siliceous chabazite the adsorbate is located almost in the center of the large cavity, whether dispersion corrections are considered or not. For methane the attractive force field of the PBE-d approach draws the molecule somewhat closer to one of the Si atoms, while the distance remains almost unchanged using the vdW-DF functional. For ethane and propane all C-Si distances are contracted compared to the PBE results for PBE-d. For these slightly more complex molecules, the vdW-DF functional allows to find a configuration which optimizes also the longer C-Si distances of the PBE results. This shows that this approach is more flexible than the simple description of the dispersion forces by pair-wise interactions.

While the influence on the geometry of the adsorption complex is modest, the dispersion corrections massively change the adsorption energies. At the PBE level, there is almost no interaction between the saturated hydrocarbon and the inert inner wall of the zeolite. At the PBE-d level, the adsorption energy of methane is -18.3 kJ/mol. It increases by an increment of about 10-12 kJ/mol per additional methyl or methylene group. vdW-DF calculations predict an even stronger adsorption - the adsorption energy for methane is -33.2 kJ/mol and increases by an increment of 15-20 kJ/mol for the longer alkanes.

Si-chabazite	CH_4	C_2H_6	C_3H_8
PBE	-2.36	-2.73	-4.17
PBE-d	-18.30	-28.14	-40.05
vdW-DF	-33.18	-48.51	-68.22
Na-Chabazite	CH_4	C_2H_6	C_3H_8
PBE	-11.60	-12.91	-14.84
	-13.36	-15.75	-16.77
	-16.68	-19.01	-18.69
Average	-13.88	-15.89	-16.77
PBE-d	-40.80	-51.37	-62.21
	-38.69	-52.53	-64.20
	-43.69	-59.30	-69.78
Average	-41.06	-54.40	-65.40
vdW-DF	-41.91	-58.42	-79.39
	-42.51	-60.20	-75.24
	-48.10	-70.73	-82.92
Average	-44.17	-63.12	-79.18
Experiment[a]	-21.6	-34.1	-46.8

Table 8.1: Adsorption energies (in kJ/mol) of methane, ethane and propane in purely siliceous and Na-exchanged chabazite, calculated at the PBE, PBE-d, and vdW-DF levels of theory. For the Na-exchanged chabazite, the first line refers to configuration (1), the second to configuration (2) etc.. The last line gives the adsorption energies averaged over all three configurations.
[a]After Ref. [239].

	PBE	PBE-d	vdW-DF
Si-Chabazite			
Methane			
C^1-Si	4.25	4.15	4.27
Ethane			
C^1-Si	4.61	4.24	4.36
C^2-Si	4.35	4.27	4.32
Propane			
C^1-Si	4.34	4.34	4.33
C^2-Si	4.37	4.26	4.33
C^3-Si	4.74	4.60	4.56

Table 8.2: Geometry of the adsorption complexes formed by alkanes in purely siliceous chabazite, calculated at the PBE, PBE-d, and vdW-DF levels of theory. Distances between the C atoms of the alkane and the nearest Si atom are listed in Å.

Na-exchanged chabazite

In Na-exchanged chabazite the weak specific interaction with the acid site adds between about 10 and 30 kJ/mol to the adsorption energy, depending on the level of theory and the location of the acid site but almost independent of the length of the alkane. At the PBE level the additional contribution ranges between $\sim$ 10 kJ/mol for configuration (1) and $\sim$ 15 kJ/mol for configuration (3) for all three alkanes, i.e. the strength of the interaction with the acid site increases with its decreasing stability (from (1) to (3)). This is also reflected in the geometry of the adsorption complexes. For methane and ethane, the shortest Na-C distance is about 2.7 Å. For ethane the distance between the second carbon atom and a Si atom of the framework remains within $\pm$0.15 Å the same as without the acid site. For propane the adsorption geometry for all three configurations is shown in Figure 8.3. The stronger binding of the adsorbate to the acid site when dispersion forces are added allows also to find a configuration where the molecules nestles somewhat closer to the surface - this is most pronounced in configuration (3). In configuration (2) we observe a slightly different structure than without the acid site were one C-Si distance is elongated and the other contracted.

If dispersion corrections are taken into account, the adsorption energy for methane is increased (average over all three configurations) from -13.9 kJ/mol to -41.1 (-44.2) kJ/mol using the PBE-d (vdW-DF) approaches - this means that the strength of the vdW interactions is about twice as large as the polarization-induced interactions described by DFT alone. For ethane and propane the adsorption energy increases by an increment of $\sim 12 \pm 1 (18 \pm 2)$ kJ/mol per additional CH_x group if PBE-d (vdW-DF) dispersion corrections are added. Hence the dispersion corrections increase the interaction of the terminal methyl group with the Na-cation more than the pure van der Waals interactions of the remaining CH_x groups with the framework, the dispersion corrections provided by the vdW-DF functional are significantly larger than those described by the empirical PBE-d force field.

There are also significant differences in the adsorption geometries. PBE-d reduces the distance between the C atom in the terminal methyl group and the Na cation by 0.05 to 0.29 Å, the variation of the C-Si distances depends on orientation of the molecule in the cavity. In general, C-Si distances are contracted, but if the molecule extends diagonally across the cavity, the shorter Na-C distance can also lead to a longer C-Si distance at the other end (see Figure 8.3). vdW-DF leaves the Na-C distance almost unchanged - the only exception is propane in configuration (1) were the distance shrinks by 0.17 Å. C-Si distances change even less, in general the vdW-DF geometry is very close to that calculated at the PBE level.

For Na-exchanged chabazite, experimental values of the adsorption energy are available form the work of Denayer et al. [239]. While the dispersion-corrected energies correctly describe the almost linear increase of the adsorption energies as a function of the carbon number with an increment of $\sim$ 12 kJ/mol , they are significantly larger than experiment. We shall come back to the critical comparison between theory and experiment after discussing the results obtained with the ACFDT-RPA method.

	PBE	PBE-d	vdW-DF
Na-Chabazite			
Methane			
C^1-Na	2.73	2.64	2.80
	2.72	2.61	2.74
	2.68	2.59	2.73
Ethane			
C^1-Na	2.75	2.64	2.78
	2.68	2.60	2.69
	2.64	2.59	2.68
C^2-Si	4.25	4.08	4.25
	4.49	4.37	4.49
	4.41	4.14	4.33
Propane			
C^1-Na	2.95	2.66	2.78
	2.70	2.59	2.70
	2.61	2.55	2.57
C^2-Si	4.25	4.23	4.23
	4.95	5.13	4.90
	4.14	4.37	4.06
C^3-Si	4.35	4.84	4.31
	4.05	3.51	4.00
	3.83	3.65	3.82

Table 8.3: Geometry of the adsorption complexes formed by alkanes in Na-exchanged chabazite, calculated at the PBE, PBE-d, and vdW-DF levels of theory. Distances between the Na-cation and the nearest carbon atom (C^1), the second (C^2) and third (C^3) carbon atom in the alkane and the closest framework Si-atom are given for the Na-exchanged zeolite. The first line refers to configuration (1), the second to configuration (2), the third to configuration (3). All distances are in Å.

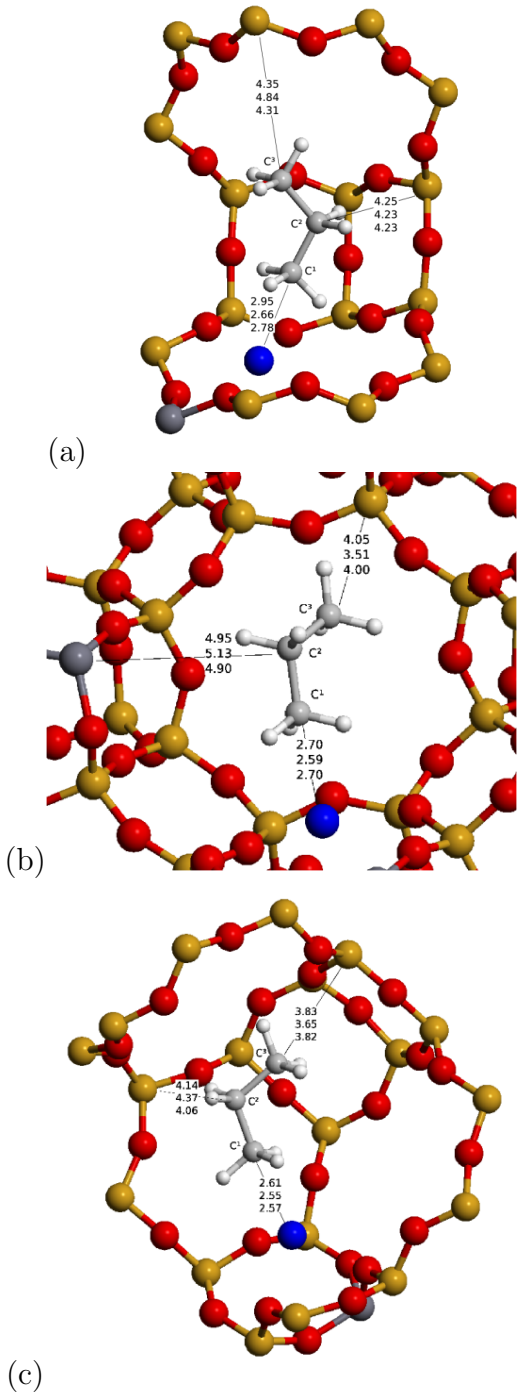

Figure 8.3: (a -c) Relaxed structure of the adsorption complex of propane in Na-exchanged chabazite [configurations (1) to (3)]. The numbers give the distances (in Å) between the C atoms of propane and the surrounding oxygen atoms of the framework, calculated in the PBE (top), PBE-d (middle) and vdW-DF (bottom) approximations. Cf. text.

Si-Chabazite		CH_4	C_2H_6	C_3H_8
PBE	RPA	-11.99	-18.21	-26.29
	RPA-HF	-14.03	-21.38	-30.78
PBE-d	RPA	-4.1	-16.72	-22.55
	RPA-HF	-8.19	-22.39	-29.92
vdW-DF	RPA	-13.20	-18.65	-26.30
	RPA-HF	-14.48	-21.51	-30.85

Table 8.4: Adsorption energies (in kJ/mol) of methane, ethane and propane in purely siliceous chabazite, calculated at the RPA and RPA-HF levels of theory and geometries optimized at the PBE, PBE-d and vdW-DF levels. The first line give the RPA results, the second line the RPA-HF results.

ACFDT-RPA calculations

Calculations at the ACFDT-RPA level undoubtedly provide the most accurate correlation energies for large periodic systems. However, to date these calculations can be performed only non-selfconsistently and for fixed geometries. Therefore we have performed RPA calculations for the geometries optimized at the PBE, PBE-d and vdW-DF levels of theory. In addition to the standard RPA calculations expressing the total energies as the sum of the exact exchange energies evaluated using PBE wavefunctions plus correlation energies from the coupling-constant integration, we have also performed RPA-HF calculations based on a self-consistent solution of the HF equations, following a suggestion of Ren et al.[87]. RPA-HF is known to provide slightly larger (and in many cases more realistic total energies), but there is no generally accepted theoretical foundation for this approach. The results are compiled in Table 8.4 and 8.5.

The question to be addressed is that for the most realistic geometry; i.e. the geometry minimizing the RPA total energy. For the purely siliceous chabazite we find that the RPA energies calculated for the PBE and vdW-DF geometries differ by much less than 1 kJ/mol, whereas the PBE-d geometry yields a significantly higher total energy. The RPA-HF energies are lower than the RPA values, the difference is largest for the PBE-d geometry and smallest for the vdW-DF geometry.

A similar picture arises from the analysis of the results for Na-exchanged chabazite. At the RPA level the total energies calculated for the PBE and vdW-DF geometries agree within ~ 1 kJ/mol and they are much lower than the energies computed for the PBE-d geometries. The difference is largest for methane and decreases with increasing carbon number. The only exception is propane in configuration (2) where the lowest energy is calculated for the PBE-d geometry. The comparison of the geometrical data in Table 8.3 suggests that this could be due to a shorter C^3-Si distance at the expense of a longer C^2-Si distance. At the RPA+HF level the PBE and vdW-DF geometries yield almost equivalent total energies which are much lower than those for the PBE-d geometries for methane, ethane and propane in configurations (3). For propane in

Na-Chabazite		CH_4	C_2H_6	C_3H_8
Configuration 1				
PBE	RPA	-19.22	-27.24	-35.43
	RPA-HF	-22.15	-31.46	-40.75
PBE-d	RPA	-9.02	-23.82	-33.98
	RPA-HF	-15.49	-30.51	-42.37
vdW-DF	RPA	-18.84	-27.08	-35.34
	RPA-HF	-22.69	-31.01	-41.30
Configuration 2				
PBE	RPA	-20.41	-28.41	-35.43
	RPA-HF	-22.57	-31.90	-42.07
PBE-d	RPA	-14.75	-26.92	-41.14
	RPA-HF	-18.89	-32.99	-49.81
vdW-DF	RPA	-20.61	-28.85	-37.26
	RPA-HF	-23.72	-33.19	-41.85
Configuration 3				
PBE	RPA	-24.19	-33.46	-36.24
	RPA-HF	-26.54	-37.40	-41.55
PBE-d	RPA	-14.00	-19.61	-24.80
	RPA-HF	-16.91	-25.12	-31.75
vdW-DF	RPA	-23.77	-33.27	-35.79
	RPA-HF	-27.15	-38.50	-42.36
Average[a]	RPA	-21.07	-29.73	-36.13
	RPA-HF	-24.52	-34.23	-42.83
Experiment[b]		-21.6	-34.1	-46.8

Table 8.5: Adsorption energies (in kJ/mol) of methane, ethane and propane in Na-exchanged chabazite, calculated at the RPA and RPA-HF levels of theory and geometries optimized at the PBE, PBE-d and vdW-DF levels. The first line gives the RPA results, the second line the RPA-HF results.
[a] Calculated using the vdW-DF geometry.
[b] After Ref. [239].

configuration (1) all three geometries yield almost the same adsorption energies, while propane in configuration (2) is again an exception, with the lowest energy for the PBE-d geometry.

While the calculation of the RPA total energies for a few discrete geometries can of course not replace a full structural optimization (which must be left to future work), the good agreement between the energies computed at the PBE and vdW-DF levels of theory, and the relatively large energy differences compared to the PBE-d geometries suggests that dispersion forces will not change the PBE geometries very much. On the other hand, the purely attractive pairwise dispersion corrections of the PBE-d approach appear to be an oversimplification because short-range repulsive forces are neglected.

8.6 Discussion

Nature of bonding forces

While in a purely siliceous zeolite saturated molecules are bound to the framework only via dispersion forces, in acid zeolites there is in addition a specific interaction attaching the adsorbate to the acid site. The physical mechanisms underlying both types of bonding are fundamentally different. Dispersion forces arise from the mutual dynamical polarization of adsorbate and framework. The specific interaction with the acid site has occasionally been described as covalent, but this can hardly been justified for such a weak interaction. We have investigated the nature of the bonding by analyzing the difference-electron densities (i) between the Na-exchanged zeolite and the neutral (but electron-deficient) zeolite framework with one Al/Si substitution and a neutral Na atom, and (ii) between the alkane-chabazite adsorption complex and pure chabazite and the gas-phase molecule (both in their geometries optimized for the adsorption complex). The constant-density surfaces for Na-chabazite (see Figure 8.4) show that electrons are transfered from the Na-atom to the zeolite framework, leading to an increased electron density not only around the "activated" O-atoms around the Al-site, but also around non-activated oxygen atoms. A Bader analysis shows that the integrated charge at the Na-cation is rather close to its formal valence of +1.

The positive charge at the cation and the negative charge of the framework form a strong dipole moment polarizing an adsorbed molecule. Constant-density surfaces for propane in siliceous and Na-exchanged chabazite, calculated at the PBE and vdW-DF level are shown in Figure 8.5.

In siliceous chabazite we find only a very modest charge-redistribution within the propane molecule and on the chabazite framework (results are almost identical at the PBE and vdW-DF levels), reflecting the absence of any specific interactions beyond the dispersion forces. For Na-exchanged chabazite the positive charge on the extra-framework cation induces a polarization of the alkane molecule, leading to an accumulation of electron density in the region between the terminal methyl group and the Na-cation. Electron density is withdrawn from the terminal methyl group in contact

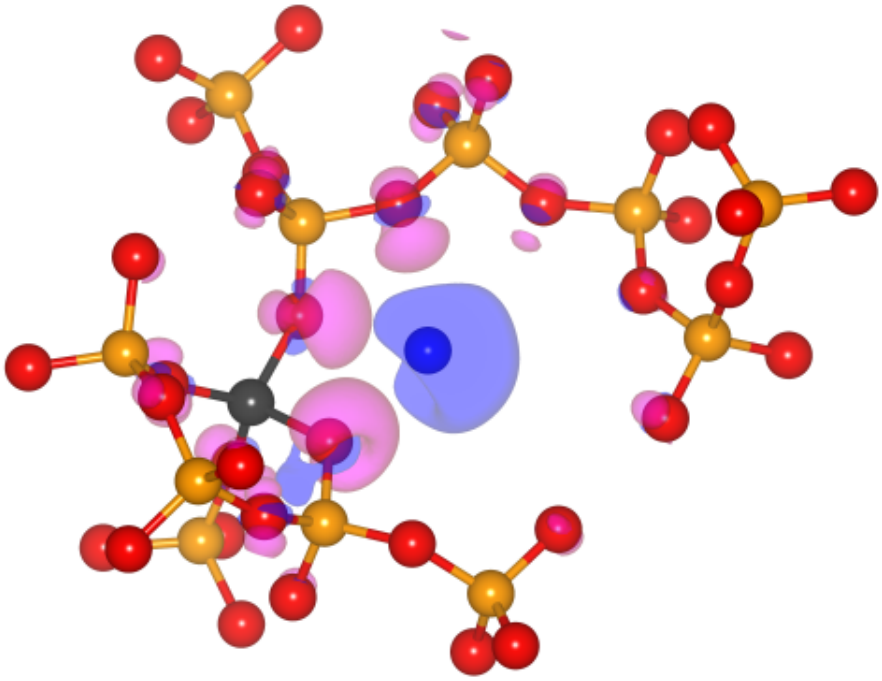

Figure 8.4: Difference-electron density between Na-exchanged chabazite [configuration(1)] and the neutral zeolite (with one Al/Si substitution site) and a neutral Na atom. Blue constant-density surfaces surround electron depleted regions, red surfaces regions of increased electron density. Contour values are $2{\times}10^{-3}$ electrons/Å^3. Cf. text.

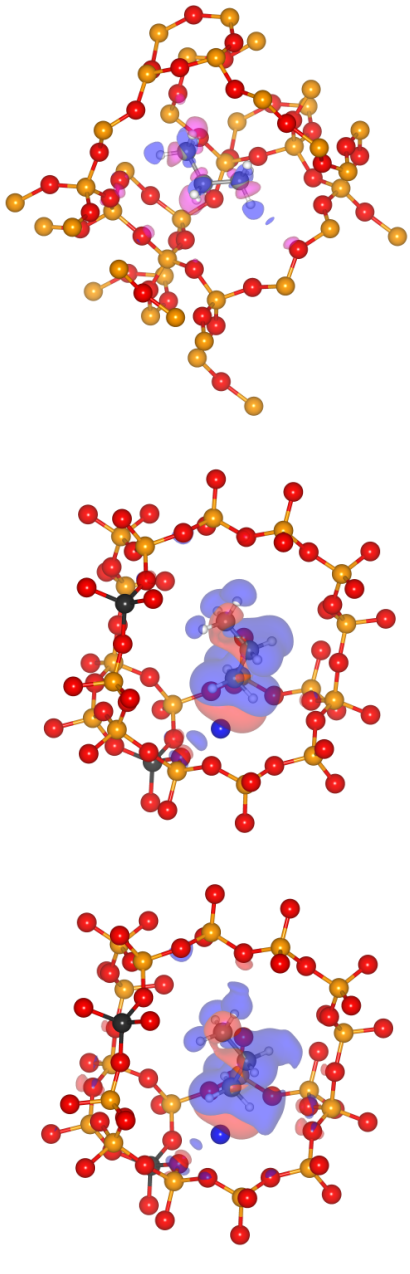

Figure 8.5: Difference-electron densities for the propane-chabazite adsorption complex in (a) purely siliceous chabazite (calculated at the vdW-DF level) and Na-exchanged chabazite [configuration 1] calculated at the PBE (b) and vdW-DF (c) levels of theory. Blue constant-density surfaces surround electron depleted regions, red surfaces regions of increased electron density. Contour values are 0.27×10^{-3} electrons/Å^3 Cf. text.

with the cation and from the methylene groups and one observes also weak polarization in the second terminal methyl group. The charge distribution on the framework on the other hand remains almost unchanged. These charge-rearrangements reflect the specific interaction of the alkane with the Lewis acid site arising from a static polarization of the alkane which is superposed to the dispersion interactions (which are not reflected in the static charge redistributions).

One should also point out that the interaction with the extra-framework cation polarizes the oxygen atoms of the framework, but not the silicon atoms. This also hints to another weakness of the PBE-d approach. Formally, the charge state in the SiO_4 tetrahedra forming the zeolite framework is $Si^{4+}O_2^{2-}$ but the C_6 parameter for the semi-empirical dispersion corrections are calculated for neutral atoms and molecules - a neutral Si atom with has a higher polarizability than a neutral O atom where the valence electrons are more strongly bound. Hence the C_6 parameter for neutral Si is larger than than for neutral O, whereas for a positively charged Si cation and a negatively charged O anion the relation should be just the inverse. However, in summary the interaction between the alkane and the constituting SiO_2 units of the framework is still relatively well described.

Comparison between theory and experiment

Comparison between theory and experiment is not straightforward. Two essential aspects have to be considered: (i) In a real zeolite cations are located at different energetically accessible cation sites. Our calculations have shown that configurations (1) and (2) are energetically almost equivalent, while configuration (3) is higher in energy - but not so much that it will not be present in chabazite. Experimental adsorption energies should therefore be compared with an average of the adsorption energies calculated for different adsorption sites. (ii) Adsorption experiments have been performed at room temperature. Since the specific binding to the acid site is weak, there is a non-negligible probability that at room temperature the molecule will already be desorbed from the cation and bound only by van der Waals interactions with the inner wall of the zeolite. For propane in protonated chabazite ab-initio molecular dynamics simulations of Bučko et al.[18] have demonstrated that at T=100 K the probability that the molecule is bound to the acid site (i.e. that the distance between the terminal C atom and the proton is less than 3 Å) is close to 100%, while at T=300 K the probability that at least one of the C atoms is found at a distance of less than 3 Å from the proton is decreased to 68%, leading to a strong decrease of the internal energy of adsorption. Since the strength of the specific binding to Lewis- or Brønsted-sites is comparable ($\sim 10-12$ kJ/mol), we can assume a similar probability of binding to the Na-cation.

Figure 8.6 compares the adsorption energies calculated at different levels of theory and averaged over all three configurations with the experimental results of Denayer et al. [239]. If no temperature effects are taken into account we find that both the semi-empirical dispersion corrections and the vdW-DF functional strongly overestimate the adsorption energies. RPA calculations (at the optimized vdW-DF geometries)

(a)

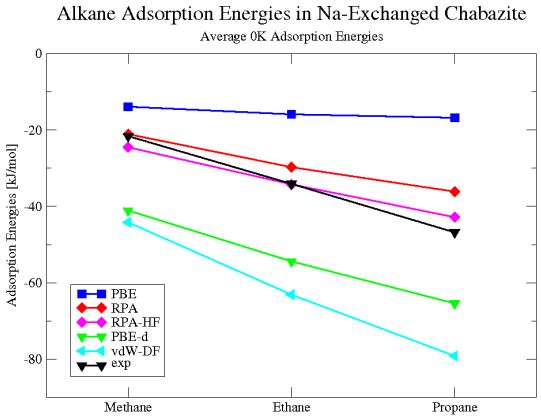

(b)

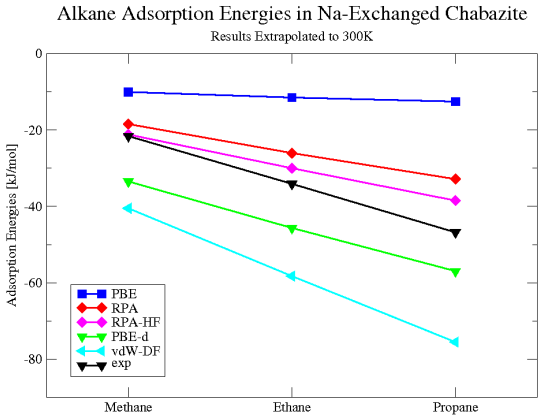

Figure 8.6: (a) Comparison of the adsorption energies calculated for methane, ethane and propane at different levels of theory (RPA and RPA-HF energies are calculated at the optimized vdW-DF geometries) and averaged over all three Na-sites with experiment (after Denayer et al.[239]). (b) To account for the effect of finite temperature, adsorption energies calculated for Na-exchanged and purely siliceous chabazite have been averaged in a ratio of 2:1 (cf. text).

somewhat underestimate the adsorption energies, while RPA-HF leads to very good agreement with experiment. PBE-d overestimates the adsorption energies of all three molecules by an almost constant amount, while the increment per additional CH_x group agrees quite well with experiment. The vdW-DF calculations overestimate the adsorption energy of methane by about the same amount, but predict an even stepper increase of the adsorption energy with increasing chain length. We think that the overestimation of the adsorption energy for methane arises from the fact that both the Grimme force field used in PBE-d and the non-local correlation functional in vdW-DF describe some short-range exchange-correlation effects which are also included in the PBE or rev-PBE functional. The same double-counting of correlation terms could also be responsible for the larger incremental vdW contributions per CH_x group calculated with the vdW-DF functional. Both the RPA and the RPA-HF predict a smaller increase with increasing chain length - correlation energies are evidently still underestimated in the RPA.

A rough estimate of the effects of finite temperature (i.e. of the probability that the molecule desorbs from the extra-framework cation but still binds to the zeolite via van der Waals interactions with the framework) can be realized by averaging the adsorption energies calculated for Na-exchanged and purely siliceous chabazite in a ratio of 2:1. The reduction of the effective adsorption energies compared to the low-temperature limit leads to a less perfect agreement with experiment, suggesting that the RPA tends to underestimate adsorption energies.

8.7 Conclusions

The adsorption of short alkane molecules in purely siliceous and Na-exchanged chabazite has been investigated at different levels of theory. DFT calculations using the gradient-corrected PBE exchange-correlation functional describe the interaction of the alkane with the acid site rather well, but fail to account for the van der Waals interactions between the molecule and the inert inner wall of the zeolite. Semi-empirical corrections for dispersion forces such as those proposed by Grimme [66] and the van der Waals exchange-correlation functional proposed by Dion et al. [94, 95] allow to perform self-consistent calculations of the optimized geometry of the adsorption complex, but strongly overestimate the adsorption energies. RPA calculations for a fixed geometry demonstrate that the vdW-DF approach leads to a more realistic geometry of the adsorption complex (which remains rather close to the PBE result), while the Grimme force fields tend to produce too short distances between the C molecules of the alkane and the zeolite. A critical comparison with experiment demonstrates that the RPA tends to slightly underestimate adsorption energies. Combining the RPA correlation energy with a self-consistent HF exchange energy further improves agreement between theory and experiment.

9 Protonated chabazite

Summary

In this chapter we investigate the adsorption of alkanes in protonated chabazite. We compare the performance of 0K energy minimization techniques using periodic boundary conditions at different levels of theory to MD-calculations and the use of embedding schemes. Especially calculations using second order Møller Plesset perturbation theory as well as MD simulations using PBE-d lead to excellent agreement with experimental data. By comparing MD calculations and 0K energy minimization we justify the use of the second approach.

9.1 Introduction

Already in the last chapter we have studied the adsorption of alkanes to Na-chabazite. We used many different methods but none of them lead to entirely satisfactory results. For this reasons we will revisit the problem in a slightly different, but for industrial applications more important system.

Describing the adsorption of alkanes in zeolites by electronic structure calculations is very tricky. The methods used have to be able to describe two contributions to bonding at a high level of accuracy. The first contribution is the interaction between the alkane and the adsorption site, the second contribution are the van der Waals (vdW) interactions between the alkane and the cavity wall.

Especially the description of the vdW-forces poses large problems for the usually applied methods of density functional theory (DFT). In the most commonly used functionals the correlation is described (semi-)locally, but vdW-forces are truly non-local interactions. It is impossible to describe them by local approximations. Several solutions have been proposed to solve this problem. They range from methods as simple as the addition of a semi-empiric force-field between the nuclei to a standard density functional (PBE-d)[66] over the addition of a non-local correlation contribution (vdW-DF)[94, 95] to methods as complex as the Random Phase Approximation (RPA)[80, 81, 82].

Recently the choice of a proper exchange functional in the vdW-DF has been a topic of discussion. Klimes et al. tested various exchange functionals to minimize the error of the vdW-DF-type functionals on a given test set [99, 100]. Additionally the efficient implementation of the Hartree-Fock exchange operator [117] has opened the doors for the use of high-level quantum chemical methods like Møller-Plesset perturbation theory for extended systems [93]. In this study we will additionally investigate the

performance of MP2 and vdW-BP86, the vdW-DF type functional leading to the smallest errors for previously mentioned predefined test-set.

In the previous chapter we also proposed an extrapolation mechanism to capture finite temperature effects. We are conscious of the fact that such an extrapolation mechanism can never be perfect. To estimate the quality of our highly simplified approximation we will perform MD simulations for methane, ethane and propane in protonated chabazite using PBE-d. This will help us to estimate the impact of entropic effects on adsorption energies.

9.2 Theory and computational setup

Theory

The adsorption of alkanes in zeolites consists of two contributions. The first contribution stems from an interaction between the alkane and the adsorption site. The second contribution comes from the vdW-type interactions between the alkane and the cavity wall. Only in high level methods, where the correlation contribution depends non-locally on occupied as well as non-occupied electronic orbitals, these vdW interactions are captured naturally. For lower level methods from density functional theory (DFT) they pose serious problems.

In DFT local and semi-local approximations of the correlation functional are very successful. But the vdW-interactions are truly non-local, which makes it impossible for (semi-)local approximations to describe them properly. This is a well known problem and in the last decade large amounts of work have been invested to cure these problems.

We already discussed PBE-d, the vdW-DF, RPA and RPA-HF in the chapter on Jacob's Ladder and the previous chapter. In this chapter we will only discuss the impact of the choice of GGA exchange functional for the vdW-DF and MP2.

Improving the vdW-DF - Adapting the exchange contribution

The original vdW-DF was proposed as

$$E_{xc} = E_x^{GGA}(n(\mathbf{r}), \nabla n(\mathbf{r})) + E_c^{LDA}(n(\mathbf{r})) + E_c^{LR}(n(\mathbf{r}), n(\mathbf{r}')). \tag{9.1}$$

The exchange and the local correlation contribution in this functional form are semi-local quantities. Only the long range correlation contribution is truly non-local.

While both correlation contributions are well defined, the exact functional form of the exchange contribution has been a topic of discussion. In the original paper by Dion et al. rev-PBE had been suggested [94, 95]. The authors argued that this functional is truly correlation free, which is the desired property for a functional in the given form.

This exact functional form still leads to rather larger errors for tests on the S22 test set of about 5.8 kJ/mol. Already Gulans found that these errors could be reduced by choosing PBE as an exchange functional [97]. The first larger systematic test of exchange functionals was performed by Klimes et al. [99, 100]. They found out that the

errors could be minimized by choosing a revised version of the BP86 functional, they called BP86b. Using this functional they were able to reduce the total error on the S22 dataset to less than 2.2 kJ/mol. In this work we will compare the performance of the original functional using rev-PBE (vdW-DF) and using BP86b-exchange (vdW-BP86).

Møller-Plesset perturbation theory

Compared to the variational approaches there is also the possibility to calculate energies perturbatively. In this approach the Hartree Fock operator is assumed to be the operator describing the unperturbed system. The perturbation $H^{(1)}$ itself is defined as

$$H^{(1)} = H^{tot} - H^{HF} \tag{9.2}$$

where H^{HF} is the Hartree-Fock and H^{tot} is the total electronic Hamiltonian.

Using this expression for the perturbation the first correction to the ground-state energy corresponds to the Hartree-Fock energy expression. The first correction to this energy is given by second order perturbation theory. After a little algebra this term in its orbital expression turns out to be

$$E^{(2)} = \frac{1}{4}\sum_{a,b}^{occ}\sum_{p,q}^{uocc}\frac{\langle a,b||p,q\rangle\langle p,q||a,b\rangle}{\epsilon_a+\epsilon_b-\epsilon_p-\epsilon_q} \tag{9.3}$$

where summation runs over occupied ψ_a and ψ_b and unoccupied ψ_p and ψ_q orbitals. ϵ_i denotes the one electron energy associated with the orbital ψ_i. Furthermore

$$\langle a,b||p,q\rangle = \int d^3\mathbf{r}d^3\mathbf{r}\frac{\psi_a^*(\mathbf{r})\psi_b^*(\mathbf{r}')\psi_p(\mathbf{r})\psi_q(\mathbf{r}')}{|\mathbf{r}-\mathbf{r}'|} - \int d^3\mathbf{r}d^3\mathbf{r}\frac{\psi_a^*(\mathbf{r})\psi_b^*(\mathbf{r}')\psi_q(\mathbf{r})\psi_p(\mathbf{r}')}{|\mathbf{r}-\mathbf{r}'|} \tag{9.4}$$

This form of perturbation theory is called second order Møller-Plesset perturbation theory (MP2) and many implementations in a localized basis set exist. When using plane waves the efficient computational evaluation is more complicated. It was preceded by an efficient implementation of the Hartree-Fock energy expression in a plane wave basis-set by Paier et al. [117]. After this first step it were Marsman et al. who succeeded in implementing MP2 [93].

Computational details

In all our calculations we used the latest version of the Vienna Ab-Initio Simulation Package (VASP) [135, 136]. The exact details of the calculations have already been given in the previous chapter. Our calculations using the vdW-BP86 were performed using the implementation by Klimes et al. described in [99, 100]. For MP2 calculations we used the implementation of Marsman et al. described in [93]. The details for molecular dynamics calculations will be described in the corresponding section.

The System

We studied the adsorption of alkanes in protonated chabazite. Chabazite is a mineral from the zeolite family with a chemical composition of SiO_2. These atoms form tetrahedrons with Si in the center and corner-sharing O atoms. These tetrahedrons form a double 6 ring structure. The minimal unit cell of chabazite consists of 12 T sites and exactly one double 6-ring structure. The cell has a rhombohedral symmetry. As geometric parameters we chose the values already discussed in chapter 4 (a=9.341 Å, α=94.0°, volume=808.94 Å).

If now one Si atom is substituted by a Al atom a local charge deficit is created in the framework. This deficit is compensated by the addition of one hydrogen atom, which creates a Brønstedt acid site. The Si→Al substitution creates a local distortion in the framework which increases the cell volume. In our calculations we assumed a high Si/Al ratio which is typical for zeolites used in catalysis. This implies that only one Si→Al substitution in several unit cells is found. For this reason we kept the volume unchanged with respect to the purely siliceous species.

In chabazite all T-sites are geometrically equivalent leading to four different O species, which can be identified via their membership in different ring structures (for a visualization see Fig. 9.1). O(1) lies in two 4-O and one 8-O ring, O(2) lied in one 4-O, one 6-O and one 8-O ring, O(3) lies in two 4-O and one 6-O ring and O(4) lies in one 4-O and two 8-O rings. Adsorption of H to the four different configurations is energetically very similar. Adsorption energy differences for PBE are smaller than 10 kJ/mol (see chapter 4). These energy differences are small enough that all configurations are accessible at room temperature. Since we are interested in adsorption of alkanes at room temperature we will investigate adsorption to all configurations.

9.3 OK adsorption energies

As a first step in our study we calculated 0K adsorption energies following a similar procedure as in the previous chapter. We optimized structures at PBE, PBE-d, vdW-DF and vdW-BP86 level of theory. We then used the obtained structures to perform RPA, RPA-HF and MP2 calculations.

PBE, PBE-d, vdW-DF and vdW-BP86 calculations

When simulating the adsorption of alkanes in zeolites the description of two specific interactions are important. On one hand the method used has to be able to describe the interactions between the alkane and the active site at a reasonable level of accuracy, on the other hand the vdW interactions between the alkane and cavity wall have to be described accurately. These two competing trends are not only important for the energetics, but are also shown in the different structures.

We find shortest distances between the Brønstedt site and the closest C atom (C_1) of the alkane for PBE-d. For methane we find a bond-length of about 2.15 Å with slight variations for different proton positions. For methane the vdW interactions

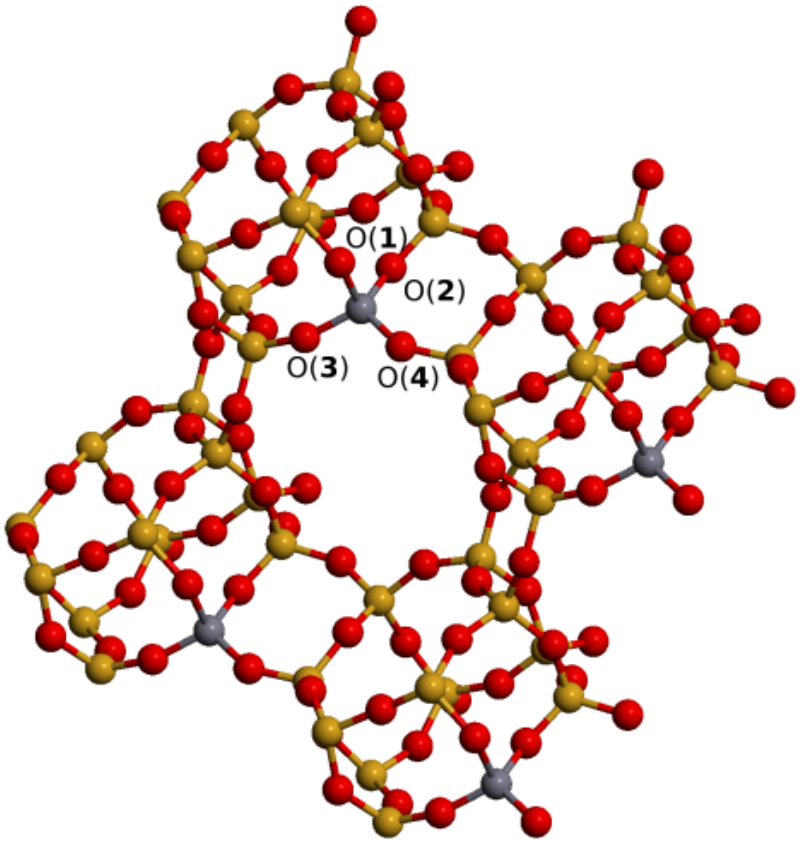

Figure 9.1: In this graph we show four unit cells of chabazite. All T-site are geometrically equivalent which leads to four different O-atoms. Our adsorption geometries are created by adsorbing hydrogen atoms to the four different O atoms. Si atoms are visualized in orange, Al atoms in dark-grey and O atoms in red.

are only of minor importance, but for longer alkanes they become more important. To maximize vdW interactions the alkane has a tendency to nestle to the wall. For selected configurations this effect influences the H-alkane bond and leads to a slightly longer C_1-H distance. Especially for the configuration where the H atom is bound to O(2) this elongation of the bond is as large as 0.25 Å.

For the other functionals we find a similar behavior but with larger C_1-H distances. For PBE the C_1-H bond is elongated by 0.1-0.2 Å, and for vdW-DF and vdW-BP86 by about 0.4 Å. The increase in bond length when moving from PBE-d to PBE can be expected due to the additional forcefield, but the further increase by as much as 0.2-0.3 Å implies a deficit of the vdW-DF type functionals to describe this covalent type of bonding correctly. Also the distances between the cavity wall and the C atoms in the alkane are elongated for PBE, vdW-DF and vdW-BP86 with a very similar behavior for all three functionals. In Fig. 9.2 and Fig. 9.3 we visualized the geometries for propane adsorption and for the interested reader the exact geometrical details for all molecules are supplied in Appendix B.

Our calculated adsorption energies are summarized in Tab. 9.1. These results are very similar to the values obtained in the previous chapter in our study on Na-chabazite. This can be expected since only the interactions between the active site and the alkane are affected when changing the active site. The chabazite framework and with it also the vdW interactions, which make up for the largest part of the adsorption energy, remain unchanged.

Again PBE leads to a constant adsorption energy of about 8 kJ/mol for the different alkane lengths. Since it does not include vdW-interactions this behavior can be expected. Adsorption energies increase when adding the dispersion correction for PBE-d. For this method adsorption energies increase with alkane-length. We find almost identical adsorption energies for vdW-DF and vdW-BP86. For these methods the adsorption energy is even higher and also the increase for every additional CH_2 group is larger.

RPA, RPA-HF and MP2

For RPA, RPA-HF and MP2 calculations a structural optimization was not possible. Therefore we had to rely on structures relaxed at a lower level of theory. In preliminary tests we found very similar energetic results for PBE, PBE-d and vdW-DF structures. For that reason we only calculated adsorption energies for the PBE-d structure. Our calculated results are summarized in Tab. 9.2.

Our calculated results for all methods lie between PBE and PBE-d results. RPA leads to the lowest adsorption energies. Similar to Na-chabazite the self-consistent calculation of exact exchange increases adsorption energies but influences the increase of adsorption energies with longer alkane lengths only to a small extent. For methane adsorption MP2 leads to very similar results as RPA-HF but we find a stronger increase for every additional CH_2 group.

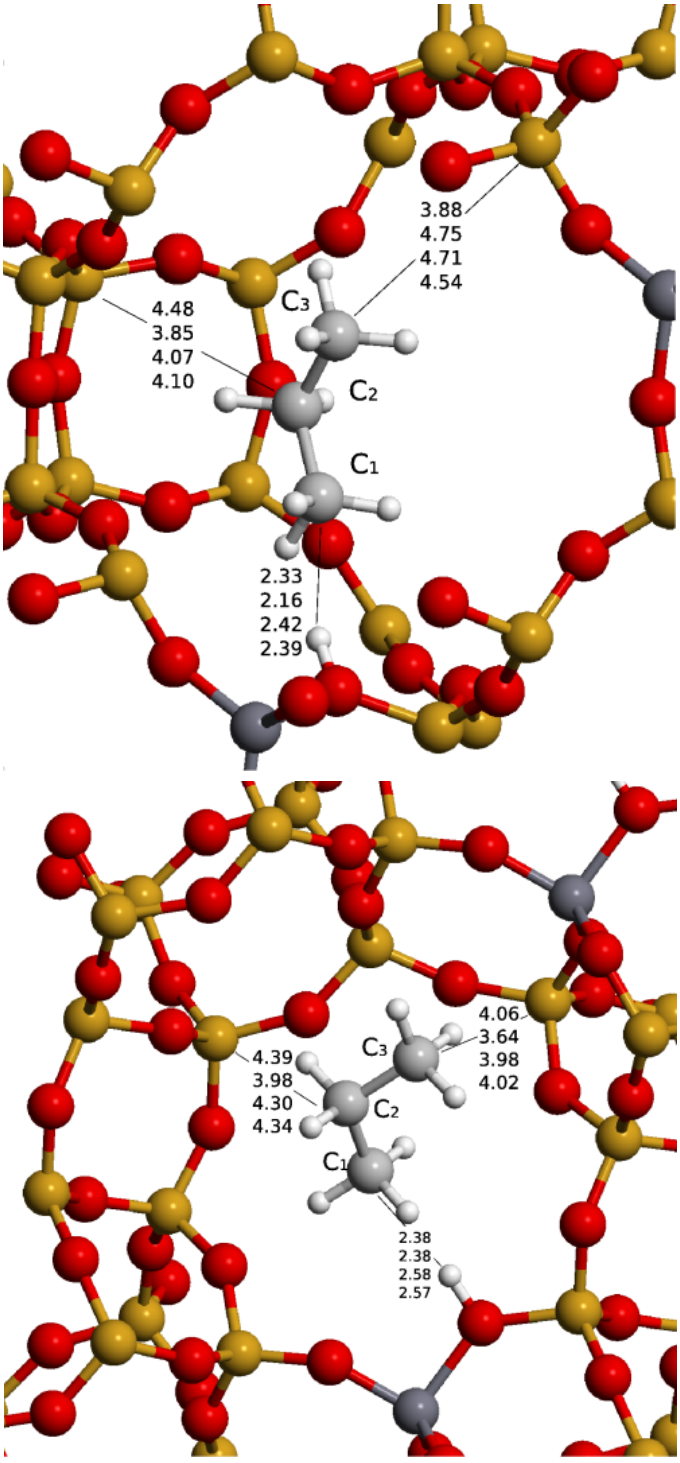

Figure 9.2: In this graph we display the geometries of propane adsorbed to Brønstedt acid sites of (a) O(1) and (b) O(2). Distances in Å are from top to bottom: PBE, PBE-d, vdW-DF, vdW-BP86.

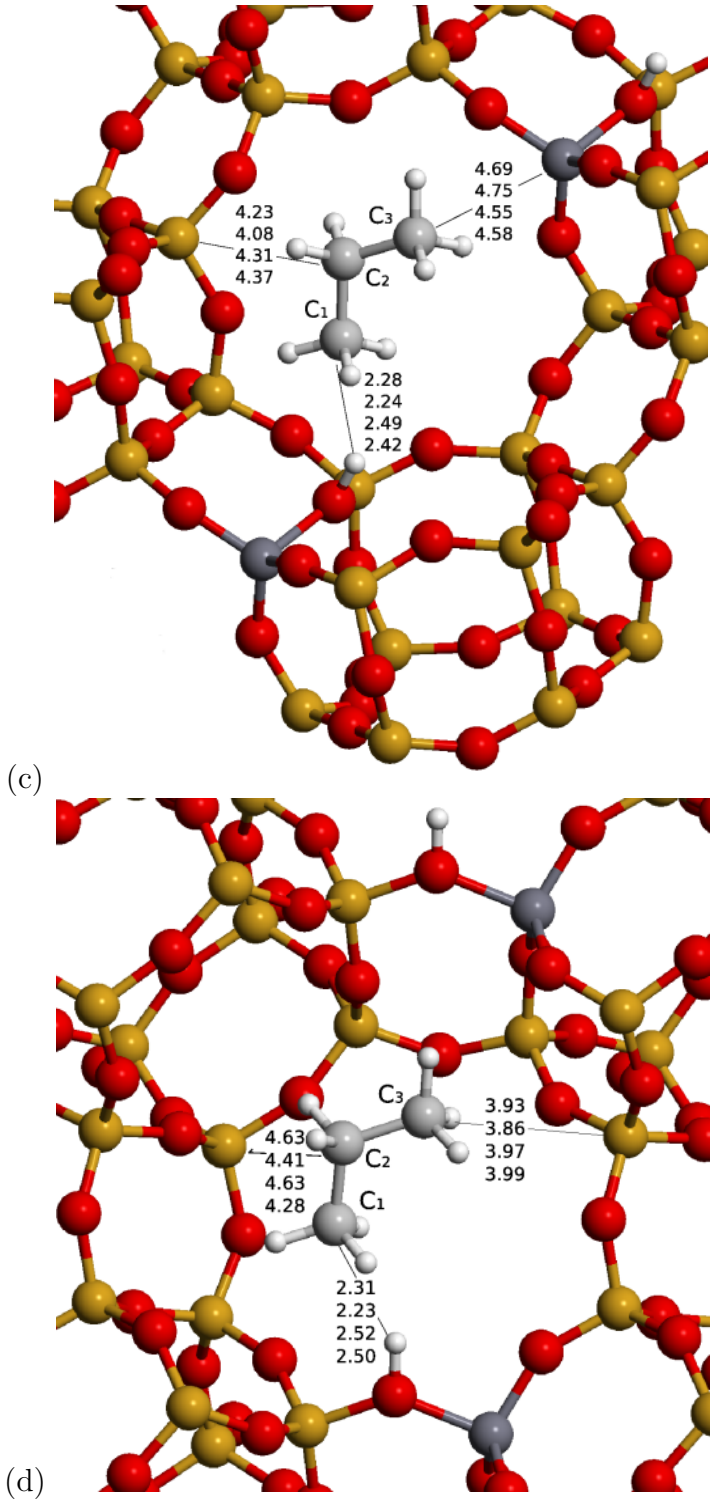

Figure 9.3: In this graph we display the geometries of propane adsorbed to Brønstedt acid sites of (c) O(3) and (d) O(4). Distances in Å are from top to bottom: PBE, PBE-d, vdW-DF, vdW-BP86.

Si-chabazite	CH_4	C_2H_6	C_3H_8
PBE	-2.36	-2.73	-4.17
PBE-d	-18.30	-28.14	-40.05
vdW-DF	-33.18	-48.51	-68.22
vdW-BP86	-30.80	-45.55	-64.37
Protonated chabazite			
PBE			
	-6.73	-8.44	-7.48
	-3.76	-5.11	-3.74
	-7.04	-7.58	-8.28
	-10.29	-12.83	-10.64
Avg.	-6.96	-8.49	-7.54
PBE-d			
	-32.46	-47.38	-59.31
	-32.32	-43.42	-59.44
	-27.78	-40.33	-50.20
	-34.76	-45.98	-58.87
Avg.	-31.83	-44.28	-56.96
vdW-DF			
	-38.39	-58.52	-81.02
	-37.92	-58.40	-74.50
	-34.85	-50.46	-67.84
	-41.75	-59.10	-78.95
Avg.	-38.28	-56.62	-75.58
vdW-BP86			
	-38.04	-58.80	-80.19
	-36.34	-55.96	-75.10
	-35.66	-51.35	-68.41
	-41.27	-59.16	-78.65
Avg.	-37.85	-56.32	-75.59

Table 9.1: In this table we summarize the 0K adsorption energies [kJ/mol] obtained in fully self-consistent calculations using PBE, PBE-d, vdW-DF and vdW-BP86. For a discussion c.f. text.

Si-Chabazite	CH_4	C_2H_6	C_3H_8
RPA	-13.20	-18.65	-26.30
RPA-HF	-14.48	-22.39	-20.85
MP2	-21.67	-31.33	-43.87
Protonated chabazite			
RPA	-19.69	-27.65	-34.96
	-17.16	-21.65	-27.21
	-16.46	-25.41	-26.46
	-26.00	-31.51	-36.92
Avg.	-19.83	-26.56	-31.39
RPA-HF	-28.17	-38.82	-47.64
	-26.08	-32.40	-43.83
	-22.40	-33.27	-35.59
	-32.65	-40.18	-47.63
Avg.	-27.33	-36.17	-43.67
MP2	-25.13	-40.68	-55.49
	-22.44	-35.14	-48.39
	-21.47	-34.28	-44.71
	-28.24	-40.43	-54.17
Avg.	-24.32	-37.63	-50.69

Table 9.2: In this table we summarize the 0K adsorption energies [kJ/mol] for PBE-d structures obtained from calculations using RPA, RPA-HF and MP2. For a discussion c.f. text.

9.4 MD-simulations

Compared to our calculations in experiment alkane adsorption is measured at finite temperature. A typical temperature range is between 300K and 600K. At these temperatures it is not clear whether the quantity we calculated has any correlation to the experimentally measured adsorption enthalpies.

To address this issue we performed molecular dynamics calculations. In experiment typically the zero coverage adsorption enthalpy is measured. To obtain conditions similar to those low pressure adsorption measurements we doubled the cell volume as it is described in [18]. In this model the H atom was attached to the O(4) position. To control the temperature in our calculations we used the Andersen thermostat [242], with a collision probability of 0.015. We fixed the temperature of the heat-bath at 300K and performed a molecular dynamics run over 148 ps with a time-step of 1 fs. Our calculations were performed using PBE-d.

Similar calculations were performed by Bučko et al. in [18]. They only investigated the adsorption of propane and found an adsorption energies of 44 kJ/mol. We were also interested in the entropic effects in dependence of the alkane length. For this reason we performed simulations methane, ethane and propane.

In the actual system we expect the alkane to sit close to the adsorption site for most of the time. But from time to time it can be expected that the thermal movement causes a breaking of the bond and the molecule starts drifting through the cavity. It will probably stay close to the cavity wall, since there is still a large attraction due to vdW interactions. After some more time the alkane will get close to the adsorption site again and move into an adsorbed position. This timespan will be shorter for the longer alkanes, since the probability to be close to the adsorption site again is larger for larger molecules.

To measure this effect we investigated the shortest distance between an alkane C-atom and the active site. The histograms and probability distributions are displayed as red lines in in Fig. 9.4. If one now considers the alkane to be adsorbed to the active site if this distance between C-atom and the Brønstedt site is smaller than 3 Å we find a probability of adsorption of 0.61 for methane, 0.60 for ethane and 0.78 for propane. This distribution is displayed in Fig. 9.5. The last value in our calculations is higher than the value of 0.68 observed by Bucko. In our calculations we used a higher accuracy for electronic relaxations. Therefore differences can be expected.

We also investigated the minimum distances between the alkane C and Si atoms. As we see in the histograms in Fig. 9.4 the variation of this parameter is far smaller than for the C-H distances. This can also be seen in the probability-distributions displayed in Fig. 9.5. They almost resemble a Gauss-curve with the maximum at about 4 Å for all molecules.

The narrowest distribution is found for propane. For this molecule the vdW-interactions with the cavity wall are largest. This paired with the large size of the molecule leads to an almost all the time vdW-bound state. The molecule geometry prohibits a perfect nestling of the molecule to the cavity wall preventing smaller values. The distribution is widened into both directions for ethane. The vdW interactions between molecule

and cavity wall are weaker, which explains the broadening of the curve to larger distances. The widening of the curve to smaller values is more difficult to understand. It seems like the ethane molecule has the perfect size to nestle to the cavity wall, where it is stabilized by vdW-interactions.

This is in perfect agreement with our statistics on the C-H distances. The probability to find the molecule in a position adsorbed to the Brønstedt acid site is similar for methane and ethane. This is contradictory at first sight. The larger molecule size would imply that ethane is more often close to the active site than methane. Only the stabilization of the ethane molecule at the opposite side of the cavity due to vdW-interactions can explain these statistics. The stabilized geometry is shown in Fig. 9.6.

For methane we find a longer tail in the probability distribution for larger Si-C distances. We explain this by the weaker vdW-interactions between molecule and framework. This makes the desorption from the cavity wall more likely. Also the diameter of methane is smaller which makes a re-adsorption to the surface less likely. The weaker vdW-interactions are not strong enough to stabilize the molecule at positions different from the adsorption geometry close to the Brønstedt acid site.

We also calculated the internal energy of adsorption by

$$\Delta U_{ads}(T) = \langle E_{zeo+alk} \rangle_T - (\langle E_{zeo} \rangle_T + \langle E_{alk} \rangle_T) \tag{9.5}$$

as difference between the calculated MD energy averages of the chabazite with alkane and the averages for the alkane and the pure zeolite. From this procedure we obtain values of -23.91 kJ/mol for methane, -34.87 kJ/mol for ethane and -45.53 kJ/mol for butane. Our value for butane is in very good agreement with the results from Bučko, who calculated a value of 44 kJ/mol.

It is difficult to estimate how well converged our MD-simulations are with respect to simulation time. The convergence of adsorption energies seems to satisfactory, but for the distribution of alkane-Brønstedt site distances this might not be the case. For that reason we are not able to estimate the entropic effects with respect to alkane length accurately.

9.5 Finite temperature adsorption energies and comparison to experiment

At finite temperature thermal movement causes the alkane to move out of its ideal adsorption position. This lowers the total energy and even leads to a breaking of the bond. This effect can only be fully captured by MD simulations. Comparing results obtained from 0K energy minimization calculations and MD calculations we find a difference of about one third of the total adsorption energy.

To at least partially correct for these effects we already proposed an extrapolation mechanism in the previous chapter. About 2/3 of the time the alkane will be close to the adsorption site. For the remaining configurations it will move through the cavity and vdW-interactions will keep it close to the cavity wall, which we were able to show

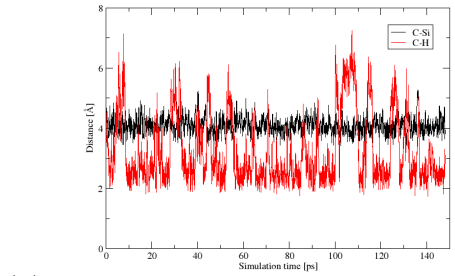

(a)

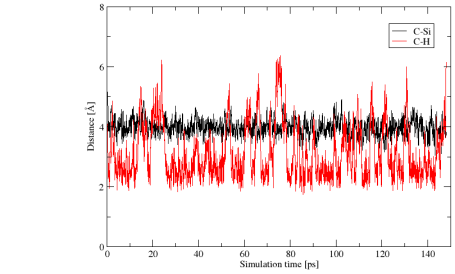

(b)

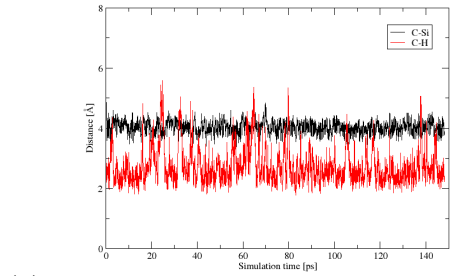

(c)

Figure 9.4: In this figure we show the histograms we show the histograms of the minimum distance between the active site and the closest C-atom in (a) methane, (b) ethane and (c) propane. The minimum distance between the active site and a C atom of the alkane is displayed in red, the minimum distance between C-atoms and framework Si atoms is displayed in black. For a detailed discussion c.f. text.

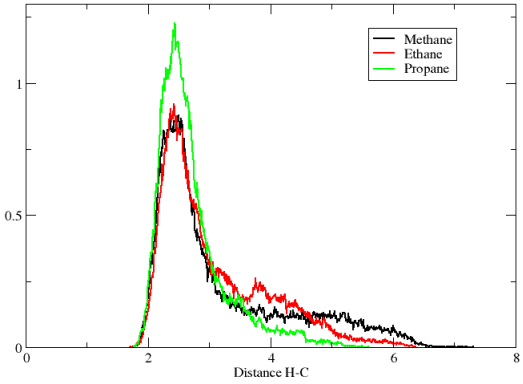

(a)

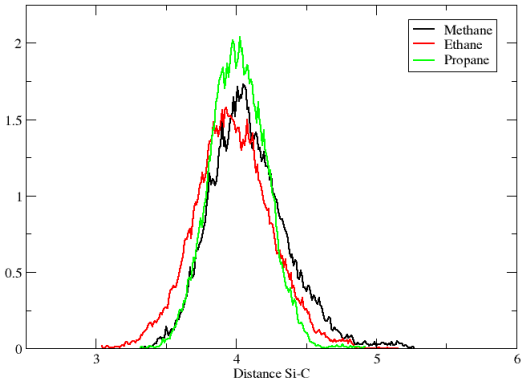

(b)

Figure 9.5: In this graph we display the probability distributions of the minimum C-H (a) and C-Si (b) distances for methane, ethane and propane. For the C-H distances we consider the alkane to be adsorbed to the active site if this distance is smaller than 3 Å. The C-Si distances show a maximum at 4Å, which seems to be the distance, where the molecule is adsorbed to the inner zeolite surface. For a more detailed discussion c.f. text.

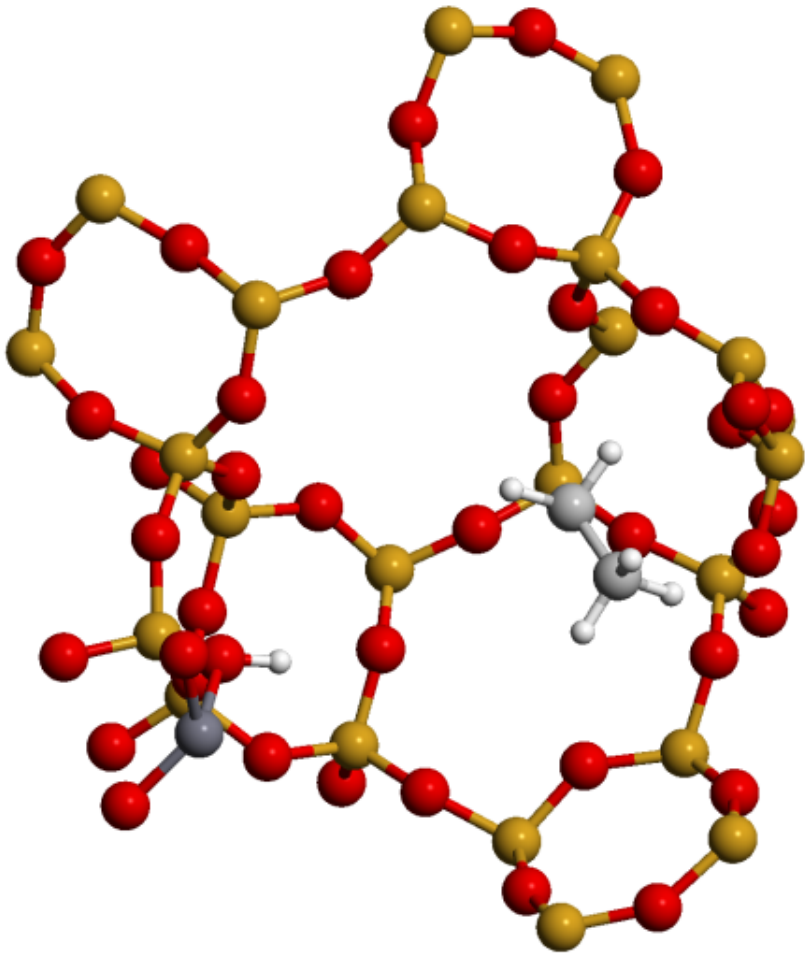

Figure 9.6: In our MD-runs we find a high probability for methane and ethane to stick to the opposite side of the cavity. This configuration for ethane is displayed in this figure. The Brønstedt site is located on the left hand side of the cavity, while the molecule stays close to the right hand side.

	CH_4	C_2H_6	C_3H_8
PBE	-5.27	-6.57	-6.38
PBE-d	-27.32	-38.90	-51.32
vdW-DF	-35.79	-53.92	-73.13
vdW-BP86	-35.50	-52.73	-71.85
RPA	-17.62	-23.92	-29.69
RPA-HF	-23.05	-34.25	-39.46
MP2	-23.91	-35.53	-48.42
MD-PBE-d	-23.91	-34.87	-45.53
Exp[a]	-21.6	-34.1	-46.8
Exp[b]	-20.4	-30.8	-37.3

Table 9.3: In this table we summarize adsorption energies [kJ/mol] for methane, ethane and propane calculated using the proposed extrapolation mechanism, MD calculations as well as measured experimentally.
[a] from [239]
[b] from [243]

by our MD-simulations. Therefore we will add 2/3 of the adsorption energy of the alkane adsorbed to the active site and 1/3 of the adsorption energy of the alkane in purely siliceous chabazite.

Due to the small differences in the stability of Brønstedt acid sites it is impossible to identify a preferred configuration. Therefore we will use an average of adsorption energies over all four adsorption sites for the following calculations. We are conscious of the fact that a factor of 2/3 can only be a rough estimate. Our MD-simulations have shown that really accurate calculations of these probability and possibly also a dependency on alkane length would need a far longer simulation time than the 148 ps we simulated. But 2/3 seem to be a good compromise.

The results of our extrapolation are summarized in Tab. 9.3 and visualized in Fig. 9.7. As expected we obtain almost constant adsorption energies for PBE. They are increased when moving to RPA and again when moving to RPA-HF. For methane and ethane MP2 results are in very good agreement with RPA-HF. For MP2 we find similar differences in adsorption energies when moving from methane to ethane and moving from ethane to propane. This increase in adsorption energies is reduced for RPA-HF. PBE-d shows a similar increment as MP2 but leads to about 3-5 kJ/mol higher adsorption energies. The highest adsorption energies with only marginal differences between them are found for the vdW-type methods. Also the increment is far larger than for the other methods.

Comparison to experiment can be a little tricky. We found two experimental studies, one on protonated chabazite [243] and one on Na-chabazite [239]. The results, however, are very different. While the adsorption energies for methane are very similar, especially the increase in adsorption energies with increased alkane chain length is reduced for the protonated system. This is unexpected, since the only difference

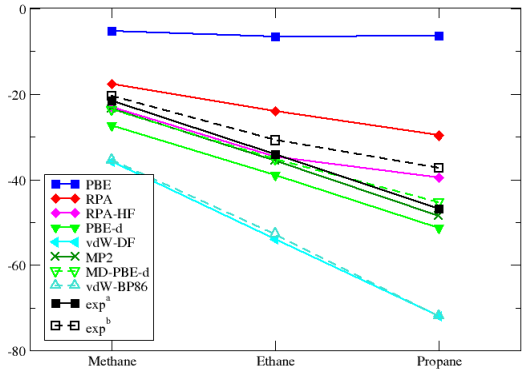

Figure 9.7: In this graph we display adsorption energies for methane, ethane and propane. Especially calculated values from MD-simulations using PBE-d (dashed light-green line) and MP2 (dark green line) show a remarkable agreement with experimental data by denayer (solid black line).
[a] from [239]
[b] from [243]

between these two studies is the choice of the adsorption site. The size and shape of the cavity remain unchanged, which should be reflected in the adsorption enthalpies.

We find excellent agreement with experimental results in Na-chabazite for MP2. Best agreement (although a slight overestimation) is found for RPA-HF and the results for protonated chabazite. RPA again underestimates adsorption energies while PBE-d, vdW-DF and vdW-BP86 overestimate them.

This behavior is actually very similar to our study on Na-chabazite in the previous chapter. We find an almost constant shift in adsorption energies between 2-7 kJ/mol to lower adsorption energies when moving from Na-chabazite to protonated chabazite. Highest shifts are found for PBE and PBE-d and smallest shifts for RPA and RPA-HF. This difference is actually in good agreement with experimental data by Denayer for adsorption energies in protonated and Na zeolite Y [244]. They find a constant shift in alkane adsorption energies of 1.5 kJ/mol between those two systems. These observations strengthen our belief that the experimental data by Barrer et al. might not be a reliable reference.

As we have already observed in our MD calculations, entropic effects are of major importance. The question is, whether our simple extrapolation mechanism can capture these effects correctly. Comparing our extrapolated results from 0K energy minimization and MD calculations we find a constant shift of about 4 kJ/mol with lower adsorption energies found for the MD runs. This very good agreement between results obtained using our extrapolation mechanisms and MD calculations justifies our approach.

9.6 Summary and conclusions

We investigated the adsorption of methane, ethane and propane in protonated chabazite. We compared two different approaches, 0K energy minimization and MD simulations. In 0K energy minimizations we compared the performance of different levels of theory, PBE, PBE-d, two different variations of the vdW-type functionals, vdW-DF and vdW-B86b, as well as the high level methods RPA, RPA-HF and MP2.

We relaxed structures at PBE, PBE-d, vdW-DF and vdW-BP86 level of theory. We found smallest Brønstedt-site-alkane distances for PBE-d, followed by PBE. For vdW-DF and vdW-BP86 we found very similar and also too large values

We then used the obtained geometries to calculate RPA, RPA-HF and MP2 adsorption energies. To account for finite temperature effects we used the extrapolation mechanism already introduced in the previous chapter. Compared to our results for adsorption to Na-chabazite we find very similar values for PBE, PBE-d, vdW-DF, RPA and RPA-HF. The results are only shifted by a constant value.

Furthermore vdW-DF and vdW-BP86 show a very similar behavior leading to a large overestimation of adsorption energies. This indicates fundamental problems in the construction of the vdW-type functionals, which can not be cured by a smart choice of the exchange part of the functional. MP2 on the other hand leads to almost perfect agreement with experimental results for Na-chabazite.

We also performed molecular dynamics calculations for adsorption of methane, ethane and propane to estimate entropic effects on adsorption energies. As a functional we used PBE-d and we calculated adsorption energies at 300 K. In our calculations 60% of the time we found methane and ethane close to the adsorption site while propane was 78% of the time close to the adsorption site. It was interesting to see, that vdW-interactions stabilized ethane at the opposite side of the cavity, a phenomenon we did not find for methane and propane. Compared to 0K calculations the adsorption energies obtained from MD similuations were only shifted by about 4 kJ/mol for all molecules. This actually justifies the calculation of adsorption energies using 0K energy minimization.

Part IV

Appendix

A Cation coordination in excited spin-states

Table A.1: Structural data for extra-framework cation Cu(I) in chabazite in its spin 1 state, calculated for different configurations and using both GGA (PW91, PBE) and hybrid (PBE0, HSE03, HSE06) functionals. All distances are given in Å.

	PW91	PBE	PBE0	HSE03	HSE06
	Configuration 1				
Cu-O(**2**)	2.068	2.069	2.010	2.014	2.009
Cu-O(**3**)	2.022	2.026	1.980	1.984	1.983
Cu-O(3)	2.712	2.712	2.776	2.764	2.806
Cu-O(2)	3.663	3.635	3.759	3.804	3.824
Cu-O(*3*)	3.644	3.593	3.480	3.299	3.312
Al-O(**2**)	1.782	1.784	1.772	1.772	1.772
Al-O(**3**)	1.806	1.808	1.800	1.799	1.799
Al-Cu	2.816	2.821	2.779	2.782	2.780
	Configuration 2				
Cu-O(**1**)	2.000	2.006	1.959	1.961	1.960
Cu-O(**4**)	2.075	2.076	2.022	2.027	2.026
Cu-O(2)	2.817	2.805	2.846	2.857	2.756
Al-O(**1**)	1.803	1.805	1.800	1.800	1.799
Al-O(**4**)	1.782	1.784	1.775	1.776	1.775
Al-Cu	2.852	2.853	2.810	2.813	2.811
	Configuration 3				
Cu-O(**2**)	2.025	2.027	1.990	1.990	1.986
Cu-O(**4**)	2.049	2.052	1.995	2.004	2.000
Cu-O(4)	3.200	3.196	3.297	3.224	3.235
Al-O(**2**)	1.785	1.788	1.778	1.781	1.780
Al-O(**4**)	1.779	1.781	1.775	1.775	1.775
Al-Cu	2.829	2.834	2.792	2.786	2.789

Table A.2: Structural data for extra-framework cation Cu(II) in chabazite in its spin 3/2 state, calculated for different configurations and using both GGA (PW91, PBE) and hybrid (PBE0, HSE03, HSE06) functionals. All distances are given in Å.

	PW91	PBE	PBE0	HSE03	HSE06
	Configuration 1				
Cu-O(**2**)	2.111	2.099	1.998	1.997	1.992
Cu-O(**3**)	2.033	2.035	2.001	2.005	2.002
Cu-O(3)	2.828	2.804	2.768	2.787	2.823
Cu-O(***3***)	3.670	3.580	3.772	3.727	3.722
Al-O(**2**)	1.782	1.786	1.783	1.783	1.783
Al-O(**3**)	1.803	1.804	1.808	1.808	1.807
Al-Cu	2.814	2.824	2.789	2.791	2.792
	Configuration 2				
Cu-O(**2**)	2.065	2.069	2.024	2.044	2.044
Cu-O(**3**)	2.045	2.049	1.995	1.996	1.994
Cu-O(3)	2.741	2.735	2.717	2.598	2.605
Cu-O(2)	3.384	3.393	3.368	3.219	3.229
Cu-O(*3*)	4.015	4.008	3.982	3.856	3.856
Al-O(**2**)	1.775	1.779	1.778	1.776	1.776
Al-O(**3**)	1.797	1.800	1.800	1.802	1.803
Al-Cu	2.791	2.796	2.771	2.782	2.781
	Configuration 3				
Cu-O(**1**)	2.008	2.011	1.969	1.971	1.970
Cu-O(**4**)	2.084	2.085	2.008	2.013	2.007
Cu-O(2)	2.941	2.968	3.032	3.000	3.037
Al-O(**1**)	1.806	1.807	1.805	1.804	1.803
Al-O(**4**)	1.794	1.796	1.786	1.786	1.786
Al-Cu	2.845	2.847	2.804	2.807	2.805
	Configuration 4				
Cu-O(**1**)	1.999	2.003	1.969	1.971	1.972
Cu-O(**4**)	2.087	2.086	2.024	2.026	2.028
Cu-O(2)	2.884	2.891	2.848	2.851	2.813
Al-O(**1**)	1.792	1.795	1.803	1.803	1.802
Al-O(**4**)	1.785	1.788	1.779	1.780	1.779
Al-Cu	2.845	2.846	2.803	2.804	2.804
	Configuration 5				
Cu-O(**2**)	2.037	2.040	1.981	1.984	1.982
Cu-O(**4**)	2.028	2.033	1.986	1.996	1.990
Cu-O(4)	3.249	3.243	3.087	3.021	3.067
Al-O(**2**)	1.789	1.791	1.779	1.780	1.779
Al-O(**4**)	1.786	1.788	1.778	1.778	1.778
Al-Cu	2.830	2.833	2.805	2.802	2.804
	Configuration 6				
Cu-O(**2**)	2.042	2.045	1.991	1.994	1.992
Cu-O(**4**)	2.047	2.050	1.989	1.992	1.991
Cu-O(4)	3.203	3.212	3.204	3.206	3.203
Al-O(**2**)	1.775	1.778	1.779	1.779	1.779
Al-O(**4**)	1.774	1.777	1.778	1.778	1.778
Al-Cu	2.729	2.823	2.781	2.782	2.781

Table A.3: Structural data for extra-framework cation Co(II) in chabazite in its spin 1/2 state, calculated for different configurations and using both GGA (PW91, PBE) and hybrid (PBE0, HSE03, HSE06) functionals. All distances are given in Å.

	PW91	PBE	PBE0	HSE03	HSE06
	Configuration 1				
Co-O(**2**)	1.914	1.926	1.968	2.085	1.963
Co-O(**3**)	1.945	1.949	1.935	1.997	1.935
Co-O(3)	2.016	2.025	2.012	2.076	2.013
Co-O(***3***)	1.993	2.005	2.015	2.000	2.024
Al-O(**2**)	1.794	1.797	1.775	1.767	1.776
Al-O(**3**)	1.835	1.836	1.828	1.819	1.827
Al-Co	2.817	2.825	2.824	2.905	2.816
	Configuration 2				
Co-O(**2**)	1.928	1.932	1.938	1.940	1.939
Co-O(**3**)	1.916	1.925	1.924	1.927	1.914
Co-O(3)	1.882	1.892	1.915	1.916	1.908
Co-O(2)	2.276	2.278	2.294	2.295	2.313
Co-O(*3*)	3.457	3.424	3.388	3.390	3.398
Al-O(**2**)	1.799	1.801	1.784	1.786	1.784
Al-O(**3**)	1.855	1.854	1.842	1.842	1.845
Al-Co	2.745	2.754	2.757	2.761	2.749
	Configuration 3				
Co-O(**1**)	1.975	1.977	1.964	1.993	1.966
Co-O(**4**)	1.934	1.933	1.869	1.934	1.869
Co-O(2)	2.183	2.188	2.116	2.161	2.118
Al-O(**1**)	1.867	1.869	1.845	1.853	1.846
Al-O(**4**)	1.808	1.811	1.798	1.791	1.800
Al-Co	2.776	2.777	2.750	2.788	2.752
	Configuration 4				
Co-O(**1**)	1.906	1.843	1.920	1.921	1.923
Co-O(**4**)	1.886	1.888	1.873	1.872	1.871
Co-O(2)	2.188	2.209	2.158	2.175	2.156
Al-O(**1**)	1.842	1.843	1.837	1.837	1.835
Al-O(**4**)	1.832	1.824	1.809	1.811	1.811
Al-Co	2.740	2.742	2.734	2.734	2.737
	Configuration 5				
Co-O(**2**)	1.910	1.908	1.844	1.901	1.840
Co-O(**4**)	1.948	1.956	1.943	1.962	1.947
Co-O(4)	2.102	2.119	2.074	2.125	2.091
Al-O(**2**)	1.805	1.809	1.799	1.790	1.801
Al-O(**4**)	1.857	1.858	1.833	1.843	1.831
Al-Co	2.761	2.764	2.745	2.767	2.739
	Configuration 6				
Co-O(**2**)	1.842	1.844	1.839	1.839	1.836
Co-O(**4**)	1.948	1.961	1.972	1.979	1.983
Co-O(4)	2.018	2.038	2.055	2.067	2.066
Al-O(**2**)	1.807	1.808	1.791	1.792	1.793
Al-O(**4**)	1.849	1.950	1.840	1.839	1.836
Al-Co	2.733	2.736	2.738	2.741	2.739

Table A.4: Structural data for extra-framework cation Co(II) in chabazite in its spin 5/2 state, calculated for different configurations and using both GGA (PW91, PBE) and hybrid (PBE0, HSE03, HSE06) functionals. All distances are given in Å.

	PW91	PBE	PBE0	HSE03	HSE06
	Configuration 1				
Co-O(**2**)	2.212	2.216	2.145	2.161	2.155
Co-O(**3**)	2.051	2.055	1.976	1.975	1.973
Co-O(3)	2.321	2.326	2.262	2.258	2.250
Co-O(***3***)	2.165	2.169	2.075	2.070	2.070
Al-O(**2**)	1.762	1.765	1.767	1.766	1.765
Al-O(**3**)	1.834	1.838	11.849	1.847	1.847
Al-Co	3.030	3.036	3.016	3.021	3.017
	Configuration 2				
Co-O(**2**)	2.089	2.091	2.179	2.180	2.175
Co-O(**3**)	2.073	2.076	2.114	2.116	2.115
Co-O(3)	2.207	2.216	2.292	2.294	2.311
Co-O(2)	3.241	3.230	3.304	3.309	3.312
Co-O(*3*)	4.071	4.045	4.097	4.084	4.096
Al-O(**2**)	1.783	1.786	1.762	1.763	1.764
Al-O(**3**)	1.813	1.815	1.796	1.796	1.796
Al-Co	2.862	2.866	2.887	2.888	2.886
	Configuration 3				
Co-O(**1**)	1.992	1.991	2.039	2.039	2.037
Co-O(**4**)	2.032	2.034	2.098	2.098	2.097
Co-O(2)	2.782	2.843	2.970	3.021	3.024
Al-O(**1**)	1.829	1.831	1.796	1.796	1.796
Al-O(**4**)	1.802	1.805	1.778	1.778	1.777
Al-Co	2.862	2.863	2.884	2.885	2.885
	Configuration 4				
Co-O(**1**)	1.981	1.957	2.061	2.061	2.060
Co-O(**4**)	2.050	2.053	2.100	2.099	2.098
Co-O(2)	2.789	2.798	2.834	2.834	2.832
Al-O(**1**)	1.815	1.818	1.803	1.803	1.802
Al-O(**4**)	1.796	1.800	1.774	1.774	1.773
Al-Co	2.850	2.853	2.865	2.865	2.863
	Configuration 5				
Co-O(**2**)	1.983	1.986	2.062	2.058	2.060
Co-O(**4**)	1.995	1.999	2.054	2.056	2.056
Co-O(4)	2.779	2.858	2.953	3.018	3.042
Al-O(**2**)	1.802	1.804	1.769	1.771	1.770
Al-O(**4**)	1.808	1.809	1.774	1.774	1.772
Al-Co	2.864	2.864	2.884	2.881	2.883
	Configuration 6				
Co-O(**2**)	2.000	2.005	2.066	2.063	2.061
Co-O(**4**)	2.007	2.015	2.060	2.057	2.062
Co-O(4)	2.932	2.959	3.170	3.172	3.246
Al-O(**2**)	1.791	1.793	1.775	1.778	1.776
Al-O(**4**)	1.799	1.802	1.777	1.779	1.773
Al-Co	2.837	2.843	2.859	2.858	2.849

B Adsorption geometries in protonated chabazite

Table B.1: Adsorption geometries for methane, ethane and propane calculated using different levels of theory. This includes the distance (in Å) between the active site and the C atom closest to it (C_1) as well as the distance between the second (C_2) and third (C_3) atom and the closest Si atom. The first line refers to the O(1)-H, the second line to the O(2)-H, the third line to O(3)-H and the fourth line to the O(4)-H adsorption configuration

	PBE	PBE-d	vdW-DF	vdW-BP86
Methane				
C_1-H	2.26	2.16	2.46	2.39
	2.27	2.12	2.69	2.55
	2.36	2.23	2.62	2.44
	2.21	2.14	2.44	2.31
Ethane				
C_1-H	2.22	2.14	2.40	2.55
	2.34	2.36	2.62	2.60
	2.32	2.23	2.50	2.43
	2.20	2.13	2.34	2.29
C_2-Si	4.00	3.79	4.05	4.09
	4.16	3.86	4.34	4.14
	4.31	4.08	4.26	4.33
	4.34	4.06	4.39	4.40
Propane				
C_1-H	2.33	2.16	2.42	2.39
	2.38	2.38	2.58	2.57
	2.28	2.24	2.49	2.42
	2.31	2.23	2.52	2.50
C_2-Si	4.48	3.85	4.07	4.10
	4.39	3.98	4.30	4.34
	4.23	4.08	4.31	4.37
	4.63	4.41	4.63	4.28
C_3-Si	3.88	4.75	4.71	4.54
	4.06	3.64	3.98	4.02
	4.69	4.75	4.55	4.58
	3.93	3.86	3.97	3.99

Bibliography

[1] C. Baerlocher, W. M. Meier, , and D. Olson, *Atlas of Zeolite Framework Types.* Amsterdam: Elsevir, 2001.

[2] W. Shi, H. Shao, H. Li, M. Shao, and S. Du *Jounral of Hazardous Mat.*, vol. 170, pp. 1–6, 2009.

[3] R. Morris and P. Wheatley *Angew. Chem. Int. Ed.*, vol. 47, pp. 4966–4981, 2008.

[4] A. Schlossbauer, S. Warncke, P. Gramlich, J. Kecht, A. Manetto, T. Carell, and T. Bein *Angew. Chem. Int. Ed.*, vol. 49, pp. 4734–4737, 2010.

[5] V. Cauda, H. Engelke, A. Sauer, D. Arcizet, C. Braeuchle, J. Raedler, and T. Bein *Nano Lett.*, vol. 10, pp. 2484–2492, 2010.

[6] J. Caro, M. Noack, P. Kölsch, and R. Sch/"afer *Micropor. Mesopor. Mater.*, vol. 38, pp. 3–24, 2000.

[7] G. Calzaferri and K. Lutkouskaya *Photochem. Photobiol. Sci.*, vol. 7, pp. 879–910, 2008.

[8] M. H. S. Roy and G. Madras *Appl. Energy*, vol. 86, pp. 2283–2297, 2009.

[9] C. Martinez and A. Corma *Coord. Chem. Rev.*, vol. 255, pp. 1558–1580, 2011.

[10] B. Smit and T. Maesen *Nature*, vol. 451, pp. 671–678, 2008.

[11] A. Skoulida and D. Scholl *J. Chem. Phys.*, vol. 113, p. 4379, 2000.

[12] D. Ford and E. Glandt *J. Membr. Sci.*, vol. 107, p. 47, 1995.

[13] S. Reitmeier, R. Mukti, A. Jentys, and J. Lercher *J. Phys. Chem. C*, vol. 112, pp. 2538–2544, 2008.

[14] J. Reitmeier, O. Gobin, A. Jentys, and J. Lercher *Angew. Chem. Int. Ed.*, vol. 48, pp. 533–538, 2009.

[15] S. Reitmeier, O. Gobin, A. Jentys, and J. Lercher *J. Phys. Org. Chem. C*, vol. 113, pp. 15355–15363, 2009.

[16] B. Smit and T. Maesen *Chem. Rev.*, vol. 108, pp. 4125–4181, 2008.

[17] T. Bucko, L. Benco, O. Dubay, C. Dellago, and J. Hafner *J. Chem. Phys.*, vol. 131, p. 214508, 2009.

[18] T. Bucko, L. Benco, J. Hafner, and J. G. Ángyán, "Monomolecular cracking of propane over acidic chabazite: An ab-initio molecular dynamics and transition path sampling study," *J.Catal.*, vol. 279, pp. 220–228, 2011.

[19] M. Iwamoto, S. Yokoo, K. Sakai, and S. Kagawa *J. Chem. Soc. Faraday Trans.*, vol. 77, pp. 1629–1636, 1981.

[20] M. Iwamoto, H. Furukawa, Y. Mine, F. Uemura, S. Mikuriya, and S. Kagawa *J. Chem. Soc. Chem. Commun.*, vol. 11, pp. 1272–1273, 1986.

[21] M. Iwamoto, H. Yahiro, Y. Mine, and S. Kagawa *Chem. Lett.*, vol. 19, pp. 213–217, 1989.

[22] M. Iwamoto, H. Yahiro, H. Tanda, K. Mizuo, Y. Mine, and S. Kagawa *J. Phys. Chem.*, vol. 95, pp. 3727–3730, 1991.

[23] R. Kefirov, A. Penkova, K. Hadjiivanov, S. Dzwingaj, and M. Che *Microporous and Mesoporous Materials*, vol. 116, pp. 180–187, 2008.

[24] W. Schneider, K. Hass, R. Ramprasad, and J. Adams *J. Phys. Chem. B*, vol. 101, pp. 4353–4357, 1997.

[25] G. Spoto, S. Bordiga, D. Scarano, and A. Zecchina *Catal. Lett.*, vol. 13, p. 39, 1992.

[26] L. Benco, T. Bucko, R. Grybos, Z. Sobalik, J. D. edeček, S. Sklenak, J. Hrusak, and J. Hafner *J. Phys. Chem. B*, vol. 111, p. 9393, 2007.

[27] M. Born and J. R. Oppenheimer, "Zur quantentheorie der molekeln," *Ann. Physik*, vol. 84, p. 457, 1927.

[28] D. R. Hartree, "The wave mechanics of an atom with non-coulombic central fields: Parts i, ii, ii," *Proc. Cambridge Phil. Soc*, vol. 24, pp. 89, 111, 426, 1928.

[29] J. C. Slater, "The theory of complex spectra," *Phys. Rev.*, vol. 34, p. 1293, 1929.

[30] V. Fock, "Näherungsmethode zur lösung des quanten-mechanischen mehrkörperproblem," *Z. Phys.*, p. 126, 1930.

[31] P. Knowles and N. Handy *Chem. Phys. Lett.*, vol. 111, p. 315, 1984.

[32] J. Olsen, B. Roos, P. J. rgensen, , and H. Jensen *J. Chem. Phys.*, vol. 89, p. 2185, 1988.

[33] J. Cizek *J. Phys. Chem.*, vol. 45, p. 4256, 2007.

[34] R. Bartlett and M. Musial *Rev. Mod. Phys.*, vol. 79, p. 291, 2007.

[35] F. Jensen, *Introduction to Computational Chemistry*, pp. 133–158. Chichester, England: John Wiley and Sons, 2007.

[36] R. M. Martin, *Electronic Structure - Basic Theory and Practical Methods*. Cambridge University Press,Cambridge, first paperback edition ed., 2008.

[37] P. Hohenberg and W. Kohn, "Inhomogeneous electron gas," *Phys. Rev*, vol. 136, pp. 864–871, 1964.

[38] W. Kohn and L. J. Sham, "Self-consistent equations including exchange and correlation effects," *Phys. Rev*, vol. 140, pp. 1133–1138, 1965.

[39] F. Aryasetiawan and O. Gunnarsson, "The gw method," *Rep. Prog. Phys.*, p. 237, 1998.

[40] J. C. Slater, "Atomic shielding constants," *Phys. Rev*, vol. 36, p. 57, 1930.

[41] S. F. Boys, "Electronic wave-functions 1: A general method of calculation for the stationary stats of any molecular system," *Proc. R. Soc.(London) Series A*, vol. 200, pp. 542–554.

[42] F. Bloch, "über die quantenmechanik der elektronen in kristallgittern," *Z. Phys.*, vol. 52, p. 555, 1928.

[43] E. Fermi, "Displacement by pressure of the high lines of the spectral series," *Nuovo Cimento*, vol. 11, p. 157, 1934.

[44] E. Amaldi, O. D'Agostino, E. Fermi, B. Pontecorvo, F. Rasetti, and E. Segre, "Artificial radioactivity induced by a neutron bombardment - ii," *Proc. R. Soc (London) Series A*, vol. 149, pp. 522–558, 1935.

[45] P. E. Blöchl, *Projector Augmented Wave Method*, vol. 50. 1994.

[46] G. Kresse and D. Joubert, "From ultrasoft pseudopotentials to the projector augmented-wave method," *Phys. Rev. B*, vol. 59, pp. 1758–1775, 1999.

[47] J. Perdew and K. Schmidt, "Jacob's ladder of density functional approximations for the exchange-correlation energy," *AIP Conf. Proc*, vol. 577, pp. 1–20.

[48] *The Bible, Genesis*, ch. 28, p. 12.

[49] J. Perdew and K. Burke, "Comparison shopping for a gradient-corrected density functional," *Int. J. Quantm Chem*, vol. 57, pp. 309–319, 1996.

[50] E. H. Lieb and S. Oxford, "Improved lower bound on the indirect coulomb energy," *Int. J. Quantum Chem.*, vol. 19, p. 427, 1981.

[51] D. M. Ceperly and B. J. Alder, "Ground state of the electron gas by a stochanstic method," *Phys. Rev. Lett*, vol. 45, pp. 566–569, 1980.

[52] E. G. Moroni, G. Kresse, J. Hafner, and J. Furthmüller, "Ultrasoft pseudopotentials applied to magnetic fe, co, and ni: From atoms to solids," *Phys. Rev. B*, vol. 56, pp. 15629–15646, Dec 1997.

[53] P. Svendsen and U. von Barth, "Gradient expansion of the exchange energy from second order density response theory.," *Phys. Rev. B*, vol. 54, pp. 17402–17413, 1996.

[54] Y. Wang and J. Perdew *Phys. Rev. B*, vol. 43, p. 8911, 1991.

[55] J. P. Perdew, K. Burke, and M. Ernzerhof *Phys. Rev. Lett.*, vol. 77, pp. 3865–3868, 1996.

[56] J. P. Perdew, A. Ruzsinszky, G. I. Csonka, O. A. Vydrow, G. E. Scuseria, L. A. Constantin, X. Zhou, and K. Burke *Phys. Rev. Lett*, vol. 100, p. 136406, 2008.

[57] B. Hammer, L. B. Hansen, and J. K. Norskov *Phys. Rev. B*, vol. 59, p. 7413, 1999.

[58] Y. Zhang and W. Yang *Phys. Rev. Lett*, vol. 80, p. 890, 1997.

[59] J. Tao, J. P. Perdew, V. N. Saroverov, and G. E. Scuseria *Phys. Rev. Lett*, vol. 91, p. 146401, 2003.

[60] L. A. Constantin, J. P. Perdew, and J.Tao *Phys. Rev. B*, vol. 73, p. 205104, 2006.

[61] V. Antropov, M. I. Katsnelson, M. van Schilfgaarde, and B. Harmon *Phys Rev. Lett.*, vol. 75, pp. 729–732, 1995.

[62] M. Uhl and J. Kübler *Phys Rev. Lett.*, vol. 77, pp. 334–337, 1996.

[63] T. Oda, A. Pasquarello, and R. Car *Phys Rev. Lett.*, vol. 80, pp. 3622–3625, 1998.

[64] D. Bylander, Q. Niu, and L. Kleinmann *Phys. Rev. B*, vol. 61, pp. R11875–R11878, 2000.

[65] K. Schwarz and P. Mohn *J. Phys. F*, vol. 14, p. L129, 1984.

[66] S. Grimme *J. Comput. Chem*, vol. 27, pp. 1787–1799, 2006.

[67] Q. Wu and W. Yang *J. Chem. Phys*, vol. 116, p. 515, 2002.

[68] A. Tkatchenko and M. Scheffler *Phys Rev. Lett*, vol. 102, p. 073005, 2009.

[69] S. Grimme, J. Antony, S. Ehrlich, and H. Krieg *J. Chem. Phys*, vol. 132, p. 154104, 2010.

[70] T. Bucko, S. Lebeque, J. Angyan, and J. Hafner *J. Phys. Chem. A*, vol. 115, pp. 10097–10105, 2011.

[71] V. Blum, "Density functional theory and beyond with numeric atom-centered orbitals: Fhi-aims," in *PSI-k-2010 conference*, 2010.

[72] J. P. Perdew, K. Burke, and M. Ernzerhof *J. Chem. Phys*, vol. 105, pp. 9982–9985, 1996.

[73] J. Heyd, G. Scuseria, and M. Ernzerhof *J. Chem. Phys.*, vol. 118, pp. 8207–8215, 2003.

[74] A. V. Krukau, O. A. Vydrow, A. F. Izmaylov, and G. Scuseria, vol. 125. 2006.

[75] J. Paier, R. Hirschl, M. Marsman, and G. Kresse *J. Chem. Phys*, vol. 122, p. 234102, 2005.

[76] J. Paier, M. Marsman, K. Hummer, G. Kresse, I. C. Gerber, and J. G.Ángyán *J. Chem. Phys.*, vol. 124, p. 154709, 2006.

[77] J. Paier, M. Marsman, and G. Kresse *J. Chem. Phys*, vol. 127, p. 024103, 2007.

[78] M. Marsman, J. Paier, A. Stroppa, and G. Kresse *J. Phys.: Cond. mat*, vol. 20, p. 064201, 2008.

[79] J. Harl, *The linear response function in density functional theory: Optical spectra and improved description of the electron correlation.* PhD thesis, University of Vienna, Computational Materials Physics, 2008.

[80] D. C. Langreth and J. P. Perdew *Solid State Commun*, vol. 17, p. 1425, 1975.

[81] O. Gunnarson and B. I. Lundqvist *Phys. Rev. B*, vol. 13, p. 4247, 1977.

[82] D. C. Langreth and J. P. Perdew *Phys. Rev. B*, vol. 15, p. 2884, 1977.

[83] J. Harl and G. Kresse *Phys. Rev. B*, vol. 77, p. 045136, 2008.

[84] N. E. Dahlen and U. von Barth *Phys. Rev. B*, vol. 69, p. 195102, 2004.

[85] F. Furche *Phys. Rev. B*, vol. 64, p. 195120, 2005.

[86] F. Furche and T. van Vorhies *J. Chem. Phys*, vol. 122, p. 164106, 2005.

[87] X. Ren, A. Tkatchenko, P. Rinke, and M. Scheffler *Phys. Rev. Lett.*, vol. 106, p. 153003, 2011.

[88] B. Levy and G. Berthier *Int. J. Quantum Chem.*, vol. 2, pp. 307–319, 1968.

[89] Z. Yan, J. P. Perdew, and S. Kurth *Phys. Rev. B: Condens. Matter*, vol. 61, p. 16430, 2000.

[90] A. Ruzsinszky, J. P. Perdew, and G. I. Csonka *J. Chem. Theory Comput.*, vol. 6, pp. 127–134, 2010.

[91] L. Schimka, J. Harl, A. Stroppa, A. Grüneis, M. Marsman, F. Mittendorfer, and G. Kresse *Nature Mat*, vol. 9, pp. 741–744, 2010.

[92] P. Atkins and R. Friedman, *Molecular Quantum Mechanics*. Oxford University Press, New York, (fourth edition ed., 2005.

[93] M. Marsman, A. Grüneis, J. Paier, and G. Kresse *J. Chem. Phys*, vol. 130, p. 184103, 2009.

[94] M. Dion, H. Rydberg, E. Schröder, D. C. Langreth, and B. I. Lundqvist *Phys. Rev. Lett.*, vol. 92, p. 246401, 2004.

[95] M. Dion, H. Rydberg, E. Schröder, D. C. Langreth, and B. I. Lundqvist *Phys. Rev. Lett*, vol. 95, p. 109902, 2005.

[96] D. C. Langreth, M. Dion, H. Rydberg, E. Schröder, P. Hyldgaard, and B. I. Lundqvist *Int. J. Quantum Chem*, vol. 101, pp. 599–610, 2005.

[97] A. Gulans, M. J. Puska, and R. M. Nieminen *Phys. Rev. B*, vol. 79, p. 201105(R, 2009.

[98] G. Román-Pérez and J. M. Soler *Phys. Rev. Lett*, vol. 103, p. 096102, 2009.

[99] J. Klimes, D. Bowler, and A. Michaelides *J. Phys. Cond. Mat.*, vol. 22, p. 022201, 2010.

[100] J. Klimes, D. Bowler, and A. Michaelides *Phys. Rev. B*, vol. 83, p. 195131, 2011.

[101] K. Lee, E. D. Murray, L. Kong, B. I. Lundqvist, and D. C. Langreth *Phys. Rev. B*, vol. 82, p. 081101, 2010.

[102] J. Wellendorff, A. Kelkkanen, J. J. Mortensen, B. I. Lundqvist, and T. Bligaard *Top. Catal.*, vol. 35, pp. 378–383, 2010.

[103] J. P. Perdew and K. Schmidt in *Density Functional Theory and its Applications to Materials* (C. v. A. V. van Doren and P. Geerlings, eds.), American Institute of Physics (Melville, NY), 2001.

[104] J. P. Perdew and S. Kurth, "A primer in density functional theory," in *Lecture Notes in Physics* (F. N. C. Fiolhais and M. Marques, eds.), vol. 620, Springer, Berlin, 2003.

[105] B. Hammer and M. Scheffler *Phys. Rev. Lett.*, vol. 74, p. 3487, 1994.

[106] A. Eichler, J. Hafner, and G. Kresse *J. Phys.: Cond. Mat.*, vol. 8, p. 7659, 1996.

[107] A. Gil, A. Clotet, J. M. Ricart, G. Kresse, M. Garcia-Hernandez, N. Rösch, and P. Sautet *Surf. Sci.*, vol. 530, p. 71, 2003.

[108] L.Benco, J.Hafner, F.Hutschka, and H.Toulhoat *J. Phys. Chem. B*, vol. 107, pp. 9756–9762, 2003.

[109] F. Göltl and J. Hafner p. preceding paper of this issue.

[110] A. Stroppa, K. Termentzidis, J. Paier, G. Kresse, and J. Hafner *Phys. Rev. B*, vol. 76, p. 1954402, 2007.

[111] L. Hedin and S. Lundqvist, *Solid State Physics*, vol. 23. Academic Press, NY, 1969.

[112] M. S. Hybertsen and S. G. Louie *Phys. Rev. B*, vol. 34, p. 5390, 1986.

[113] M. Shishkin and G. Kresse *Phys. Rev. Lett.*, vol. 99, p. 246403, 2007.

[114] A. Becke *J. Chem. Phys.*, vol. 98, p. 5648, 1993.

[115] S. Kurth, J. P. Perdew, and P. Blaha *Intern. J. Quantum Chem.*, vol. 75, p. 889, 1999.

[116] C. Franchini, R. Podloucky, J. Paier, M. Marsman, and G. Kresse *Phys. Rev. B*, vol. 75, p. 195128, 2007.

[117] J. Paier, R. H. M. Marsman, and G. Kresse *J. Chem. Phys.*, vol. 122, p. 234102, 2005.

[118] E. L. Uzunova, F. Göltl, G. Kresse, and J. Hafner *J. Phys. Chem. C*, vol. 113, p. 5274, 2009.

[119] K. Hummer, J. Harl, and G. Kresse *Phys. Rev. B*, vol. 80, p. 115205, 2009.

[120] B. F. Mentzen and G. Bergeret *J. Phys. Chem. C*, vol. 111, p. 12512, 2007.

[121] C. Lamberti, S. Bordiga, M. Salvaggio, G.Spoto, . Zecchina, F. Geobaldo, G. Vlaic, and M. Bellatreccia *J. Phys. Chem. B*, vol. 101, p. 344, 1997.

[122] K. Pierloot, A. Delabie, C. Ribbing, A. A. Verbreckmoes, and R. A. Schoonheydt *J. Phys. Chem.*, vol. 102, p. 10789, 1998.

[123] A. Delabie, K. Pierloot, M. H. Groothaert, R. A. Schoonheydt, and L. G. Vanquickenborne *Eur. J. Inorg. Chem.*, p. 515, 2002.

[124] Z. Sobalik, J. D. edeček, D. Kaucký, B. Wichtlerová, L. Drozdová, and R. Prins *J. Catal.*, vol. 194, p. 330, 2000.

[125] C. Resini, T. Mantanari, L. Nappi, G. Bagnasco, M. Turco, G. Busca, F. Bregani, M. Notaro, and G. Rocchini *J. Catal*, vol. 214, p. 179, 2003.

[126] L. B. Guttierrez, E. E. Miró, and M. A. Ulla *Appl. Catal. A*, vol. 321, p. 7, 2007.

[127] J. Hafner, L. Benco, and T. Bucko *Topics in Catal.*, vol. 37, p. 41, 2006.

[128] R. Grybos, J. Hafner, L. Benco, and H. Toulhoat *J. Phys. Chem. B*, vol. 111, p. 6454, 2007.

[129] R. Grybos, J. Hafner, L. Benco, and P. Raybaud *J. Phys. Chem.*, vol. 112, p. 12349, 2008.

[130] M. Sierka and J. Sauer *J. Chem. Phys.*, vol. 112, p. 6983, 2000.

[131] R. Bulanek, H. Drobna, P. Nachtigall, M. Rubes, and O. Bludsky *Phys. Chem. Chem. Phys.*, vol. 82, p. 5535, 2006.

[132] A. Pulido and P. Nachtigall *Phys. Chem. Chem. Phys.*, vol. 11, p. 1447, 2009.

[133] O. Bludski, M. Silhan, P. Nachtigall, T. Bucko, L. Benco, and J. Hafner *J. Phys. Chem.*, vol. 109, p. 9631, 2005.

[134] J. A. Swisher, N. Hansen, T. Maesen, F. J. Keil, B. Smit, and T. A. Bell *J. Phys. Chem.*, vol. 114, p. 10229, 2010.

[135] G. Kresse and J. Hafner *Phys. Rev. B*, vol. Rev. B **48**, p. 13115, 1993.

[136] G. Kresse and J. Furthmüller *Comput. Mat. Sci.*, vol. 6, p. 15, 1996.

[137] H. J. Monkhorst and J. D. Pack *Phys. Rev. B*, vol. 13, p. 5188, 1976.

[138] S. H. Vosko, L. Wilk, and M. Nusair *Can. J. Phys.*, vol. 58, p. 1200, 1980.

[139] P. H. Dederichs, S. Blügel, R. Zeller, and H. Akai *Phys. Rev. Lett.*, vol. 53, p. 2512, 1984.

[140] A. R. Williams, V. L. Moruzzi, J. Kübler, and K. Schwarz *Bull. Am. Phys. Soc.*, vol. **29**, p. 278, 1984.

[141] M. M. Harding and B. M. Kariuki *Acta Crystallogr. C*, vol. 50, p. 852, 1994.

[142] P. J. Smeets, J. S. Woertink, E. I. Solomon, and R. A. Schoonheydt *Inorgan. Chem.*, vol. 49, 2010.

[143] W. Löwenstein *Am. Mineralog.*, vol. 39, p. 92, 1954.

[144] L. J. Smith, A. Davidson, and A. K. Cheetham *Catal. Lett.*, vol. 49, p. 143, 1997.

[145] D. W. Fickel and R. F. Lobo *J. Phys. Chem. C*, vol. 114, p. 1633, 2010.

[146] Y. Jeanvoine, J. Ángyán, G. Kresse, and J. Hafner *J. Phys. Chem. B*, vol. 102, p. 5573, 1998.

[147] F. Cora, M. Alfredsson, C. M. Barker, R. G. Bell, M. D. Foster, I. Saadoune, A. Simperler, and C. R. A. Catlow *J. Solid State Chem.*, vol. 176, p. 496, 2003.

[148] R. F. Bader, *Atoms in Molecules: A Quantum Theory, Intern. Series of Monographs on Chemistry, vol.22*. Clarendon Press, Oxford, 1990.

[149] W. Tang, E. Sanville, and G. Henkelman *J. Phys.: Cond. Mat.*, vol. 21, p. 2009, 2009.

[150] P. Nachtigall, D. Nachtigallová, and J. Sauer *J. Phys. Chem. B*, vol. 104, p. 1738, 2000.

[151] I. Georgieva, L. Benco, D. Tunega, N. Trendafilova, H. Lischka, and J. Hafner *J. Chem. Phys.*, vol. 131, p. 054101, 2009.

[152] E. El-Malki, D. Werst, P. Doan, and W. Sachter *J. Phys. Chem. B*, vol. 104, p. 5924, 2000.

[153] Y. Kuroda, Y. Yoshikawa, S. Konno, H. Hamano, H. Maeda, R. Kumashiro, and M. Nagao *J. Phys. Chem.*, vol. 99, p. 10621, 1995.

[154] W. Grünert, N. W. Hayes, R. W. Joyner, E. S. Shpiro, M. Rafiq, H. Siddiqui, and G. N. Baeva *J. Phys. Chem.*, vol. 98, p. 10832, 1994.

[155] S. A. Yashik, Z. R. Ismagilov, and V. A. Anufrienko *Catal. Today*, vol. 110, p. 310, 2005.

[156] X. Solans-Monfort, V. Branchadell, M. Sodupe, C. M. Zicovich-Wilson, E. Gribov, G. Soto, C. Busco, and P. Ugliengo *J. Phys Chem. B*, vol. 108, p. 8278, 2004.

[157] S. T. Korhonen, D. W. Fickel, R. F. Lobo, B. M. Weckhuysen, and A. M. Bale *Chem. Commun.*, vol. 47, p. 800, 2011.

[158] M. Zamadics and L. Kevan *J. Phys. Chem.*, vol. 96, p. 8989, 1992.

[159] M. Calligaris, G. Nardin, and L. Randaccio *Zeolites*, vol. 4, p. 251, 1984.

[160] Y. Xu and W. Y. Ching *Phys. Rev. B*, vol. 44, p. 11048, 1991.

[161] C. Sevik and C. Bulutay *J. Mater. Sci.*, vol. 42, p. 6555, 2007.

[162] L. Martin-Samos, G. Bussi, A. Ruini, E. Molinari, and M. J. Caldas, "Sio2 in density functional theory and beyond," *physica status solidi (b)*, vol. 248, no. 5, pp. 1061–1066, 2011.

[163] F. Mauri, A. Pasquarello, B. G. Pfrommer, Y. G. Yoon, and S. G. Louie *Phys. Rev. B*, vol. 62, p. R4786, 2000.

[164] Z. A. Weinberg, G. W. Rubloff, and E. Bassous *Phys. Rev. B*, vol. 19, p. 3107, 1979.

[165] L. E. Ramos, J. Furthmüller, and F. Bechstedt *Phys. Rev. B*, vol. 69, p. 085102, 2004.

[166] P. Umari, Q. X, N. Marzari, G. Stenuit, L. Giacomazzi, and S. Baroni *phys. stat. solidi B*, vol. 248.

[167] T. Demuth, J. Hafner, L. Benco, and H. Toulhoat *J. Phys. Chem. B*, vol. 104, p. 4593, 2000.

[168] J. B. Nicholas and J. A. A. C. Hess *J. Am. Chem. Soc.*, vol. 116, p. 5428, 1994.

[169] D. Kaucký, J. D. edeček, and B. Wichtlerová *Micropor. Mesopor. Mater.*, vol. **31**, p. 75, 1999.

[170] J. Dedecek, L. ˇ Capek, D. Kaucký, Z. Sobalik, and B. Wichtlerová *J. Catal.*, vol. 211, p. 198, 2002.

[171] J. Janas, T. Shishido, M. Che, and S. Dzwigaj *Appl.Catal. B*, vol. 89, p. 196, 2009.

[172] J. Dedecek, B. Wichtlerová, and P. Kubát *Micropor. Mesopor. Mater.*, vol. 32, p. 63, 1999.

[173] J. Dedecek, Z. Sobalik, Z. T. zková, D. Kaucký, and B. Wichtlerová *J. Phys. Chem.*, vol. 99, p. 16327, 1995.

[174] D. Nachtigallová, P. Nachtigall, and J. Sauer *Phys. Chem. Chem. Phys.*, vol. 3, p. 1552, 2001.

[175] M. H. Groothaert, J. A. van Bokhoven, A. A. Battiston, B. M. Weckhuysen, and R. A. Schoonheydt *J. Am. Chem. Soc.*, vol. 125, p. 7629, 2003.

[176] P. J. Smeets, M. H. Groothaert, and R. A. Schoonheydt, vol. 110. 2005.

[177] J. Dedecek private communication and to be published.

[178] J. Dedecek and B. Wichtlerová *J. Phys. Chem. B*, vol. 103, p. 1462, 1999.

[179] J. Dedecek, D. Kaucký, B. Wichtlerová, and O. Gonsiorová *Phys.. Chem. Chem. Phys.*, vol. 4, p. 5406, 2002.

[180] K. Hadjiivanov and G. Vayssilov *Adv. Catal.*, vol. 47, p. 307, 2002.

[181] E. Garrone and C. Otero-Arean *Chem. Soc. Rev.*, vol. 34, p. 846, 2005.

[182] K. Hadjiivanov *Catal. Rev. Sci. Eng.*, vol. 42, p. 71, 2000.

[183] Y. Kuroda, Y. Yoshikawa, R. Kumashiro, and M. Nagao *J. Phys. Chem. B*, vol. 101, p. 6497, 1997.

[184] Y. Fu, Y. Tian, and P. Lin *J. Catal.*, vol. 132, p. 85, 1991.

[185] K. Hadjiivanov and H. Knözinger *Phys. Chem. Chem. Phys.*, vol. 3, p. 1132, 2001.

[186] G. T. Palomino, S. Bordiga, A. Zecchina, G. L. Marra, and C. Lamberti *J. Phys. Chem. B*, vol. 104, p. 8641, 2000.

[187] V. Y. Borovkov, M. Jiang, and Y. Fu *J. Phys. Chem. C*, vol. 103, pp. 5010–5019, 1999.

[188] E. Broclawik, J. Datka, B. Gil, W. Piskorz, and P. Kozyra *Topics in Catalysis*, vol. 11+12, p. 335, 2000.

[189] R. Bulánek *Phys. Chem. Chem. Phys*, vol. 6, p. 4208, 2004.

[190] N. Jardillier, E. A. Villagomez, G. Delahay, B. Coq, and D. Berthomieu *J. Phys. Chem. B*, vol. 110, pp. 16413–16421, 2006.

[191] K. Góra-Marek, B. Gil, and J. Datka *Appl. Catal. A: General*, vol. 353, pp. 117–121, 2009.

[192] O. Bludsky, M. Silhan, D. Nachtigallova, and P. Nachtigall *J. Phys. Chem. A*, vol. 107, p. 10381, 2003.

[193] D. Nachtigallová, O. Bludsky, C. O. Areán, R. Bulánek, and P. Nachtigall *Phys. Chem. Chem. Phys.*, vol. 8, p. 4859, 2006.

[194] P. Rejmak, M. Sierka, and J. Sauer *Phys. Chem. Chem. Phys.*, vol. 9, pp. 5446–5456, 2007.

[195] K. Hadjiivanov, B. Tsyntsarski, T. Venkov, M. Daturi, J. Saussey, and J. C. Lavalley *Phys. Chem. Chem. Phys.*, vol. 5, pp. 243–245, 2003.

[196] K. Hadjiivanov, E. Ivanova, M. Daturi, J. Saussey, and J.-C. Lavalley *Chem. Phys. Lett.*, vol. 37, p. 712, 2003.

[197] G. Kresse, J. Furthmüller, and J. Hafner *Europhys. Lett*, vol. 32, p. 729, 1995.

[198] P. Ugliengo, "Anharm - a program to numerically solve the mononuclear schrödinger equation.".

[199] I. N. Senchenya, E. Garrone, and P. Ugliengo *J. Molec. Struct. - THEOCEM*, vol. 368, p. 93, 1996.

[200] A. W. Mantz, J. K. G. Watson, K. N. Rao, D. L. Albrotton, A. L. Schmeltekope, and R. N. Zare *J. Molec. Spectroscop.*, vol. 39, p. 180, 1971.

[201] M. Zhou and L. Andrews *J. Chem. Phys.*, vol. 111, pp. 4548–4557, 1999.

[202] D. D. W. J. D. Cox and V. A. Medvedev, *CODATA Key Values for Thermodynamics*. New York: Hemisphere, 1984.

[203] *Handbook of Chemistry and Physics*. Boca Raton, FL: CRC Press, 85th ed., 2004-2005.

[204] K. Nakamoto, *Infrared and Raman Spectra of Inorganic and Coordination Compounds*. New York: Wiley, 4th ed., 1986.

[205] F. Meyer, Y. M. Chen, and P. B. Armentrout *J. Am. Chem. Soc.*, vol. 177, p. 4071, 1995.

[206] J. Pilme, B. Silvi, and M. E. Alikhani *J. Phys. Chem. A*, vol. 107, pp. 4506–4514, 2003.

[207] M. Zhou and L. Andrews *J. Phys. Chem. A*, vol. 103, pp. 7773–7784, 1999.

[208] M. Zhou and L. Andrews *J. Phys. Chem. A*, vol. 104, pp. 2618–2625, 2000.

[209] M. Zhou and L. Andrews *J. Phys. Chem. A*, vol. 104, pp. 3915–3925, 2000.

[210] K. Koszinowski, D. Schröder, H. Schwarz, M. C. Holthausen, J. Sauer, H. Koizumi, and P. B. Armentrout *Inorg. Chem.*, vol. 41, p. 5882, 2002.

[211] M. Davidova, D. Nachtigallova, P. Nachtigall, and J. Sauer *J. Phys. Chem. B*, vol. **108**, pp. 13674–13682, 2004.

[212] A. E. Reed, L. A. Curtiss, and F. Weinhold *Chem. Rev.*, vol. 88, p. 899, 1988.

[213] Z. Sojka and S. Witkowski *Topics in Catalysis*, vol. 18, pp. 279–282, 2002.

[214] L. Gutierrez, E. Miró, and S. Irusta *Micropor. Mesopor. Mater.*, vol. 114, p. 281, 2008.

[215] A. Gervasini, C. Picciau, and A. Aroux *Micropor. Mesopor. Mater.*, vol. 35-36, p. 457, 2000.

[216] D. B. Akolekar, S. K. Bhargava, and K. J. Foger *J. Chem. Soc. Faraday Trans*, vol. 94, p. 155, 1998.

[217] A. Frache, B. Calella, M. Cadoni, R. Pirone, P. Ciambelli, H. O. Pastore, and H. Marchese *Catal. Today*, vol. 75, p. 359, 2002.

[218] W. O. Haag *Struct. Surf. Sci. Catal.*, vol. 84, p. 1375, 1994.

[219] J. A. Biscardi and E. Iglesia *Phys. Chem. Chem. Phys.*, vol. 1, p. 5753, 1999.

[220] A. Auroux, A. Tuel, J. Bandiera, Y. B. Taarit, and J. Guil *J. Appl. Catal.*, vol. 93, p. 181, 1993.

[221] F. Eder and J. A. Lercher *J. Phys. Chem.*, vol. 100, p. 16460, 1996.

[222] F. Eder, N. Stockenhuber, and J. A. Lercher *J. Phys. Chem. B*, vol. 101, p. 5414, 1997.

[223] F. Eder and J. A. Lercher *J. Phys. Chem. B*, vol. 101, p. 1273, 1997.

[224] J. F. M. Denayer, N. Souverijus, P. A. Jacobs, J. A. Martens, and G. V. Baron *J. Phys. Chem. B*, vol. 102, p. 4588, 1998.

[225] H. Stach, K. Fiedler, and J. Jäucher *Pure Appl. Chem.*, vol. 10, p. 2193, 1993.

[226] E. G. Derouane, J. M. André, and A. A. Lucas *J. Catal.*, vol. 110, p. 58, 1988.

[227] B. Smit and J. Siepman *J. Phys. Chem.*, vol. 98, p. 8442, 1996.

[228] M. S. Lee, P. E. Maslen, and M. Head-Gordon *J. Chem. Phys.*, vol. 112, p. 3592, 2000.

[229] C. Tuma and J. Sauer *Chem. Phys. Lett.*, vol. 387, p. 388, 2004.

[230] A. Grüneis, M. Marsman, J. Harl, L. Schimka, and G. Kresse *J. Chem. Phys.*, vol. 131, p. 143115, 2009.

[231] D. L. et al. *J. Phys.: Cond. Mat.*, vol. 21, p. 084203, 2009.

[232] T. Thonhauser, V. R. Cooper, S. Li, A. Puzder, P. Hyldgaard, and D. C. Langreth *Phys. Rev. B*, vol. 76, p. 125112, 2007.

[233] Y. M. Niquet, M. Fuchs, and X. Gonze *Phys. Rev. A*, vol. 68, p. 032507, 2003.

[234] S. Adler *Phys. Rev.*, vol. 126, p. 413, 1962.

[235] N. Wiser *Phys. Rev.*, vol. 129, p. 62, 1963.

[236] F. Furche *Phys. Rev. B*, vol. 64, p. 195120, 2001.

[237] M. Fuchs and X. Gonze *Phys. Rev. B*, vol. 65, p. 235109, 2003.

[238] M. Gajdos, J. F. K. Hummer, G. Kresse, and F. Bechstedt *Phys. Rev. B*, vol. 74, p. 035101, 2006.

[239] J. Denayer, L. Devriese, S. Couck, J. Martens, R. Singh, P. Webley, and G. Baron *J. Phys. Chem. C*, vol. 112, p. 16593, 2008.

[240] S. I. Zones and R. A. V. Nostrand *Zeolites*, vol. 8, p. 166, 1988.

[241] I. Leardini, S. Quartieri, and G. Vezzalini *Micropor. Mesopor. Mater.*, vol. 127, p. 219, 2010.

[242] H. Andersen *J. Chem. Phys.*, vol. 72, p. 2384, 1980.

[243] R. Barrer and J. Davies *Proc. Roy. Soc. London A*, vol. 322, pp. 1–19, 1971.

[244] J. Denayer and G. Baron *Adsorption*, vol. 3, pp. 251–265, 1997.

List of publications

1. E. Uzunova, F. Göltl and J. Hafner, *Application of Hybrid Functionals to the Modeling of NO Adsorption on Cu-SAPO-34 and Co-SAPO-34: A Periodic DFT Study*, J. Phys. Chem. C **113**, 5274-5291, 2009

2. F. Göltl, J. Hafner, *Alkane adsorption in Na-exchanged chabazite: The influence of dispersion forces*, J. Chem. Phys **134**, 064102,2011

3. F. Göltl, J. Hafner, *Structure and Properties of Metal-exchanged Zeolites Studied Using Gradient-corrected and Hybrid Functionals: I. Structure and Energetics*, submitted to J. Chem. Phys., 2011

4. F. Göltl, J. Hafner, *Structure and Properties of Metal-exchanged Zeolites Studied Using Gradient-corrected and Hybrid Functionals: II. Electronic Structure and Photoluminescence Spectra*, submitted to J. Chem. Phys., 2011

5. F. Göltl, J. Hafner, *Structure and Properties of Metal-exchanged Zeolites Studied Using Gradient-corrected and Hybrid Functionals: III. Energetics and Vibrational Spectroscopy of Adsorbates*, submitted to J. Chem. Phys., 2011

Oral and poster presentations

Oral presentations

1. F. Göltl and J. Hafner, *CO and NO adsorption in Cu- and Co-exchanged chabazite - a comparative DFT- and hybrid functional study*, 22. Deutsche Zeolith Tagung, Munich, March 2010

2. F. Göltl and J. Hafner, *Alkane adsorption in chabazite The influence of dispersion forces*, Seminar of the Science College CMS, Vienna, December 2010

3. F. Göltl and J. Hafner, *Akane adsorption in protonated and Na-exchanged chabazite - comparing different ways to model van der Waals interactions*, Frülingstagung der DPG, Dresden, March 2011

4. F. Göltl and J. Hafner, *Adsorption of small molecules in chabazite - Modelling van der Waals interactions*, FEZA 2011, Valencia, July 2011

5. F. Göltl, *Alkane adsorption in chabazite - Modelling van der Waals interactions accurately*, Group Seminar of the catalysis department of the ENS Lyon, Lyon, September 2011

Poster presentations

1. F. Göltl and J. Hafner, *CO-Adsorption in Cu-Exchanged Chabazite A Comparative DFT- and Hybrid Functional Study*, Catalysis from First Principles, Vienna, May 2009

2. F. Göltl and J. Hafner, *Alkane Adsorption in Protonated and Na-Exchanged Chabazite - Comparing Different Ways to Model Van Der Waals Interactions*, TOCAT6/APCAT5, Sapporo, July 2010 - Awarded with best young scientist award - poster presentation

3. F. Göltl and J. Hafner, *Alkane adsorption in protonated and Na-exchanged chabazite Comparing different ways to model van der Waals interactions*, Ψ_k 2010 conference, Berlin, September 2010

4. F. Göltl and J. Hafner, *Do hybrid functionals improve the description of adsorption sites in Cu- and Co-exchanged chabazte?*, Catalysis from First Principles, Magleås, May 2011

Curriculum vitae

Personal Information

Name: Mag. Florian Göltl
Date of birth: January 24^{th}, 1981
Place of birth: Vienna
Nationality: Austrian
Parents: Mag. Elfriede Göltl, Dipl.-Ing. Franz Göltl
Contact: florian.goeltl@univie.ac.at

Education

1987-1991	Volksschule (primary school) in Vienna, Austria
1991-1999	Bundesgymnasium Wien 6 (secondary school/highschool) in Vienna
1999-2000	Zivildienst (civil service) at BGRG21 Ödenburgerstraße, Vienna
2000-2007	Study of physics at the University of Vienna, graduation in mathematical physics Diploma-thesis: "Bosons in elongated traps: The one-dimensional limit of the wave function" Supervision: o. Univ.-Prof. Dr. Jakob Yngvason
2005-2006	Education as Lehrwart (Instructor) for pool-billiard at the Bundesanstalt für Leibeserziehung Innsbruck
2006-(2012)	Work as instructor for pool-billiard at University Sports Institute, Vienna
2007-(2011)	Doctoral studies in computational physics at the University of Vienna PhD-thesis: "The Catalytic Properties of Chabazite - A Computational Study" Supervisor: o. Univ.-Prof. Dr. Dipl.-Ing. Jürgen Hafner
2009-(2012)	Education as trainer for pool-billiard at the Bundessportakademie Vienna